Microfabricated Sensor Arrays for Life Science Applications

THÈSE N^{O} 6100 (2014)

PRÉSENTÉE LE 28 FÉVRIER 2014
À LA FACULTÉ DES SCIENCES ET TECHNIQUES DE L'INGÉNIEUR
LABORATOIRE DE CAPTEURS, ACTUATEURS ET MICROSYSTÈMES
PROGRAMME DOCTORAL EN MICROSYSTÈMES ET MICROÉLECTRONIQUE

ÉCOLE POLYTECHNIQUE FÉDÉRALE DE LAUSANNE

POUR L'OBTENTION DU GRADE DE DOCTEUR ÈS SCIENCES

PAR

Frédéric LOIZEAU

acceptée sur proposition du jury:

Prof. Ph. Renaud, président du jury
Prof. N. de Rooij, Dr S. Gautsch, directeurs de thèse
Prof. J. Brugger, rapporteur
Prof. B. Pruitt, rapporteur
Dr P. Vettiger, rapporteur

ÉCOLE POLYTECHNIQUE
FÉDÉRALE DE LAUSANNE
Suisse
2014

Logic will get you from A to B.
Imagination will take you everywhere.
— Albert Einstein

Abstract

Cancer is the third cause of death in the world. Despite recent advances in medical science, mortality rates are stagnating for most of diagnosed tumours and cancer is foreseen as the disease of the 21st century. Indeed, the capability of cancer to eventually form metastases is a major obstacle towards full and definitive recoveries. Hence, the development of new early screening tools or the formulation of models describing the spreading capability of cancerous cells will be instrumental in cancer research.

In this thesis, I will discuss how microfabricated sensors, when arranged in arrays, could advantageously solve the above-mentioned problems. In particular, the development of two devices will be presented. First, a two-dimensional cantilever array capable of simultaneously assessing the mechanical properties of multiple cells is proposed. The design of the array introduces a new technique that allows the batch fabrication of spherical tips with a radius of curvature up to 7 μm. Thus eliminating the tedious manual gluing of beads at the cantilever end to provide a spherical tip. The fabricated cantilever arrays were successfully integrated within a custom-made AFM system and multiple force-indentation curves on cancerous cells were acquired with a throughput of 4 cells/min.

In a second part, I present a molecular sensing platform based on a membrane-type surface stress sensors (MSS). Finite element simulations based on ANSYS were used to optimise the sensor design towards highest signal-to-noise ratio. MSS were then functionalised with a polymer layer (Cellulose acetate butyrate) sensitive to water molecules and characterised as humidity sensors. The sensors presented a linear response from 0% to 70% of relative humidity. Time constants were 0.8 s ± 0.1 s. Compared to classical cantilever-based sensors, the MSS were on average 7.5 times more sensitive. In addition, while the reproducibility of cantilevers is closely correlated with that of their coating, the MSS were five times less sensitive to the same coating variability. The high sensor-to-sensor reproducibility, combined with a sub-second response time and linear behaviour, makes the MSS a powerful platform for molecular detection. As a demonstration, an MSS array of eight sensors, each functionalised with a different polymer, was used in an electronic nose system. The system successfully distinguished healthy persons from patients suffering from neck-and-head cancer based on the analysis of their exhaled breath.

While the two proposed microfabricated sensor arrays have been specifically designed for cancer research, they could find numerous applications in life sciences, from mechanobiology studies to the detection of specific antigens in the blood.

Keywords: Microsystems, Microfabrication, Piezoresistive readout, Cell force spectroscopy, Nanomechanical sensors, Electronic nose

Résumé

Le cancer est la troisième cause de mortalité dans le monde. Malgré les récentes avancées médicales, les taux de mortalité stagnent pour la plupart des tumeurs diagnostiquées et certains prédisent que le cancer sera la maladie du $21^{\text{ème}}$ siècle. En effet, sa capacité naturelle à former des métastases est un obstacle majeur à une guérison totale et définitive. Par conséquent, le développement de nouveaux outils de dépistage précoce ou bien la formulation de modèles décrivant la propagation des cellules métastatiques sont des enjeux primordiaux pour la recherche contre le cancer.

Dans cette thèse, je vais explorer diverses solutions aux problèmes ci-dessus qui peuvent être proposées par des micro-capteurs. Le développement de deux dispositifs sera présenté. Dans un premier temps, un réseau de micro-leviers est suggéré pour mesurer les propriétés mécaniques de plusieurs cellules en parallèle. Son développement introduit une nouvelle technique qui permet la fabrication en série de pointes sphériques ayant un rayon de courbure jusqu'à 7 μm. Ainsi, l'étape fastidieuse consistant à coller une micro-bille à la fin des leviers pour obtenir une pointe sphérique est supprimée. Des courbes "force-indentation" ont été finalement obtenues sur plusieurs cellules cancéreuses avec une vitesse d'exécution d'environ 4 cellules/minute.

Dans un second temps, je présente une plateforme de détection moléculaire basée sur des capteurs de stress de surface de la forme d'une membrane suspendue (MSS). A l'aide du logiciel de simulation par éléments finis ANSYS, le design du capteur a été optimisé pour un ratio signal-sur-bruit maximal. Des MSS ont ensuite été fonctionnalisés avec une couche de polymère (Cellulose acetate butyrate) sensible aux molécules d'eau, puis ils ont été caractérisés en tant que capteurs d'humidité. Ils ont présenté une réponse linéaire entre 0% et 70% d'humidité relative avec des temps de réponse de 0.8 s ± 0.1 s. Comparés à des capteurs plus classiques de type micro-leviers, les MSS sont 7.5 fois plus sensibles. Alors que la répétabilité des leviers dépend fortement de celle de leur couche active, les MSS sont cinq fois moins sensibles aux variations de leur fonctionalisation. Cette haute répétabilité, combinée à un temps de réponse sous la seconde ainsi qu'un comportement linéaire, fait du MSS une plateforme de détection moléculaire idéale. Pour en faire la démonstration, un réseau de huit MSS a été utilisé dans un système de nez électronique. Ce dernier a permis de distinguer un groupe de personnes saines d'un groupe de personnes souffrantes d'un cancer de la gorge grâce à la seule analyse de leur haleine.

Bien que les deux réseaux de micro-capteurs présentés dans cette thèse ont été développés pour la recherche contre le cancer, ils auraient potentiellement des applications très diverses en science de la vie.

Mots clés : Microsystèmes, Microfabrication, Piezorésistances, Spectroscopie de force sur cellule, Capteurs nanomécaniques, Nez électronique

Contents

List of Figures

List of Tables

Thesis introduction

Some people think that microtechnology was born with the invention of the transistor at Bell's Lab in 1947. I prefer to believe that it has its roots from an earlier time, when batteries did not yet exist and steam engines were still experimental. Between 1767 and 1774, Pierre Jaquet-Droz, with the help of his son and Jean-Frédéric Leschot, created three automata dolls with the goal of showing off his watchmaking skills. The most famous one, known as "The Writer", has in his chest a mechanism composed of more than 6,000 parts and is still in working order. With the help of exchangeable cams, it is capable of writing any sentence up to 40 characters. Miniaturised, programmable, and reliable, these automata are a perfect example of microtechnology, 150 years before the first computers developed by IBM.

Today, we, as engineers, face challenges that cannot be solved only with our mechanical or electrical background. As these precursors who relied equally on mechanics, material sciences, and their fabrication skills to create incredibly complicated pieces, we have to combine our knowledge with the expertise of others, such as biologists and medical researchers. Silicon was the material of the 20th century, cells and DNA will probably be those of the 21st. Therefore, the combination of microtechnology and life sciences may well lead us to new paradigm shifts in many domains.

Motivations

Despite the fact that tumours have been known since ancient Egypt, cancer is still the third cause of death in the world today. In comparison, the human immunodeficiency virus (HIV) was only discovered thirty years ago but through research, proper care and awareness, is slowly shifting from a lethal to a chronic disease. While medical researchers are able to control a virus with such a high mutability, they are struggling to decrease the mortality rate of cancer, despite the arsenal of available therapeutic treatments. Why is it so? If the risk factors are known, if the treatments are established, what is preventing them from curing cancer?

Without answering this challenging question, one aspect is crucial to understand the difficulty to treat such a disease: its capability to form metastases. This fact describes a unique characteristic of cancer, which allows it spreading from its initial location to other organs in the body. Once diagnosed with cancer, a patient has very different chances of survival depending on whether it has metastasised or not: a localised tumour is much easier to remove and treat. Since every cancer will eventually evolve to a metastatic stage, the moment of diagnosis becomes critical. The earlier the disease is detected, the higher are the chances of recovery for the patient. While routine diagnoses already exist for a few cancers, such as breast or prostate tumours, many are still detected too late, when the disease has reached an advanced state. To prevent cancer from becoming the disease of the 21st century, researchers and medical doctors must not only develop new diagnostic tools but they need also to understand the spreading capabilities of tumorous and metastatic cells.

Some solutions to such challenge may come from a field that is now mature enough to explore applications in life sciences. Micro-electro-mechanical systems, or MEMS, have evolved from the semiconductor industry since the 1970's and are now part of our daily life as much as microprocessors. Accelerometers and pressure sensors help us drive safely while gyroscopes and RF-switches can be found in any new smartphone hitting the market. These demanding fields have pushed for more reliable fabrication processes while driving the costs down. Other domains, which were once unreachable by the MEMS technology, can now benefit from these tiny sensors or actuators, from the space industry to, of course, life sciences. Their dimensions are, without any doubt, their main advantage over traditional devices. Indeed, in many cases, size does matter. Economically first, since smaller sensors can be produced in larger quantities on the same surface. Physic laws are also different at the micro- or at the nano-scale. Hence, MEMS can be sensitive to forces that we, at the human scale, are not even aware of.

Another very interesting strategy, which is allowed once more by their small size, is to rely not on a single but on arrays of MEMS. In the case of a serial process, such a parallelisation can dramatically increase its throughput by dividing the work between each unit within the array. Following this principle, IBM developed a decade ago the Millipede: an ultra-high density data storage system that used an array of 64x64 probes to write and read bits with a rate in the range of 100 Megabytes/sec. Additionally, an array of sensors can give a more reliable and detailed result compared to that of a single sensor. The CMOS sensor found in digital cameras is a perfect example of the advantage of numbers. It is composed of thousands of photodiodes that individually capture light to form the pixels of the picture. Therefore, the more photodiodes are contained in the CMOS sensor, the closer to reality the picture will be.

In the field of life sciences, microsystems are ideal tools to interact with bio-components, from DNA to living cells. Faster, smaller, and even cheaper than the gold standards, they may revolutionise how health care services are managed. Today, our cellphones are capable of taking pictures. Tomorrow, they will probably perform health checks and blood tests as quickly as a snapshot. While such a vision may still be long-term, I will show in this thesis two examples of how MEMS-based sensor arrays could be used to advance cancer research and develop applications in life science in general.

Context of the thesis work

The work I present in this thesis has been accomplished within the framework of a Swiss-funded project called "Probe Array Technologies for Life Science Applications" (PATLiSci), which involved multiple laboratories and research partners between March 2010 and October 2013. It focused on the development of probe-based MEMS arranged in arrays for applications in cancer research and diagnostics. The project aims were to take advantage of MEMS-based arrays to investigate (1) the mechanical properties of cancerous cells and (2) the possibility of a non-invasive diagnosis of lung and neck-and-head cancers.

The Sensors, Actuators and Microsystems Laboratory (SAMLAB), of which I am part, was responsible for the design and fabrication of two distinct MEMS-based platforms, one for each aim. Among the various partners of the project, I collaborated closely with Dr. Martha Liley's group from the Swiss Center for Electronics and Microtechnology (CSEM) and Prof. Christoph Gerber's group at the University of Basel (UniBas). CSEM was coordinating the parallel force spectroscopy on cells while UniBas was responsible for the non-invasive diagnosis of cancer.

As the two tasks were running in parallel, I had to regularly switch from one to the other. It was initially decided to develop two generations of devices for each side of the project. I had to design and fabricated four MEMS platforms during the three years and a half of my thesis. Hence, beside the technological challenges, I also had to face time management aspects to keep the delivery times as tight as possible.

Overview of dissertation

This thesis presents two distinct technologies separated in two parts. In part one, I introduce a two-dimensional cantilever array developed for parallel force spectroscopy on cells. Designed specifically for cancer research, this tool is capable of assessing the mechanical properties of multiple tumorous cells. The second part of this thesis is dedicated to a membrane-type sensor for molecular detection in gaseous phase. Arranged in arrays, it has been used as a non-invasive screening tool for lung and neck-and-head cancers. Only an exhalation was necessary to distinguish sick patients from healthy people.

Both parts focus on the technology aspects of the sensors, from their design to their fabrication and characterisation. As these platforms are meant to be used in arrays, a particular attention was directed on their reproducibility and the homogeneity of their characteristics. Results, which were obtained with these sensors within the framework of the PATLiSci project, are presented at the end of each part. While these results represent the successful demonstration of the microfabricated sensors presented in this thesis, they were obtained by other researchers and do not belong to me. As a consequence, I have deliberately restrained their presentation to the essential.

Part I

2D Cantilever Array for Parallel Force Spectroscopy on Cells

1 || Introduction and fundamentals

Cells are one of the oldest forms of life on Earth. They are known as "the building blocks of life", of which all living organisms are made. From a single cell, they grow, divide, and differentiate themselves to finally form complex organs perfectly interconnected. More than just bricks, cells are therefore capable of actions independently, such as motility, reproduction, and cell-cell communications. These activities are made possible by the collaboration of proteins, amino acids and lipids, working in concert at a smaller scale than a human hair. In some cases however, this beautiful mechanics spirals out of control. Cells that were supposed to die continue to divide, again and again. They do not respect their natural order any more and create clusters of useless cells, which are called tumours. Eventually, some cells will detach from their primary tumour and migrate throughout the body to form secondary clusters, or metastases.

The transformation of normal cells into highly malignant cells is neither instantaneous nor trivial. It is a multistep process that requires a succession of genetic changes [1]. Several milestones, which have to be reached by the cell in order to become malignant, have been identified [2, 3]. These ones include, for instance, the ability of the cell to evade its programmed death or its ability to proliferate. Each of these hallmarks are made possible with the acquisition by the cell of molecular, biochemical, or biomechanical traits that are passed over its daughters. While most of the mechanisms involved in this progressive evolution are understood, little is known about the invasion and metastasis characteristics of cancerous cells, which is their ultimate, and mostly fatal, state [3]. The loss of cell-cell adhesion molecules [4] or the cross-talk between cancer cells and surrounding healthy cells [5] have been, for example, identified to contribute to the spreading of metastatic cells. As metastases are responsible for 90% of all human cancer deaths [6], depicting the full mechanism that enables their migration is instrumental. The development of new models and theories would allow, for instance, creating cancer treatments that efficiently target metastatic cells.

For the past few years, advances in biomechanical tools have raised new interests in the mechanical properties of cells. With the help of microsystems, such as the atomic force microscope (AFM) or microfluidic devices, researchers have been able to probe and mechanically interact with individual cells or micro-organisms. These tools have provided them the capability to apply and sense forces and displacements at the cellular level. As with electrical or chemical stimuli, cells react to these mechanical signals and convert them into biochemical responses that can be recorded. This new apparatus has lead to discoveries in fields as broad as touch sensitivity [7, 8] or stem cell differentiation [9, 10]. Rapidly, cancer cells have also attracted some attention. It is not surprising that researchers found discrepancies in the mechanical properties of cancerous and metastatic cells compared with healthy ones. The complex transformation experienced by cells during the evolution of a tumour has critical impacts on their shape, stiffness, and adhesion forces. Hence, the assessment of those properties would lead to (i) further improve the existing models of cancer evolution, (ii) enable straightforward diagnostics strategies, and (iii) develop new drug screening methods.

I have organised this first thesis part in the following sequence: the rest of the current chapter focuses, first, on cell mechanics and on the existing technologies to assess their mechanical properties. The latter are then discussed as possible cancer biomarkers. Finally, I introduce the fundamentals of cantilever microfabrication and the two-dimensional array approach that we have chosen to probe cancerous cells in parallel. The design strategies that I have adopted for the 2D cantilever array are presented in chapter 2 and are followed, in chapter 3, by its fabrication and characterisation results. This part is concluded by the parallel force spectroscopy experiments on cancerous cells that were conducted in collaboration with CSEM.

1.1 | Cell mechanics

While cells are about 70% water, they mechanically do not behave just as tiny water balloons. Besides the cell membrane and the cytoplasm, i.e. the liquid medium within the cell, there are several components that participate to the cell structure, such as the nucleus or the cytoskeleton. In this section, I will briefly introduce the mechanical properties of these elements as well as the forces experienced or generated by cells. Additional information about the cell functions and general biology can be found in very good books such as the "Molecular Biology of the Cell" [11].

1.1.1 | Structural components of the cell

Figure 1.1 represents a schematic view of a typical animal cell. It is composed of many subcellular components but three of them mainly are responsible, at different degrees, of the structural behaviour of the cell: the membrane, the nucleus, and the cytoskeleton.

The membrane

The cell membrane consists of a phospholipid bilayer measuring ≈ 6 nm in thickness that delimits the boundaries of the cell. Glycolipids, cholesterol, and various membrane-associated proteins, which are responsible for the cell-cell and cell-extracellular matrix communications, are integrated within this bilayer. While these proteins account for 50% of the membrane by weight, they are too dispersed on the cell surface to have a significant influence on its

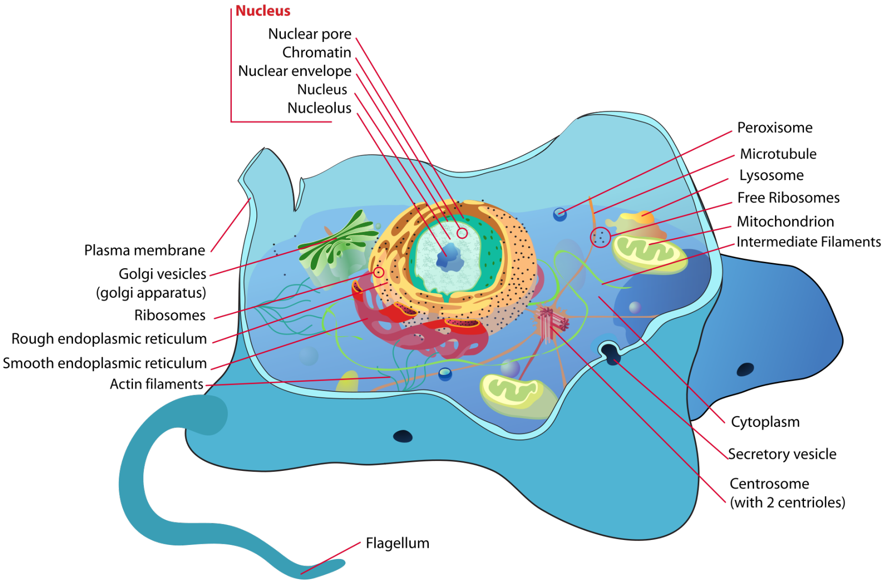

Figure 1.1: Diagram of a typical eukaryote cell. Its mechanical properties are mostly defined by the cytoskeleton, the nucleus, and, to a lesser extent, the membrane. Adapted from [12].

mechanical properties. Cholesterol is however critical for the integrity of the membrane. It adds firmness and makes the membrane less permeable to water-soluble molecules [13].

The nucleus

From all the organelles of a cell, the nucleus is the biggest and stiffest. Various studies of its mechanical properties showed a broad range of measured Young's moduli up to two orders of magnitude depending on the cell type [14]. All of them agree however on the significant difference of stiffness between the nucleus and its surrounding cytoplasm, and on its viscoelastic behaviour [15].

This stiffness difference between the nucleus and the rest of the cell highlights the fact that a cell cannot be modelled as a uniform body. There are significant intracellular discrepancies of viscosity, stiffness, and rheology that have to be considered. The choice between a measurement technique that probes the overall rather than the local surface of the cell will therefore influence the result analysis. In the former case, for instance, statistical results would be needed to average the influence of the nucleus.

The cytoskeleton

The cytoskeleton is a network of biopolymers contained in the cytoplasm that provides the structural support to the cell. As such, it has the most influence on the cell shape, viscosity, or migration. The cytoskeleton is composed of three main components that have various

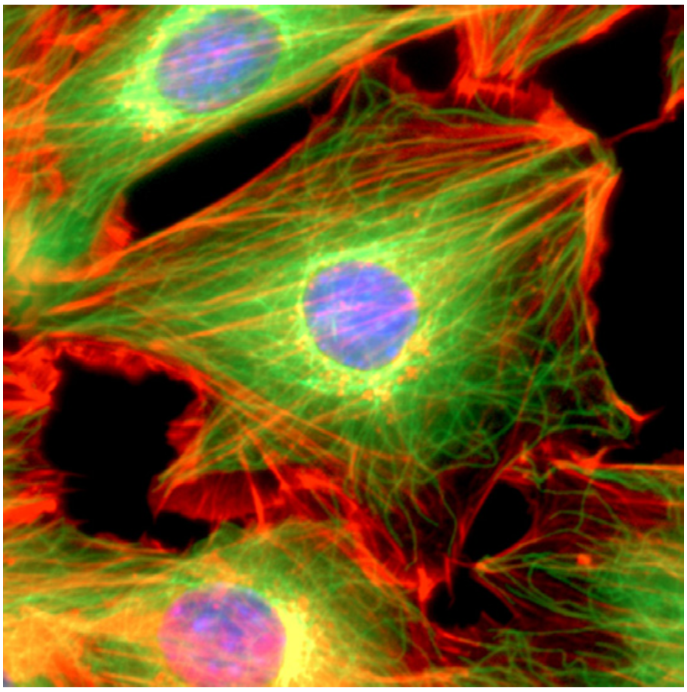

Figure 1.2: Fluorescence image of a mouse fibroblast. The cell was fixed and stained for DNA (blue), actin filaments (red), and microtubules (green). Image reproduced with permission from [16].

functions and mechanical properties: actin microfilaments, intermediate filaments, and microtubules. Figure 1.2 highlights perfectly those polymers and their distribution within a mouse fibroblast (reproduced from [16]).

Actin filaments, with a diameter of 6-8 nm and a length up to 100 μm, play a vital role in almost every cellular processes involving motility. Their polymerisation has been shown, for instance, to be one of the factors correlated with cell migration [17]. By measuring the thermal fluctuation of actin filaments, their flexural Young's modulus was found to be in the range of 1.5-2.5 GPa [18].

Intermediate filaments are the most compliant polymers of the cytoskeleton. By gently pulling on single intermediate filaments with an AFM, it has been shown that their bending stiffness is one order of magnitude lower compared to actin filaments [19]. In contrast with the latter, they are not involved in cell motility functions. Instead, they act as tension-bearing elements to maintain the cell shape and rigidity, and hold organelles in place within the cell [20].

Compared to actin and intermediate filaments, microtubules have a larger diameter ($\approx$ 25 nm) and are more rigid [18]. Besides their structural properties, they also have an important role in the intracellular transport of substances and during the mitosis, i.e. the DNA strands separation during the cellular division process [21].

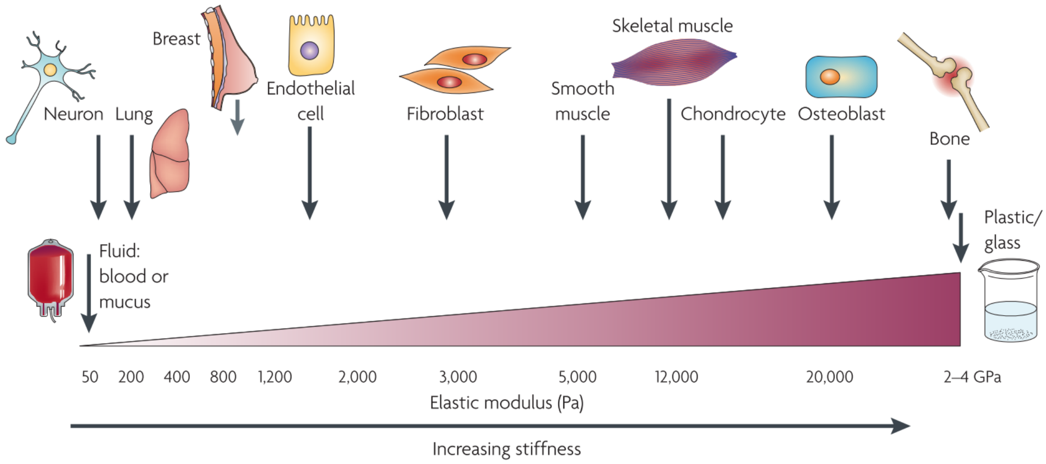

Figure 1.3: The mechanical properties of cells are defined by their environment. As osteoblasts, which synthesise bone tissues, are subject to larger forces compared to neurons due to their location, they exhibit a higher stiffness as well. Adapted with permission from [23].

1.1.2 | Importance of forces at the cellular level

Mechanical forces are omnipresent at the cellular level. Similarly to chemical and electrical signals, forces trigger specific events related to the cell development, survival, and migration. It is now clear, for example, that stem cells differentiate under the influence of their external environment. Soft matrices, such as brain, impose them a neurogenic lineage while stiffer environments, such as bones or muscles, direct them towards osteogenesis or myogenesis, respectively [9]. Hence, each cell type, from neurons to muscle cells, are tuned to the mechanical properties of their surrounding matrix. As shown in Figure 1.3, cells stiffness can range between 0.4 kPa and 20 kPa depending on their locations and functions.

Cells do not only passively experience external stress but also react with cell-generated forces or signals. For instance, specialised cells in the ear vibrate under pressure waves and convert them into electrical signals that are recognised by our brain as sounds. Likewise, in the event of a wound to the skin, keratinocytes modify their cell-cell adhesion properties to promote their migration and fill the gap created by the wound [22].

Based on these observations that show the importance of forces in various aspects of cellular biology, the development of tools capable of applying or detecting forces at the cellular level has become critical. While standard tools, such as micro-pipettes, have been originally used, MEMS-based devices tend to replace them more and more as we will see in the next section.

1.1.3 | Cell mechanics in cancer research

As previously highlighted, cells feel forces and respond to them. They constantly adapt to their environment by remodelling their shape and modifying their behaviour. Hence, each tissue has an optimum set of mechanical properties that can change over time in response to various situations, internal or external, planned or unexpected. Infections, wounds, and diseases belong to the latter. While flu is unlikely to radically modify cells to this extent, cancer, among other diseases, has been identified to change their stiffness and adhesion properties [24, 16]. This is not surprising when considering the significant physiological changes affecting cancerous cells.

Quantifying the mechanical properties of cancer cells is particularly challenging in regards to the various states and the complexity of the disease. At the tissue level, tumours tend to exhibit an increased stiffness compared to healthy tissues due to fibrosis and extracellular matrix (ECM) remodelling [25]. At a cellular level however, recent studies showed that malignant cells have smaller Young's moduli compared to healthy cells of the same line [26, 27]. Discrepancies have also been found between metastatic and non-metastatic cells. While metastatic cells are even more compliant in carcinomas, e.g. lung or breast tumours, [26, 28, 27], they are significantly stiffer in sarcomas, e.g. melanoma [29].

These observations taken all together suggest that the migration capabilities of cancerous cells are closely related to their change of stiffness and adhesion properties (cell-cell or cell-substrate) [16]. Assessing these parameters in various cancer stages and types could definitely improve our understanding of their migration schemes into the cardiovascular or lymphatic system, which eventually lead to the formation of metastases. The cell stiffness could also be envisaged as a cancer biomarker. The mechanical heterogeneity found between cancer types and even within a same tumour tissue requires however a high confidence in the diagnosis, which is enabled by large statistical results. Similarly, the efficiency of newly developed cancer drugs could be evaluated by this means [30]. To be viable, these two last applications require however a high throughput capability from the measurement setup.

1.2 | Poking cells with MEMS

By their size, microsystems would be ideal tools to interact with cells. They can detect and apply forces that are compatible with those experienced by cells. However, microsystems are usually made from materials far from any biological background. Silicon, aluminium, or glass, all these materials come from the semiconductor industry and were not chosen based on their biological compatibility. The latter, which I summarise in this section, has been however widely studied for the last two decades. The main MEMS-based tools that are used to probe the mechanical properties of cells are then presented.

1.2.1 | Do MEMS get along with living organisms?

Living cells are rather different substrates to work with compared to inert surfaces and particles. While designing a biocompatible microsystem, one must be aware of various facts. First, cell culture environments typically employ saline at a constant temperature of 37°C. Second, cells are living organisms that evolve in time. Their physiological characteristics are not constant and can affect, or be affected by their surrounding. Hence, special care must be taken in the choice of materials while interacting with living organisms. Cytotoxicity and also adhesion properties and long-term stability in liquid environments need to be assessed.

Cytotoxicity

Since the development of microsystems, numerous studies have been conducted on the biocompatibility of standard MEMS materials. Cytotoxicity tests of silicon and its derivatives (silicon dioxide, silicon nitride, silicon carbide) with mouse fibroblasts revealed no significant inflammatory or irritative responses [31, 32]. Biocompatibility studies on gold, platinum, or titanium show similar results. Polymers, such as polymethylmethacrylate (PMMA), SU-8, or polydimethylsiloxane (PDMS), are also widely used in microsystems and microfluidics applications, and show also no cytotoxicity effects [33]. Hence, there are few concerns about the impact of these materials on cellular health in culture.

Adhesion properties

Interacting with cells involves adhesion to the MEMS. While strong cell adhesion is usually preferred, some designs try to prevent it to avoid clogging or any accumulation of cells, also called biofouling. The adhesion properties of cells on a substrate depend essentially on its surface conditions. Its chemistry, charge, or hydrophilicity, are mainly responsible for cells attachment [34]. As silicon is hydrophobic by nature, cells are less inclined to spread on this substrate. On the other hand, silicon dioxide and silicon nitride are hydrophilic. Numerous studies have also shown that porous or microstructured surfaces can strongly enhance the adhesion of cells [35, 36, 37].

A very popular method to modify the adhesion properties of a surface is to functionalise it with specific self-assembled monolayers (SAMs) or proteins for adhesion promotion or prevention. While CH_3, PEG, and OH terminated SAMs tend to provide a weak cell adhesion, COOH and NH_2 are good candidates to promote a strong cell adhesion [38]. Fibronectin and vitronectin are proteins that can also be easily coated on surfaces to provide highly adherent sites [39, 40]. There are therefore various possibilities to modify the adhesion properties of microsystems and allow them to interact as required with biological samples.

Long-term stability

Another biocompatibility characteristic is the long-term stability of the device. It has been shown for example that prolonged contacts of silicon with living tissues may produce biofouling [32]. Silicon dioxide and silicon nitride are, on the other hand, less impacted by this problem. While PDMS is supposed to be biocompatible, this polymer is not very stable in time. Degradation, swelling, or delamination, are common issues that can rise in aqueous environments [41, 42]. On the other hand, it has been shown that a hard baking step minimises stress and ageing in the case of SU-8 [43]. Such physical changes in the MEMS material may strongly influence its mechanical performances. While microchannels would not suffer from water swelling, the mechanical behaviour of a polymer-based cantilever will definitely change over time with the absorption of water molecules. The use of polymers as the MEMS main material and its consequences need therefore to be carefully studied during the design and characterisation phase.

Compatible readout systems

Capacitive, piezoresistive, or optical readouts are among the most popular methods to measure the displacements of MEMS, as small as nanometres. Similarly to the previous section, working in liquid-based environments has an impact on the choice of the readout system. Capacitive sensors are stable and extremely sensitive but they are hardly compatible with aqueous solutions for obvious reasons. On the other hand, piezoresistive readout is possible as long as the resistors and their electrical connections are passivated. Finally, optical-based systems, such as laser interferometry, are also suitable for liquid applications. The medium has, however, to be transparent for the laser to reach the device. Whole blood is not an adequate environment for this reason. The heat produced by the laser would also need to be kept at a minimal value to avoid any cell damage.

1.2.2 | MEMS-based techniques to probe cells

Several techniques have been designed to assess the mechanical properties of single cells. While standard methods, such as micropipette aspiration, exist, I have restricted the following list to MEMS-based techniques that replace them advantageously thanks to their size or ease of use (Figure 1.4). In the following paragraphs, I present their working principle and how they have been used. Table 1.1 finally summarises their performances and characteristics.

Atomic force microscope

The AFM was invented by Binnig, Quate, and Gerber in 1986 following the development of the scanning tunnelling microscope at IBM [44]. It consists of a flexible micro-cantilever with a sharp tip sitting at its end. In a well-controlled environment, this tool is capable of scanning a surface and rendering a three-dimensional profile with a lateral and vertical resolution of fractions of nanometres. Two important features of AFM cantilevers to achieve such performances are the sharp tip apex and the cantilever, which bends under very small force interactions. Depending on their stiffness, micro-cantilevers can apply and sense forces over a relatively large range (10 pN - 1,000,000 pN). The choice of a suitable spring constant, which is defined by the cantilever material and dimensions, is therefore an important aspect of the design.

Although this tool has historically been used for the imaging of immobile substrates, the wide

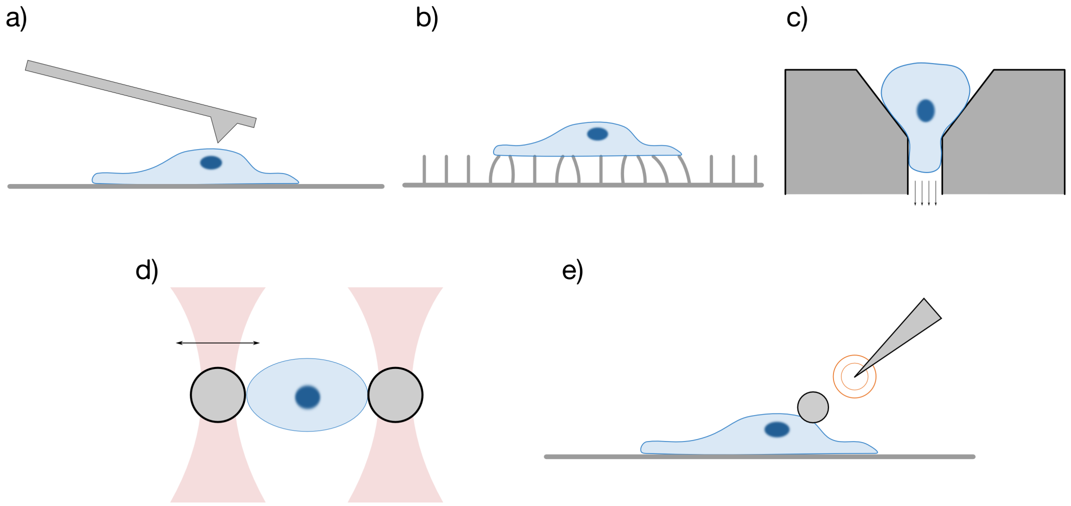

Figure 1.4: Schematics of various single-cell biomechanical assays, including (a) AFM, (b) micropost arrays, (c) microchannels, (d) optical tweezers, and (e) magnetic tweezers.

choice of cantilever characteristics has considerably facilitated force spectroscopy experiments on cells. Unlike the imaging mode where a high spatial resolution is required, force spectroscopy on cells usually requires larger tip radii of curvature to prevent puncturing the cell membrane [45].

To retrieve the Young's modulus of a cell, an analytical model, such as the Hertz model, is fitted to the obtained force-distance curve. This model was initially developed by Heinrich Hertz to describe the response of an elastic half-space surface to a rigid spherical indenter or "punch" [46]. Since then, variants have been developed for different contact modes such as conical tip on half-space surface, spherical tip on spherical surface, or cylindrical tip on half-space surface [47]. Still, the Hertz model assumes a perfectly elastic and homogeneous sample but most biological samples are viscoelastic, heterogeneous, and may adhere to the tip. Probing cells at higher velocity may result in measuring higher apparent Young's moduli [48]. Hence, the indentation rate should be lower than the viscous relaxation rate of the cell to stay in an elastic regime. Other models have also been developed to take into account the adhesion forces between the tip and the substrate [49, 50]. As for the inhomogeneity of the cell, it may result in variation of the Young's modulus depending on both the indentation depth or location on the cell. Mapping the Young's modulus over the entire cell can therefore efficiently highlight the local changes of rigidity or adhesion [51, 52]. On the other hand, tips with larger radius of curvature will probe the cell in a more global way [53]. Fewer indentations are required per cell but the obtained values of Young's modulus will likely vary between cells due to their inhomogeneity. Most of the time however, indentations of 200 nm - 500 nm are performed in order to only probe the stiffness of the cell membrane or of its cytoskeleton.

Despite these advances, AFM-based experiments are fundamentally slow. They rely on a single probe that is able to scan one local area at a time. However, as we will see later in this chapter, this process can be accelerated either by increasing its operation speed or by scaling up the number of cantilevers and making them work together in arrays.

Microchannels

Microchannels and microfluidic devices in general are attractive solutions when working with cells. Usually made out of glass or PDMS, they can trap, sort, count, and analyse cells with a very high throughput [54, 55]. By controlling the size of the microchannels and the flow rate or pressure inside them, various forces can be applied on the cells. They are the MEMS duplicates for micropipettes. Compared to the latter, microchannels can be parallelised and require smaller sample volumes. In addition, they can be fabricated with various shapes and surface roughness [56].

Using microchannels, a large set of cell mechanical characteristics can be extracted. Viscoelastic properties [56, 57], motility [58], and clogging time [59] have been reported. Thanks to more complex structures including side-vacuum chambers, cells can also be laterally stretched inside their microchannel [60].

Micropost arrays

To measure the traction forces exerted by cells, two-dimensional micropost arrays have been developed. Made out of PDMS, these carpets of vertical cantilevers serve as substrates for the culture of cells. While adhering to the substrate, the latter pull on the microposts underlying their focal adhesion points [61]. By optically measuring the bending of each post, one can map the force field of a cell [62]. Such microposts have been used to study various cellular behaviours, such as cellular migration [61] or the contractile properties of cardiomyocyte [63]. Micropost arrays are not limited to the measurement of forces. Recently, cobalt nanowires have been integrated into such posts to apply a force, based on magnetic actuation, to these adhesion sites and record the cell reaction [64].

While several cells could in theory be analysed in parallel, the throughput will eventually be limited by the image processing time. This technology is therefore more suitable for the detailed force mapping at the cellular and subcellular levels rather than large statistical studies.

Optical tweezers

Also called optical traps, these particular tweezers rely on the momentum of photons to hold microscopic particles in place. When light interacts with a particle, the latter experiences a radiation pressure produced by the photons. In a focused laser beam, this pressure is always oriented towards the focus point. Hence, the particle is trapped in the middle of the beam and will follow its displacements [65]. Optical tweezers can apply forces between 1 pN and 100 pN. Higher forces may be obtained but at the expense of a higher laser power, which would thermally damage the biological sample [66]. While optical traps are not, strictly speaking, a

Technology	Force [pN]	Measurements	Features	Limitations	Ref.
AFM	$10 - 10^6$	Adhesion forces Stiffness mapping	High res. imaging Large force range	Low throughput	[76, 45, 27]
Microchannels	$10^4 - 10^6$	Deformation Motility	High throughput	Large applied forces	[54, 58]
Microposts	$10^2 - 10^5$	Traction forces Cell migration	Subcellular force gradient	Low throughput	[63, 77]
Opt. tweezer	$1 - 10^2$	Deformation Stiffness	Low noise Non-contact	Photodamage Thermal heating	[69, 67, 78]
Magn. tweezer	$10^{-2} - 10^2$	Viscoelasticity Mechanotransduction	Bead rotation	Complex setup	[79, 73]

Table 1.1: Existing technologies for single cell probing and their characteristics

MEMS-based technique, they are often combined with microfluidics systems to handle the microparticles.

Optical traps have been extensively used to manipulate cells and apply forces to them [67, 68]. The deformation and movement of the cells are usually determined by video tracking. Mechanical properties such as adhesion forces, membrane elasticity, or cell motility, have been determined with this method [69, 70]. The throughput of optical tweezers is mainly determined by the image processing time and the number of cells captured by the traps. Maximum rates of ≈ 1 cell analysed per minute have been reported [28].

Magnetic tweezers

Unlike optical tweezers where cells are directly trapped into the laser beam, magnetic tweezers have to use an intermediate microbead to interact with them. The bead, usually superparamagnetic, can be positioned via a magnetic needle, or an electromagnetic coil. A configuration with up to six coils is required to fully control the three-dimensional position and rotation of the bead. Forces between 0.01 pN and 100 pN can be achieved depending on the strength of the magnets and their distance with the bead [71]. Similarly to optical traps, magnetic tweezers are not necessarily microfabricated.

Due to the very low forces and torques that magnetic tweezers can apply, they have been mainly used for single molecule and DNA studies [72, 73]. Experiments on cells have been conducted as well to probe local viscoelastic parameters [74]. By using sub-micrometre beads, intracellular manipulations have been made possible [75].

1.3 | Fabrication of a micro-cantilever

Since the development of the AFM in 1986, various techniques have been developed to fabricate micro-cantilevers. While the first ones were basically cut out of gold sheets or tungsten wires [44, 80], microfabrication processes were quickly adopted to create cantilevers in batch with precise dimensions and characteristics. As low spring constants (≈ 1 N/m) for force sensitivity and high resonance frequencies (> 10 kHz) for scanning speed and noise filtering are required, microfabrication techniques are ideal to scale down the cantilever dimensions and fulfil these requirements.

1.3.1 | Microfabrication processes

The methods to fabricate microsystems are called microfabrication processes. They are derived from the integrated circuit (IC) industry, which produces the microprocessors and chips that are found in many electronic objects of our daily life, from our computers to cars and smartphones. While some processes are common to both fields, others have been developed particularly for the MEMS industry. Lithography, thin film deposition, wet etching, are basic techniques that will not be discussed in this thesis since excellent books explain them already extensively [81]. However, I will still introduce those which were essential in either the design or the fabrication of the 2D cantilever array.

Thermal oxidation of silicon

Silicon dioxide created by thermal oxidation is a basic additive process. Already at room temperature, silicon oxidises to form a thin layer of native oxide approximatively 2 nm thick [82]. Once the silicon substrate heated at temperatures between 600°C and 1200°C in a water-contained atmosphere, thick oxide layers can be quickly obtained. Due to the chemical reaction of silicon with water molecules:

$$Si + 2H_2O \longrightarrow SiO_2 + H_2 \tag{1.1}$$

a ratio of silicon thickness is converted into the silicon dioxide layer. Indeed, for each 1000 Å of grown oxide, 460 Å of silicon have been consumed. Oxidation in a dry atmosphere, i.e. in absence of water, is possible as well but it will take much longer time to achieve a similar thickness [83]. However, the obtained oxide layer is of better quality: it has a higher density and is pinhole-free.

The oxidation rate depends as well on the crystalline orientation of silicon. This effect is due to differences in silicon bonds availability between the crystalline orientations [84]. Since these rates change with temperature, it is possible, in a certain extend, to tune their ratios. As an example, the ratio of oxidation rates in (110) and (100) planes is 1.29 at 800°C but it drops at 1.05 at 1100°C [85].

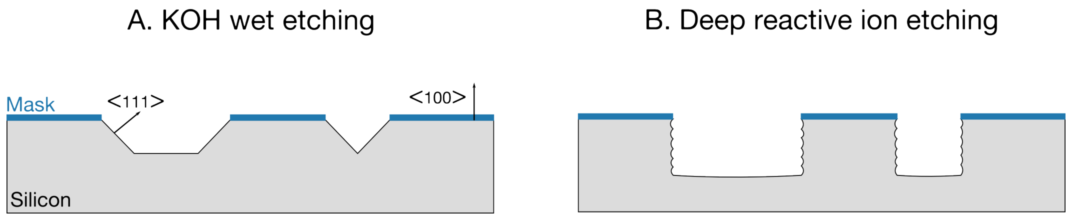

Figure 1.5: (A) KOH etching process on (100) silicon wafer. As (111) planes serve as etch stops, various depths can be achieved depending on the initial width of the mask openings. Inversed pyramidal shapes are obtained with squares. (B) DRIE is a dry etching process that enables deep vertical structures. An isotropic ion etching is repeatedly alternated with a passivation sequence to only promote a vertical structuration. These two steps result in scalloping of the side walls.

Since the development of trenched capacitor structures in the early 1980's, researchers have discovered non-uniform oxidations in silicon structures compared to flat surfaces [86, 85]. During oxidation, intrinsic tensile or compressive stresses appear in convex or concave angles, respectively, and locally reduce the supply of oxygen. As a result, the oxidation rate at these particular points is significantly reduced. Similarly to the orientation dependence, the temperature plays a role in this non-uniformity. The suppression of oxidation is more pronounced at lower temperature and in concave structures, and less pronounced at higher temperature and in convex structures.

KOH etching

Among other structurating processes of silicon, potassium hydroxide (KOH) etching is one of the most used in the MEMS industry due to its anisotropy, relatively large rate, and batch compatibility. Because of the crystalline structure of silicon, KOH displays different etch rates depending on the exposed crystalline plane [87]. While (100) and (110) silicon planes are etched at similar rates, (111) planes are etched 400 times slower. Hence, the latter often serve as etch stops to determine the final structure. With (100) oriented silicon wafers, pyramidal shapes can therefore be obtained once all (111) planes have converged (Figure 1.5 A).

Deep reactive ion etching

Deep reactive ion etching (DRIE), also known as Bosch process, was developed in the 1990's by the same company. An isotropic ion etching is repeatedly alternated with a passivation sequence to only promote a vertical structuration of silicon. It allows anisotropic etching, which results in vertical structures with high aspect ratios (Figure 1.5 B). The repeated sequence of etching and passivation creates however a scalloping effect on the walls. Hence, smooth vertical surfaces are hardly achievable with this technique.

Wafer bonding

The fabrication of MEMS requires sometimes multiple levels stacked on top of each other, either for packaging or to bring additional features. Several methods exist to bond two wafers together, either permanently or temporary.

Fusion bonding relies on the pre-bonding of two silicon wafers at room temperature due to Van der Waals forces and hydrogen bonds. The wafers are then annealed at high temperature, typically 1000°C, to create strong covalent bonds. This technique, also called direct bonding, does not require an intermediate layer between the wafers. Fusion bonding of silicon to silicon dioxide and silicon nitride surfaces have been demonstrated [88].

Anodic bonding is another very popular technique to bond a silicon wafer to a glass surface [89]. An electric field, which is applied between the two wafers, enhances the thermal diffusion of negative oxygen ions from the glass to the silicon. The resulting oxidation creates a strong and irreversible bond. The required voltage ranges from a few hundreds to a thousand of volts, while typical temperatures are between 200°C and 400°C.

Unlike the above mentioned methods, thermocompressive and adhesive bonding techniques rely on an intermediate layer to bond the wafers. Metals, such as gold, copper, or platinum, are used as intermediate materials in thermocompressive bonding. The wafers, both covered with a thin layer of metal, are pressed together and heated at a temperature between 300°C and 500°C [90]. The bonding is permanently created by the inter-diffusion of metallic ions between the layers and the subsequent formation of an alloy. For adhesive bonding, polymers, such as SU-8 or Benzocyclobutene (BCB), are used as intermediate layers. Similarly to thermocompression, the wafers are pressed together but at a lower temperature, which rarely exceeds 300°C [91]. Hence, thermal mismatch stress is reduced at the interface. It is also possible to later separate the two wafers by dissolving the polymer layer.

1.3.2 | The micro-cantilever

Since the invention of AFM, numerous processes have been developed to fabricate micro-cantilevers. They can be however divided in two classes. Either the wafer is thinned down and structured to the shape of the cantilever (Figure 1.6 A), or it serves as a mould and a thin film is deposited onto it to create the cantilever (Figure 1.6 B). Both techniques have advantages and inconveniences but crystalline silicon cantilevers can only be fabricated via the bulk etching fabrication. The thin film technique is, on the other hand, more appropriate for silicon nitride or polymer cantilevers.

Bulk micromachining

As silicon is a basic material in microfabrication, cantilevers has been quickly fabricated out of it. Wolter et al. reported the first cantilever micromachined out of bulk silicon in 1991 [92].

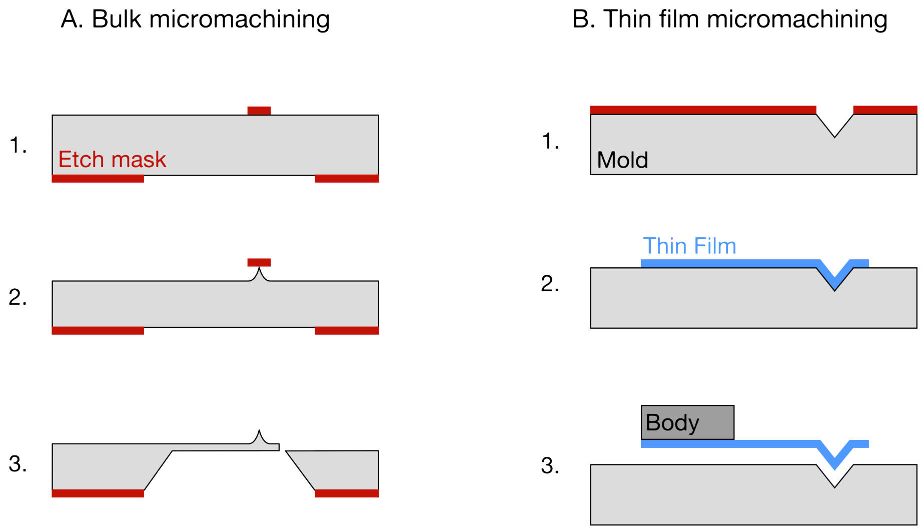

Figure 1.6: Two main techniques exist to fabricate micro-cantilevers. (A) Bulk micromachining is usually used for silicon cantilevers and (B) thin film micromachining is more suited for cantilevers made out of silicon nitride or polymers.

The cantilever body is first defined by lithography on a mask layer (Figure 1.6 A1). The tip is then created by under-etching of a circular mask on the top side of the wafer (Figure 1.6 A2). An isotropic etching process will result in a conical shaped tip while anisotropic etching with, for instance, KOH will create pyramidal tips. Typical obtained radii of curvature are in the range of 100 nm. The cantilever is finally released from the back side (Figure 1.6 A3).

Since this initial fabrication process flow, numerous tweaks and optimisations have been developed mainly to improve the tip shape in term of radius of curvature or aspect ratio. Boisen et al. have, for instance, added a vertical anisotropic etching step after the isotropic under-etching to create rocket-like tip shapes with high aspect ratios [93]. A major advance in tip sharpness has been achieved by Marcus et al. [94]. After a wet oxidation of the silicon tip and subsequent removal of the oxide layer, they observed a clear sharpening effect due to the non-uniform growth rates in curved structures mentioned earlier (section 1.3.1). This method allowed for the first time tips with sub-nanometre radius of curvature. Additionally, thinner cantilevers can be fabricated with the use of silicon-on-insulator (SOI) wafers instead of bulk silicon wafers, although the former are significantly more expensive compared to the latter [95].

Thin film micromachining

The fabrication of micro-probes from bulk silicon is very efficient for cantilevers thicker than 2 μm. The thickness control below this value becomes too challenging. Thinner cantilevers can however easily be fabricated from thin film deposition [96]. The silicon wafer is, this time, structured to form a mould on which a thin film is deposited (Figure 1.6 B1 and B2). The structure shown in Figure 1.6 A2 can also serve as a mould. The cantilever is finally released either by etching the mould wafer or by attaching a body chip to the cantilever, usually by wafer bonding (Figure 1.6 B3). Beside the fabrication of thin cantilevers, this method allows a wide choice of materials. Silicon dioxide, silicon nitride, but also polymers and metals can be moulded to form cantilevers [97, 98].

Various techniques were again developed to sharpen the tip of these moulded cantilevers. Similarly to the silicon cantilevers, the mould can be sharpen by means of thermal oxidation [99]. Radii of curvature of ≈ 10 nm have be achieved with silicon nitride while SU-8 cantilevers with 30 nm tip radius have been fabricated [99, 97].

Creating a spherical tip shape

While AFM imaging requires sharp tips for resolution aspects, blunt or, ideally, spherical tips are necessary for force spectroscopy on cells [45]. Since other domains, such as surfaces and interfaces studies, require larger tip radius as well, various techniques have been developed to create spherical tip shapes. The most widely used method by far is the attachment of a microbead, in which a polystyrene or a silica particle is manually glued at the tip location (Figure 1.7 A) [100, 101]. While this method demands patience and dexterity from researchers, the obtained radii of curvature are broad (1 μm - 50 μm) and very repeatable. Cantilever tips can also be altered by depositing a conformal thin film on their surface (Figure 1.7 B) or by thermal oxidation (Figure 1.7 C) [102, 103]. Compared to the microbead attachment, these two methods can modify cantilevers in batch. However, the obtained radii of curvature cover a much smaller range and are less repeatable, especially in the case of the thin film deposition.

While these methods rely on finished cantilevers, it is possible to create the spherical tip during the microfabrication itself. As previously presented, pyramidal moulds can be sharpen by thermal oxidation due to the non-uniform growth of silicon dioxide in concave cavities. However, if the oxide layer is removed, the mould is actually rounded (Figure 1.7 D) [104]. Since thermal oxidation is a uniform process over the whole wafer, the obtained radii of curvature should be very uniform as well. Their range is however limited between 10 nm and 250 nm. Another original technique has been developed by Yapici et al. to extend the latter [105]. Instead of oxidation, they spun photoresist on the wafer to partially fill the pyramidal cavities. With the help of solvent evaporation and surface tension, the dry photoresist creates a rounding effect (Figure 1.7 E). Many parameters, such as viscosity, spin speed and duration, and baking time, can be used to adjust the radius of curvature between 1 μm and 10 μm. However, the presence of photoresist in the moulds limits the choice of the cantilever material to those with low temperature of deposition, such as polymers. Compared to the three post-processing methods, these two techniques have to be integrated within the cantilever fabrication. Hence, it demands more preparation and planning of the process flow but the mechanical properties of the final cantilevers are not altered by an additional step. Table 1.2 summarises the characteristics of the presented technologies.

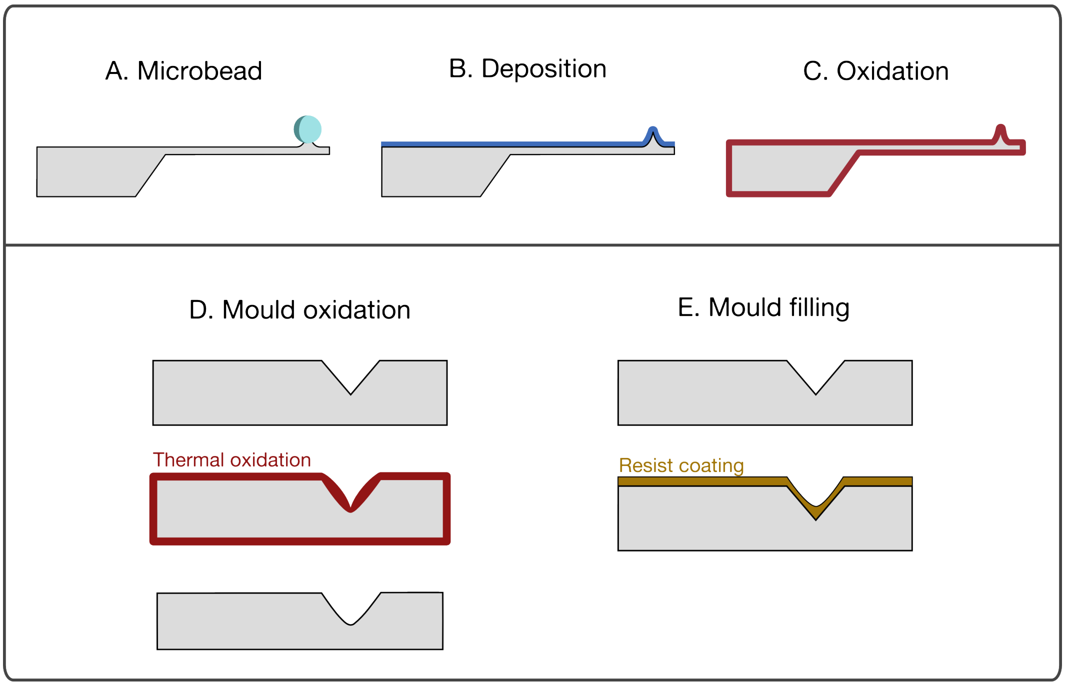

Figure 1.7: Various technologies already exist to create cantilevers with round or spherical tips. Finished cantilevers can be post-processed either by (A) gluing a microbead, (B) depositing of a thin film, or (C) oxidation. During the fabrication, it is possible to alter the tip mould either by (D) thermal oxidation and subsequent removal of the oxide layer or (E) photoresist filling.

1.4 | The 2D probe array platform

1.4.1 | The AFM throughput, a major drawback

AFM has many advantages for probing biological samples, including cells. In cancer research, this tool has been successfully used several times to quantitatively compare the stiffness of malignant and benign cells. Its throughput remains however a major drawback, especially when statistical results are required. The use of a classic AFM is therefore hardly possible as a diagnostics or drug screening tool where both the analysis time and the confidence in the results are critical.

There have been many attempts towards an improvement of AFM throughput. A first approach is to increase the scanning speed. As trivial as it sounds, there are many constraints that set a maximum rate. Three components of the AFM system, namely the cantilever, the driving stage, and the data acquisition card, limit the AFM scanning speed with their own bandwidth [106]. While shorter cantilevers can be driven at higher frequencies, the driving stage and the data acquisition must also be able to follow the movement. It is only recently that some significant progress has been made with the demonstration of 1-frame-per-second acquisition speed [107].

The second approach to increase the throughput of AFM is the parallelisation of this serial

Technology	Radius range [μm]	Features	Limitations	Ref.
Glued microbeads	1-50	Standard beads Real spherical shape	Serial process Presence of glue	[100, 101]
Deposition	0.1-2	Deposition of various materials	Lack of uniformity at a wafer scale	[102]
Oxidation	0.03-2	Repeatable radius uniform process	Modification of the cantilever properties	[103]
KOH mould oxidation	0.01-0.25	Repeatable radius uniform process	small range of radius of curvature	[104]
Mould filling	1-10	large range of curvature	Only suitable for polymers cantilevers	[105]

Table 1.2: Existing technologies for blunt tips fabrication

process. A highly parallel probe AFM system is much more efficient than a single-probe approach. The idea of an array came pretty early since Minne et al. successfully proposed a simple 1x2 design less than ten years after the invention of AFM [108]. The most famous and advanced example of massively parallel cantilevers remains the IBM project "Millipede". Their revolutionary concept was to use the cantilever tip as a nano-puncher for highly dense data storage [109]. They demonstrated indentations in a thermoplastic polymer that produce holes with a diameter of about 30 nm [110]. A single probe could be used to read, write, and erase holes, which are denoted as bits. An array composed of 32x32 cantilevers working in parallel demonstrated a density of 500 Gbit/in^2 and data rates of 10 Mbit/s and 100 kbit/s for reading and writing, respectively [109]. While the data storage concept had to be abandoned due to the continuously increasing performances of flash memories, the "Millipede" has recently been adapted for 3D nano-lithography. The heated tips can locally evaporate polymer to sculpt any 3D shape with a resolution below 30 nm [111].

From these two concepts, the parallelisation seems to be more adapted to force spectroscopy on living cells. Indeed, while the high speed AFM is much more simple to implement due to the availability of a commercial system, the high velocity of the tip during force-distance curves on viscoelastic cells will definitely have an influence on the measured stiffness. With an array of cantilever, the approach (speed, depth, contact duration, etc.) can be finely tuned to suppress (or highlight) the viscoelastic effect of the cells. This is the main reason of our choice of a 2D array approach.

1.4.2 | Approach

A two-dimensional parallel probe system which allows simultaneous investigations on multiple cells with a high throughput has already been proposed and demonstrated by CSEM team

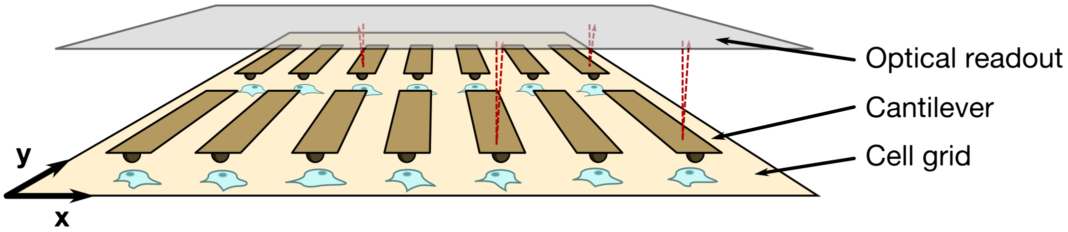

Figure 1.8: Schematic of the 2D probe array AFM system composed by three distinct platforms, namely the cell grid, the cantilever array and the parallel optical readout. The system is optimised for specific pitches in x- and y-directions.

[112]. As depicted in Figure 1.8, the proposed 2D probe array system is composed of three levels, namely a cell grid, a cantilever array, and a parallel optical readout stacked onto one and another. For the system to work properly, these three platforms are optimised for specific pitches in x- and y-directions. Cells are cultured on functionalised substrates with preferred adherence spots small enough to ensure a single cell per spot. The optical readout is an interferometric-based system. A laser beam is first expanded to the size of the cantilever array and split into a reference beam and a sample beam that hits the array. The recombination of both beams is finally focused on a CMOS camera chip to extract the interference patterns of each cantilever.

With a field of view of approximately 1 mm x 1 mm for a resolution of 1024 x 1024 pixels and an acquisition speed of 150 frames per second, this CMOS chip is an ideal system for the simultaneous readout of parallel cantilevers. It brings however a few design constraints on the 2D cantilever array. First, a minimum length of 40 pixels is required to detect the interference fringes of each cantilevers, which corresponds to a minimum cantilever width of 40 μm. Second, the interferometric readout allows for a maximum deflection angle of 3°. Long cantilevers are therefore preferred to keep their deflection angle below this value. Finally, due to the image processing time, the number of cantilevers within each array is limited between 20 and 40 cantilevers. Higher numbers could eventually be processed by increasing the computational power.

1.4.3 | Cell experiments and requirements

As highlighted in Section 1.1.3, both the adhesion and stiffness properties of cancerous cells are of interest as biomarkers. Based on the relative low stiffness of cells, very flexible cantilevers would be needed to assess their Young's modulus with a sufficient resolution. Typically, cantilevers with spring constants between 0.01 N/m and 0.05 N/m are used for stiffness measurements. On the contrary, cell-cell or tip-cell adhesion forces are relatively significant and stiffer cantilevers, between 0.5 N/m and 5 N/m are required for these experiments.

In addition to the cantilever stiffness, the tip shape is also important. As explained previously, spherical tips are required for the cell stiffness experiments. On the contrary, flat tips, or even tipless cantilevers, are preferred for the adhesion experiments in either cell-tip or cell-cell

Probe requirements	**Stiffness measurements**	**Adhesion forces measurements**
Spring constant [N/m]	0.03	0.3 and 3
Tip shape	Spherical	Flat or tipless
Tip radius [μm]	5	-
Minimum width [μm]	40 (limited by the resolution of the CMOS)	
Maximum tilt [°]	3 (limited by the interferometric measurement)	

Table 1.3: Probe specifications for stiffness or adhesion forces measurements

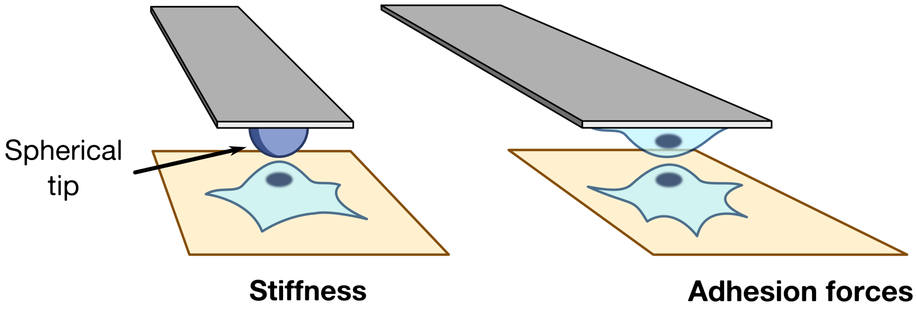

Figure 1.9: Schematics of two single cell experiments that are of interest using an AFM. Due to the softness of cells, very flexible cantilevers are needed to measure their stiffness. In comparison, more rigid cantilevers are required for tip-cell and cell-cell adhesion measurements.

configuration (Figure 1.9). Such tip configurations allow the number of adhesion sites staying constant during the force-distance curve. Hence, the measured adhesion forces do not depend on the applied force any more. Table 1.3 summarises the needed specifications for both the stiffness and adhesion forces measurements.

Finally, as all the three stages share common x- and y-pitches, the various fabricated probe arrays should ideally have similar dimensions and pitches between cantilevers. Hence, the user would be able to replace an array with another without having to modify the geometrical parameters of the optical stage and of the cell grid. While this last requirement seems trivial, it limits the design possibilities of the cantilevers, as I will later present.

1.4.4 | Goals of the presented work

Towards the fully functioning system, custom-made 2D cantilever arrays with the above-mentioned specifications have to be produced and characterised. More important than the fulfilment of the specifications are the homogeneous characteristics of the cantilevers composing each array. As cells mechanical properties will be directly calculated from the force-distance curves obtained with each cantilever, any inhomogeneity in, for instance, their stiffness, will result in approximated measurements.

The goals of the current work are therefore:

1. To fabricate 2D cantilever arrays of various spring constants and tip shapes specifically designed for force spectroscopy on living cells
2. To characterise their properties and their homogeneity within each array
3. To demonstrate that they can be successfully used in the 2D probe array platform with multiple force-distance curves on living cells

2 || Design of the 2D probe array

As we have seen in the previous chapter, cantilevers and MEMS in general are already mature enough to have standard fabrication processes well established. Even massively parallel probes have been developed to a pre-production phase. Micro-probes specifically designed for biological applications remain however limited. In particular, while it has become relatively easy to fabricate tips sharp enough to image atoms, researchers still mainly rely on glued beads for their indentations on cells.

In the next chapter, I will present the strategies that I have adopted to meet the requirements imposed by the proposed 2D cantilever array. Two critical issues must be overcome by the design. First, the arrays should be available with various cantilever stiffnesses while their x- and y-pitches stay constant. Second, the spherical tips have to be fabricated in batch due to the number of cantilevers involved per array. Such a feature is not only mandatory for a 2D cantilever array, but it would also dramatically improve the use of single micro-probes in life science applications.

2.1 | Tuning of cantilever stiffness

One of the most important characteristics of a micro-cantilever is its spring constant. It is probably the most important. It defines critical aspects of its behaviour such as its force sensitivity or its actuation speed. As discussed in Section 1.4, cantilevers with spring constants of 0.03 N/m, 0.3 N/m and 3 N/m are required for the different force spectroscopy experiments on cells. The spring constant of a cantilever of any prismatic shape is given by:

$$k = \frac{3EI_y}{L^3} \tag{2.1}$$

where E is the Young's modulus of the cantilever material, I_y is its cross-sectional moment of inertia and L is its length. For a plain rectangular shaped cantilever (Figure 2.1 a), the moment of inertia is defined by $I_y = wt^3/12$ and Equation 2.1 becomes:

$$k = \frac{Et^3w}{4L^3} \tag{2.2}$$

where t, w, and L are the thickness, width, and length of the cantilever, respectively. Based on this equation, there are several options to modify the stiffness of a cantilever. While modifying the thickness is in theory a very effective way to do so, microfabrication processes do not permit to easily create various film thicknesses over the same wafer. Hence, the length is usually the preferred parameter to vary the spring constant of a cantilever. However, one of the system constraints is to keep the lateral pitches constant between the 0.03 N/m, 0.3 N/m, and 3 N/m cantilever arrays. Changing their length would automatically change their pitch. Consequently, none of the rectangular cantilever parameters can be used to change its spring constant.

Looking back at the initial Equation 2.1 of the spring constant, there are two other terms that are independent from the cantilever dimensions: the Young's modulus and the moment of inertia of the cantilever. Modifying the Young's modulus would require to fabricate cantilevers of various materials on the same wafer. This solution would not only be particularly challenging but it would also deviate from the batch structuration advantage of microfabrication processes. On the other side, these same fabrication techniques could be advantageously used to create cantilevers with very different moments of inertia, i.e. cross-sections. Figure 2.1 shows two examples of cantilevers that have either (b) a higher or (c) a lower moment of inertia compared to their equivalent flat cantilever (a).

Rib-stiffened thin films have already been developed in the past. MEMS requiring flat surfaces, such as micro-mirrors, can be ideally stiffened while keeping a relatively light mass. Honeycomb-like structures etched by DRIE are efficient to cover large surfaces [113, 114]. Similarly, cantilevers have been stiffened by increasing their moment of inertia. Lin et al. have also used DRIE to introduce U-grooves that increased the spring constant of the cantilevers up to 30 times [115]. At a smaller scale, Brügger et al. also fabricated U-grooved cantilevers based on 3D focused ion beam milling [116]. They could achieve a stiffness increase of 120 times between a flat and a U-shaped cantilever.

In order to quantify the range of stiffnesses that could be obtained by varying the section of a cantilever, I have investigated two designs either for its softening or its stiffening.

2.1.1 | Cantilever softening

In order to soften a cantilever, a slit can be introduced next to its clamping edge (Figure 2.1 c). The decrease of spring constant depends on the length and width of the slit, as well as on its distance away from the clamping edge. Since the cantilever shape is not constant along its x-axis, equation 2.1 becomes:

$$k = \int \frac{3EI_y(x)}{L^3} dx \tag{2.3}$$

The analytical model calculation of such slitted cantilevers can be found in Appendix A. Figure 2.2 shows the resulting spring constants based on this model for various slit widths and

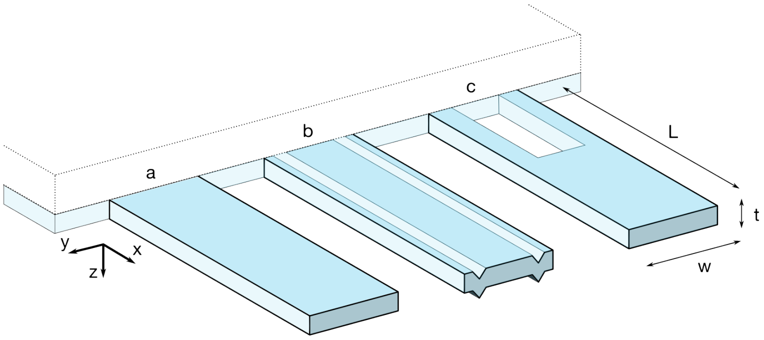

Figure 2.1: Cantilevers with same lateral dimensions and thickness can have different spring constants. A rectangular cantilever (a) is stiffened by introducing V-grooves along it (b). Similarly, a slit at its base will considerably decrease its spring constant (c).

lengths on a cantilever of dimensions 200 μm x 40 μm x 0.4 μm. With a slit half the width of the cantilever, it is possible to decrease the spring constant up to an order of magnitude. For a steeper decrease, a wider slit is however required.

This design has the advantage of keeping the cross section of the cantilever flat. Hence, tipless cantilevers could be fabricated based on this solution. However, the slit introduces a discontinuity in the stiffness that will produce an irregular bending line of the cantilever. This effect will be even more present in the case of a wider slit, which is required to obtain a large range of spring constants. Moreover, such cantilevers would be strongly affected by bending if their material is subject to internal stress.

2.1.2 | Cantilever stiffening

For increasing I_y, integrating V-grooves along the cantilever is particularly of interest if a moulding process is used (Figure 2.1 b). KOH etching of silicon produces 54.7° inclined walls that are very reproducible over the whole wafer. Unlike U-grooves produced by DRIE as proposed by Lin et al. [115], this structuration technique can be used to create V-grooves of various heights within the same wafer. As both the height and the width of the V-grooves contribute to the moment of inertia, a higher spring constant increase can be expected.

The stiffness increase given by the introduction of V-grooves along the cantilever is modelled in Appendix A. The model takes into account the shift of the neutral axis as well as the constant thickness of the thin film in the V-grooves. Considering a flat rectangular cantilever of dimensions 200 μm × 40 μm × 0.4 μm with a silicon nitride Young's modulus of 270 GPa, equation 2.1 gives a spring constant of 0.022 N/m. With two V-grooves of height h = 3.4 μm, the analytical model calculates a stiffness of 2.16 N/m, which is 100 times larger than that of the flat cantilever. To obtain a similar stiffness with a flat cantilever, its thickness would need to be increased from 0.4 μm to 1.9 μm. Figure 2.3 shows the resulting spring constant of a cantilever for various V-grooves numbers and heights.

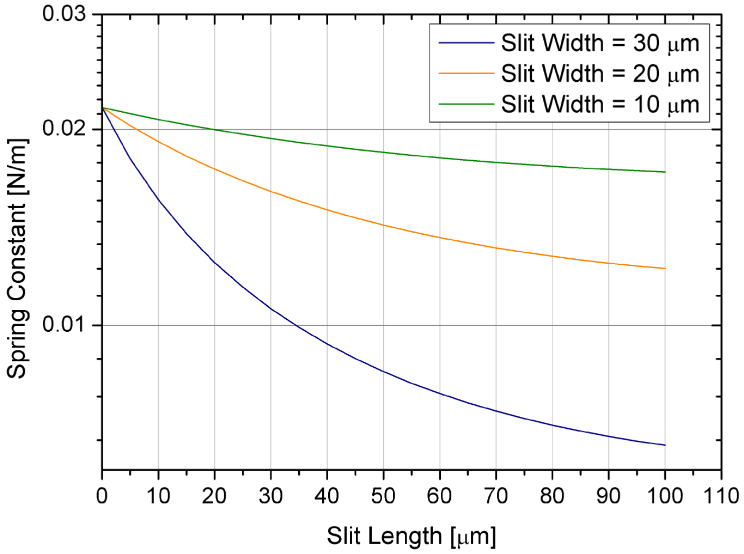

Figure 2.2: Analytical spring constant of a slitted cantilever made out of silicon nitride (Young's modulus = 270 GPa) based on equation A.14. The cantilever dimensions are 200 μm x 40 μm x 0.4 μm and the slit starts at 10 μm from the clamping edge.

Compared to the slitted design, the introduction of V-grooves into the cantilever body create protrusions out of its plane. Hence, the tip should always be kept higher. Beside this minor constraint, the V-groove cantilever has very strong arguments over the slitted design. First, its stiffness is constant along its length, which will result in a regular bending profile. Second, the covered range of stiffnesses is potentially huge. Given a cantilever of dimensions 200 μm × 40 μm × 0.4 μm, a spring constant increase from 0.02 N/m to more than 10 N/m can be achieved with a V-groove maximum height of less than 6 μm.

2.2 | Defining the tip shape

To create a relatively blunt and well-controlled tip apex, I have developed a new mould enlarging/rounding method based on the technique introduced by Kim et al. [104]. Compared to other existing techniques, I particularly liked this one because of the oxidation-based smoothing effect of the silicon surface. Thermal oxidation of silicon is also a standard and cost-efficient technique in microfabrication. Moreover, the achieved films are homogeneous over the whole wafer. The final mould shapes would therefore be well controlled, repeatable, and incredibly sleek. I will present two designs to extend the range of radii of curvature obtained by Kim et al.

As presented in Section 1.3.1, the oxidation rate varies depending on the crystalline orientation. It can fortunately be strongly diminished by (i) performing the oxidation at higher temperature

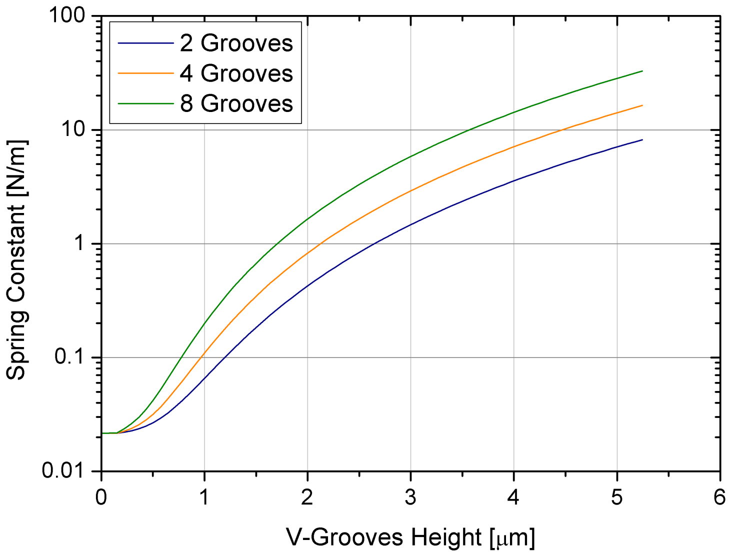

Figure 2.3: Analytical spring constant of a grooved cantilever made out of silicon nitride (Young's modulus = 270 GPa) based on equation A.24. The cantilever dimensions are 200 μm x 40 μm x 0.4 μm.

and (ii) growing a thick oxide layer. After ten hours of oxidation at 1050°C, which corresponds to an oxide thickness of about 2 μm, the thickness ratio between (100) and (110) planes drops below 1.025 [84]. Hence, thick oxide layers grown at high temperature are required for symmetrical growth rates.

To predict the shape of the moulds after oxidation, I have simulated this process using the ATHENA solver from Silvaco [117]. This software can efficiently simulate most of the microfabrication processes, from dopants distribution to chemical etching and thermal oxidation.

2.2.1 | Truncated pyramidal moulds

Unlike the pyramidal mould used by Kim [104], which has four (111) planes crossing at one point, the KOH etching is stopped before the deepest point, resulting in a truncated mould. A thermal oxide is then grown and subsequently removed to smooth the mould edges. This operation can be repeated for a further enlargement of the mould radius. The introduction of this initial flat allows an extension of the maximum radius of curvature obtained by Kim et al. [104].

Formations of both pyramidal and truncated moulds are simulated in two-dimensional cross-sections, and the resulting intermediate steps are shown in Figure 2.4. The chosen simulation model is based on the viscous method calculation with an oxidation performed at 1050°C in wet atmosphere [117]. After a thermal oxidation of 1 μm and its removal, the pyramidal mould obtains a radius of curvature of 240 nm. With a truncation width of only 400 nm, this value is already doubled. A second oxidation/removal step results in a radius of curvature of 1100 nm. Figure 2.5 shows the simulated radii of curvature for various initial truncation widths and two subsequent oxidations of 2 μm.

By introducing this initial plateau, it is possible to obtain tips with radii of curvature up to 4 μm. Even larger radii could be obtain by performing additional oxidation steps. However, these moulds suffer from two problems. First, from a fabrication point of view, the plateau width would be extremely difficult to control between wafers due to the timed etching. Second, the sphericity of the tip is limited to its very end. Hence, the created tips would only be indented of a few micrometres to respect the Hertz model (see section 1.2.2).

2.2.2 | Cylindrical moulds

In order to overcome the issues of the pyramidal mould, i.e. hardly controlled radius of curvature and limited sphericity of the tip shape, I have designed cylindrical moulds. Similar to the truncated pyramids, these moulds have an initial plateau that will define their final radius of curvature after a few oxidations steps (Figure 2.6). Their vertical walls result in a real, half-sphere tip apex that could be deeply indented into a cell without compromising the Hertz model. Furthermore, as such moulds are etched by DRIE, their initial diameter is defined by the lithographic mask rather than the etching process. Hence, the obtained tip radius is much more controlled compared to that of the truncated pyramids.

Figure 2.6 shows ATHENA simulations of such a mould with a 2 μm initial plateau after one, two, and three successive thermal oxidations (2 μm thick oxide). The DRIE scalloping has not been modelled in the simulations and may affect the experimental results compared to these simulations.

Figure 2.7 shows the simulated radii of curvature for various initial widths and oxidation steps. Depending on the plateau width, several oxidations are required before obtaining a spherical shape. Similarly to the pyramidal moulds, the radius of curvature increases linearly with the initial width. This is expected as an increase of the plateau is automatically added to the final diameter of the tip. Some simulations did however not converge due to meshing errors. This issue arose for narrow initial widths and multiple oxidations steps.

2.3 | Consequences on the microfabrication

Based on the presented design solutions, which are both moulding techniques, I have naturally chosen to fabricate the cantilevers from thin film deposition rather than bulk etching. As for the cantilever material, I have decided to use LPCVD silicon nitride. In section 1.2, I have already highlighted this biocompatible material as ideal for biological applications. Moreover, its deposition by LPCVD yields to very conformal and homogeneous layers. As thin films can be deposited, soft cantilevers are easily fabricated. Stiffer ones will be produced by introducing

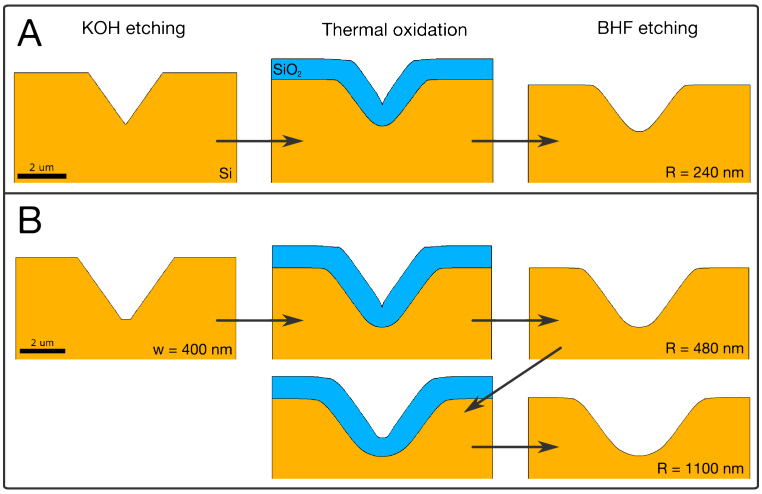

Figure 2.4: Two-dimensional FE simulations of silicon mould profiles before and after oxidation. (A) The mould is pyramidal, as introduced by Kim [104]. It results, after an oxide growth of 1 μm, in a mould radius of 240 nm. (B) The KOH etching is stopped before reaching the deepest point, resulting in a truncated pyramid. After the first oxidation, the mould shows a doubled radius of curvature compared to the pyramidal mould. The second oxidation step further enlarges the bottom profile. The simulations were performed with ATHENA.

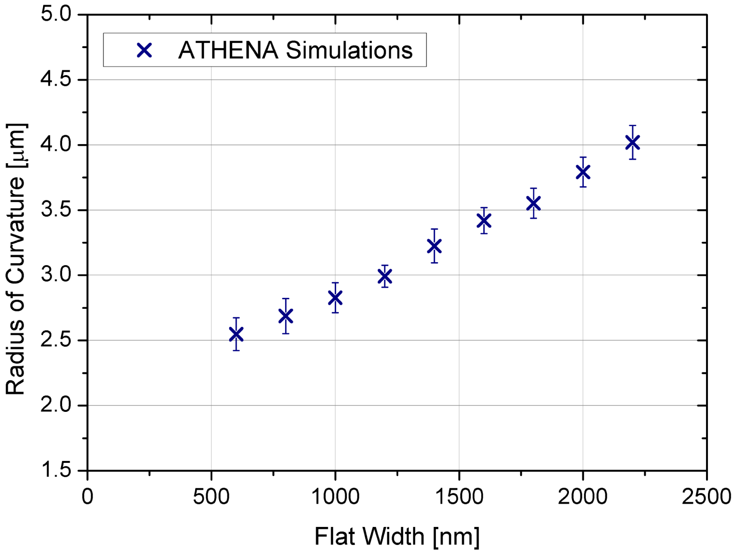

Figure 2.5: Simulated radii of curvature of truncated pyramidal moulds with various initial widths. Two oxide growth/removal steps (2 μm thick) were simulated.

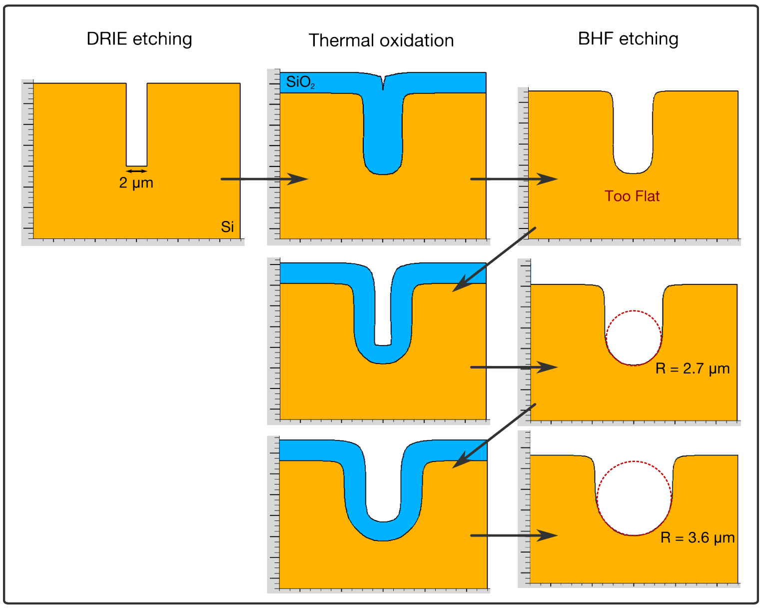

Figure 2.6: Two-dimensional FE simulations of a vertical mould profile before and after oxidations. With an initial plateau of 2 μm, it takes two oxidation steps to obtain a circular shape. The simulations were performed with ATHENA.

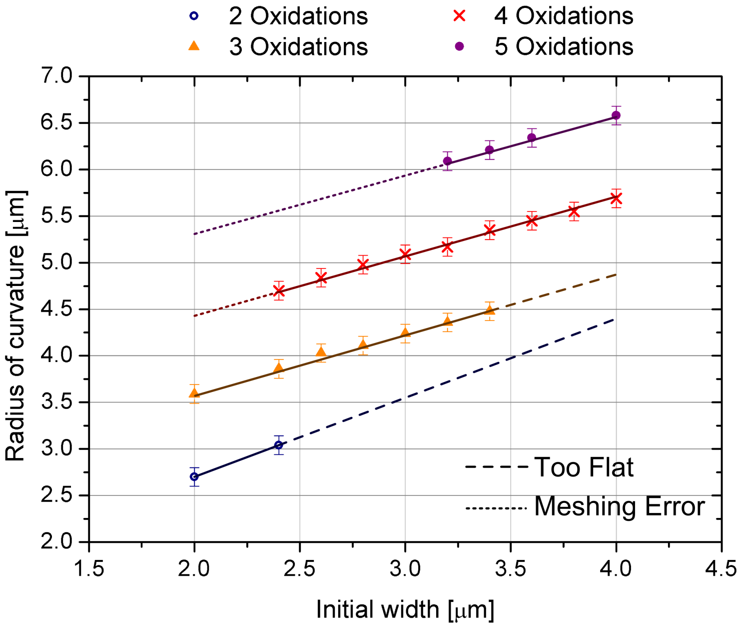

Figure 2.7: Simulated radii of curvature of cylindrical moulds. Similarly to the pyramidal moulds, both the initial width and the number of oxidations influence the obtained radius. Some simulations did not converge due to meshing issues.

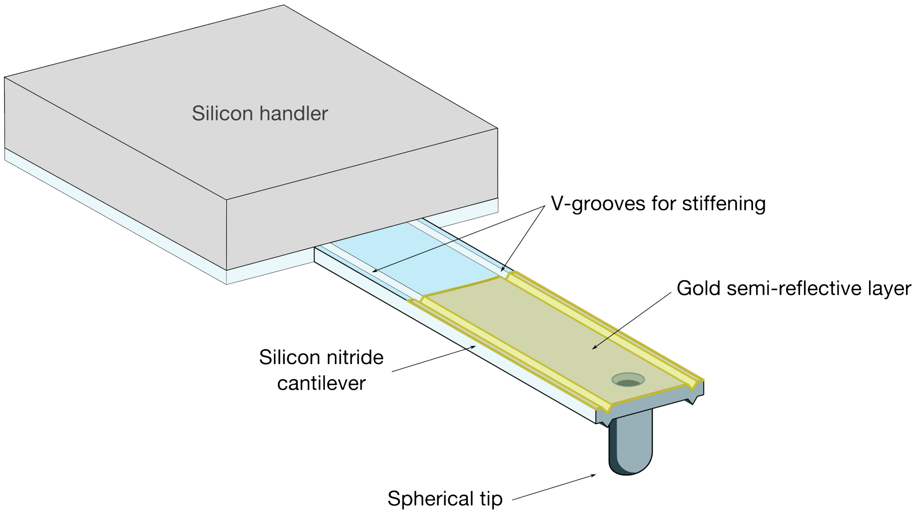

Figure 2.8: Schematical view of the designed cantilever.

V-grooves along them. Finally, as silicon nitride is transparent, a reflective layer will be needed for the optical readout. Interestingly, by choosing an adequate thickness of this layer, the cantilever will be opaque enough for the laser reflection but transparent as well to observe the cells through them. Figure 2.8 shows a graphical representation of the designed cantilever.

In summary, and based on the system constraints, I suggest a silicon nitride cantilever of dimensions 200 μm x 50 μm x 0.4 μm. With an expected spring constant of 0.03 N/m, it can be stiffened up to 10 N/m with the introduction of two V-grooves on its sides. Moreover, the proposed rounding technique allows the batch fabrication of spherical tips with a radius of curvature between 2.5 μm and 6.5 μm.

3 || Fabrication and characterisation

During a MEMS design, one chooses the characteristics that one wants. It is only after the fabrication that we discover those that we really have. In the previous chapter, I have presented spherical tips that could be fabricated in batch and cantilevers with varying spring constants. In this chapter, I will present the fabrication results of the 2D cantilever array. Two generations were fabricated. The major difference between them is the tip shape, which is pyramidal for the first generation and cylindrical for the second generation. More importantly, the experimental results will be compared with the simulations and/or analytical models.

3.1 | Preliminary study on mould rounding

Controlling the tip shape was primordial in the success of these cantilevers. Hence, prior to their actual fabrication, I started with the creation of test moulds based on the ATHENA simulations presented in Section 2.2. V-grooves, etched by KOH, and U-grooves, etched by DRIE, were rounded by means of oxidation steps and then cleaved perpendicularly. I finally measured the radius of curvature of the obtained cross section by SEM and compared it with the simulations.

3.1.1 | Pyramidal moulds

V-groove moulds were the closest adaptation from Kim's technique [104]. They were etched with KOH (40% at 60°C) and a silicon dioxide mask and the etching was stopped before reaching the end of the (111) planes. Different plateau widths were obtained by stopping the etching at various times. A thermal oxide layer was then twice grown at 1050°C and removed in buffered HF. Figure 3.1 A shows an SEM observation of such a V-groove after two subsequent oxidation/removal steps of 2 μm. An additional oxide layer of 200 nm was finally grown to enhance the contrast of the image. The radius of curvature of each groove was measured during the SEM observations. Figure 3.1 B shows the resulting radii of curvature together with the values obtained with the ATHENA simulations. The radii of curvatures are in good agreement with the simulations. The x-error bars of the experimental data correspond to uncertainties of the flat width measurements by SEM. The y-error bars on both simulation and experimental data are based on possible circle approximation.

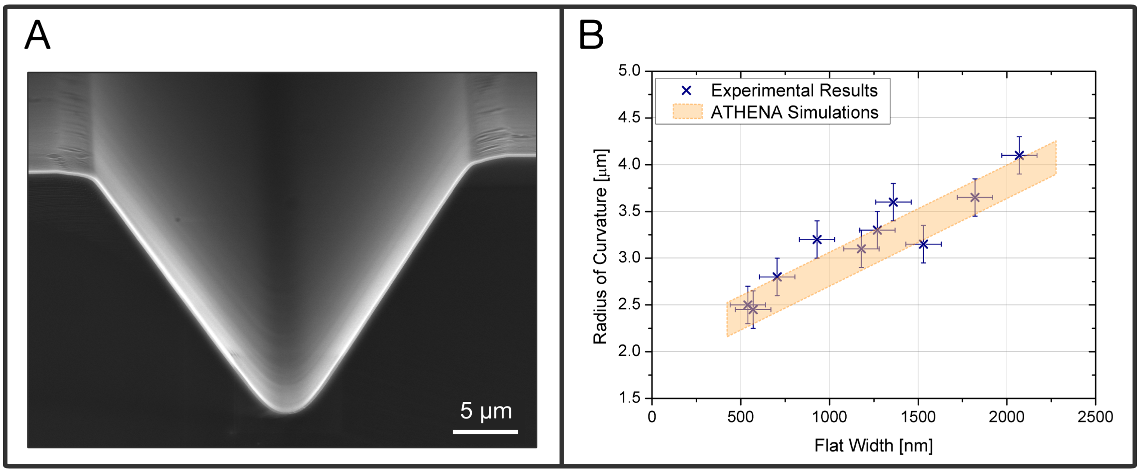

Figure 3.1: (A) SEM observation of a cleaved V-groove after two oxide growth/removal steps (2μm each time). (B)Comparison between the obtained and simulated radii of curvature in V-groove moulds. The orange area represents the simulated radii and their y-uncertainties.

First of all, The range of obtained radii of curvature could be furthermore increased by growing additional oxide layers. Hence, the target radius of curvature of 5 μm could easily be reached with this mould. However, and as predicted, I was not able to precisely control the width of each plateau with the KOH etching. This is especially true for narrow flats below 1 μm. Indeed, with a vertical etching rate of 15 μm/h, one minute difference corresponds to a width variation of already 350 nm. For a more precise control, room temperature KOH, with a lower etching rate, should be used. Width differences may still be present within the same wafer due to various etching rates in the KOH bath. While truncated pyramidal moulds could in theory be used to create tips with large radii of curvature, they are in practice not well controllable and repeatable.

3.1.2 | Cylindrical moulds

Similarly to the test structures above, U-shaped grooves of various widths were etched by DRIE with a silicon dioxide mask, oxidised and cleaved. The oxide was grown in a wet atmosphere at 1050°C. Figure 3.2 A shows SEM observations of four cross-sections of a 3 μm wide U-groove after (1) DRIE, (2) first, (3) second, and (4) third oxidation process. Between each step, the previous oxide layer has been etched in vapour HF. The rounding effect of the mould is particularly obvious after the first oxidation where the oxide has grown slower in the edges due to the higher stress. The following oxidation steps are much more homogeneous and keep enlarging the width of the groove and, by consequence, its radius of curvature. Interestingly, while the DRIE scalloping is present in the initial groove, it has already disappeared after the first oxidation. This smoothing effect of thermal oxide growth can therefore quickly remove roughness and irregularities from the surface, leaving a sleek mould.

Figure 3.2 B shows the radii of curvature obtained with grooves of various widths and oxidation

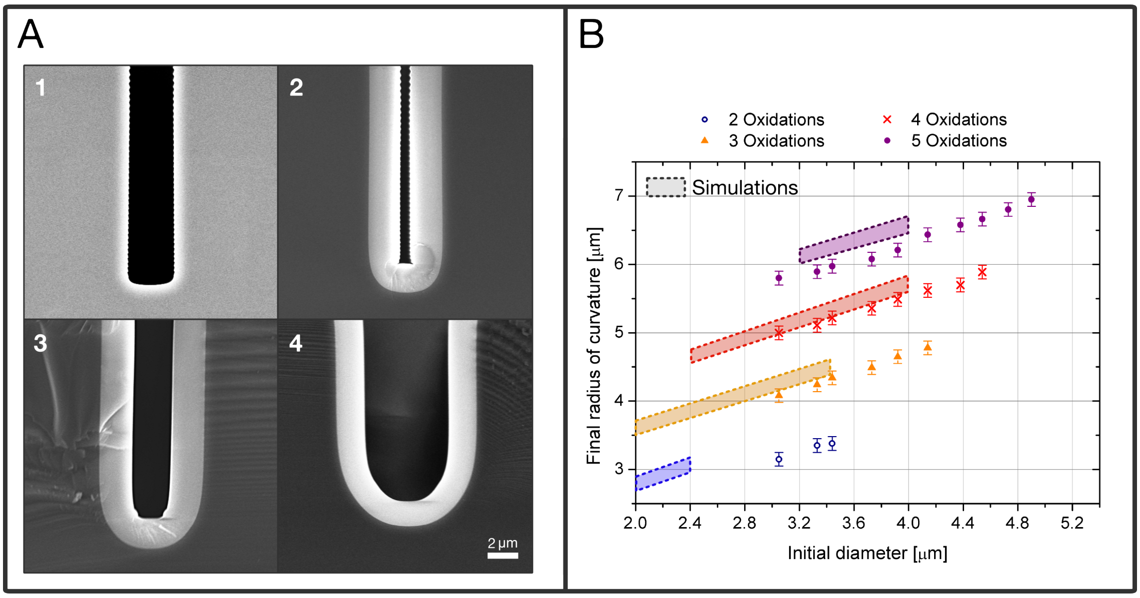

Figure 3.2: (A) SEM observations of a cleaved U-groove after (1) DRIE, (2) first, (3) second, and (4) third oxidation/removal step. (B) Obtained radii of curvature in U-grooved moulds for various initial widths and oxidation steps. Simulated results and their y-errors are highlighted in coloured zones.

steps. The simulation results with their minimum and maximum values are also highlighted for comparison. Even though the radii of curvature have been well predicted by the simulations, they have also been slightly overestimated, especially for narrower grooves. This error may come from the slower diffusion of oxygen into these grooves that has not been taken into account in the simulations. On the other hand, the flatness of the mould bottoms has been overestimated by the simulations. Indeed, it always takes in reality less oxidation steps to obtain a circular shape compared to the simulations. This difference comes from the initial shape mould, which is not completely flat after the DRIE compared to the simulation model.

U-grooves created by DRIE are much better candidates for tip moulding compared to truncated V-grooves. First of all, their final radius of curvature is better controlled due to the vertical DRIE that defines accurately their initial width. Secondly, the bottom of the mould has a characteristic cylindrical shape. Hence, as long as the oxide growth rate is similar in all crystalline planes, the obtained tip shape will be very close to a sphere. Finally, the scalloping effect is completely suppressed during the process.

Based on the experimental data, the initial width and the number of 2 μm-thick oxidations (grown at 1050°C) can be calculated for any radii of curvature between 3 μm to 7 μm (Table 3.1).

R_{tip} [± 0.1 μm]	3.0	3.5	4.0	4.5	5.0	5.5	6.0	6.5	7.0
w [μm]	2.8	3.6	2.9	3.7	3.1	3.9	3.5	4.3	5.0
Oxidations	2	2	3	3	4	4	5	5	5

Table 3.1: Initial widths and number of oxidation steps required for various tip radii

3.2 | Process flow

The fabrication process of the 2D cantilever arrays requires two (100) silicon wafers, one to make the cantilever mould and the other one to create the supporting frame. The two wafers are then joined together with a gold-gold thermocompression bonding. 200 chips on a 4-inch wafer are processed using seven lithography steps (Figure 3.3).

First, the V-grooves used to stiffen the cantilevers are created by KOH etching on the mould wafer. At the same time, deep pyramidal moulds are also etched at each array corners. These tips are used to adjust the parallelism of the cantilever array against the cell grid. Then, the probe tips are structured either by KOH or DRIE to obtain pyramidal or cylindrical shapes, respectively (Figure 3.3 2a). A 2 μm-thick thermal oxide (1050°C in wet condition) is grown and subsequently removed. In the case of the cylindrical moulds, this step is performed three times to obtain a radius of curvature of 4 μm (Figure 3.3 3a). After an additional oxidation of 200 nm, a 350 nm-thick LPCVD silicon nitride layer is deposited and structured by RIE to form the cantilevers (Figure 3.3 4a).

A 50 μm-thick frame to support the cantilevers and elevate the array from the chip surface is structured on the second wafer by DRIE (Figure 3.3 2b). This recess prevents collisions of the chip with the substrate. A thermal oxide of 500 nm is then grown to serve as an etch stop (Figure 3.3 3b). 500 nm of gold is deposited on both wafers as the adhesive layer for the thermocompression bonding (Figure 3.3 5a and 4b). The two wafers are then bonded together in a 10^{-4} mbar vacuum at a temperature of 350°C during 90 minutes with a pressure load of 8 bar (Figure 3.3 6 and 7). A silicon nitride layer is deposited on the front side by plasma-enhanced chemical vapour deposition and structured by RIE to create the mask for the final KOH etching (Figure 3.3 8). The chips are finally structured in KOH and released from the remaining oxide in BHF (Figure 3.3 9). While the opening window could be etched by DRIE, the inclined walls of KOH etching improve the optical access to the cantilevers. The detailed run card of the process can be found in appendix B for additional information and parameters.

Figure 3.4 shows different SEM observations of a cantilever array of the first generation. It is composed of 3x8 cantilevers with integrated V-grooves and 4 alignment probes located at its corners. Cantilevers with 0.03, 0.3, and 3 N/m spring constants were designed based on the height of the V-grooves. The x- and y-pitches were kept constant for all arrays with values of 100 μm and 400 μm, respectively. All cantilever tips were pyramidal, with or without

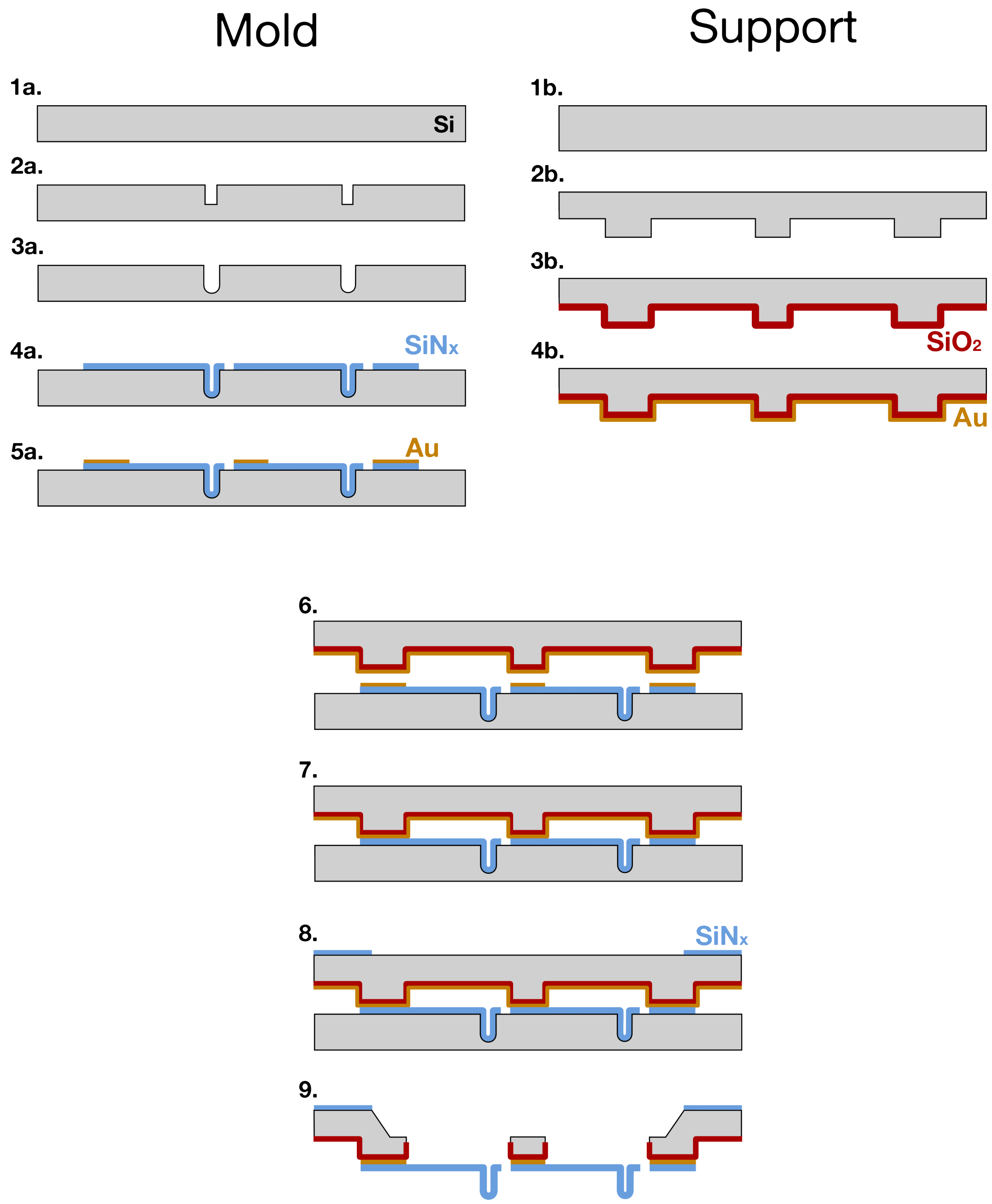

Figure 3.3: Process flow of the 2D cantilever array. Two (100) silicon wafers are separately processed to create the cantilevers and the support frames. A 500 nm gold layer is deposited on both wafers as an adhesive layer for thermocompression bonding. The chips are structured by KOH etching and finally released in BHF.

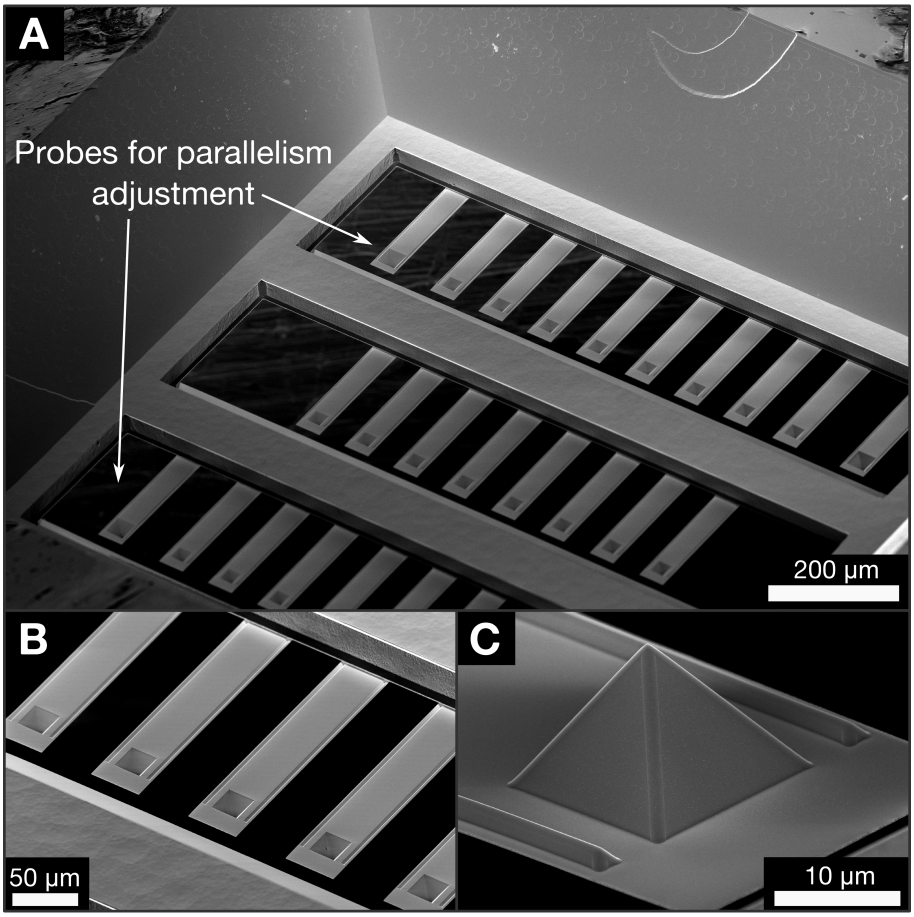

Figure 3.4: SEM observations of the first generation: (A) 2D cantilever array, in which cantilevers (200 μm x 50 μm x 0.45 μm) are placed in a 1 mm^2 working area, (B) four typical cantilevers with integrated V-grooves and (C) a close up view of cantilever end with the molded tip and two V-grooves.

truncation.

Figure 3.5 shows similar views from the second generation of probes. Unlike Figure 3.4 however, observations A and B are taken from below, with the tips facing up. Two cantilevers next to an alignment tip are shown in Figure 3.5 B. The height difference is 15 μm. A close view of a typical spherical tip is shown is Figure 3.5 C, with a tip radius of 3.9 μm. Compared to the 4.0 μm target, this is 2.5 % smaller than expected. Based on the results presented in section 3.1.2, this difference is explained by the slower oxygen diffusion into the mould during the oxidation.

3.3 | Cantilever stiffness

The introduction of V-grooves along the cantilevers allowed to substantially increase their stiffness. Based on an analytical model, I have shown that three orders of magnitude of spring constants could be covered with this technique. In order to validate the model, the spring

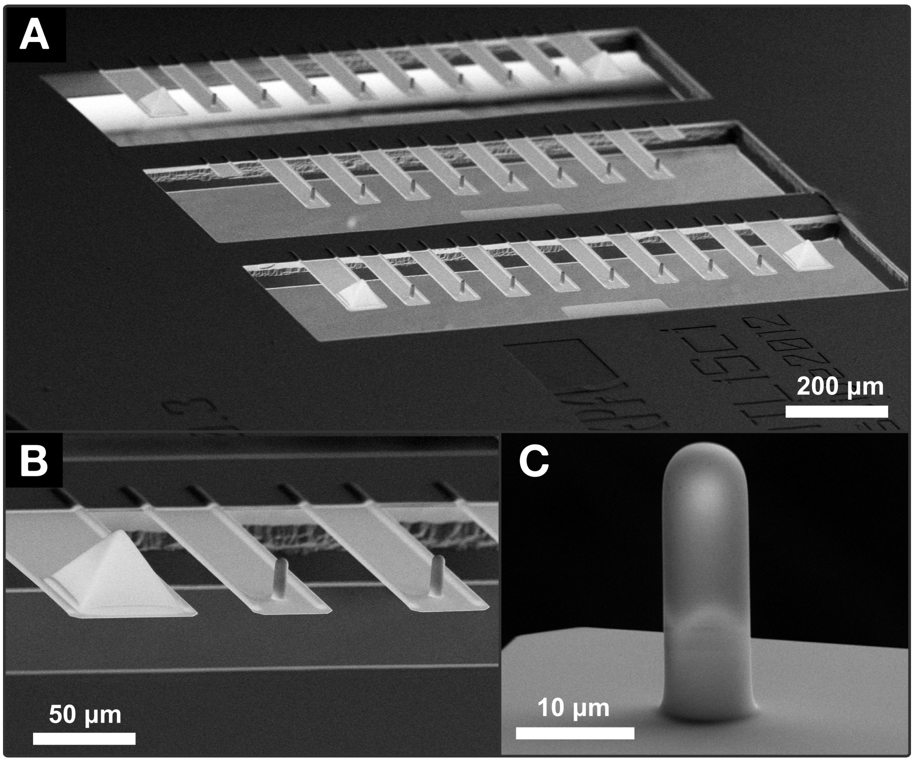

Figure 3.5: SEM observations of the second generation: (A) Back side view of a 2D array of 3x8 cantilevers (200 μm x 50 μm x 0.4 μm). (B) Two cantilevers with integrated V-grooves and spherical tip next to an alignment probe with a higher tip. (C) Close up view of a typical spherical tip of radius 3.9 μm.

constant of cantilevers with various V-groove heights was measured. Equally important is the repeatability of these structures within an array.

3.3.1 | V-grooves stiffening

The measurement of the cantilever spring constants have been done with two different techniques. The first one, called cantilever-on-cantilever (CoC), relies on another cantilever that has been previously calibrated [118] (Figure 3.6 A). Such a calibration can be done either by measuring the resonant frequency of the cantilever [118] or with the use of an electrostatic force balance [119]. In both cases, uncertainties between 2-3% are introduced. The cantilever with unknown stiffness is inserted in an AFM system and a force-distance curve is recorded on an hard substrate, such as silicon. Then, a second force-distance curve is performed on the calibrated beam. The sensitivity difference between those two curves is finally used to calculate the spring constant of the cantilever based on that of the reference beam:

$$k_{test} = k_{calib}\left(\frac{S_{ref}}{S_{hard}}\right)\left(\frac{L}{L-\Delta L}\right)^3 \tag{3.1}$$

where k_{test} is the spring constant of the unknown cantilever, k_{calib} is that of the calibrated beam, S_{ref} and S_{hard} are the deflection sensitivities obtained by the unknown cantilever on the calibrated beam and on the hard surface, respectively. L is the length of the calibrated cantilever and ΔL is the offset between its free end and the point of application of the cantilever. Uncertainties in the calibration are dominated by errors in the measurement of the sensitivity values, which are in the range of 10-20%.

To double check the obtained spring constants, I used another method based on the cantilever thermal fluctuations [120]. Similarly to an harmonic oscillator, cantilevers experience fluctuations induced by thermal noises (Figure 3.6 B). These oscillations can be related to the cantilever spring constant by the equipartition theorem:

$$k_{test} = k_B T \langle x^2 \rangle \tag{3.2}$$

where k_B is the Boltzmann's constant, T is the temperature and $\langle x^2 \rangle$ is an estimation of the squared displacement of the cantilever. The latter is found by integrating the power spectral density of the fluctuations, which can be measured using the optical readout of an AFM system. As most of the oscillations occur at the cantilever resonance frequencies, the latter can be easily extracted from their power spectral density. Uncertainties are mainly due to the calibration errors of the deflection detector, which corresponds to ±5% of the measured spring constants.

The spring constant of cantilevers with V-groove heights from 2.8 μm to 4.4 μm were measured by both techniques. CoC was performed with a Dimension AFM system at Samlab while the other measurement was performed with a Bruker Fastscan Dimension system in Bruker offices in Paris. The results are summarised in Figure 3.7 along with the analytical model presented in section 2.1.2. A spring constant increase of more than two orders of magnitude, from 0.03 to 6 N/m, has been achieved with the integration of V-grooves. The cantilevers have, however, lower spring constants than estimated by the analytical model. This error comes most likely from the V-groove shape modelling. In the model, the shape was approximated to have a sharp knife edge. In reality, the oxidation/removal process steps smoothed the V-grooves as shown in Figure 3.4 C. Their moment of inertia is therefore decreased compared to the model. This mismatch could be suppressed in future fabrication if the V-grooves are created after the rounding step. They would therefore keep their initial sharpness and would correspond closer to the analytical model.

The main limitation for a fine spring constant definition is the lithography resolution during the V-groove opening step. E-beam lithography could ultimately replace the classic UV light exposure to overcome this limitation and achieve cantilevers with well-defined stiffness in a very broad range.

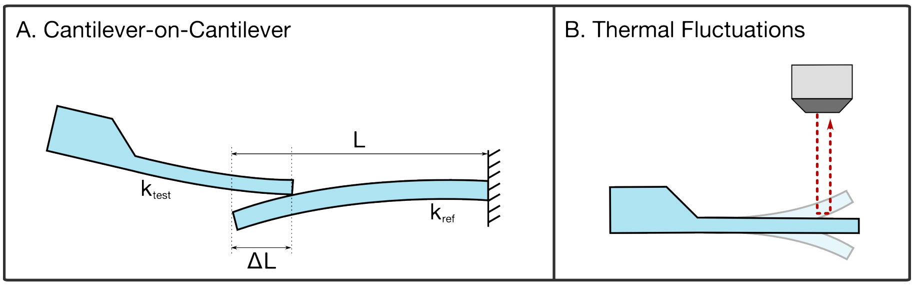

Figure 3.6: Two standard methods were used to measure the cantilever spring constants.

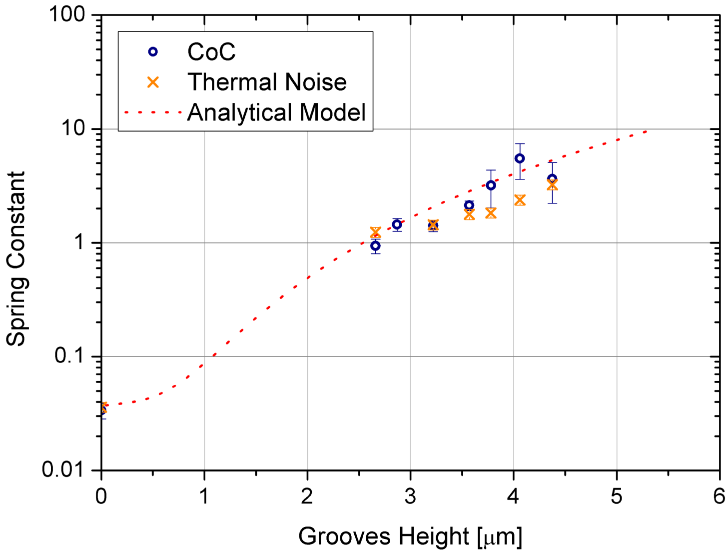

Figure 3.7: Variation of cantilever spring constants as a function of V-groove heights. The spring constant was measured either by pushing the test cantilevers with the calibrated cantilever or by measuring their thermal fluctuations.

3.3.2 | Reproducibility within an array

Ultimately, all cantilevers within an array should have a similar stiffness to minimise uncertainties during simultaneous force-distance curves. Due to the design of the 2D cantilever array, it was not possible to measure their spring constant with the above techniques. In collaboration with FemtoTools, a company developing microforce sensors and precision micro-grippers, two cantilever arrays were mechanically characterised with their FT-FS1000 Mechanical Probe and FT-S100 Microforce Sensing Probe. As the latter is vertically oriented, it could probe each cantilever separately. A precise calibration of the tool allows calculating their spring constants.

The measured arrays were composed of 3x8 cantilevers (200 μm x 50 μm x 0.35 μm). In one case, the cantilevers had two V-grooves of height 3.8 μm along them. The spring constants calculated with the analytical model were 3.14 N/m and 0.0243 N/m with and without the

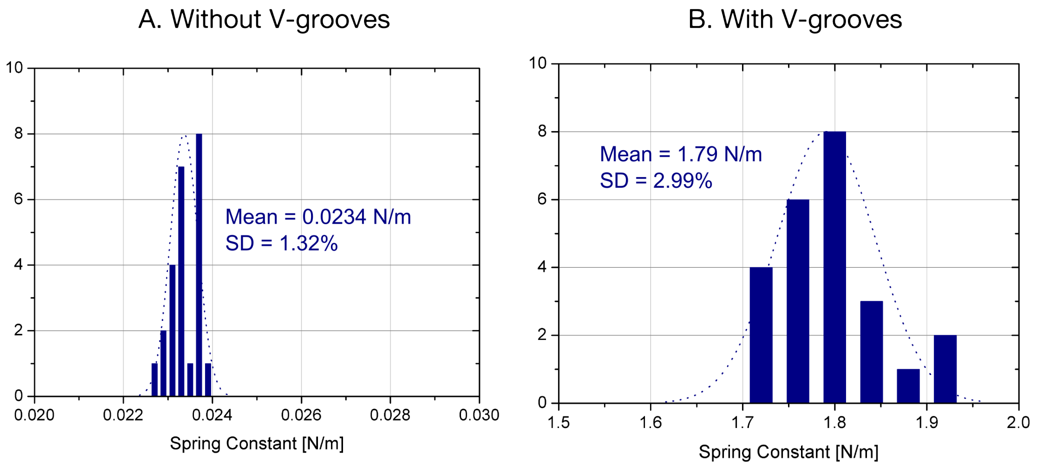

Figure 3.8: Stiffness distribution of an array of 24 cantilevers (A) without and (B) with integrated V-grooves.

V-grooves, respectively. Figure 3.8 shows the stiffness distribution obtained for each array.

For the flat cantilevers, an average stiffness of 0.0234 N/m with a standard deviation of 1.32 % within an array has been measured. The experimental result is very close to the analytical value with an error of 3.7%. Moreover, all cantilevers are mechanically very reproducible since 95% of them are within a 2.6% margin. As for the V-grooved cantilevers, their average spring constant is 1.79 N/m compared to an expected value of 3.14 N/m. The difference of nearly 45% is coherent with the results presented in section 3.3.1, which showed that the rounding effect is likely responsible of a significant drop of the cantilever stiffness. Beside this difference, the measured spring constants are repeatable as well with a standard deviation of 3%. Hence, 95% of the cantilevers are in the range of 1.79 ± 0.1 N/m.

3.4 | Tip shapes

Prior to the fabrication, I have presented a study on the rounding technique by means of oxidation steps on V-grooves and U-grooves. The results presented in section 3.1 are however based on cross-sectional moulds and can differ from real three-dimensional structures. Here, I present the various tip shapes that were fabricated during the two generations of probe arrays.

3.4.1 | Pyramidal tips

Tips based on pyramidal moulds, truncated or not, were fabricated during the first generation of probe arrays. Based on the cross-sectional mould study, tip radii ranging from 2.5 μm to 4 μm have been obtained with truncated moulds.

The transition between the two-dimensional cross-sections and the three-dimensional pyramidal moulds is however not trivial. First, as the 2D simulations predict well the intersection

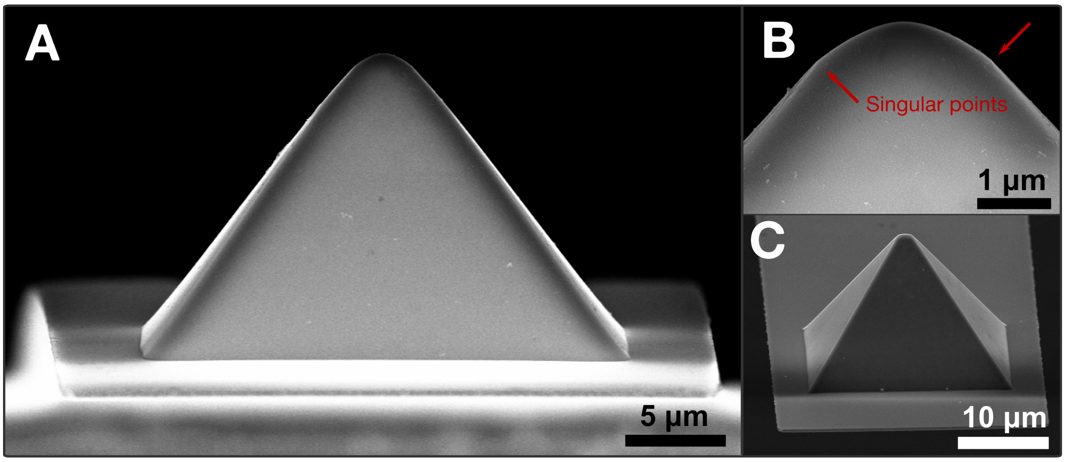

Figure 3.9: SEM observations of the tip shapes obtained with the truncated pyramidal moulds. While the tip seems to be well rounded by the oxidation steps (A), a close up view shows singular points due to the four initial corners of the truncation (B). A Misaligned mask can also result in edged tips (C).

between an inclined walls and the plateau of the truncated mould, it does not provide information on the oxidation behaviour in corners located at the tip apex. To illustrate this issue, a pyramidal tip that had an initial plateau of 500 nm is shown in Figure 3.9 A. The rounding effect is present as expected after two oxidation-removal steps of 2 μm. While the tip apex seems well defined with an observed radius of curvature of ≈ 2.2 μm, a closer view highlights the singular points created by the four initial corners of the truncated mould (Figure 3.9 B). Second, an eventual misalignment of the mask for the KOH etching of the mould will result in rectangular plateaus instead of squared ones. Hence, after the rounding process, the obtained tips are not symmetrical any more (Figure 3.9 C).

These two issues, combined with the difficult control of the initial width during the KOH etching, yield non-spherical tips with a poor radius reproducibility between wafers. Hence, a second generation had to be fabricated with improved tip shapes.

3.4.2 | Cylindrical tips

The cylindrical tip shape was developed for the second generation of probe arrays. Compared to the first generation, the aims were to improve both the sphericity of the tips and the control of their final radius.

Unlike pyramids, cylindrical moulds do not have vertexes that would produce singularities after oxidation. The obtained tips are therefore regular and with a more pronounced sphericity (Figure 3.10 A). The circularity, defined as $4\pi(\text{area}/\text{perimeter}^2)$, is easily calculated from a top view of the tip (Figure 3.10 B). While it does not give any information about the sphericity itself, this value can highlight the diameter variations due to the different oxidation rates between the (100) and the (110) planes. As a circularity of 1 defines perfect circles, that of various tips was about 0.9, which indicates a very good circularity.

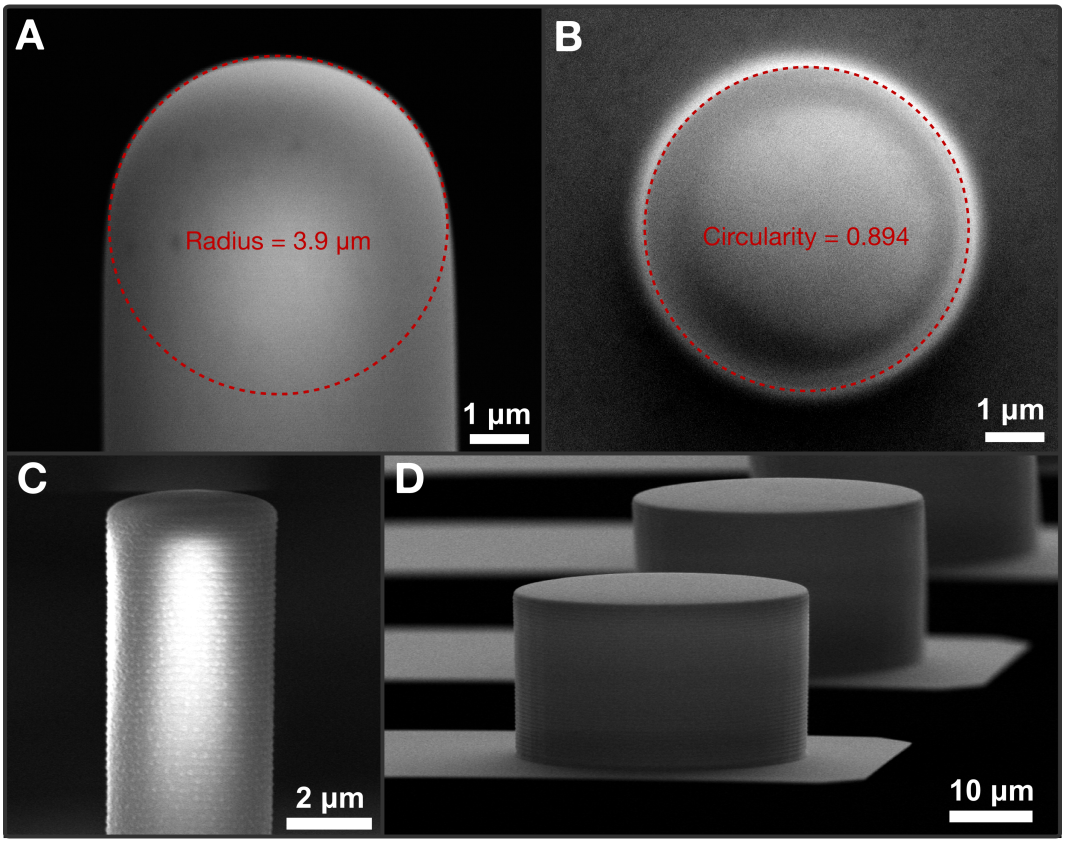

Figure 3.10: SEM observations of various spherical and cylindrical tips. The side view and top view highlight the sphericity of a tip obtained after three oxidation steps (A and B). If the latter are omitted, relatively flat tips can be obtained (C and D).

In order to quantify the reproducibility of the obtained tips, I have measured the radii of curvature of 60 of them, distributed within four cantilever arrays. The latter were taken at different locations of a same wafer. Figure 3.11 shows the distribution of the measured tip radii. With an average value of 3.81 μm and a standard deviation of 0.034 μm (0.9%), their reproducibility is very good. Moreover, with a target radius of curvature of 4 μm based on the preliminary results (Section 3.1.2), the obtained tips are only 5% off. Hence, the final tip shape can be well predicted with the current model (Table 3.1).

3.4.3 | Flat tips

By omitting the oxidation/removal steps, I have also fabricated flat cylindrical tips of various diameters (Figure 3.10 C and D). Since these tips do not fit the Hertz model, they cannot be used to measure the Young's modulus of a cell, but are ideally shaped to assess their adhesion properties as presented in Section 1.4.

Since the DRIE is less pronounced in the edges, the obtained tips are not perfectly flat, especially the narrow ones (Figure 3.10 C). A height difference of 400 nm between the centre and

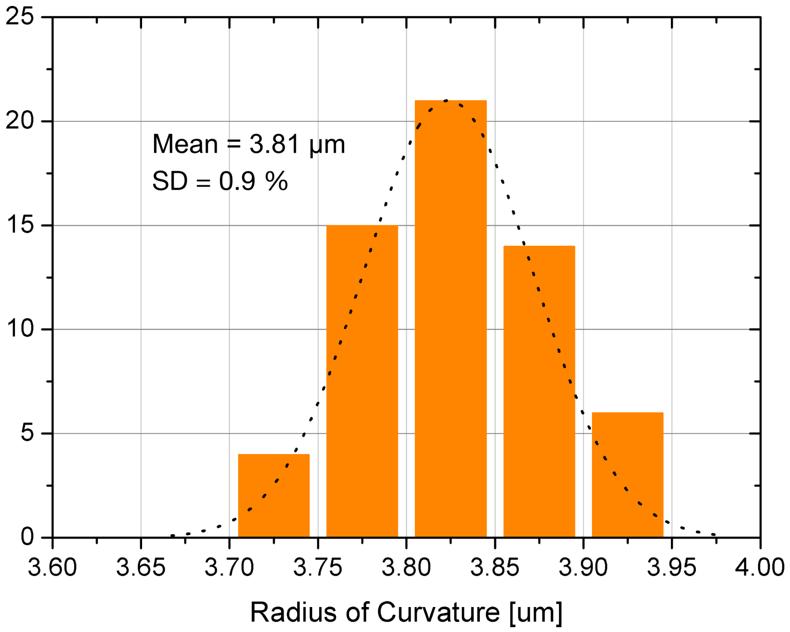

Figure 3.11: Distribution of the measured radii of curvature. Four chips were selected from one wafer and 15 tips were measured within each array.

the tip edges has been measured. Hence, the first half micrometre of the force-distance curve with a cell has to be discarded for the adhesion surface to be constant. For further flatness improvement, SOI wafers, instead of bulk silicon, could be used as moulds. The buried oxide would serve as an etch stop, which would result in very flat tips.

3.5 | Summary

I have described the fabrication of two-dimensional cantilever arrays with novel characteristics for cell-based spectroscopy. A new process for cantilever stiffness modification and controlled tip rounding has been successfully proposed and experimentally demonstrated. The formation of two V-grooves along each side of the cantilevers was quite effective to obtain a relatively high stiffness with silicon nitride. Cantilevers with spring constants between 0.02 N/m and 6 N/m were fabricated out of 0.35 μm silicon nitride layer on a 200 μm x 50 μm footprint, which is within the constraints required for the parallel AFM system.

Furthermore, a new tip moulds enlarging/rounding technique that allows the batch fabrication of spherical tips with a radius of up to 7 μm has been demonstrated. Tedious post processing steps are therefore eliminated. By varying the initial diameter of the moulds, it is also possible to create spherical tips of different radii of curvature within the same wafer. Moreover, these tips are highly reproducible and their final dimension is easily predicted by the simulations. Such repeatability is critical for confident results in parallel spectroscopy.

4 || Parallel force spectroscopy on living cells

In this chapter, I present force spectroscopy results that were obtained with the fabricated 2D array probes and the custom made parallel prober system (Figure 4.1). While I have followed the measurement procedure a couple of times, the pictures and data were kindly provided by Dr. Cristina Martin-Olmos, Dr. Mélanie Favre, and Dr. André Meister of CSEM. Dr. Martin-Olmos was, together with Dr. Mélanie Favre, responsible of the force spectroscopy experiments and analysis with the provided cantilever arrays. Dr. Meister developed the software to analyse the force-distance curves and extract the cell Young's modulus based on the Hertz model.

4.1 | Methods

The creation of cell arrays with the same pitch as the cantilever arrays is required to perform parallel force spectroscopy on living cells. The cell array is obtained using CYTOO chips^{TM} micropatterned with fibronectin on glass. WM239 cells, a melanoma cell line in metastatic phase, are collected by trypsinisation and let sediment and adhere on the spots of fibronectin for two hours. The cell chip is then washed with PBS to remove all unattached cells and re-placed in PBS.

Both the cantilever array and the cell grid are mounted on the probe array system with optical readout [112]. Figure 4.2 shows the interferometric image obtained once an array is mounted. Interference fringes are clearly visible on each cantilever. Using a custom made Labview software, measurement lines (in red on the picture) are drawn at the starting and ending points of each cantilever to solve the phase ambiguity of the interferometric readout. This strategy allows analysing small areas of the image, resulting in short computational time. A last line (in green) is defined on a silicon nitride board sticking out of the frame. It will serve as the reference point for the interferometric measurements.

Initially, the parallelism is adjusted by observing the deflections of the pyramidal tips that are designed on each corner (Figure 3.5 B). A phase contrast microscope is used for this manual course alignment (Figure 4.3). Due to the relatively thin gold reflection layer (40 nm), the

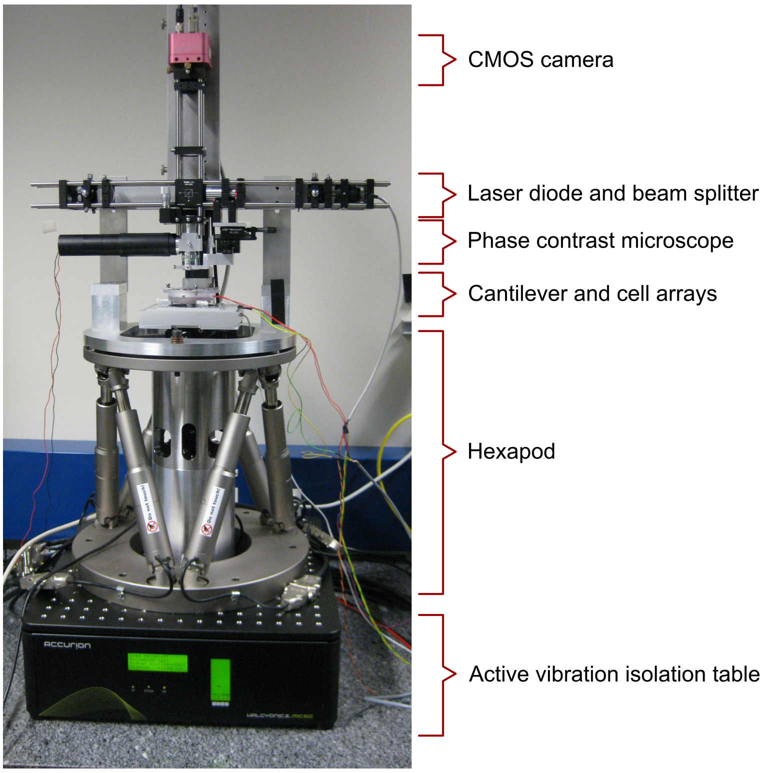

Figure 4.1: Picture of the whole system including a phase contrast microscope and an active anti-vibration table.

cantilevers are transparent enough to observe through them. The alignment of the tips with the cells is therefore facilitated. Once the cantilever array is aligned with the cell grid, a 500 nm x 500 nm square is defined and a deflection-indentation curve is retrieved at each corner. These four curves will provide four Young's modulus values that will be averaged. This is done to minimise the influence of misalignments of each cantilever-cell couple within the array.

4.2 | Results and discussion

Figure 4.4 shows 13 deflection-indentation curves simultaneously recorded in an approach step. Since the height of each cell varies, the contact between the tips and the cells do not occur at the exact same time. Hence, the contact force cannot be defined separately for each cell. The various discrepancies that can be observed within the curves come as well from small alignment differences between the cantilevers and their corresponding cells. As cells are highly heterogeneous, deflection-indentation curves differ depending on their probing zone. Cellular shape, nucleus position, or adhesion forces, may influence the force spectroscopy results.

The Young's modulus of a cell is determined with a Hertz model fitting of the force-indentation curve. Figure 4.5 shows a typical curve. As the cell is a heterogeneous sample, its stiffness

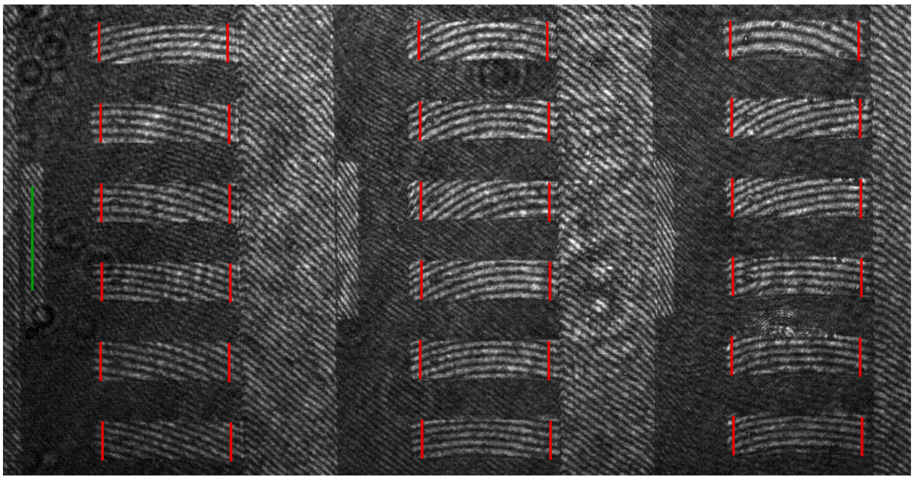

Figure 4.2: Interference fringes on a partial top view of a cantilever arrays. Cantilever lateral dimensions are 200 μm x 50 μm. Red lines are drawn in the custom made software to define zones of measurements. Two lines per cantilever are needed to solve the phase ambiguity. A green line is defined as reference.

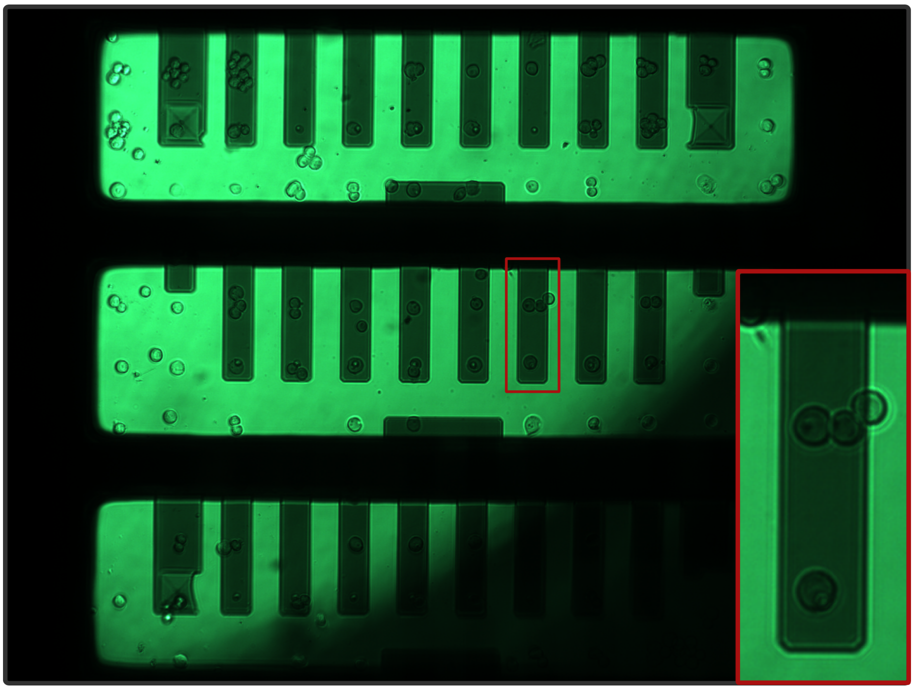

Figure 4.3: Contrast phase microscopy image of a 2D cantilever array aligned with a CYTOO chip^{TM} with attached WM239 cells. A close view of one of the cantilevers is also shown. The window measures 1 mm x 1 mm. Cells can be seen through the cantilevers due to the thinness of the reflective gold layer (40 nm).

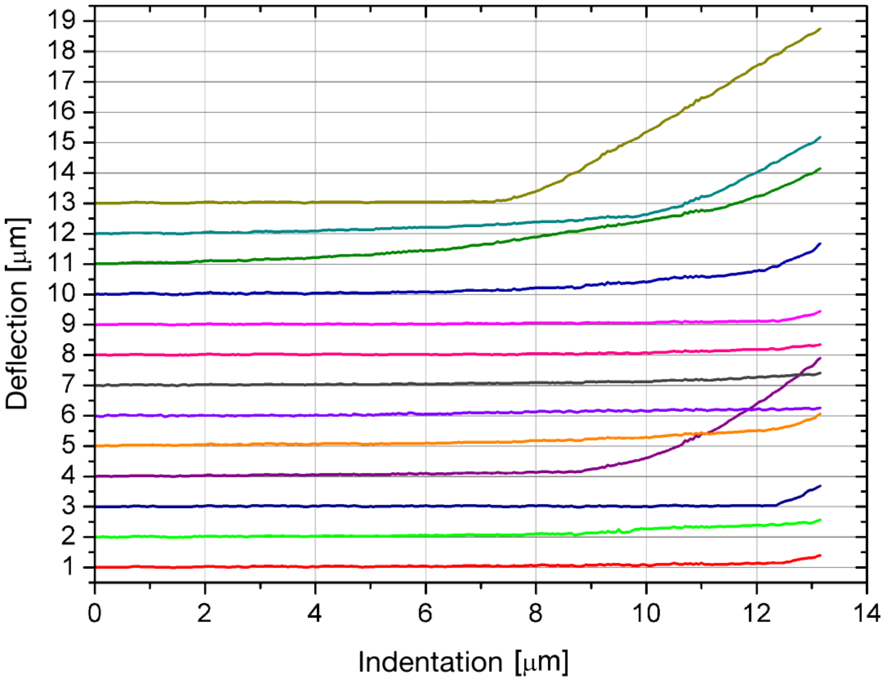

Figure 4.4: Deflection-indentation curves of a cantilever array on a grid of WM239 cells. The cantilevers touch the cells at different moments depending on their initial bending and on the height of their corresponding cell. Curve 13 directly touched the substrate.

varies with the penetration distance of the tip. On the plot, zone B characterises the stiffness of the cytoskeleton while zone C shows a stiffness increase, which may be explained by the presence of the nucleus. In zone D, the probe reached the substrate. As explained in Section 1.2.2, the Hertz model assumes a homogeneous sample. Hence, it has only be fitted to zones A and B, where the influence of the nucleus or other organelles are assumed to be negligible. For this particular curve, the measured Young's modulus is 131 Pa. The cell height, measured from the start of zone B to the end of zone C, is 5.9 μm.

A typical approach-retraction step takes between 6 to 8 minutes depending on the indentation step and speed. If all 24 probes are aligned with a cell, we obtain a measurement rate of one cell every 15 to 20 seconds. This measurement speed could still be improved with further optimisations on the readout system bandwidth and the introduction of additional probes within each array. Compared to other cell mechanical probing systems, the obtained measurement speed is comparable or even faster [28]. The main advantage of the parallel force spectroscopy lies in the fact that, despite this fast overall measurement rate, each cell is still probed slowly enough to avoid any viscoelastic effect. From these results, we have demonstrated that parallel force spectroscopy on cells is feasible. As expected, discrepancies in the obtained deflection-indentation curves are observed due to the heterogeneousness of the probed cells. As each cantilever cannot be perfectly aligned with its corresponding cell, some of them will probe the nucleus region while other will probe the periphery of the cell.

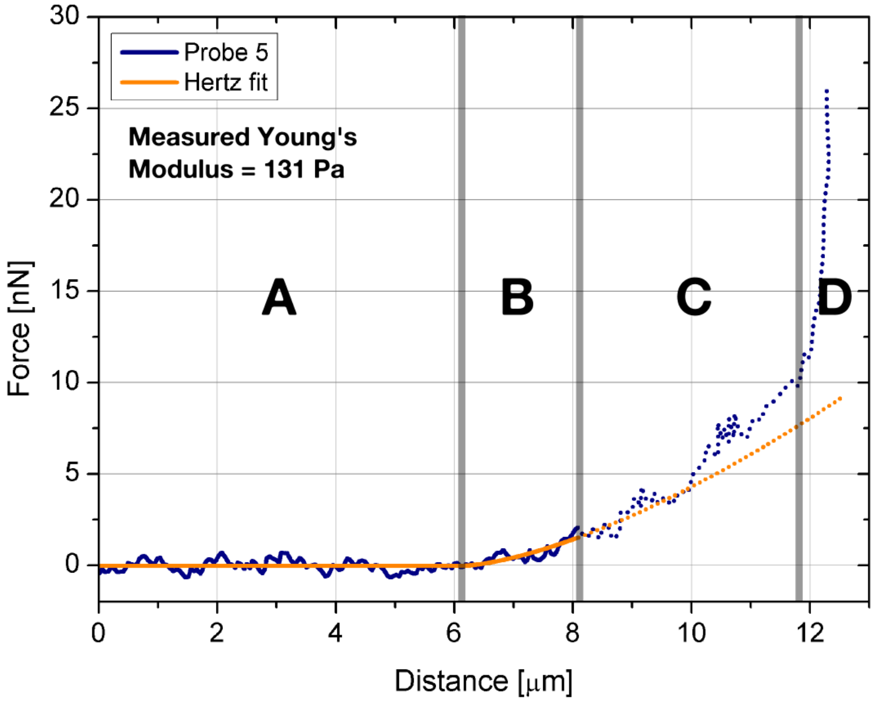

Figure 4.5: Force-indentation curve of probe number 5 with its corresponding Hertz fit. The probe approaches the cell surface (A). The probe penetrates the cell cytoskeleton (B) and reaches the nucleus (C) until it touches the substrate (D). The Hertz model has been fitted to zones A and B in order to calculate the stiffness of the cytoskeleton only. The measured Young's modulus of this cell is 131 Pa.

While taking into account the shallow indentation depth may reduce these discrepancies, only statistical results on large set of cells will give confident analyses, which was exactly the purpose of this project.

5 || Conclusion

Probing the mechanical properties of cells is instrumental in understanding how they spread, attach, and, generally speaking, behave under certain stress conditions. Many fields in biology and medicine may benefit from mechanobiology studies. Cancer is one of them. The assessment of the stiffness and the adhesion forces of cancerous cells could lead to the creation of new spreading models of metastases or to new screening methods for cancer drugs.

In this first part, a 2D probe array was proposed as an adapted tool for high throughput force spectroscopy measurements on multiple cells. Its design, fabrication, and characterisation were thoroughly presented. With the integration of V-grooves of different heights along the cantilevers, I have designed cantilever arrays of various spring constants while keeping the same footprint. This allows always having the same x- and y-pitches between the probe array, the optical readout, and the cell grid. Hence, the replacement of an array with another one of different stiffness in the system is simplified. In addition, I have developed a new process for the batch fabrication of spherical tips with a radius of curvature up to 7 μm. Since most researchers still rely on glued beads for their biological experiments with AFM, the proposed method has applications beyond the scope of this particular project.

A particular attention was brought to the reproducibility of each process. As the probes are used in parallel, their uniformity is indeed critical for the confidence of the obtained results. With a standard deviation of 3% within an array, the cantilever spring constant is particularly well defined. The spherical tips are very reproducible as well. 60 of them were measured among four chips and showed a standard deviation of 1%. Their final radius of curvature is also well controllable with an error of only 5% with the expected value.

The fabricated 2D arrays were tested in the parallel force spectroscopy system developed by CSEM with cancer living cells. Simultaneous force-deflection curves were successfully obtained and the proof of concept was demonstrated with a throughput of four cells per minute. This rate can still be increased with a better image processing algorithm of the system and an array containing more probes. Further experiments are currently undergoing at CSEM to explore all the capabilities of this tool.

Part II

Membrane-Type Sensors for Molecular Detection

6 || Introduction

As any living creatures, we are occasionally subject to diseases that alter, in one way or another, the normal function of our body. As a result, we may experience discomfort, pain, distress, or even death in the most severe cases. It is therefore not surprising that mankind has quickly relied on medicine to prevent or heal the various encountered health problems. For the past decades, tremendous progress has been made in this area. Surgeons are now being assisted by robots while artificial organs are being grown from stem cells [121, 122]. Full genome sequencing, which can now be performed for a few thousands of US dollars [123], will likely allow personalised medicine, where medical decisions and drug prescriptions are tailored to the individual patient.

These few examples of the recent medical breakthroughs have helped us, or will help us, to live better and longer with a life expectancy that has never been so high. There are, however, some shadows on this depicted situation. While hospitals were acquiring highly technological equipments required for these state-of-the-art procedures, the health care costs have dramatically increased. In Europe, they reached in average 7.3% of the gross domestic product in 2000 and 9.0% in 2010 and are projected to increase more and more [124]. As a result, our health care system has concentrated its services in huge medical centres, while small regional hospitals are being reduced or even shut down. The situation is even worse in developing countries that cannot afford the expensive equipment or drugs for the proper care of local populations.

Point-of-care (PoC) systems are expected to revolutionise the way doctors care for patients and solve some of the above-mentioned problems [125]. Instead of centralising the patients into sophisticated medical centres, care services such as diagnostics or health monitoring are either handled by their family doctor or directly brought to their home. This change in settings of health supervision can dramatically reduce costs and diagnosis delays while increasing the patient quality of life [126]. PoC devices require however to be portable, easy-to-use, and cost efficient in order to be accepted in our daily life. Most importantly, they must be reliable as their results are usually interpreted by the patient and not by his or her doctor. Two of the most successful examples of PoC systems to date are the home pregnancy test and the single-use glucose sensors used by diabetics, which have been already available for a few decades [127, 128].

The use of PoC systems could also be instrumental in cancer therapy. Apart from prostate, breast, and cervical cancers, there are very few routine checks for possible tumours. As a result, the majority of cancers are diagnosed at a late stage, where survival rates are dramatically low. Due to their characteristics, PoC systems may be ideal platforms as rapid and non-invasive screening tools for many cancer types. The detection of biomarkers [1] is therefore critical towards the development of PoC devices for cancer diagnosis.

As regards to the required features of PoC systems, bio/chemical sensors based on microsystem technologies are ideal platforms to be incorporated into them owing to their small size, low power consumption, and high sensitivity. In this chapter, I will briefly discuss about how cancer is diagnosed nowadays and what solutions or improvements PoC systems may bring to this field. The existing microsystem-based platforms capable of molecular detection will then be summarised. Finally, I will present the approach and the technologies that were selected in the framework of the PATLiSci project to propose a non-invasive cancer screening tool.

The rest of this thesis part is divided according to the following order: theoretical background on piezoresistive surface stress sensors is discussed in Chapter 7 while design guidelines based on finite element simulations is presented in Chapter 8. The sensor fabrication results and characterisation is then presented in Chapter 9. Finally, preliminary results on cancer diagnosis via the analysis of breath samples are discussed in Chapter 10. Conclusions and outlooks bring this second part to an end in Chapter 11.

6.1 | Cancer diagnosis

6.1.1 | History

Unlike other diseases, cancer has been known for quite some time. The oldest reference to such a disease can be traced back in 3000 BC, in ancient Egypt [130]. At that time, tumours were treated, more or less successfully, with cauterisation, ablation, or even arsenic paste. Surgical removal was the standard procedure in Ancient Greece and Rome. Skin, stomach, colon, liver, and spleen tumours were already recognised at that time, while firmness of the body part has been identified as a symptom. Most of the time however, the prognosis, i.e. the medical prediction of the disease evolution, was death.

Surgery remained the principal therapeutic intervention mean until the 19th century and the invention of radiotherapy. Diagnoses still relied on palpations or indirect symptoms, such as chronic cough in the case of lung cancer or constipation in the case of bowel cancer. At these stages of detection, metastases were frequent [131, 132]. The first cancer screening test was invented in 1928 by Georgios Papanikolaou with the development of the cervical smear [133]. Nowadays, standard screening methods have been developed for breast, prostate, bowel, and

---

[1] Defined by the US National Cancer Institute as "biological molecules found in blood, other body fluids, or tissues that are signs of a normal or abnormal process or of a condition or disease. Biomarkers may be used to see how well the body responds to a treatment for a disease or condition" [129].

cervical cancers.

6.1.2 | Towards non-invasive screening tools

Until the middle of the 20th century, external symptoms were the only reliable proofs to support the existence of a tumour. As those usually appear at a developed stage of cancer, the survival rates were often pessimistic in contrast to early diagnoses [133]. Since then, several routine screening tests have been developed based on medical imagery but some of them are still subject to controversy. In the case of breast cancer for instance, a recent study showed that for every 2,000 screened women, one of them had her life prolonged due to an early breast tumour detection. On the other hand, ten of them were misdiagnosed and overtreated [134]. In the case of bowel cancer, screening by colonoscopy has been found to be very effective with a 40% decrease in mortality rate [135]. However, colonoscopies cannot be described as non-invasive and require heavy equipment.

Other screening tools have been developed based on the analysis of body fluids. This is the case for cervical cancer, which is screened by observing cervical smear, or for prostate cancer, which is framed by measuring the concentration of a particular protein in the blood. While misdiagnoses are still possible, these methods are non-invasive and do not require a significant involvement of the patient. They rely on the detection of biomarkers that indirectly highlight the presence of a tumour. In any cases, such screening tools do not intend to replace a biopsy, which is the final step taken by doctors to diagnose a tumour.

Routine screening tests of biomarkers could advance the time of diagnosis and improve the survival rates of most cancers. Due to the complexity of the human body and its constant physiological changes, many of these biomarkers may not exclusively signify the presence of a tumour. Detection of multiple targets, which form a more reliable fingerprint, is therefore preferred over single detection to significantly decrease false positives [136].

6.1.3 | Biomarkers: types and roles

Besides their use as diagnostic elements, biomarkers could also be targeted to follow the evolution of the disease or test its resistance to certain drugs [137]. Hence, the discovery of new biomarkers is instrumental in many aspects of cancer therapy. They can be of various origins, from cells to proteins or volatile organic compounds. I present in the following paragraphs the main types of existing biomarkers together with a few examples. More details on existing and emerging cancer biomarkers can be found in various papers [138].

Cells

Once cancerous cells start to migrate from their original tumour site to form metastases, they appear in bloodstream. These cells are called "circulating cancer cells" (CTCs). While a simple blood sample is sufficient to assess these biomarkers, the very low proportion of CTCs compared to other cells (about 1 per billion), and their capture and enumeration may be challenging [139]. The monitoring of CTCs is a powerful tool to follow the development and the progression of the disease [140].

DNA

Similarly to CTCs, free floating fragments of DNA can be found in body fluids, such as blood or urine, as a consequence of dead tumour cells [141]. While abnormal levels of DNA can be caused by a tumour, they may also results from other states, such as severe infections or autoimmune diseases. The observation of genetic modifications due to cancer provides however a much more accurate biomarker [142]. Genetic alterations may also occur at the RNA level. Hence, selected RNA fragments found in body fluids could also be used as biomarkers.

Proteins

Cancer cells release quantities of proteins that can later be found in various body fluids. One of the best known protein biomarkers is the prostate specific antigen (PSA) [143]. PSA can be traced in serum of all men but in more elevated quantities in case of prostate tumour. Colon, breast, or pancreas cancer can also be screened with a protein-based assay [137].

VOCs

Our breath contains several hundreds of components known as volatile organic compounds (VOCs). Traces of acetone, methanol, or carbon monoxide have been, for instance, detected [144]. Despite its high number of components, exhaled breath is still less complex than other body fluids, such as blood or saliva, and has been proposed as a complementary analysis medium for diseases [145]. One of the most interesting applications would be the detection of cancer in the respiratory region. Volatile aldehydes have been identified as potential biomarkers for lung cancer while six VOCs were highlighted in the case of head-and-neck cancers [146, 147].

6.1.4 | Gold standard methods for the detection of molecules

Biomarkers, and molecules in general, can already be detected and distinguished by several methods. Labelled assays, such as the enzyme-linked immunosorbent assay (ELISA), are the preferred techniques to detect molecules in liquid media [148]. These methods rely on highly specific bindings, such as antigen-antibody or DNA hybridisation, to detect the presence of the corresponding analyte. A fluorescent label is then chemically linked to the analyte and allows very sensitive detection by colourimetry.

Gas chromatography combined with mass spectrometry (GC-MS) is also widely used to

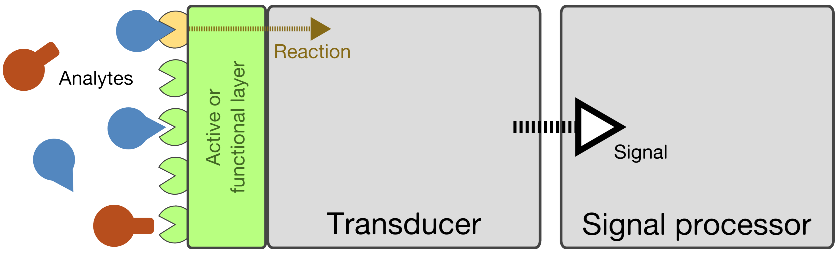

Figure 6.1: Graphical representation of a generic molecular sensor. It is composed of a transducer that is coated with an active layer. The reactions with the analytes are then transformed into a readable signal.

analyse gaseous or liquid mixtures [149]. The sample to analyse is first ionised in a chamber and the ions are then selected according to their mass-to-charge ratio. The beam of ions is finally electrically detected to quantify the number of ions. This result is compared with reference charts to identify the present analytes in the mixture.

While the classic methods presented above show impressive performances, they represent well the archetype of modern health care equipments: highly sensitive and specific but skilled technicians and/or expensive laboratories tools are required. PoC systems could therefore advantageously replace, in some cases, these standard laboratory tests. Potentially less expensive, their results are obtained in minutes and are simpler to analyse. On the other hand, their sensitivity, selectivity, or repeatability are often not as optimum, but may suffice for selected applications.

6.2 | Micro- and nanotechnologies in point-of-care systems

All PoC systems rely on a sensing device for the detection of particular molecules. A molecular sensor can be represented by the general schematic shown in Figure 6.1. It is composed of three parts, namely a transducer, an active layer, and a signal processing unit. The active layer, also called functionalisation layer, is designed to react with the molecule to detect. The reaction is then passed to the transducer, which transforms it into a readable signal. The latter is finally amplified, stabilised, and recorded by the signal processing unit. Ideally, a sensor should have a high sensitivity and selectivity. While a fast and linear response is appreciable, its reliability and sensor-to-sensor reproducibility is critical, especially in PoC applications.

In this section, I summarise various active layers that can be used to trap molecules and the major micro- and nanosystems that are being investigated as potential molecular sensors for gaseous or liquid applications. The typical detection limits of these technologies in liquid applications are displayed in Figure 6.4. As not all the discussed platforms are compatible with gaseous analytes, the limits of detection for these species are provided for each sensor, if applicable.

6.2.1 | The active layer

The choice of the active layer is fundamental in molecular sensors. Its main goal is to allow molecules to physically or chemically interact with the sensor platform. Its affinity towards certain analytes defines the type of molecules that will be detected by the sensor. Selectivity, reproducibility, and detection speed of the sensor strongly depend on its functionalisation and the quality of its deposition.

Functional materials

There are almost infinite functionalisation possibilities, depending on the analyte to detect. They can be however classified in two categories based on the adsorption or the absorption of molecules. In the first case, molecules adsorb at the surface of the functionalisation layer due to physical forces or chemical reactions. Beside the added mass, the adsorbate may modify the surface characteristics of the polymer. Conductivity changes or surface stress can be, for instance, observed. Active layers based on molecular adsorption can be highly specific. A surface covered with DNA strands will only react to the complementary strands. Similarly, antibodies-functionalised surfaces remain active only to the corresponding antigens. Proteins, cells, or viruses can be selectively adsorbed with an adequate functionalisation layer [150, 151, 152].

In the second category, analytes are absorbed into the functionalisation layer, which is usually composed of a polymer. As a consequence, variations in mass, dielectric properties, or swelling, can be observed with the polymer. Depending on the chemical properties of the polymer, such as hydrophilicity or polarity, it interacts with more or less affinity with its surrounding molecules [153]. However, the selectivity of polymers on their own will never reach that of antibody-antigen bindings. The selectivity can be improved with the mixing of active particles, such as carbon nanotubes or functionalised nanoparticles, in the polymer [154, 155]. Another promising technique to enhance the selectivity of polymer-based functionalisation is molecular imprinting [156]. The molecules to be detected are incorporated in the polymer solution prior to its polymerisation. Subsequent removal of the molecules leaves cavities of shapes and properties tailored to them. The polymer layer inherits then a molecular memory and will be capable of selectively interacting with this type of molecules.

Deposition techniques

Various techniques exist for the deposition of organic thin films. Spin coating, spray coating, or dip coating are well established and convenient methods but they are limited to wide surface coverages. Local depositions are however possible using screen printing, microcontact printing, or inkjet printing (Figure 6.2) [157, 158, 159] .

Screen printing is a deposition technique that is widely used in the industry, from marking logos on T-shirts to printed electronics. A stencil is first placed on the substrate and the desired

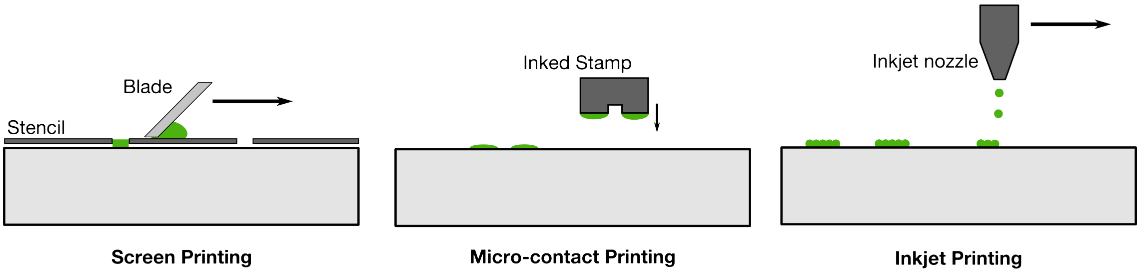

Figure 6.2: Screen printing, micro-contact printing, and inkjet printing are common methods to selectively deposit a functional layer on a substrate.

functionalisation material is poured over it. A blade is then moved across the stencil to fill its openings with a layer of the functional material. Screen printing allows depositing various materials in high volume and for a unbeatable price. Indeed, most of commercially available biosensors rely on this printing technology [160]. The physical contact of the sensor platforms with the stencil is however a limitation in the presence of fragile or moving elements on the surface.

In microcontact printing, a stamp, usually made out of PDMS, is created with a relief pattern. Once "inked" with a chosen solution, the stamp is brought into contact with the substrate to be functionalised and the ink pattern is transferred by contact. Patterns as small as 50 nm have been reported [161]. Various materials, such as SAMs, proteins, DNA, and even cells can be patterned by microcontact printing [162].

Inkjet printing is widely used to functionalise nanomechanical sensors [163]. Unlike microcontact imprint, the material deposition is contactless as microdroplets (typical volume of 10 - 200 pl) are ejected from a nozzle onto the substrate (Figure 6.3 A). Hence, there is no risk of damaging or contaminating the sensor surface. Furthermore, the printer can easily switch from one solution to the other without any additional tool or step. Inkjet printing is therefore a versatile dispensing method suitable for research applications. This printing technique is however affected by the coffee stain effect. As the solvent evaporates on the substrate surface, the dispersed material is carried towards the edges of the liquid interface. After complete solvent evaporation, the remaining material is deposited as a ring that marks the original contact line (Figure 6.3 B) [164]. The final deposited pattern is highly heterogeneous and of poor reproducibility. The control of the deposition can be improved to reduce the heterogeneity and randomness of the polymer pattern [165, 166]. For example, it was demonstrated that mixing solvents with different surface tensions can effectively decrease and even suppress the coffee-ring effect [167].

6.2.2 | The transducers

Numerous platforms have been developed towards molecular detections. The main technologies, classified according to their transduction principle, include electrochemical, optical, or

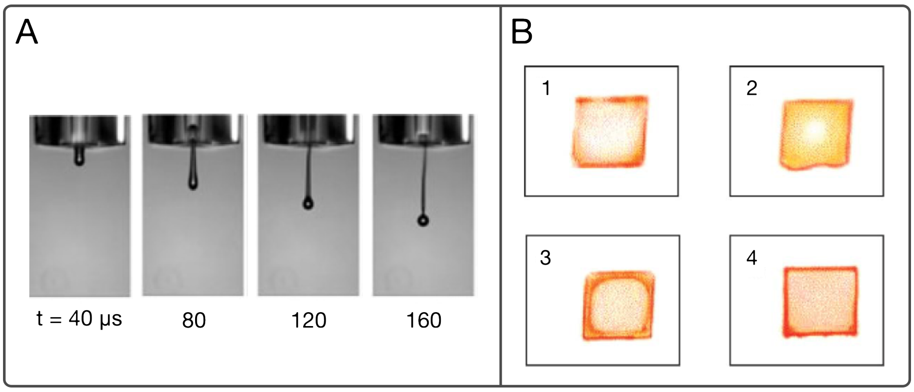

Figure 6.3: (A) Droplet ejection from a nozzle. Adapted with permission from [159]. (B) Polystyrene films, ink-jet printed using a solution containing 2.0% polystyrene and 0.05% Disperse Red 1 by weight. Different solvents were used: 1) toluene; 2) ethyl acetate; 3) anisole; 4) butyl acetate. Adapted with permission from [167].

mechanical transducers. Figure 6.4 compares the limits of detection and analysis times of several sensor technology for protein sensing.

Electrochemical sensors

Electrochemical test strips: Historically, electrochemical test strips were one of the first developed biosensors suitable for PoC applications . They rely on an electrode (the transducer) covered with an enzyme (the active layer). Oxidation/reduction reactions with a corresponding analyte produce a current through the electrode that can be measured. The latter is proportional to the amount of oxidised analyte. This technology has been widely used in glucose monitoring for more than 30 years [168]. Despite a relatively low sensitivity, electrochemical test strips have fast detection time and can be fabricated in mass using screen printing technologies [169].

Conductive polymer based sensors: These sensors are widely used in gas sensing applications [170]. A conductive polymer layer is coated on top of an interdigitated electrode. The absorption of volatile molecules into the polymer induces swelling as well as changes of its electrical properties. The latter can be measured via capacitance or resistance measurements [171].

Alternatively, metal oxides (MOx) layers can replace the polymer. Conductance changes are observed during the adsorption of volatile molecules on the oxide surface due to charge trapping [172]. MOx gas sensors are fast but they need to operate at high temperature, typically 200°C - 500°C. They are also subject to cross-sensitivity although the latter can be diminished by changing the operating temperature [173]. Sub-ppm detection levels of various gases have been measured depending on the chosen oxide layer [174].

Nanowire-based sensors: Nanowire field effect transistors (NWFETs) rely on the same sensing principle as ion-sensitive field effect transistors (ISFETs) [175]. In the latter, the gate is exposed to a solution and any ionic changes at its surface, such as pH or DNA hybridisation, will influence the drain current of the transistor [176, 177]. In the case of NWFETs, the wire acts as the channel connecting the source to the drain. The increased surface-to-volume ratio of NWFETs induces an increased sensitivity.

Nanopores: Nanopores are particular molecular sensors that are mainly designed towards DNA sequencing [178]. A molecular-sized pore is created into an insulated membrane that separates two chambers filled with an electrolyte. Charged molecules are driven through the pore by electrophoresis. Each passage of a molecule modulates the ionic current of the pore that is recorded by an electrode. As this current depends on the type of molecule, it is possible to count and distinguish those passing through the hole. Current detection limits are in the range of the nM with a analysis throughput of about one DNA molecule per second [179].

Optical sensors

Surface plasmon resonance (SPR) sensors: Surface plasmon resonance sensors are already well established in the molecular detection field. As molecules bind on a functionalised surface, the local refractive index between the liquid medium and the surface varies [180]. This refraction change can be monitored with an incoming light wave reflected on the functionalised surface. SPR sensors are usually not portable, although a compact design has been proposed to be integrated in cell phones [181].

While the optical coupling between the adsorbed molecules and the reflected light wave is almost immediate, standard label-free SPR technologies are not very sensitive. The limit of detection can however be enhanced with the help of label probes incorporating gold nanoparticles [182].

Ring resonator-based sensors: Similarly to SPR sensors, ring resonator-based sensors rely on the propagation of light at interfaces. While the light propagation is linear in SPR sensors, the waves are trapped and amplified in a ring-shape resonator [183, 184]. Hence, the sensitivity can be increased.

Mechanical sensors

Acoustic wave sensors: In electro-acoustic devices, two electrodes are applied on a piezoelectric material, such as quartz [185]. Sinusoidal electrical signals between the two electrodes produce acoustic waves that travels at high frequency from one electrode to the other. The resonance frequency of the acoustic waves is closely related to the geometry and the mass of the device. Hence, any added mass produces a frequency shift that can be measured.

In the case of electrodes applied on both sides of the material, the acoustic waves travel in the bulk. Quartz crystal microbalances (QCMs) work in this mode [186]. On the other hand, the electrodes could be placed at the same side and the acoustic waves travel then in the surface only. this configuration is employed by surface acoustic waves (SAW) sensors [187].

For both configurations, higher quality factors yield higher sensitivity. Hence, they work best in vacuum. In gaseous phase, QCMs have been used to detect various VOCs with limits of detection ranging from 5 ppm to 700 ppm [188]. In liquids, the Q factor is significantly attenuated. However, by desiccating the sensor after the analyte bindings and measuring the frequency shift in air, the sensitivity can be greatly increased. This additional step increases the analysis time.

Nanomechanical sensors: Initially designed for AFM, micro-cantilevers are more and more used in various sensing applications [189]. Their unique capability of being sensitive to forces at the atomic scale can be used to detect very small chemical or physical interactions without the need of a tip. Instead, a functionalisation layer is deposited on the surface of the cantilever.

The presence of analytes on the cantilever is detected either by measuring a change of mass of the cantilever or by observing the formation of a surface stress on the cantilever. In the first case, the cantilever is actuated at its resonance frequency and any added mass will result in a frequency shift. Single cell detection as well as attogram (10^{-18} g) mass resolution have been reported with this method but the sensor performance rapidly decreases in aqueous environments due to the degradation of the cantilever quality factor [190, 191]. In the second case, the major sensing principle is based on analyte-induced surface stress, which makes the cantilever bend. While this technique is less sensitive than the mass sensing method, it does not require any actuation and enables the setup to be simpler and less power demanding. The cantilever deflection is usually measured optically, but integrated readouts, such as capacitive, piezoelectric, or piezoresistive, have been employed [192, 193, 194].

Since nanomechanical sensors can be used equally in gaseous or liquid media, they are very versatile platforms for molecular detection. Depending on the functionalisation layer, various analytes, such as explosives, antigens or VOCs, can be detected [195, 196, 197].

6.3 | Sniffing out the odours of cancer

Since cancer cells have a different metabolism compared to healthy cells, they produce substances that may differ either in quantity or in typology. Those biomarkers can therefore be detected for tumour diagnosis or evolution purposes. Various research groups have recently discovered that dogs are able, if adequately trained, to detect cancer scents with their sense of smell, similarly to explosives or drugs. In a study on breath analysis, five dogs were able to distinguish patients suffering from lung cancer from healthy people with an accuracy of 99% [199]. A similar study was performed with urine samples to detect prostate tumour [200]. The decisions of the trained dog were in agreement with prior biopsies in 30 of 33 cases. One of the three healthy persons wrongly diagnosed by the dog was re-biopsied and a prostate cancer was diagnosed.

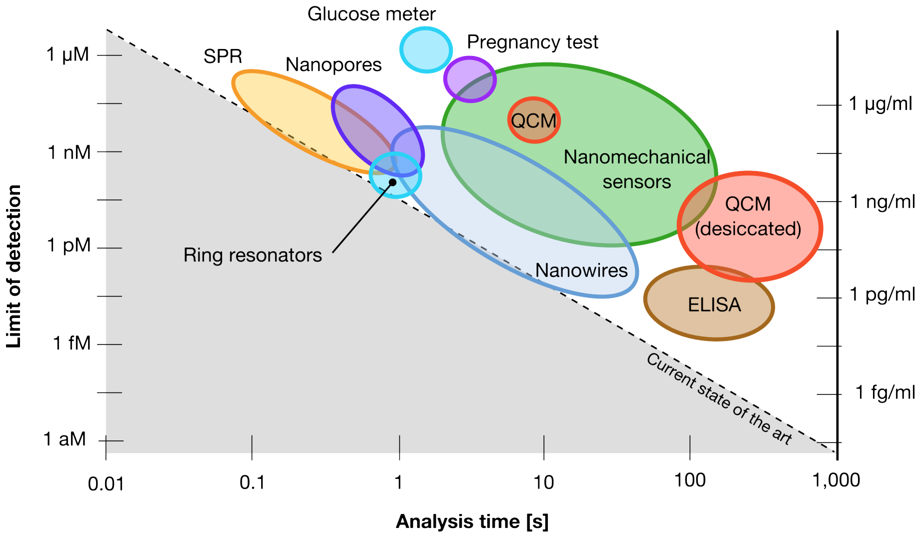

Figure 6.4: Detection limits of common label-free point-of-care technologies. The ellipses shows standard performances. The ELISA test is shown as well and serves as a reference point. As longer analysis times lead to lower limits of detection, a trade-off must be found for each application. This graph as been inspired from [198].

Analyses of breath samples by GC-MS confirmed that lung, head-and-neck, bowel, or even breast cancers have a unique scent signature based on the concentration of various VOCs that can be identified [147, 146]. Hence, it would be possible to replace the dog with a highly sensitive PoC system capable of identifying those biomarkers.

6.3.1 | Electronic nose approach

History and concept

The idea of sniffing out cancer in the breath naturally leads to electronic noses. The concept of artificial olfactory systems that would be capable of discriminating various odours has been developed a few decades ago [201]. Several systems based on gas chromatography coupled with mass spectrometry are already commercially available. While they are extremely versatile and sensitive, their size and price limit their use to security and military applications.

In 1982, Persaud et al. proposed a new concept modelled on mammalian olfactory organs [202]. Instead of one sophisticated sensor, three simple gas sensors with partial selectivity and of different characteristics were coupled in parallel. As each of them reacted slightly differently to volatile molecules, the combination of their responses acted as a molecular fingerprint. The latter could later be compared with previously recorded "known" gaseous species for pattern recognition.

Since then, numerous electronic noses were developed, all of which shared three basic building blocks, namely a gas chamber, an array of partially specific gas sensors, and a data analysis

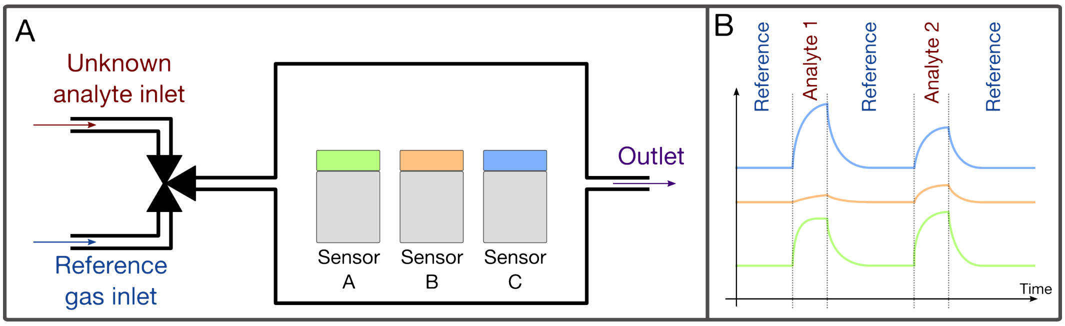

Figure 6.5: (A) General schematic of an electronic nose composed of an array of three sensors in a gas chamber. The inlet can be chosen between a reference gas, such as nitrogen, and the gas to be analysed. Typical sensor responses are shown in (B) for two different analytes. As each sensor is differently functionalised, each of them responses differently to surrounding molecules. The combination of all signals gives a fingerprint of the gas present in the chamber. The reference gas is used to purge the chamber and reset the electronic nose.

software to produce and compare the fingerprints (Figure 6.5). Conductive polymers, metal oxides, SAW, QCM, and nanomechanical sensors were mainly used as sensing platforms. They were designed for applications as various as hazardous gas recognition [203], food quality control [204], and medical diagnoses [205]. There are already several "proof-of-concept" studies on cancer recognition involving either commercial or research-level electronic noses. Hakim et al. showed that an array of five sensors based on conductive polymers with gold nanoparticles was more efficient in distinguishing head-and-neck cancer compared to a classic GS-MS decomposition method [147]. Lung, breast, colorectal, and prostate cancers were also successfully identified with a similar technology [206, 207].

Current limitations

There are a few reasons why we still rely on our own nose for checking the milk or pairing the perfect wine for our Sunday meals. First, electronic noses give qualitative results. They compare two mixtures of gas and show if there are any differences between them but are unable to distinguish and quantify the components within the mixtures. For instance, it has been shown that sensors based on polymers as functionalisation layers are already struggling to decompose ternary mixtures [208, 209]. This is purely due to the limited variety of the non-binding interactions between the molecules and the polymer layers, which cannot describe differently infinite mixture compositions. As metal oxide sensors rely on similar physical interactions, they should logically inherit the same limitation. Increasing the number of sensors, i.e. introducing additional complexity to the fingerprint, has a limited impact as well. An array of 4 to 8 sensors has been demonstrated to be optimal [210, 211]. A lower number of sensors limits the distinction capabilities of the devices while a higher number introduces redundancy.

Electronic noses are therefore limited to differential results and rely on a reference database to compare unknown scents with pre-recorded ones. Similarly to crime investigators who are searching a fingerprints database for a match, if the mixture has not been recorded before, it will not be recognised. Building such scents database is therefore instrumental for a successful nose application and can take quite some effort and time.

Beside these limitations, electronic noses are also subject to reproducibility issues. As their functionalisation layers need to be partially selective, they can be influenced by unwanted parameters and cross-talks. In particular, humidity and temperature changes are important factors that need to be controlled. In addition, as inkjet printing is usually the preferred method of functionalisation, the coffee stain effect may affect the sensor reproducibility as well.

6.3.2 | Project objectives

The objective of this second part in the PATLiSci project is to develop a portable and non-invasive screening tool based on exhaled air analysis. It will focus on lung and head-and-neck cancers with the possibility of extension to other tumours. The long term vision of such a device can be represented by current breathalysers. Portable and easy to use, they give an immediate result that is easily interpreted.

As previously mentioned, exhaled breath is a complex mixture of hundreds of VOCs and cancer influences the concentration of many of them. Based on this fact and on the recognition limitation previously presented, it is unrealistic to detect those particular VOCs from the rest with a high selectivity. An electronic nose principle has therefore been selected. The following guidelines were suggested:

1. **Portability:** PoC diagnostic devices are meant to be portable. The whole setup should be carried in a small luggage and be laptop-powered. The device will be able to be further miniaturised in case of commercialisation.
2. **Array configuration:** Based on previous studies on the ideal sensors number, the electronic nose will be composed of an array of eight sensors individually functionalised. Their limit of detection and sensor-to-sensor reproducibility are equally important.
3. **Sensor technology:** Piezoresistive surface stress sensors were selected as the transducer technology. Compared to other sensors, they are sensitive, versatile, and do not need active parts, such as heating or vibrating elements. The self-sensing capability brought by the piezoresistive readout allows an optimal integration and miniaturisation.
4. **Active layers:** Polymers will be carefully selected for their affinity towards cancer-linked VOCs. They can be easily deposited on each transducer via inkjet spotting or capillaries.
5. **Breath study:** In order to build a solid scent library, 30 breath samples will be collected from both cancer patients and healthy people of similar age. The breath study will be

conducted in a double-blind trial, in which neither the participants nor the researchers know who belongs to the control group, as opposed to the test group.

6.3.3 | Goals of the presented work

Three groups were collaborating in this task. While SAMLAB was responsible for the development and microfabrication of the sensor array, the clinical breath sampling was conducted by the Pluridisciplinary Centre for Clinical Oncology from the Lausanne University Hospital, and the Cantilever Sensors group from University of Basel was responsible for the electronic nose integration, polymer deposition, and of the breath analyses.

The goals of SAMLAB's contribution to this project were:

1. To design and fabricate highly sensitive piezoresistive surface stress sensors suitable for gas sensing and electronic nose applications.
2. To assess their performances. Speed, sensitivity, and reproducibility are key characteristics for the proposed application.
3. To demonstrate their successful integration in an electronic nose system and present preliminary results on cancer diagnoses via breath analysis.

7 || Piezoresistive surface stress sensors: fundamentals

Nanomechanical sensors are a promising technology for chemical and biosensing applications. They were chosen as the core elements of our electronic nose due to their sensitivity and their aptitudes to be fabricated in arrays and be easily functionalised. Unlike other more exploratory technologies, nanomechanical sensors benefit also from the reliability and history of standard microfabrication processes.

Cantilevers are widely used platforms in nanomechanical sensors. While their shape and size vary depending on the operation mode or readout system, those sensors are always based on a thin plate, of which one side is clamped to the bulk. Unlike the mass-sensing mode, the detection of surface stress does not require any actuation as the static bending of the cantilever is measured. Usually, readout of this bending is performed by optical means with a laser. However, the miniaturisation of the setup is limited in these cases. On the other hand, integrated readout methods, such as piezoresistors, can significantly reduce the size of the whole device.

In this chapter, I will first discuss the theory behind these sensors (Figure 7.1). The origin of surface stress, the swelling mechanisms of polymer, and the cantilever bending will be presented. I will then explain how piezoresistors can efficiently detect such bendings and how the design guidelines differ from those developed for AFM applications. Finally, I will introduce a new type of surface stress sensor that was imagined during a collaboration between Dr. Genki Yoshikawa from the *International Center for Materials Nanoarchitectonics* in Tsukuba, Japan, Dr. Heinrich Rohrer, and SAMLAB.

7.1 | Mechanical deformation induced by polymer swelling

7.1.1 | Origins of surface stress

Surface stress occurs when the bonding between atoms at the surface differs from that of the bulk. The inter-atomic forces are therefore different and induce a stress that keeps a structural coherence between the bulk and the surface (Figure 7.2). Surface stress can either

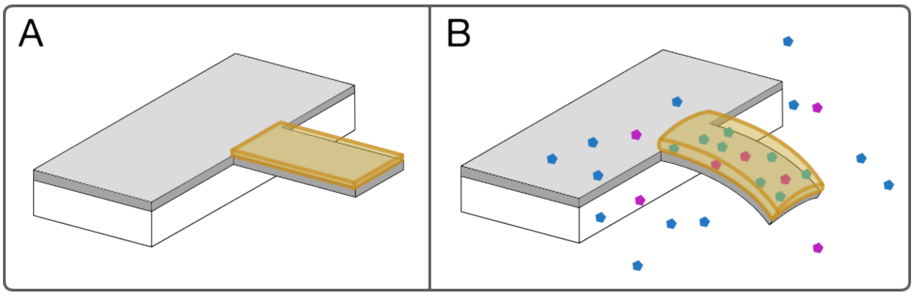

Figure 7.1: (A) Schematic of a cantilever coated with a thin layer of polymer. (B) Molecules that are present in its immediate surrounding will diffuse into the polymer. Different molecules will have different diffusion rates. Upon absorption, the polymer will swell and create a surface stress at the cantilever interface. Due to the viscoelastic properties of polymers, the surface stress is neither immediate nor constant. Eventually, it will produce bending of the cantilever that can be detected.

be compressive or tensile, depending on the surface properties. Although surface stress can be compared to surface tension, the two phenomena are different. Surface tension, or surface free energy λ, is defined as "the amount of reversible work dw performed to create a new area dA of surface" [212]:

$$\lambda = \frac{dw}{dA} \tag{7.1}$$

During plastic deformation or expansion of a solid, atoms from the bulk move to its surface to keep the inter-atomic distances constant. Surface tension represents the amount of energy required for these atomic movements. On the other hand, surface stress is defined as "the amount of reversible work per unit area needed to elastically stretch a pre-existing surface" [213]. Unlike surface tension, the number of atoms at the surface does not increase, but so does their atomic distance. Hence, this process alters the density of atoms at the surface. Surface stress is represented by a tensor σ_{ij}:

$$\sigma_{ij} = \frac{dw}{dA} = \frac{1}{A}\frac{dw}{d\varepsilon_{ij}} \tag{7.2}$$

where ε_{ij} is the strain tensor ($d\varepsilon = dA/A$). In most cases however, surface stress is isotropic and can take a scalar form σ as $\sigma_{zz} = 0$ and $\sigma_{xx} = \sigma_{yy}$. By convention, a negative surface stress is compressive while a positive surface stress is tensile.

Surface stress is induced by numerous phenomena. Physical processes, such as thin film deposition [214] or ions implantation [215], will likely create atomic mismatches near the surface. Similarly, thin film expansions created by temperature differences [216] or molecular absorption [197] will induce surface stress. Chemical reactions are involved as well. DNA hybridisation [217], antigen-antibody bindings [218], and electrochemical reactions [219] are known to induce surface stress. These few examples highlight the various processes that could be monitored by detecting the surface stress they induce.

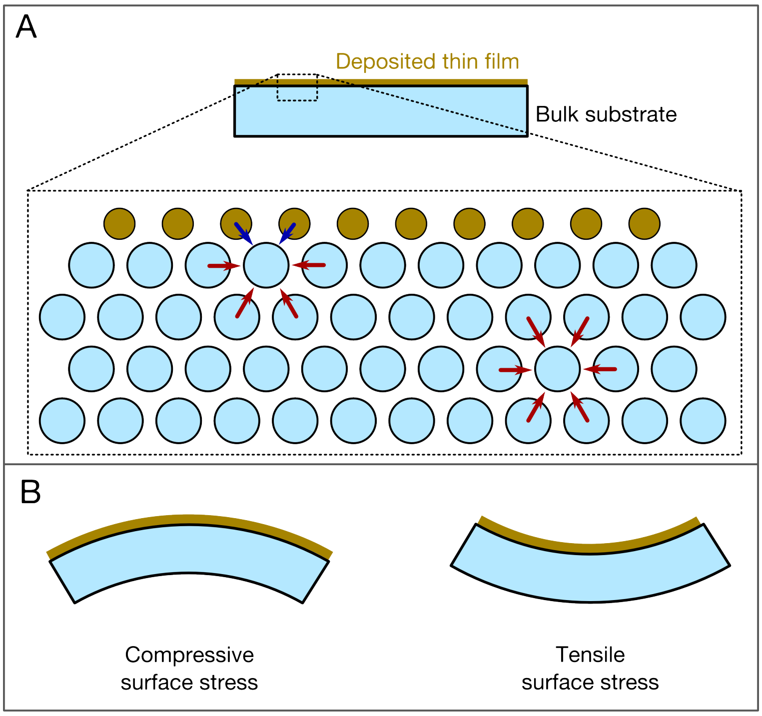

Figure 7.2: (A) Surface stress originates from atomic mismatches at the surface. The atomic forces at the surface differ from those in the bulk, producing a surface stress as a compensation. (B) Surface stress can be either compressive or tensile.

7.1.2 | Absorption and swelling mechanisms of polymers

The functionalisation layer is the key component that induces the surface stress. Since volatile molecules are naturally absorbed into polymers, like water into a sponge, those materials can be effective coatings for gas sensing applications. This absorption of molecules induces a swelling of the polymer layer and, subsequently, a surface stress is created at the interface between the polymer and the plate.

According to Fick's second law, the diffusion of molecules into polymers is not instantaneous. The absorption rate in one dimension is given by:

$$\frac{\partial C}{\partial t} = D\frac{\partial^2 C}{\partial x^2} \tag{7.3}$$

where C is the molecular concentration in the polymer, D is the diffusion coefficient of the molecule into the polymer, and x is the position from the interface. The solutions to Fick's second law depend on the boundary conditions. Figure 7.3 A is a particular case of such a Fickian absorption kinetics, when (i) the diffusion coefficient is constant ($D(x,t) = D$), (ii) the molecular concentration at the interface is constant ($C(0,t) = C_{sat}$), and (iii) the initial molecular concentration in the polymer is null ($C(x,0) = 0$ for $x < 0$). The solution with these initial conditions is an asymptotic expression based on the complementary error function

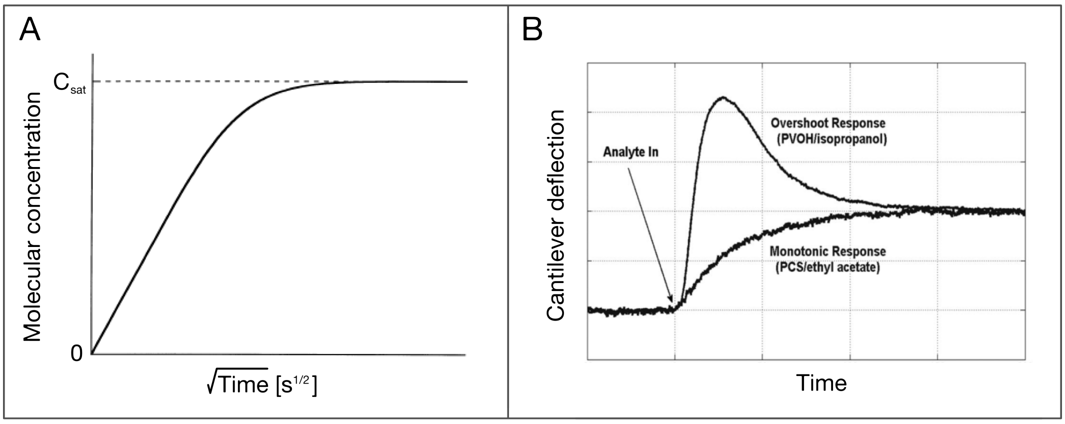

Figure 7.3: (A) Schematic of a typical Fickian absorption curve. Adapted with permission from [220]. (B) Overshoot and monotonic responses for polymer-coated, static- mode cantilever-based chemical sensors. Adapted with permission from [221].

(erfc(x)). As shown, the kinetics smoothly levels off to a saturation concentration C_{sat}. An absorption time constant τ_{abs} can be defined to describe the dynamic of the reaction:

$$C(x,\tau_{abs}) = \left(1 - \frac{1}{e}\right) C(x,\infty) \cong 0.632 C(x,\infty) \tag{7.4}$$

Several observations can be made based on Equation 7.3. First, a thicker layer of polymer will result in a longer saturation time. On the other hand, it will enable a higher number of molecules to be absorbed before saturation. Second, the diffusion coefficient D and the saturation concentration C_{sat} are closely related to the polymer-absorbant couple. Different molecule-polymer sets will likely have different absorption kinetics. Hence, selecting polymers of various chemistries is instrumental for an electronic nose to obtain results of high quality. Some polymers will favour hydrogen bonds while other will prefer Van der Waals interactions [153]. An array composed of polymers with different absorption characteristics will have a greater selectivity and efficiency. As described in Section 6.3.1, 5 to 8 polymers are enough to cover all the possible chemical interactions.

Hence, polymer-based sensors have to measure the whole absorption kinetics. That is not necessary the case with highly selective functionalisation layers, where the steady-state response is usually enough to distinguish analytes. This distinction is important to make while choosing the frequency bandwidth of the sensor.

Due to molecular absorption, the polymer will expand. In the case of humidity absorption, it has been shown that the relation between the polymer swelling and the moisture concentration is linear in a large humidity range [222]. Hence, an analogy with a thermal expansion can be made and the polymer swelling is given by:

$$\varepsilon_H = \beta \Delta C \tag{7.5}$$

where ε_H is the hygroscopic strain (typically 0.1 - 0.5 % at saturation), β is the coefficient of moisture expansion and ΔC is the change of moisture concentration. It is expected that polymers react with other volatile molecules in a similar way [223].

Finally, the swelling strain induces stress. In purely elastic materials, these two values are linearly dependent according to the Hooke's law. However, polymers are known as viscoelastic materials, which exhibit creep and stress relaxation. In other words, the surface stress induced by the polymer swelling decreases over time due to the reorganisation of polymeric chains. If the absorption rate of the polymer is faster than its relaxation rate, the polymer shows an overreaction and the molecular diffusion is not considered as Fickian any more [224]. Instead of monotonic kinetics, overshoots in the response of surface stress sensors coated with polymers have been reported [221]. Figure 7.3 B illustrates cantilever deflections in both cases.

The response of a cantilever is closely related to the characteristics of its polymer coating as described in the previous paragraphs. While a thicker layer will be able to absorb more molecules, resulting in higher surface stress, it will also stiffen the transducer plate, resulting in lower sensitivity. There is therefore an optimum layer thickness that depends on the mechanical characteristics of both the transducer and the polymer [225]. For a silicon cantilever (1 μm thick) Yoshikawa's analytical results suggest that polymers with Young's moduli of 1 GPa and 10 GPa, have an optimum thickness of 2 μm and 0.5 μm, respectively. In addition, the polymer thickness will also influence the dynamic behaviour of the sensor as absorption takes more time in thicker polymer layers. Overshoots should be minimised as well to preserve the sensor linearity. Polymers with a relaxation time longer than the molecule absorption time are therefore preferred.

7.1.3 | Static deformation of thin plates

Since surface stress limits its influence on the surface region of any object, its macroscopic effect is better observed with shapes of high surface/volume ratios, such as micro-plates or micro-cantilevers. The static deformation of a plate due to surface stress was originally described by Stoney with the following equation [226]:

$$\Delta\sigma_s = \frac{Et^2}{6(1-\nu)R} \tag{7.6}$$

where $\Delta\sigma_s$ is the stress difference between the upper and lower surfaces of the plate, E and ν are the Young's modulus and Poisson's coefficients of the plate, respectively. t is the thickness and R is the radius of curvature of the bending. Sader later introduced a correction factor to adapt the Stoney's equation to single clamped cantilevers [227]:

$$\delta = \frac{3k(1-\nu)\Delta\sigma_s}{E}\left(\frac{L}{t}\right)^2 \tag{7.7}$$

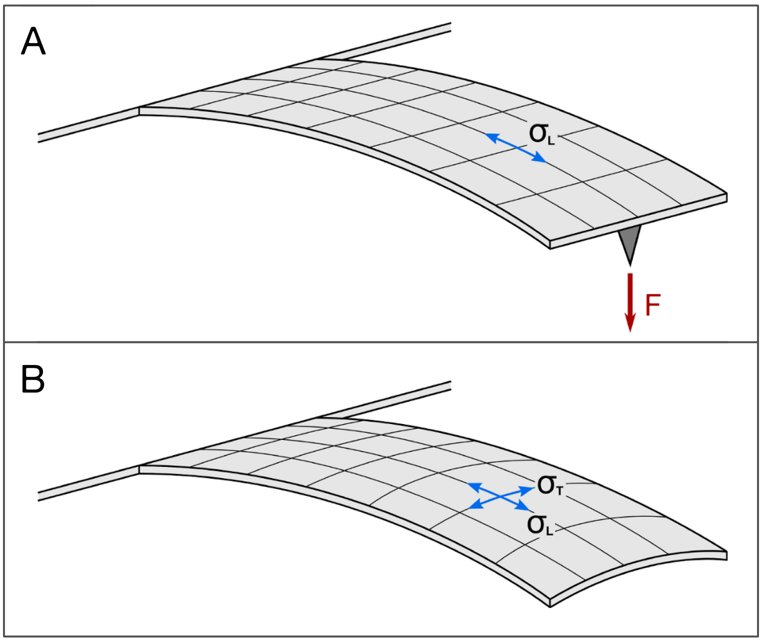

Figure 7.4: Schematics of a cantilever loaded (A) with a point force at the end of its tip and (B) with a surface stress. In the former case, the stress is unilateral and oriented along the cantilever. In the latter case, the stress is equally distributed in all directions except near the clamping edge.

where δ is the cantilever deflection at the free end, k is the correction factor, and L and t are the cantilever length and thickness, respectively. For a typical silicon cantilever (E = 169 GPa, ν = 0.28, length = 120 μm, width = 60 μm), the factor k is equal to 1.083.

Unlike a point force load (Figure 7.4 A), surface stress generated with a functional layer is isotropic and applies a uniform stress in any directions on the cantilever surface (Figure 7.4 B). Far away from the clamping edge, the transversal stress σ_T and the longitudinal stress σ_L are equal:

$$\sigma_T = \sigma_L \tag{7.8}$$

Near the clamping edge, the transverse strain is null, and σ_T is significantly reduced:

$$\sigma_T = \nu\sigma_L \tag{7.9}$$

7.2 | Piezoresistive sensing of surface stress

In the previous sections, I have presented how polymers react to the absorption of molecules and how cantilevers can advantageously transform the induced surface stress into an out-of-plane bending. While optical readout is commonly used to detect this deflection, it has been discarded for our application due to its bulkiness. Interferometric and capacitive readout systems provide a miniaturisation improvement but they both require some additional sensing elements beside the cantilever that could complicate its functionalisation or limit its operation mode. On the other hand, piezoelectric and piezoresistive readout methods are completely integrated into the cantilever. Since piezoelectric devices respond mostly to vibrations and mechanical shocks, piezoresistors are more suitable for the detection of static bending.

In this section is presented the theory of piezoresistors and how can they be integrated into cantilever-based surface stress sensors. Key aspects, such as sensitivity, noise, or self-heating, will be discussed as well.

7.2.1 | Working principle

Piezoresistivity describes the property of a material to change its resistivity under a mechanical strain. Piezoresistors are usually made out of semiconductors or metals. Metallic piezoresistors are also called strain gauges. Considering a straight resistor of length l, cross-sectional area A, and resistivity ρ, its resistance value R is given by the Ohm's law:

$$R = \rho \frac{l}{A} \tag{7.10}$$

Under an applied strain ε along the resistor length, its general change of resistance is due to geometrical effects (shrinkage of the cross-section) and to intrinsic resistivity changes as well:

$$\frac{\Delta R}{R} = (1+2\nu)\varepsilon + \frac{\Delta\rho}{\rho} \tag{7.11}$$

where ν is the Poisson's ratio. The gauge factor GF, which represents the piezoresistive efficiency of a resistor, is calculated as:

$$GF = \frac{\Delta R/R}{\varepsilon} = (1+2\nu) + \frac{1}{\varepsilon}\frac{\Delta\rho}{\rho} \tag{7.12}$$

In the case of metallic strain gauges, the geometrical part $(1+2\nu)$ is dominant compared to the resistivity change and gauge factors are in the range of 2 - 5. On the other hand, piezoresistors made out of semiconductor materials have much higher gauge factors due to the significant change of their intrinsic resistivity. For instance, $\Delta\rho/\rho$ in silicon or germanium may be 50 - 100 times higher than the contribution of the geometrical part [228]. The physical origin of such high resistivity variation to strain in semiconductors is to be found in the deformation of the energy bands resulting from the applied stress [229]. The deformed bands change the effective mobility and mass of the charge carriers, inducing a resistivity shift. The magnitude of the latter depends on the material, the crystalline orientation, and on the doping type and concentration.

Due to their higher gauge factors, piezoresistors made out of silicon are usually preferred in microsystems applications although metallic strain gauges can be easily integrated in SU-8 or polyimide-based sensors [230].

Piezoresistors are usually measured with a Wheatstone bridge configuration, which cancels temperature variations and stabilises the voltage. If the four resistors are equivalent, the output voltage of such circuit is given by:

$$V_{out} = \frac{V_{cc}}{4}\frac{\Delta R}{R} \tag{7.13}$$

where V_{cc} is the bias voltage of the Wheatstone bridge. More details about the use of this electrical circuit will be given in Section 7.2.4.

Piezoresistivity in silicon

In most cases, semiconductors are anisotropic materials. Hence, their properties vary depending on the orientation and have to be described in tensor notations. In a three-dimensional space, the resistivity of a material under stress is described as:

$$[\rho] = [\rho^0](I + [\Delta\rho/\rho]) \tag{7.14}$$

or:

$$\begin{pmatrix} \rho_{xx} & \rho_{xy} & \rho_{xz} \\ \rho_{xy} & \rho_{yy} & \rho_{yz} \\ \rho_{xz} & \rho_{yz} & \rho_{zz} \end{pmatrix} = \begin{pmatrix} \rho^0_{xx} & 0 & 0 \\ 0 & \rho^0_{yy} & 0 \\ 0 & 0 & \rho^0_{zz} \end{pmatrix} \left[\begin{pmatrix} 1 & 0 & 0 \\ 0 & 1 & 0 \\ 0 & 0 & 1 \end{pmatrix} + \begin{pmatrix} \frac{\Delta\rho}{\rho}_{xx} & \frac{\Delta\rho}{\rho}_{xy} & \frac{\Delta\rho}{\rho}_{xz} \\ \frac{\Delta\rho}{\rho}_{xy} & \frac{\Delta\rho}{\rho}_{yy} & \frac{\Delta\rho}{\rho}_{yz} \\ \frac{\Delta\rho}{\rho}_{xz} & \frac{\Delta\rho}{\rho}_{yz} & \frac{\Delta\rho}{\rho}_{zz} \end{pmatrix} \right] \tag{7.15}$$

where $[\rho]$ is the resistivity under load, $[\rho^0]$ is the initial resistivity, I is the unity matrix, and $[\Delta\rho/\rho]$ is the fractional change of resistivity. The latter is linked to the applied stress as:

$$\{\Delta\rho/\rho\} = [\pi]\{\sigma\} \tag{7.16}$$

or:

$$\begin{pmatrix} \Delta\rho/\rho_{xx} \\ \Delta\rho/\rho_{yy} \\ \Delta\rho/\rho_{zz} \\ \Delta\rho/\rho_{xy} \\ \Delta\rho/\rho_{xz} \\ \Delta\rho/\rho_{yz} \end{pmatrix} = \begin{pmatrix} \pi_{11} & \pi_{12} & \pi_{13} & \pi_{14} & \pi_{15} & \pi_{16} \\ \pi_{21} & \pi_{22} & \pi_{23} & \pi_{24} & \pi_{25} & \pi_{26} \\ \pi_{31} & \pi_{32} & \pi_{33} & \pi_{34} & \pi_{35} & \pi_{36} \\ \pi_{41} & \pi_{42} & \pi_{43} & \pi_{44} & \pi_{45} & \pi_{46} \\ \pi_{51} & \pi_{52} & \pi_{53} & \pi_{54} & \pi_{55} & \pi_{56} \\ \pi_{61} & \pi_{62} & \pi_{63} & \pi_{64} & \pi_{65} & \pi_{66} \end{pmatrix} \begin{pmatrix} \sigma_{xx} \\ \sigma_{yy} \\ \sigma_{zz} \\ \sigma_{xy} \\ \sigma_{xz} \\ \sigma_{yz} \end{pmatrix} \tag{7.17}$$

where: $\{\Delta\rho/\rho\}$ is a vector composed of all resistivity changes, $\{\sigma\}$ is a vector composed of all stress components (σ_{xx}, σ_{yy}, σ_{zz} are normal stresses, and σ_{xy}, σ_{xz}, σ_{yz} are shear stresses),

Piezoresistive coefficients ($10^{-11} Pa^{-1}$)	**p-type**	**n-type**
π_{11}	6.6	-102.2
π_{12}	-1.1	53.4
π_{44}	138.1	-13.6

Table 7.1: Piezoresistive coefficients for single-crystal silicon for a doping concentration of 2E+16 cm^{-3} as found by Smith [231].

and $[\pi]$ is the piezoresistive coefficients tensor. if the x-, y- and z-axes are aligned with the <100> crystalline planes of silicon, the piezoresistive coefficients tensor can be simplified as followed [231]:

$$[\pi] = \begin{pmatrix} \pi_{11} & \pi_{12} & \pi_{12} & 0 & 0 & 0 \\ \pi_{12} & \pi_{22} & \pi_{12} & 0 & 0 & 0 \\ \pi_{12} & \pi_{12} & \pi_{33} & 0 & 0 & 0 \\ 0 & 0 & 0 & \pi_{44} & 0 & 0 \\ 0 & 0 & 0 & 0 & \pi_{44} & 0 \\ 0 & 0 & 0 & 0 & 0 & \pi_{44} \end{pmatrix}$$

Historically, Smith discovered the piezoresistive property of silicon and experimentally calculated its piezoresistive coefficients for a doping concentration of 2E+16 cm^{-3} (Table 7.1) [231]. For both p- and n-type silicon, the piezoresistive coefficients decrease with increasing temperature and doping concentration. Kanda suggested a correction factor based on repopulation effects for higher doping concentrations (Figure 7.5 A) [232]. This model describes very successfully the piezoresistivity in n-type silicon but severely underestimates this effect in p-type silicon. More recently, Richter et al. carried out a detailed analysis based on the Boltzmann transport equation that shows a more accurate fit at higher doping concentrations (Figure 7.5 B) [233].

Piezoresistor fabrication

Diffusion, ion implantation, and epitaxial growth are the main techniques for doping silicon substrates (Figure 7.6).

Historically, diffusion was the first process developed to create doped junctions in silicon substrates [234]. This method relies on the deposition of a heavily doped layer on the silicon substrate. Due to a gradient of concentration, dopants from the deposited layer diffuse towards the undoped silicon. A temperature between 900°C and 1300°C is required to activate the diffusion. The diffusion depth depends mainly on the temperature, the diffusion time, the dopant type, and the substrate type and orientation. As arsenic has a low diffusibility in silicon,

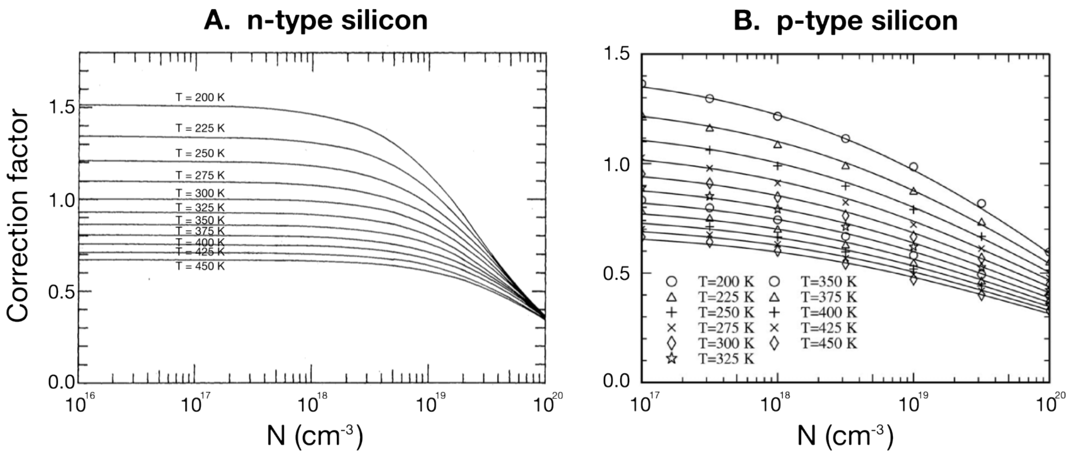

Figure 7.5: Temperature and doping level dependence of piezoresistive coefficients for n-type and p-type silicon as calculated by Kanda [232] and Richter et al. [233], respectively. Adapted with permission from [232] and [233].

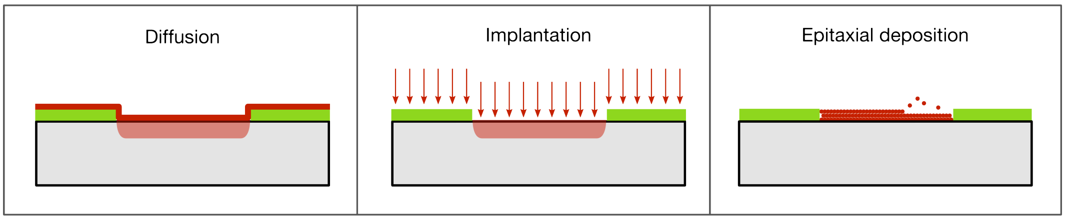

Figure 7.6: Schematics of the three main methods used to dope silicon.

very shallow n-type junctions can be created with this dopant [234].

In ion implantation, the dopants are accelerated in an electrical field at high energy (keV to MeV) into the substrate [235]. The regions that should not be doped are recovered with a mask layer, such as photoresist, where the ions are stopped. Unlike diffusion, particles do not penetrate silicon by themselves, but because of their high velocity. Collisions with silicon atoms slow them down. The penetration depth depends on the dopant type and on their velocity. Due to the particles impacts, the crystal lattice of silicon is heavily damaged and is recovered by recrystallisation at high temperatures (600°C - 1400 °C depending on the substrate) [236]. To minimise the diffusion of ions, rapid thermal annealing (RTA) can be used to reach the required temperature in seconds [237]. Shallow junctions as thin as 100 nm and 200 nm can be achieved for arsenic (n-type) and boron (p-type) dopants, respectively [238, 237]. While the doping reproducibility is very high with ion implantation, the cost per wafer is relatively high due to the required equipment.

While diffusion and implantation introduce dopants in an undoped substrate, epitaxial growth is different as the doped material is directly grown on the substrate [234]. The silicon surface serves as a seed crystal for the growth of atomic layers that keep the crystalline arrangement of the seed layer. Hence, single crystalline silicon can be deposited by epitaxy. This process is highly controlled and results in the formation of very thin piezoresistors [95]. Unlike the two other methods, the doping profile is a step function.

7.2.2 | Sensitivity

Equation 7.14 describes resistivity changes in all directions, independently of the current and stress orientations. In the case of a straight resistor, modelled as long and narrow, both the current and electric field directions are aligned along the resistor length. In addition, only longitudinal (parallel to the current) and transverse (perpendicular to the current) stresses are of significant value. It is therefore possible to simplify the matrix equation and the sensitivity of this simple case is [239]:

$$\frac{\Delta R}{R} \cong \pi_L \sigma_L + \pi_T \sigma_T \tag{7.18}$$

where π_L and π_T are the longitudinal and transverse piezoresistive coefficients, and σ_L and σ_T are the longitudinal and transverse stresses, respectively. To enhance the sensitivity, one must find piezoresistor configurations that maximise the piezoresistive coefficients. Figure 7.7 shows π_L and π_T calculations for various crystalline orientations in the (100) plane [240], while Table 7.2 summarises the longitudinal and transverse coefficients obtained for the preferred orientations.

For n-type silicon, the <100> directions have the highest longitudinal coefficient. In the case of p-type silicon, <110> directions are preferred. Interestingly, transverse and longitudinal coefficients are opposed and of similar value in those directions, which enables a full Wheatstone bridge configuration composed of two longitudinal and two transverse resistors of similar behaviour. Such a design is, for instance, widely used in pressure sensors. Since π_{11} and π_{12} are small compared to π_{44}, they are often neglected and Equation 7.18 can be rewritten for p-type piezoresistors as:

$$\left(\frac{\Delta R}{R}\right)_{p-type} \cong \frac{\pi_{44}}{2}(\sigma_L - \sigma_T) \tag{7.19}$$

In the early days of the cantilever-based sensors history, piezoresistive probes developed for AFM were employed [241]. Today, it is more evident that piezoresistive cantilevers for AFM are not ideal for applications related to surface stress sensing because they are optimised for a point load force sensing, not for surface stress sensing. Although many extensive works have been conducted to optimise the shape and process parameters of piezoresistive cantilevers for AFM applications [242, 243, 244], all their considerations are based on the fact that a point force generates unilateral stress in the direction of the cantilever length, (Figure 7.4 A), whereas the surface stress generated with the functional layer is isotropic and applies a uniform stress in any directions on the cantilever surface (Figure 7.4 B). While this difference in stress distribution is not important in the case of an optical readout, it does play a role in the sensitivity of piezoresistive sensors.

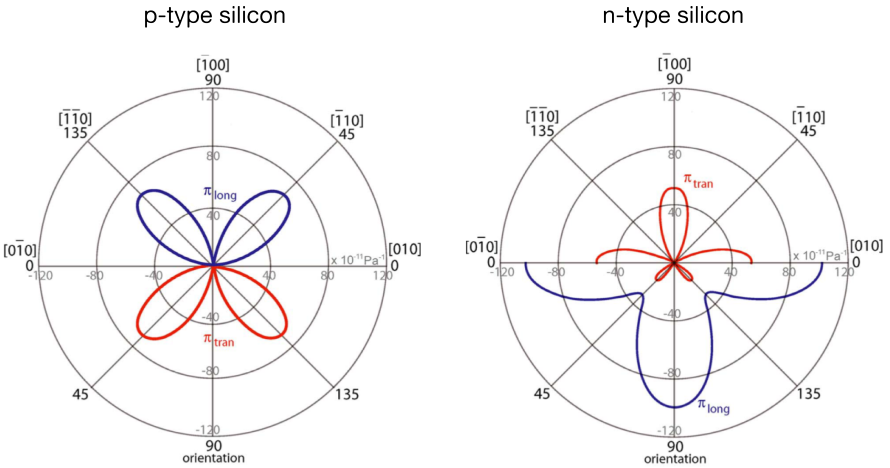

Figure 7.7: Room temperature piezoresistive coefficients in the (100) plane of p-type and n-type silicon. These graphics predict piezoresistive coefficients very well for low doses of dopants. Adapted with permission from [240].

Direction of strain	Direction of current	Configuration	Effective piezo. coeff.	p-type	n-type
< 100 >	< 100 >	Longitudinal	π_{11}	6.6	-102.2
< 100 >	< 010 >	Transverse	π_{12}	-1-1	53.4
< 110 >	< 110 >	Longitudinal	$(\pi_{11}+\pi_{12}+\pi_{44})/2$	71.8	-31.2
< 110 >	< 1$\bar{1}$0 >	Transverse	$(\pi_{11}+\pi_{12}-\pi_{44})/2$	-66.3	-17.6

Table 7.2: Formula for transverse and longitudinal piezoresistive coefficients for various commonly encountered resistor configurations and a doping concentration of 2E+16 cm^{-3}. For higher doping levels, the piezoresistive coefficients have to be compensated with the correction factors shown in Figure 7.5.

Rasmussen et al. have well described the difference between point force and surface stress sensing for both p-type and n-type piezoresistive cantilevers [245]. By using Finite Element (FE) mechanical analyses, they simulated the transversal and longitudinal stresses within a modelled cantilever to approximate a sensitivity based on equation 7.18. They showed that a p-type piezoresistor should be placed as close as possible to the clamping edge to yield a highest sensitivity.

In another work, which is also based on mechanical FE simulations, Privorotskaya et al. considered in detail the p-type cantilever design to optimise its sensitivity. They showed that cantilevers for surface stress sensing should be shorter and wider, compared to a classic AFM cantilever, to have an optimal sensitivity [246].

Beside the optimisation of the cantilever dimensions, some studies focused on the creation of stress concentration zones. For instance, Yang et al. introduced holes next to the piezoresistor that favour longitudinal stress over transverse stress [247]. Another possibility is to design four resistors (two transverse and two longitudinal) on the cantilever in order to build a full Wheatstone bridge and provide four times the sensitivity and twice the noise compared to a single resistor [248].

7.2.3 | Noise and limits of detection

Noise directly affects the limit of detection of any sensor. In the case of molecular sensors that need to detect infinitesimal amounts of analytes, minimising noise is critical. The limit of detection of any sensor is reached when its signal and its noise are of the same level, i.e. its signal-to-noise ratio equals one. The optimisation of the SNR, instead of the sensitivity alone, is therefore more interesting.

There are two major noise sources in piezoresistors: Hooge noise, or 1/f noise, and Johnson noise [249]. Johnson noise is a white noise generated by the thermal fluctuations of the carriers. It depends primarily on the temperature and on the resistance value of the piezoresistor. Hooge noise is a pink noise. While it is not yet fully understood, it is attributed to carrier fluctuations, due to the presence of defects or traps [250]. These two noise sources can be expressed as:

$$\overline{V_H^2} = \frac{\alpha V_B^2}{N} ln\left(\frac{f_{max}}{f_{min}}\right) \tag{7.20}$$

$$\overline{V_J^2} = 4k_b TR(f_{max} - f_{min}) \tag{7.21}$$

where $\overline{V_H^2}$ and $\overline{V_H^2}$ are the Hooge and Johnson voltage noise power, respectively, α is the Hooge constant, V_B is the bias voltage, N is the total number of carrier contributing to the current, k_b is the Boltzmann's constant, T is the temperature, R is the resistance value, and f_{min} and f_{max} are the boundaries of the frequency bandwidth.

There is a third noise attributed to the thermal fluctuations of the cantilever itself. According to the equipartition theorem, the mean-square displacement of a cantilever free end is given by:

$$\frac{1}{2}k\langle x^2\rangle = \frac{1}{2}k_B T \tag{7.22}$$

where k is the cantilever spring constant and $\langle x^2\rangle$ is the mean-square vertical displacement integrated over the entire frequency spectrum. Most of these fluctuations come however from the eigenmode frequencies of the cantilever. Hence, this noise only becomes significant above the first resonant frequency and can be neglected for smaller measurement bandwidths.

As suggested in Section 7.1.2, measuring surface stress in static mode has two sub modes: (i) only the final, steady state deflection is of interest to compare one and the other sensors. This is the case where the cantilevers are coated with very selective functionalisation layers, such as antibodies-antigens bindings. In this sub mode, the measurement bandwidth can be in the range of a few Hertz. (ii) On the other hand, less selective layers, such as polymers, require comparing the adsorption/absorption rate of the analytes as well to distinguish one between the others. To correctly detect this transient characteristic, the measurement bandwidth should be sufficiently large and it can be more than a thousand Hertz.

In both cases however, the upper boundary of the frequency bandwidth is much lower than the resonance frequency of the cantilever. Hence, thermomechanical noise can be neglected for surface stress sensing and the total noise voltage in piezoresistive cantilever-based sensors is composed only of Johnson and Hooge noise:

$$\overline{V_{Tot}^2} = \overline{V_J^2} + \overline{V_H^2} \tag{7.23}$$

$$= 4k_b TR(f_{max} - f_{min}) + \frac{\alpha V_B^2}{N} ln\left(\frac{f_{max}}{f_{min}}\right) \tag{7.24}$$

If the cantilever is placed in a standard Wheatstone bridge configuration composed of four identical resistors, the SNR can be calculated from Equations 7.13 and 7.24:

$$SNR = \frac{\Delta R}{R}\frac{V_{cc}}{8}\frac{1}{\sqrt{4k_b TR(f_{max} - f_{min}) + \frac{\alpha V_{cc}}{2N} ln\left(\frac{f_{max}}{f_{min}}\right)}} \tag{7.25}$$

Numerous studies have been published on how to minimise both noise sources in piezoresistive cantilevers, especially for AFM applications [240]. Smaller Hooge constant α, obtained with long and high temperature anneals [248], will help decreasing the Hooge noise. Increasing the total number of carriers N in the piezoresistor will have a similar effect. This is achieved with larger piezoresistors and higher doping concentrations. In a straight resistor, N can be approximated as [249]:

$$N = V_r p = lwtp \tag{7.26}$$

where V_r is the volume of the resistor (l x w x t) and p is the carriers density. In the case of more complicated resistor shapes, the carriers do not participate equally to the current transport and this approximation is not valid any more. N has to be calculated following a relation that weights the carriers by their contribution to the current [251]:

$$\overline{V_H^2} = \frac{\alpha\rho^2}{pI^2}\iiint (J \cdot J)^2 dxdydz \tag{7.27}$$

where ρ is the electrical resistivity, I is the current, and J is the current density.

Johnson noise depends on the resistance value of the piezoresistor. Shorter resistors or of larger cross-sections, or higher doping levels will decrease the Johnson noise level. Interestingly, decreasing the length of the resistor will increase the Hooge noise, while a larger resistor cross-section will diminish its level. Generally speaking, increasing the doping concentration has a positive effect on both noise sources but the piezoresistive coefficients decrease as well. Hence, there is an optimum doping level where electronic noise is low enough while the piezoresistive coefficients are still significant.

7.2.4 | Self-heating in piezoresistors

Like any resistors, piezoresistors are affected by the Joule effect. A current passing through a conductor will release heat:

$$P = RI^2 = \frac{V^2}{R} \tag{7.28}$$

where P is the dissipated heat power, R is the resistance value, I is the current passing through, and V is the voltage drop across the element. Due to the micro-scale size of cantilevers, heat conduction from their body to the substrate is usually not enough to dissipate all the produced heat and their temperature increases easily. While this effect has been advantageously used in some applications, such as the Millipede [110], it has usually the following unwanted consequences for piezoresistive sensors:

1. Temperature-dependent properties, such as electrical resistance and piezoresistance coefficients, will vary, leading to an additional fractional resistance [252]. As the electrical noises are also temperature dependent, their levels will increase.
2. As cantilever-based sensors are multi-layered, thermal expansion mismatches between the cantilever body and the functionalisation layer may appear [253]. Due to a bimorph effect, the cantilever will bend. Hence, an additional fractional resistance, which is completely unrelated to the molecular detection, will appear.
3. Any temperature increase may affect the behaviour of the functionalisation layer and the surrounding analytes, particularly when biomolecules or cells are involved.
4. The equilibrium temperature is mostly defined by the thermal conduction between the cantilever and its substrate. However, convection between its surface and the surrounding molecules is not negligible. As the convection rate depends on the present molecules, any environmental variation, e.g. switching between two gas species, will change the equilibrium temperature[253].

Consequently, the polymer swelling due to molecular absorption cannot be considered as the only source of resistance fractional change:

$$\left(\frac{\Delta R}{R}\right)_{Tot} = \left(\frac{\Delta R}{R}\right)_{\sigma} + \left(\frac{\Delta R}{R}\right)_{\pi} + \left(\frac{\Delta R}{R}\right)_{B} \tag{7.29}$$

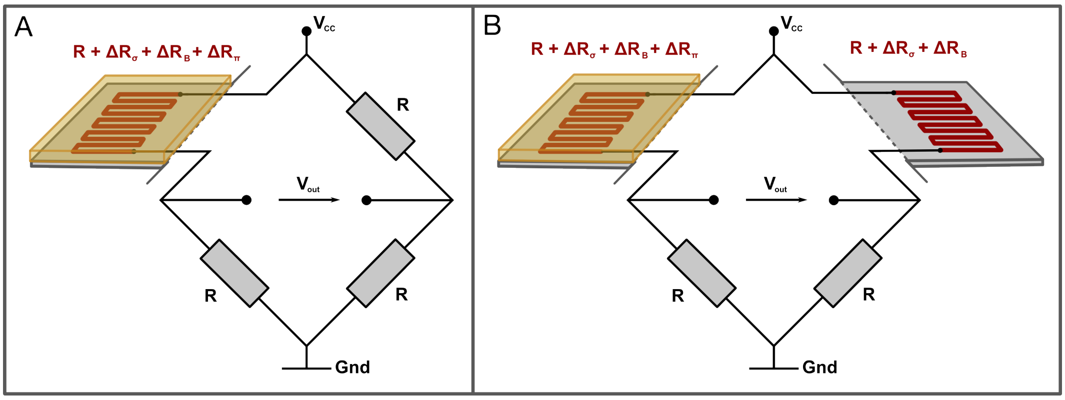

Figure 7.8: (A) The functionalised cantilever is mounted in a Wheatstone bridge configuration. Due to the piezoresistor self-heating, additional fractional resistances are introduced. (B) A second cantilever of similar characteristics is connected in the Wheatstone bridge. Uncoated, it serves as a reference, which compensates the fractional resistance changes due to the thermal variations of the resistance and of the piezoresistive coefficients.

where $(\Delta R/R)_{Tot}$ is the total resistance change, $(\Delta R/R)_{\sigma}$ is that due to the molecular absorption, $(\Delta R/R)_{\pi}$ is that due to the change of resistivity and piezoresistive coefficients, and $(\Delta R/R)_{B}$ is that due to the bimorph effect.

These additional fractional changes of resistance are known as thermal drift and can cause to piezoresistive sensors calibration errors or false positives that would not be present in the case of an optical readout. Therefore, self-heating needs to be minimised as much as possible.

From the two components of the thermal drift, the one that is produced by the variations of the resistivity and of the piezoresistive coefficients is easily compensated with the introduction of an uncoated reference cantilever in the Wheatstone bridge (Figure 7.8) [254]. The cantilevers are supposed to be close enough to experience the same environment parameters. Hence, they will both yield a similar fractional change of resistance $(\Delta R/R)_{\pi}$, which compensate each other in the Wheatstone bridge.

The second component of the drift is produced by the thermal expansion mismatches between the cantilever and its functionalisation layer. As the reference cantilever is, by definition, uncoated, it cannot cancel $(\Delta R/R)_{B}$. Depending on the functionalisation layer, the drift can be significant. Ansari et al. have shown that a 50 nm gold layer deposited on a 700 nm silicon cantilever with a 5 V bias voltage induces more resistance change than a 1 N/m surface stress [255].

Several models have been developed to predict and reduce the self-heating in piezoresistive cantilevers [256, 257, 253]. Heat is dissipated from the cantilever either by conduction to the bulk via the clamping edge or by convection with the surrounding medium. By increasing the dissipation rate of conduction and convection losses, the self-heating in piezoresistors can be limited. As conduction is limited by the clamping point, wider cantilevers will definitely enhance it. Similarly, designing the piezoresistor as close as possible to the clamping point helps to dissipate the heat by conduction [255]. In the case of convection the heat losses can be increased with surrounding media of higher thermal conductivity, e.g. switching from air to water [256]. Finally, Loui et al. suggested an analytical model that predicts well the thermal drifts in a cantilever-based sensor [253]. Hence, the thermal drifts experienced by a surface stress sensor could be predicted and compensated with additional temperature sensors and software capabilities.

7.2.5 | Reproducibility

Cantilever-based sensors usually suffer from a poor sensor-to-sensor reproducibility, independently of the chosen readout system. This lack of repeatability is likely to be found in poor functionalisation rather than in fabrication disparities. Indeed, cantilever-based sensors are very sensitive to inhomogeneous coatings. As an example, Mertens et al. have functionalised various cantilevers with thin gold layers and exposed them to mercaptohexanol in water [258]. The optical measurements of the cantilever deflections showed dispersions between 10% and 110% depending on the chosen gold deposition process.

To overcome the reproducibility issue, Bosco et al. proposed to use multiple cantilevers in parallel [259]. The cantilever-based sensors can be addressed in arrays to average their signals and improve the reliability of the response. In their study, the deflection measurement of 7 cantilevers functionalised with tetraTTF-calix[4]pyrrole (specificity to DNT) showed a standard deviation of about 25%. In the same time, 7 cantilevers that were coated with biotin, which should not react with DNT, showed a standard deviation of 50%.

7.3 | In a nutshell

The theory behind piezoresistive cantilevers for surface stress sensing and a few design guidelines were presented in the previous sections. The following statements serve as a summary:

1. Surface stress sensors operate in a static mode. Their measurement bandwidth may range between 1 mHz to 1 kHz.
2. Polymers used as functionalisation layers are partially selective. Analytes are discriminated with their absorption rate and solubility.
3. Unlike point force loads, surface stress applies an omnidirectional stress over the cantilever surface. This difference is particularly important in the case of piezoresistive sensing.
4. For p-type piezoresistors, the sensitive part is located near the clamping edge since σ_L and σ_L cancel each other away from the bulk. The cantilever should be wide while its length is not very important.

5. For n-type piezoresistors, σ_L should be favoured over σ_T. Similarly to p-type piezoresistors, the clamping edge is the preferred location as its reduces σ_T significantly.

6. Self-heating induces thermal drifts and increased noise levels. Since the temperature increase depends on conduction and convection, cantilevers for surface stress sensing should be less impacted than those adapted for AFM applications due to their wider clamping edge and larger area.

7. Cantilever-based sensors suffer from poor reproducibility. This is mainly due to the heterogeneity of their functionalisation layer.

7.4 | A membrane-type platform

Recently, a collaboration between Dr. Genki Yoshikawa from the *International Center for Materials Nanoarchitectonics* in Japan, Dr. Heinrich Rohrer, and SAMLAB started with the goal of rethinking the concept of nanomechanical sensors. In 2011, our collaboration came up with a radically different nanomechanical sensor specially designed towards surface stress sensing: the membrane-type surface stress sensor (MSS) [260].

7.4.1 | Working principle

Instead of a single-clamped cantilever, it consists of a round silicon membrane supported with four sensing beams, on which transverse and longitudinal p-type piezoresistors are integrated (Figure 7.9 A). A typical MSS has a diameter between 300 μm - 500 μm and a thickness between 2 μm - 4 μm. The functionalisation layer, e.g. a polymer, is deposited on the top side of the membrane. Upon absorption of volatile molecules, the polymer swells and produces a membrane deflection, which is eventually detected by the piezoresistors (Figure 7.9 B).

Unlike cantilever-based sensors where the cantilever simply bends (Figure 7.9 C), the deflection of the membrane is constrained with the four clamping beams. Hence, the surface stress applied on the membrane by the polymer layer induces two different types of stress on the clamping beams: (i) compressive stress nearly in the plan of the membrane and (ii) stress due to bending of the clamping beam.

In addition, surface stress transduction and detection are decoupled between the membrane and the sensing beams in the case of MSS as opposed to cantilevers, which transduce and sense at the same time. Hence, each element of the MSS can be optimised according to their own task (sensing or transducing). Additionally, as the functionalisation layer is not in contact with the piezoresistor any more, the fractional resistance change $(\Delta R/R)_B$, which is induced by a bimorph effect during the self-heating of the resistor (see Section 7.2.4), is not present. Hence, the thermal drift can be expected to be less important than in standard cantilever-based sensors. Finally, the full Wheatstone bridge configuration of the piezoresistors allows obtaining a much more stable and larger signal compared to the typical quarter bridge configuration of cantilever-based sensors.

7.4.2 | Initial performances and potential

In the initial study, MSS with diameters of 300 μm and 500 μm and a thickness of about 3.5 μm were compared with piezoresistive cantilevers and showed 15 x and 22 x improved sensitivity, respectively [260]. The cantilevers were however thinner and had slightly different process parameters [261]. Moreover, they were designed for AFM applications.

While a comparison between MSS and cantilevers optimised for surface stress sensing is still required, some observations, which highlight the potential of the MSS, can already be made between the cantilever and the membrane platforms:

1. The sensitivity of the MSS scales up with its size. This is hardly the case for cantilever-based sensors.
2. The full Wheatstone bridge configuration brings a free SNR increase of two and is more stable against thermal variations.
3. Unlike the cantilever-based sensor, the MSS transducer, i.e. the membrane, is distinct from the sensing parts, i.e. the hinges. Hence, each element of the MSS can be optimised according to their own task (sensing or transducing). In addition, the unwanted bending due to thermal mismatches should be significantly reduced since the functionalisation layer is not in contact with the piezoresistors.

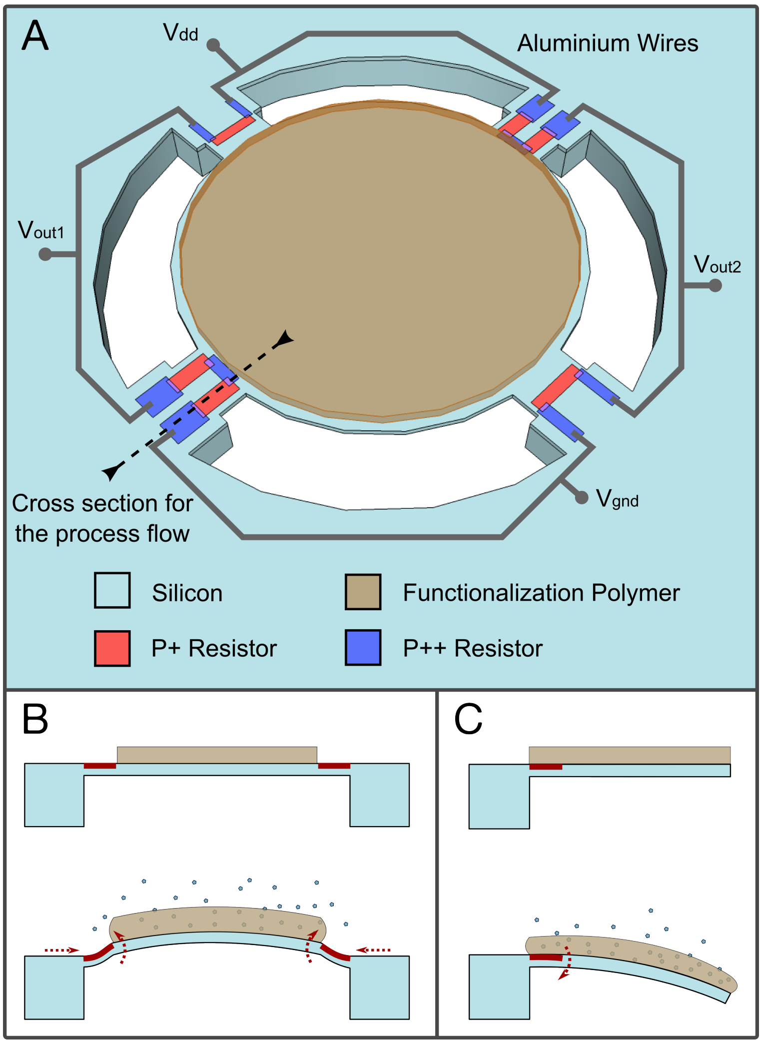

Figure 7.9: (A) Graphical representation of a membrane suspended by four constricted beams with integrated piezoresistors connected in a full Wheatstone bridge configuration (two longitudinal and two transverse resistors). (B) The membrane is coated with a polymer that reacts to surrounding molecules. Its swelling induces a surface stress and a deformation of the membrane that is transduced to the sensing beams. Each beam experiences compression and deflection stresses. (C) Similarly, a single clamped cantilever will bend due to the polymer swelling. However, only the deflection stress exists since the cantilever does not have any planar constraints.

8 || Piezoresistive simulations for sensors optimisation and comparison

Surface stress sensors behave differently from those used for AFM applications. In particular, the stress distribution is unidirectional in one case and omnidirectional in the other. The optimisation of p-type piezoresistive surface stress sensors is particularly interesting since the sensitivity of the piezoresistor is, approximately, proportional to the difference between its longitudinal and transverse stress ($\sigma_L - \sigma_T$), as described by Equation 7.19. Away from the clamping point, any resistor will therefore yield a null sensitivity.

Despite of the precise stress analyses presented in Section 7.2.2, none of them addressed the optimisation of the piezoresistor itself. For example, it is not obvious whether or not a piezoresistor in meander configuration has a better sensitivity than a simple U-shape one for surface stress sensing, and if so, how many meanders are required. Quantitative comparisons between sensors of radically different shapes is also tricky.

In this chapter, I will present in details the piezoresistive simulation script based on finite element (FE) analyses that I have developed during my thesis. Unlike purely mechanical simulations, it couples both mechanical and electrical models to simulate not only the structural behaviour of the sensor but also the piezoresistive response of its resistor. Both the cantilever and MSS designs will be simulated with p-type piezoresistors. SNR optimisations but also repeatability simulations will be presented. New design guidelines for piezoresistive surface stress sensors were developed from those results.

8.1 | Piezoresistive simulation flowchart

In this section, I introduce in detail an FE simulation flowchart, which leads directly to the minimum detectable surface stress value of a defined sensor geometry. It combined mechanical and electrical models to simulate an actual resistor. Hence the piezoresistive sensitivity is not derived from an approximated equation (Equation 7.18) any more but from the exact matrix equations (Equation 7.16). To illustrate the different steps of my simulation tool, I have modelled a simple cantilever design and used it as an example. The optimisation will be covered in the following section.

8.1.1 | Simulation architecture

Figure 8.1 represents a flowchart of the algorithm where the different operations and data flows are shown. In ANSYS, most of the operations are, in reality, simultaneously done but this flowchart gives a logical procedure. In the initial step, the sensor geometry is numerically described and all the constraints and materials properties are entered into the simulation tool. Two different operations are then launched: The mechanical simulation begins after a load (surface stress or a point force) is defined. It returns a structural response of the model. In the electrical simulation, a current density with and without the mechanical load is computed at each element of the resistor. Those values are used to calculate a corresponding resistance and a sensitivity $\Delta R/R$ of the sensor. The electrical noises are then calculated by an individual program based on the outputs of ANSYS, which are the sensitivity $\Delta R/R$, the total number of carriers inside the resistor N, and the maximum deflection of the sensor d. The SNR is finally obtained and a minimum detectable surface stress is defined, which is the value when the SNR equals one. A typical ANSYS script that follows this flowchart can be found in Appendix C.

8.1.2 | Modelling

Figure 8.2 shows an example of a modelled cantilever sensor with a U-shaped resistor. Table 8.1 summarises its dimensions and characteristics. The bulk and the cantilever parts are made of undoped single crystalline silicon. The resistor is made of p-doped crystalline silicon. The dopant concentration is a simulation parameter. The resistivity and piezoresistive coefficients are then calculated with the expressions of Shapiro [262] and Richter et al. [233], respectively. In the case of n-type doping, expressions from Kanda would be used to calculate the piezoresistive coefficients [232].

The cantilever is oriented in the <110> plane in order to maximize the piezoresistive effect in p-doped silicon. The dimensions are 120 μm-long, 60 μm-wide and 1 μm-thick. The resistor legs are 30 μm-long, 15 μm-wide and 200 nm-thick. 1 V is applied between the two terminals of the resistor, which are located on the bulk surface. The 3D elements SOLID186 and SOLID226 in the ANSYS library are used for the modelling of the structural and piezoresistive parts of the cantilever, respectively. Unlike SOLID186, which is a purely mechanical element, SOLID226 is a coupled-field element that is used to compose the piezoresistor model in my simulations. It combines different physics fields and produces an output as a function of an applied load to the other fields. I use this element to carry out structural and electrical analyses, where a mechanical input produces an electrical output. Each element includes 20 nodes at which voltage, forces, or current density and its direction are retrieved. A typical model is composed of about 40,000 elements.

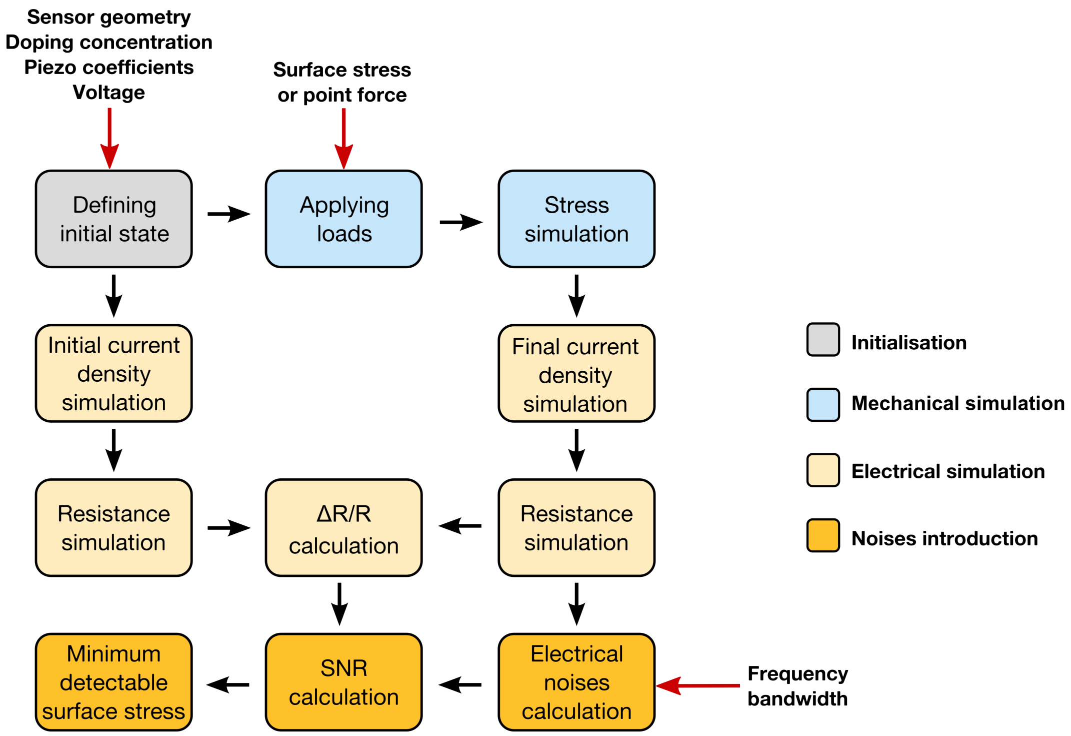

Figure 8.1: Flowchart of the simulation tool. While it does not represent the exact steps followed by Ansys, it gives to the reader a clear view of the process. It starts with the model initialisation of the sensor (in grey), followed by the mechanical simulation of the sensor (in blue). The electrical behaviour of the resistor in then simulated (in yellow) and the electrical noises are finally derived from the latter (in orange). This last step is done outside the Ansys framework.

Process parameters are not optimised with such modelling. The Hooge constant, of which depends the electrical noise level, has been for instance arbitrary set at 10^{-5}. This value, typical for implanted piezoresistors, can be further decreased with process optimisations [248]. Similarly, the dopant concentration in my models is constant along the resistor depth. In reality, it is not, except for epitaxially grown resistors, and can also be optimised based on process parameters [243, 244]. Therefore, this simulation tool is not meant to yield absolute performance expectations of **fabricated devices**, but rather compare various **designs** between each others.

8.1.3 | Mechanical simulation

Firstly, the cantilever deflection is considered under an applied load, i.e. a surface stress. In my simulation example, a constant compressive surface stress of 0.1 N/m is loaded on the whole cantilever surface with the element SURF154 and the deformation was simulated. Such a surface stress level is often measured during experiments with polymer coated cantilevers. Figure 8.3 A shows the z-axis deflection of the cantilever under a 0.1 N/m surface stress. As a comparison, a result with a point force of 50 pN, showing a similar deflection, is shown in Figure 8.3 B. To ensure the accuracy of the simulation, I compared the obtained results with

Characteristic	**Value**
Length [μm]	120
Width [μm]	60
Thickness [μm]	1
Resistor length [μm]	30
Resistor width [μm]	15
Resistor thickness [μm]	0.2
Doping level [cm^{-3}]	1E+18
Hooge constant	1E-5
Voltage [V]	1
Surface stress [N/m]	0.1

Table 8.1: Dimensions and characteristics of the simulated example cantilever.

the analytical values derived from 7.7. This is important not only to validate the mechanical load applied by the elements SURF154, but also to find an appropriate number of elements consisting of the model. Through all the simulations, I found that the difference between their results and the analytical values was less than 0.6% with surface stress ranging from 0.005 N/m to 10 N/m.

While the cantilever bending is of importance for optical readout, for piezoresistive devices, distribution of mechanical stress is concerned. As presented by Equation 7.19, the piezoresistive sensitivity $\Delta R/R$ in p-type silicon is proportional to the difference of the two stresses in different directions, i.e.$(\sigma_{//} - \sigma_{\perp})$ or $(\sigma_x - \sigma_y)$ in our example. Figures 8.3 C and D show mappings of stress under the same load conditions as surface stress and point force, respectively. To have a better overview of stress distribution, the mappings are coloured as a function of stress difference $(\sigma_x - \sigma_y)$. The cantilever is oriented in x-direction. In the case of a point force, σ_y is negligibly small compared to σ_x, which has a maximal value at the clamping edge. In the case of homogeneous surface stress, $(\sigma_x - \sigma_y)$ has a maximal value near the clamping area of the cantilever, where the bulk absorbs most of σ_y. Its influence slowly decreases as the distance increases and σ_y eventually equals σ_x, yielding in a null difference far from the clamping point.

The piezoresistor should be placed where this stress difference is maximal. A mechanical simulation can be used to find such area. This is how previous simulation studies were performed [245, 246]. However, like the case in Figure 8.3 C, it is not obvious how the piezoresistor should be placed in some cases. One cannot intuitively judge, for instance, whether one piezoresistor designed at the middle point of the clamped edge gives a higher sensitivity in a final bridge configuration than two small piezoresistors placed exactly at the most stressed area close to the side edges of the cantilever. Therefore, electrical simulations combined with a mechanical analysis are required to find a preferred sensor configuration.

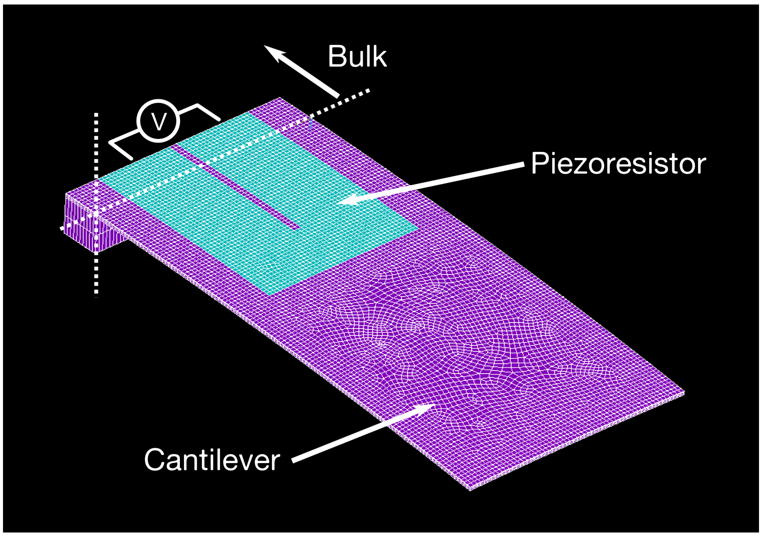

Figure 8.2: ANSYS model of a 120 μm x 60 μm x 1 μm cantilever with a U-shaped resistor. The cantilever is made out of crystalline silicon while the resistor itself is created with Boron ions implantation. ANSYS elements SOLID186 and SOLID223 are used to model the structural undoped silicon and the piezoresistive layer, respectively.

8.1.4 | Electrical simulation

As described in section 8.1.2, I use SOLID226 to carry out the structural and electrical analyses. The resistance value of the piezoresistor with or without mechanical load is calculated by accumulating the results from each element on the piezoresistor region, which includes not only positive sensitivity regions, but also the negatively influencing parts where the current flow is perpendicular to the stress direction. The magnitude of resistivity change on each local segment can be mapped by calculating the variation of the current density with and without the mechanical load ($J_{load} - J_{initial}$). Figure 8.3 E shows a result under a surface stress and Figure 8.3 F is the one under a point force load. The simulation parameters are the same as mentioned above. In the case of the surface stress load, the highest sensitivity regions exist near to the cantilever fixed end and rather close to the side edges of the cantilever. While the other case, the highest region is spread along with the cantilever fixed end. Interestingly, in small regions of the bottom neck of the U-shape, where the current density is relatively high, the sensitivity is as high as that of the cantilever fixed edge. In terms of the straight part of the resistor, a graduation in sensitivity is observed in the case of the surface stress load, whereas a relatively uniform sensitivity is expected in the case of the point force load. The U-turn gives a negative effect in sensitivity in both cases. However, the magnitude of the influence is rather limited in the case of the surface stress load. This can be explained by a low ($\sigma_x - \sigma_y$) value at this distance from the clamping edge. In the case of a point force, the impact of the negative region cannot be negligible since the stress difference is still high in this region of the cantilever (Figure 8.3 D).

Compared to the conventional method where only a mechanical simulation is done and a

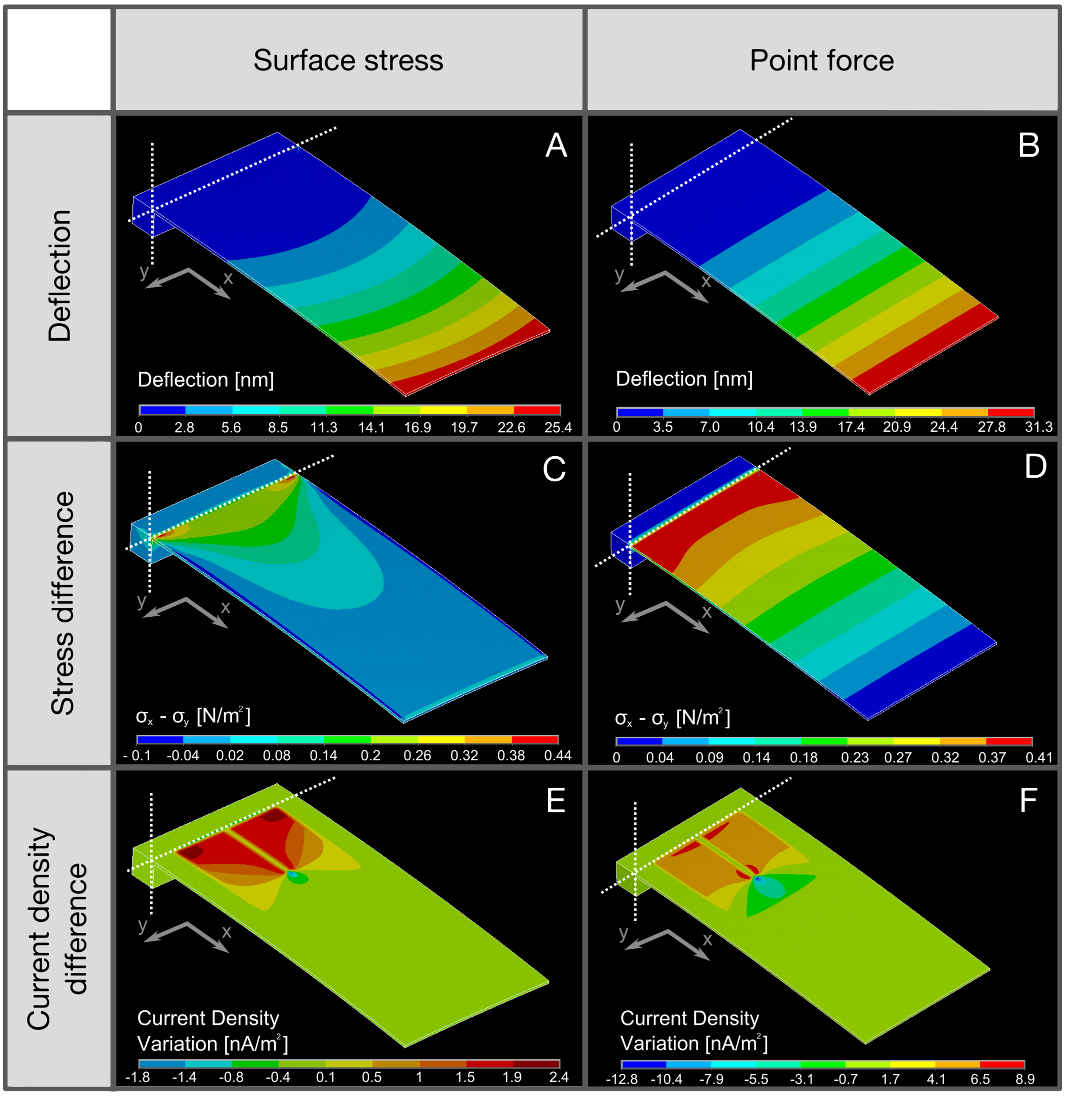

Figure 8.3: Mechanical and electrical simulations of the cantilever presented in Figure 8.2 loaded with either a surface stress of 0.1 N/m or a point force of 50 pN. Simulations A, B, C, and D are mechanical only. Simulations E and F show the current density difference with and without the load. They are real piezoresistive simulations.

piezoresistor is arbitrarily designed at the most stressed region, this simulation tool can present a much accurate expected sensitivity of the designed piezoresistor. Since the amount of current flow and its direction at each local segment is taken into account, different shapes/dimensions of a piezoresistor can be quantitatively compared one and the others. Hence, it is feasible to find an optimised design in terms of sensitivity. The sensitivity $\Delta R/R$ is not approximated from equation 7.19 any more.

8.1.5 | Noise simulation

Beside the simulation of a real $\Delta R/R$, the use of an electrical model allows estimating the Hooge and Johnson noise as well (see Equations 7.20 and 7.21). For a simple resistor shape, e.g. straight or U-shape, the resistance value R and the carriers number N can be analytically calculated from the resistor geometry (see Equation 7.26) [249]. For more complex geometries, electrical simulations are required. As described in section 8.1, R is calculated from the given voltage and the integration of the current density over the entire resistor volume. As for N, the relation developed by Vandamme and van Bokhoven is used (see Equation 7.27) [251]. For each element of the piezoresistor, the carrier density is weighted by the simulated local current density. Hence, the carriers from the U-turn end are discarded. I compared the simulated noises with the analytical values for a straight resistor shape of length between 10 μm and 100 μm. The deviation was always less than 0.5%, which confirms that the electrical simulations are consistent with the theory.

8.1.6 | Self-heating considerations

Those optimisations do not take into account the self-heating effect in piezoresistors. As described in Section 7.2.4, most of the thermal drifts induced by temperature variations in the cantilever can be significantly compensated with a proper Wheatstone bridge configuration. An adequate thermal model, such as developed by Loui et al. [253], can also be implemented during the signal processing to compensate those drifts.

Nevertheless, temperature variations also have an impact on electrical noise. To approximate the Johnson noise increase due to temperature, a back-to-the-envelope calculation of a cantilever self-heating can be made. If only conduction is considered to evacuate heat, the temperature increase is described as:

$$\Delta T = R_{th} P = R_{th} \frac{V_{cc}^2}{R} \tag{8.1}$$

where R_{th} is the thermal resistance of the cantilever and P is the power dissipated in the piezoresistor. The thermal resistance of a cantilever is approximated as [263]:

$$R_{th} \cong \frac{1}{2} \frac{l_p}{k_{th} w t} \tag{8.2}$$

where l_p is the resistor length, k_{th} is the thermal conductivity of the beam material, and w and t are the width and thickness of the beam, respectively. In the case of a silicon cantilever for AFM applications (890 μm x 10 μm x 2 μm) [256], the calculated temperature increase is 53 K for a dissipated power of 1.5 mW. On the other hand, surface stress sensing with p-type piezoresistors requires wider cantilevers, e.g. 120 μm x 120 μm x 2 μm, and the temperature increases only of about 4 K for a similar dissipated power. The Johnson noise difference from such temperature increase is about 1%.

Hence, as long as the dissipated power is limited to values in the range of 1-2 mW, I have considered that the noise increase due to the self-heating of the piezoresistor can be neglected. Similarly, the piezoresistive coefficients and the Hooge constant α are temperature dependent but their variations have been considered negligible for such a range of temperature.

8.2 | Sensor optimisation

The primary goal of the developed simulation tool was to optimise the shape and dimensions of both the cantilever-based sensor and MSS based on their SNR.

8.2.1 | Cantilever-based sensor

Design and parameters

Ideally, the cantilever design parameters can be arbitrarily chosen. In practice, some of them are limited by the fabrication technology or other reasons. I have purposely decided to restrain the variations of the cantilever shapes and focus on the resistor itself since optimisations of the cantilever alone have already been studied and published. The cantilever length is a design parameter. It gives, however, a limited impact on the sensor sensitivity [246]. I have fixed it at 120 μm in these simulations. On the other hand, the cantilever width has been shown to strongly influence the sensitivity [246]. Hence, two different widths, 120 μm and 240 μm, are chosen as a comparison.

In terms of the piezoresistor, the junction depth is totally determined by the fabrication process. The best achievable boron-doped shallow junction is approximately 0.2 μm in depth, which is done by ion implantation and RTA recovery. In reality, the dopant concentration is a function of the depth. A correction factor β^*, introduced by Park et al. can be retrieved from any set of process parameters to take the dopant profile into account [243]. I have chosen a fixed Boron concentration of 1E+18 cm^{-3} for all these simulations. It will be varied later. The shape, dimensions, and placing position of the piezoresistor are simulation parameters and can be arbitrary chosen. Two piezoresistor configurations are modelled: a meander configuration widely used in both point-force and surface stress sensing (Figure 8.4 A) and a so-called lines configuration (Figure 8.4 B). The latter, with resistor lines connected in parallel, is expected to have a lower Johnson noise compared to the meanders configuration. It would

Characteristic	Resistor in meanders	Resistor in lines
Length [μm]	120	120
Width [μm]	**120 and 240**	**120 and 240**
Thickness [μm]	1	1
Resistor length [μm]	**10-90**	**10-80 and 10-200**
Resistor width [μm]	5	5
Resistor thickness [μm]	0.2	0.2
Meanders/lines number	**1-8 or 1-16**	**1-8**
Doping level [cm^{-3}]	1E+18	1E+18
Hooge constant	1E-5	1E-5
Voltage [V]	1	1
Surface stress [N/m]	0.1	0.1
Measurement Bandwidth [Hz]	0.01-10 and 0.01-1000	0.01-10 and 0.01-1000

Table 8.2: Dimensions and characteristics of the simulated example cantilever. The optimisation focused on the resistor dimensions and cantilever width, highlighted in bold.

be possible to achieve the same result with only a wider resistor line but thin lines are best to restrain the current flow perpendicularly to the cantilever.

As described in Section 7.1.2, the measurement bandwidth differs whether highly or partially selective layers are coated on the cantilever. I will consider both piezoresistor configurations first in a (0.01 Hz – 10 Hz) bandwidth, which is suitable for highly selective layers. A second bandwidth (0.01 Hz – 1000 Hz) is then considered for partially selective layers, such as polymers.

Table 8.2 summarises the parameters that were defined for the following simulations. Since several of them were arbitrarily defined, the resulting simulations cannot be considered as a full optimisation. They rather point towards preferred cantilever configurations for surface stress sensing.

Steady-state measurement mode (0.01 Hz – 10 Hz)

Figure 8.5 shows simulation results of cantilevers with the meander shape piezoresistors. The only difference between Figure 8.5 a and b is the cantilever width. Each black dot represents a single simulation result. The coloured map shows the minimum detectable surface stress with the bandwidth 0.01 Hz - 10 Hz and was constructed based on the results of each simulated point. The pink dot indicates the lowest value point, which corresponds to an optimal sensor configuration among the sensors in the same series. For example, in the case of Figure 8.5 a, all the simulated cantilevers have the same width of 120 μm. The pink dot shows the one with the piezoresistor consisted of 7 U-shaped resistors with 40 μm-long legs, connected in series

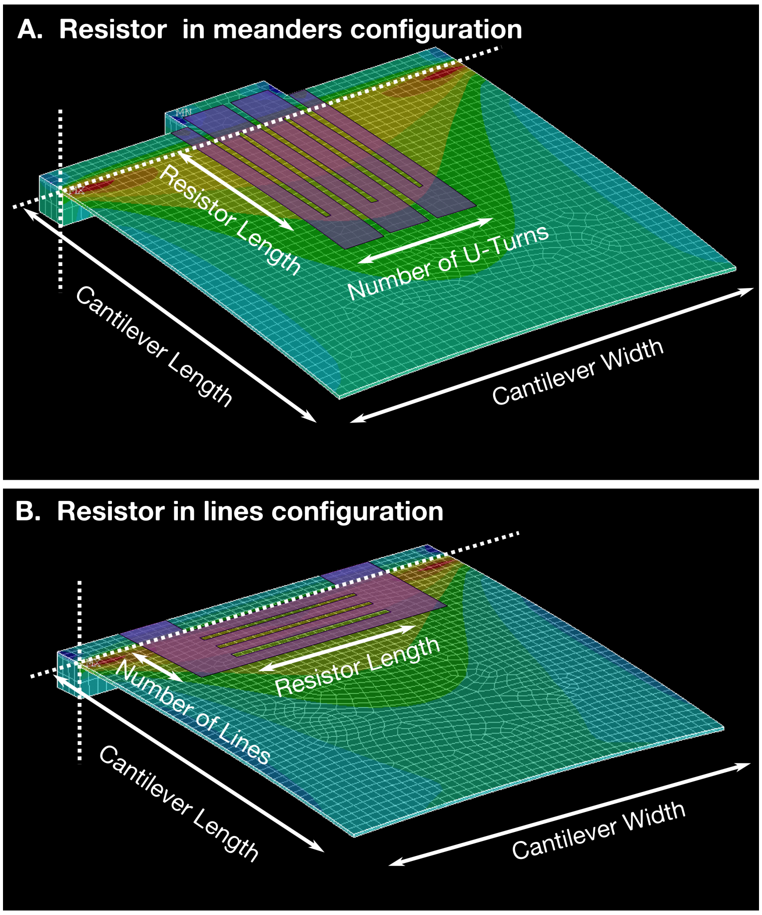

Figure 8.4: Ansys model of a cantilever (120 μm x 120 μm x 1 μm) with a resistor in (a) a 3-meanders configuration and (b) a 4-lines configuration. The colour scale shows the simulated stress difference described by Equation 7.19.

with the meander configuration similarly to Figure 8.4 A.

In a comparison between Figure 8.5 a and b, it is obvious that the wider cantilever has a lower detectable surface stress in overall. In the case the meander piezoresistor configuration is used, the best sensor is the 240 μm-wide cantilever, with a piezoresistor consisting of 6 U-shapes resistors of 75 μm-long. This sensor has a minimum detectable surface stress of 0.5 mN/m, which is a 24% improved value than that of the best 120 μm-wide cantilever. The total length of the piezoresistor amounts to 900 μm in this specific case. The overall Hooge noise in the limited bandwidth is still slightly higher than that of the Johnson noise. In contrast, the dominant noise in the sensors with a higher number of straight resistors is the Johnson noise. Those sensors should have shorter resistor length to yield a lower detectable surface stress.

Simulations of the sensors with the line configuration piezoresistor show contrasted results (Figure 8.6). The 240 μm-wide cantilever with 3 straight resistors of 200 μm (maximum length) showed a minimum detectable surface stress only 5% higher than that of the best meander configuration sensor (Figure 8.5 B). The 120 μm-wide cantilever has lower performances due to the short resistor lengths, which generates a larger Hooge noise.

Adsorption/absorption rate measurement mode (0.01 Hz – 1 kHz)

In the adsorption/absorption rate measurement mode, the measurement bandwidth should be wider than the other mode to record the transient behaviour of the sensor. It is typically from 0.01 Hz to 1 kHz. In this range, the Johnson noise becomes dominant. The straight resistor length directly influences the resistance value of the piezoresistor and, hence, it should be at a low value to prevent a drastic drop of the SNR. As a result, the sensors with the meander configuration show completely different results (Figure 8.7) compared to the results mentioned above. It should be noted that the only different parameter is the bandwidth. In both cantilever cases in Figure 8.7, the best performance sensors have only one U-shape piezoresistor. In a comparison of the two graphs in Figure 8.5, it is obvious that the 240 μm-wide cantilever sensors have better performance in overall. The best 240 μm-wide cantilever has a straight resistor of 65 μm, which is about a half of the cantilever length. It has a minimum detectable surface stress of 3.5 mN/m, which is about 7 times larger than that of the optimal sensor for the steady state measurement mode. This is mainly due to the much wider bandwidth and is comprehensible. However, these simulations clearly revealed that there is no unique sensor which shows the best performance in both modes, if the meander configuration is employed.

The structure of the line configuration has many resistors in parallel and has a big advantage to lower the Johnson noise. This configuration tends to show a lower minimum detectable surface stress than the sensors with the meander configuration (Figure 8.8). Interestingly, the optimal designs of each cantilever widths are exactly the same as those for the steady state measurement mode in Figure 8.6. The best sensor with the line configuration piezoresistor is the 240 μm-wide cantilever with 3 resistor lines having the maximum length. It shows the minimum detectable surface stress of 2.5 mN/m in the adsorption/absorption rate measurement

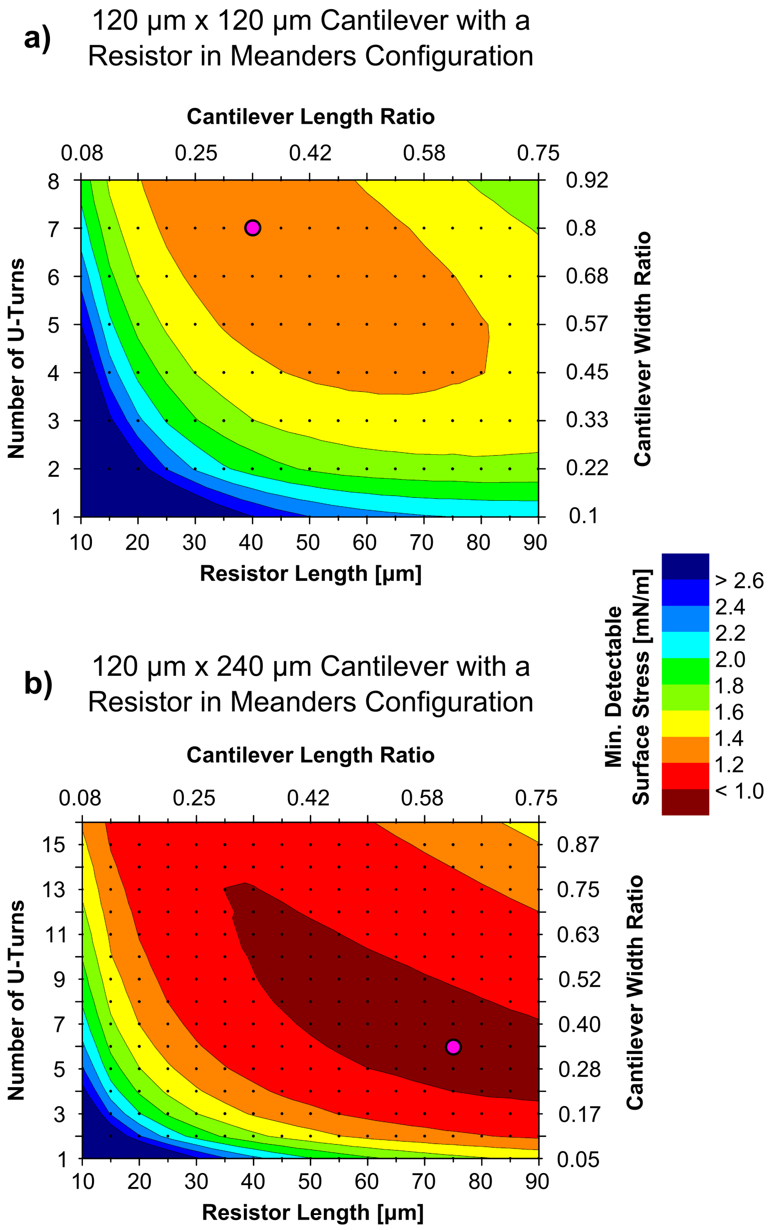

Figure 8.5: FE results of the minimum detectable surface stress of a cantilever with a resistor in meanders configuration (bandwidth 0.01 Hz – 10 Hz). The cantilever dimensions are fixed, i.e. 120 μm x 120 μm x 1 μm and 120 μm x 240 μm x 1 μm for a and b, respectively, and the resistor lateral dimensions vary. Each black dot represents a single simulation. The optimal design for both cantilever widths is highlighted with a pink dot.

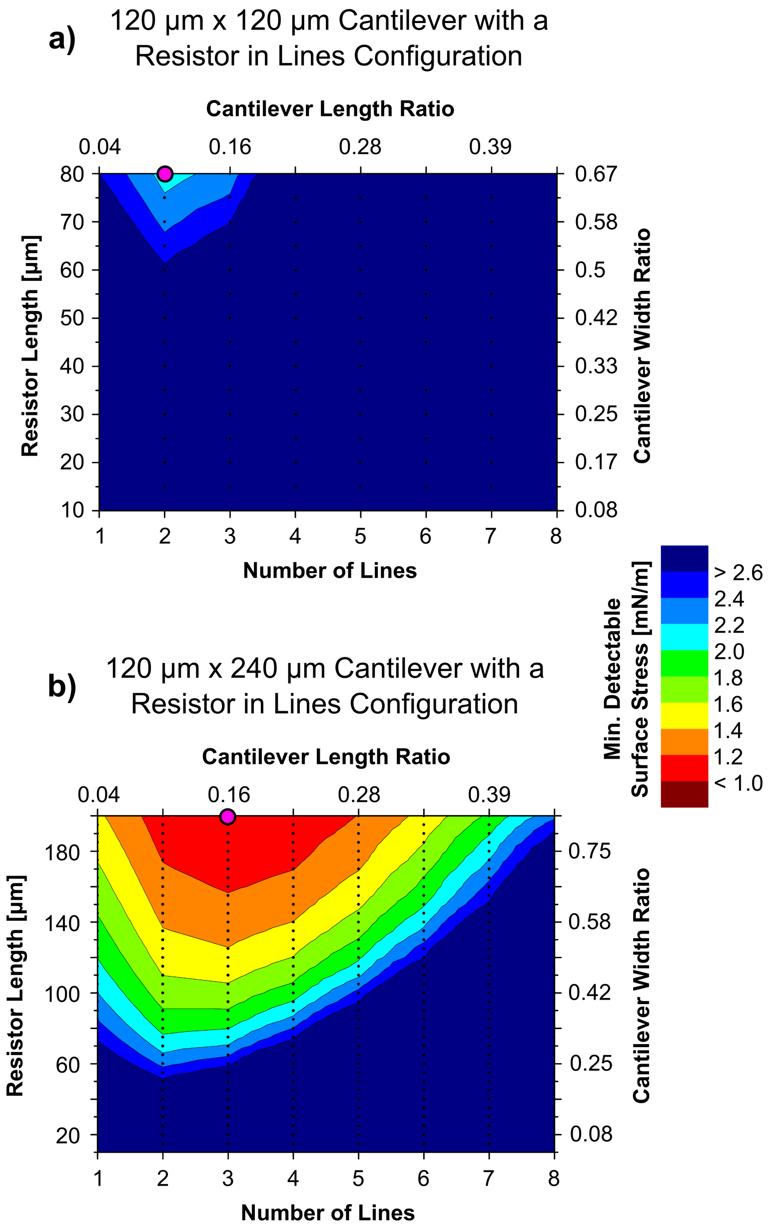

Figure 8.6: FE results of the minimum detectable surface stress of a cantilever with a resistor in lines configuration (bandwidth 0.01 Hz – 10 Hz). The cantilever dimensions are fixed, i.e. 120 μm x 120 μm x 1 μm and 120 μm x 240 μm x 1 μm for a and b, respectively, and the resistor lateral dimensions vary. Each black dot represents a single simulation. The optimal design for both cantilever widths is highlighted with a pink dot.

mode and 1.1 mN/m in the steady state measurement mode, respectively. It is fair to say that the sensors with the line configuration piezoresistor are less influenced by the bandwidth.

Impurity concentration of piezoresistor

The Boron concentration of the piezoresistor is one of the most important parameters that determine the SNR of the sensor. A lower concentration assures a larger piezoresistive coefficient, i.e. higher sensitivity, but both Johnson and Hooge noises are relatively higher as well. At a higher Boron concentration, both noises are relatively lower but the piezoresistive coefficient is lower. Hence, a reasonable trade-off point has to be found to obtain the highest SNR. This problem has already been discussed in detail for point-load cantilevers by Doll et al. [242].

As described above, the Boron concentration was fixed at 1E+18 cm^{-3} to calculate a theoretical SNR through all simulations presented so far. There is still room to improve the SNR by employing different impurity concentrations. Since piezoresistive sensors always have to be connected to an amplifier in a real application, it is practical to take into account the amplifier noise to consider sensor performance. The electrical noises of the piezoresistor could be much lower than that of the amplifier, or vice versa. Therefore, I have simulated sensor performance as function of different Boron concentrations, including the amplifier noise. Three cases are studied: without amplifier noise, with amplifier noise of 10 $nV/\sqrt{Hz}$, which corresponds to the typical noise of a high performance instrumentation amplifier (in-amp), e.g. AD8221 or INA128, and with that of 40 $nV/\sqrt{Hz}$, which corresponds to the typical noise of a low-power in-amp, e.g. AD627. From the previous results, one of the best sensors is employed for this simulation: 120 μm-long, 240 μm-wide, 1 μm-thick cantilever with the line configuration piezoresistor consisted of 3 straight lines of maximum length (200 μm). As it shows good performance in both narrow and wide bandwidths, this design is a well-balanced choice.

Figure 8.9 shows the minimum detectable surface stress of the sensor under the different conditions. The bandwidth was set from 0.01 Hz to 1 kHz. In the ideal case where no amplifier noise is taken into account, the piezoresistor should have a relatively high Boron concentration of 3E+20 cm^{-3} to achieve the best performance. On the other hand, if the amplifier noise exists and defines the minimum noise floor, there is no need to decrease furthermore that of the resistor. Hence, the best performance point is shifted as a function of magnitude of the amplifier noise, down to 5E+18 cm^{-3} for the highest amplifier noise. This is another very important aspect to take into account while designing a surface stress sensor.

8.2.2 | Membrane-type sensor

Yoshikawa et al. have already presented mechanical optimisations of the MSS design [260]. They show a clear dependence between the sensitivity and the size of the suspended membrane, as larger membranes induce a higher sensitivity. Instead of reinventing the wheel, I have

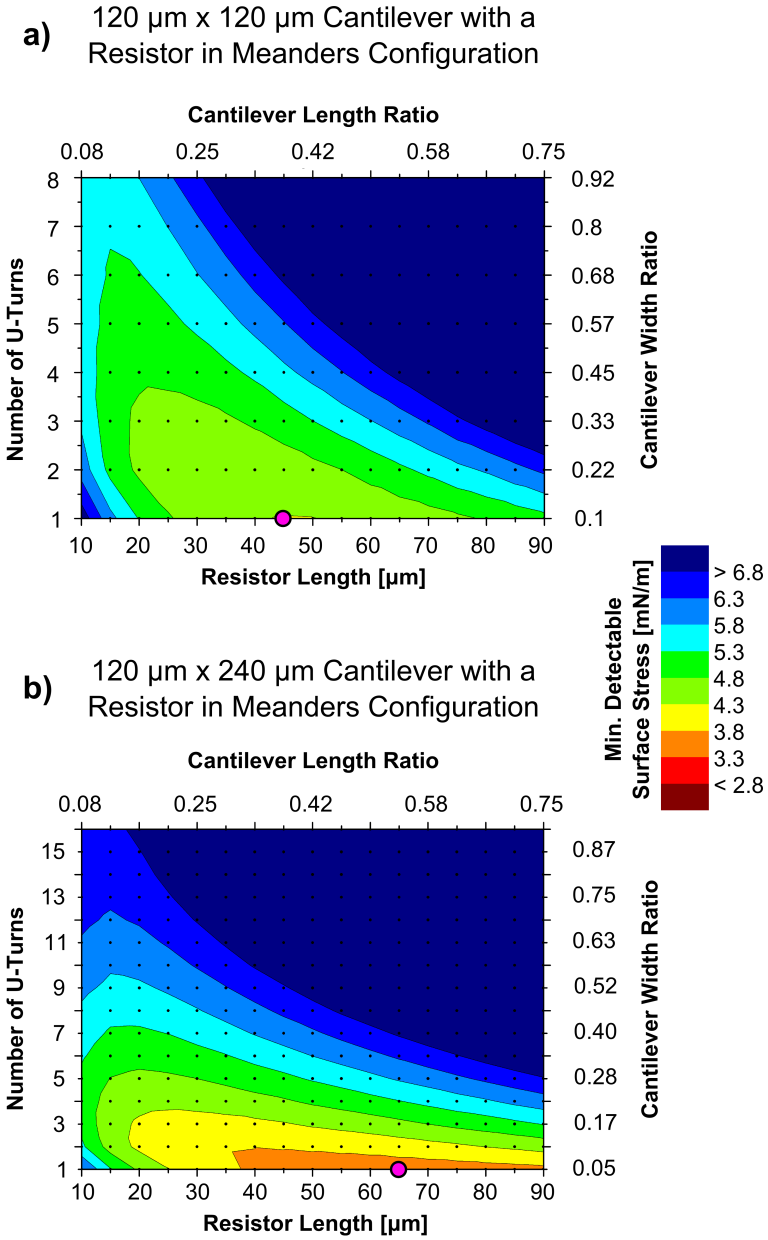

Figure 8.7: FE results of the minimum detectable surface stress of a cantilever with a resistor in meanders configuration (bandwidth 0.01 Hz – 1000 Hz). The cantilever dimensions are fixed, i.e. 120 μm x 120 μm x 1 μm and 120 μm x 240 μm x 1 μm for a and b, respectively, and the resistor lateral dimensions vary. Each black dot represents a single simulation. The optimal design for both cantilever widths is highlighted with a pink dot.

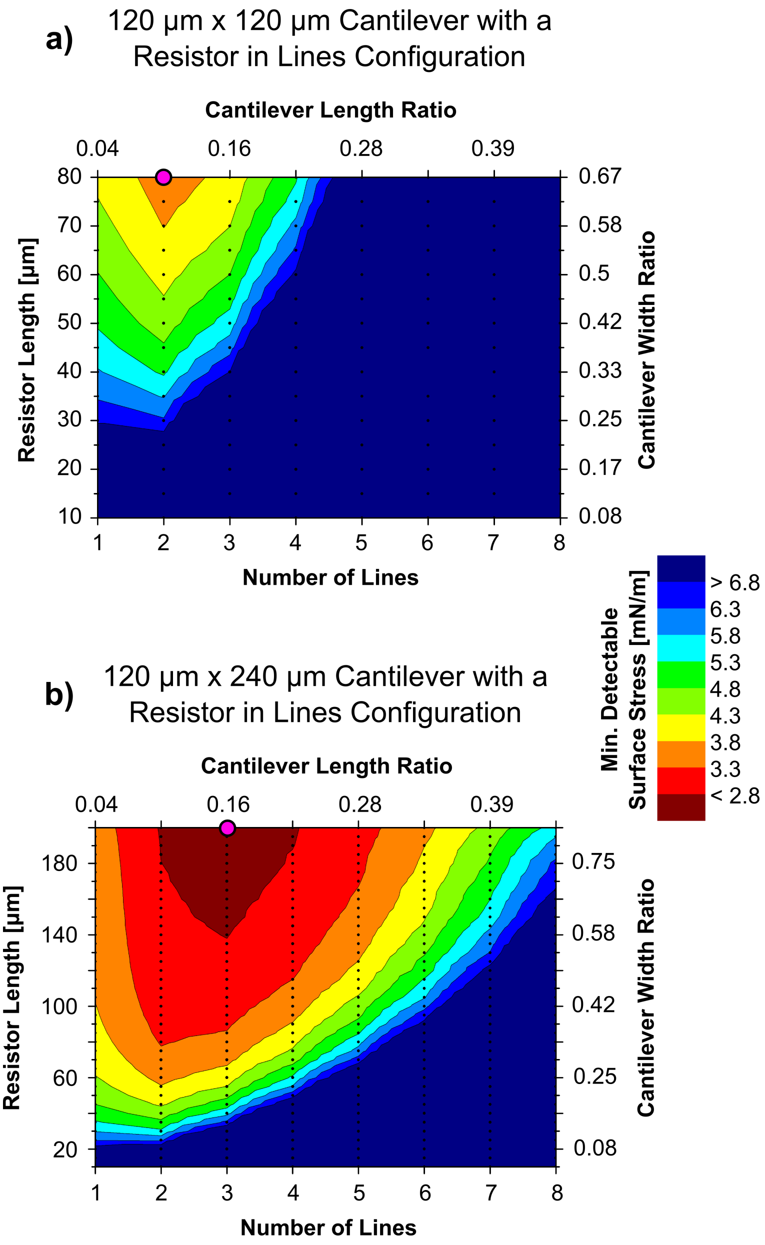

Figure 8.8: FE results of the minimum detectable surface stress of a cantilever with a resistor in lines configuration (bandwidth 0.01 Hz – 1000 Hz). The cantilever dimensions are fixed, i.e. 120 μm x 120 μm x 1 μm and 120 μm x 240 μm x 1 μm for a and b, respectively, and the resistor lateral dimensions vary. Each black dot represents a single simulation. The optimal design for both cantilever widths is highlighted with a pink dot.

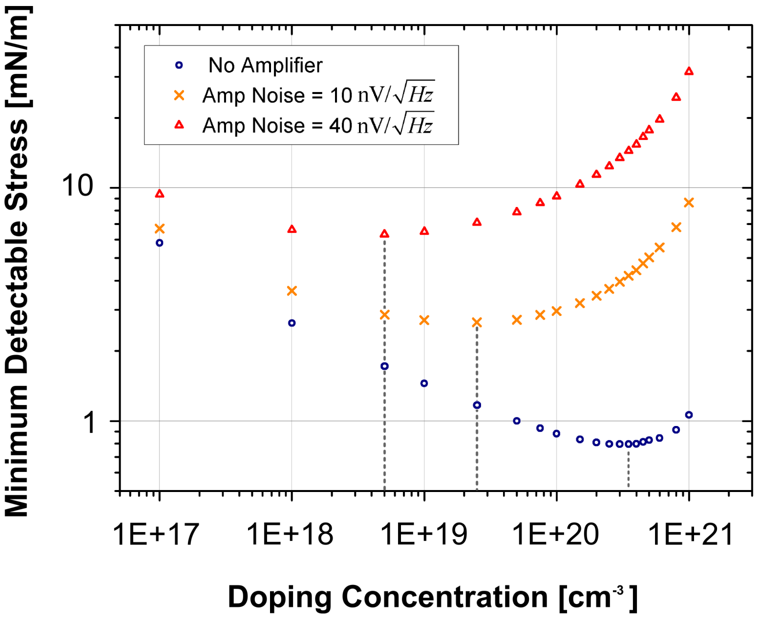

Figure 8.9: Minimum detectable surface stress simulated for various doping concentrations of the optimum design highlighted in Figure 8.8 b. Unlike the previous simulations, an amplifier noise is taken into account.

decided to take advantage of my piezoresistive simulation tool and focus on the piezoresistors dimensions.

Based on the cantilever-based sensor optimisation presented in the previous section, I have chosen a doping concentration of 1E+19 cm^{-3}, which is more adapted to the electrical noise of existing amplifiers. The membrane thickness was also modified to a more suitable value, in terms of fabrication, of 3 μm. Finally, I have kept the 0.01 Hz - 1 kHz bandwidth since the MSS are, at least initially, meant to measure dynamic changes of deflection as well.

Figure 8.10 A and B shows the model of the membrane hinges with the perpendicular and parallel resistors, respectively. The parameters are the width and length of each resistor while the offset, gap, and W values stay constant. The dimensions of the hinges follow then those of the resistors. Figure 8.11 A and B shows the simulated minimum detectable surface stress for various dimensions of the perpendicular and parallel resistors, respectively. In both cases, while the two resistors of the same kind are being varied, the two others keep the same dimensions.

Intuitively, smaller hinges should be more efficient to transduce the surface stress from the membrane to the resistor. In fact, sensitivity simulations do reflect this hypothesis. Once the electrical noises are taken into account, the optimum values slightly change, especially for the parallel resistor, which should be 16 μm long and 4 μm wide (Figure 8.11 B). In the case of the perpendicular resistor, the smallest simulated model is still the best one with resistors that are 10 μm long and 5 μm wide (Figure 8.11 A). The best MSS design, when both these resistor

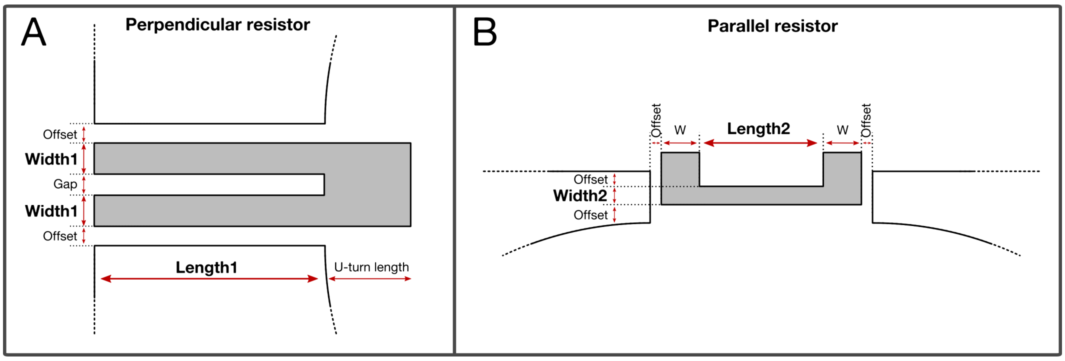

Figure 8.10: Models of the (A) perpendicular and (B) parallel resistor of the MSS. Parameters are Width1, Width2, Length1, and Length2. The Offset, Gap, and W dimensions are kept constant.

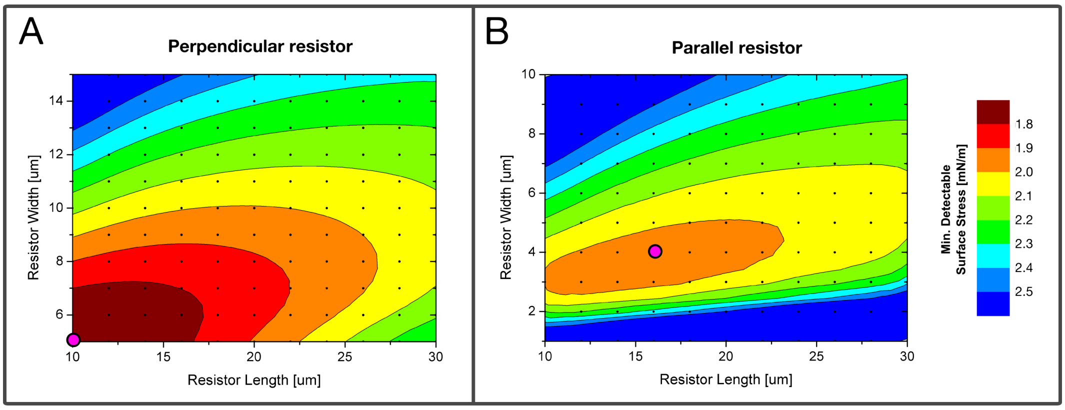

Figure 8.11: FE results of the minimum detectable surface stress of the MSS resistors (bandwidth 0.01 Hz – 1000 Hz). The membrane dimensions are fixed, i.e. 500 μm x 3 μm. On the left plot (A), the dimensions of the two parallel resistors are fixed, i.e. 20 μm x 5 μm, while those of the two perpendicular ones vary. On the right plot (B), the opposite is true with the dimensions of the fixed perpendicular resistors being 20 μm x 10 μm. Each black dot represents a single simulation. Red colour highlights configurations with lower detectable surface stress. The optimal design for both resistors is highlighted with a pink dot.

configurations are combined, has a sensitivity of 1.1 mV/N/m and a minimum detectable surface stress of 1.62 mN/m. Similarly to the cantilever models, this particular design is not fully optimised since not all parameters were varied.

In order to compare this preferred design with the best cantilever-based sensor found in the previous simulations (Figure 8.8 b), I have simulated the latter with similar doping concentration and membrane thickness. The obtained sensitivity is 0.08 mV/N/m and the minimum detectable surface stress is 20.3 mN/m. Based on these values, MSS is 13.75x more sensitive and has a 12.5x lower limit of detection compared to that cantilever design. This comparison includes the 4x amplification factor given by the full Wheatstone bridge configuration of MSS.

8.3 | Influence of the coating variability

Beside the optimisation of the sensor geometry, I have applied this simulation tool to assess the influence of the coating quality on the sensor repeatability. In all the previous simulations, the coating was supposed to be homogeneous. Hence, a constant surface stress has been applied. In order to model a inhomogeneous thickness of the coating, a random component can be introduced to the applied surface stress. The idea is the following: predefined small and random variations in stress were added to a constant value when the computer calculates properties of each local element of the modelled structure. Instead of a constant surface stress, e.g., 0.2 N/m, a random value based on a prefixed mean and standard deviation σ, e.g., 0.2 ± 0.02 N/m, is applied to each surface element of the sensor. Various models can be therefore simulated for different means and standard deviations in surface stress. In this manner, two identical cantilevers loaded with the same surface stress defined with the same standard deviation will never have the same stress distribution, which is closer to the reality.

As an illustration, I have modelled a cantilever (Figure 8.12 A) with a surface stress of various standard deviations and simulated the stress difference. The results are shown in Figure 8.12 B for a surface stress of 0.2 N/m and standard deviations (SD) of 0 N/m, 0.01 N/m, 0.02 N/m, and 0.04 N/m. In the case of a null standard deviation, the classic bell-shape distribution is found, as expected. In the cases of non-null standard deviations, irregularities appear but similar stress distributions are obtained. Based on these mechanical simulations, it is impossible to say anything about the influence of these irregularities on the sensor response. The electrical simulations are again required.

I have simulated both the cantilever and MSS designs with the above surface stress parameters, i.e. 0.2 N/m surface stress with standard deviations of 5%, 10%, and 20%. In each case, 100 cantilever simulations and 100 MSS simulations were performed. The distributions of their resulting output signals are summarized in Figure 8.13 A and B for cantilevers and MSS, respectively. In the case of the cantilevers, their output signals show reproducibility similar to that of their coating. However, in the case of the MSS, the standard deviation of their output signals is reduced by a factor 50. From these simulations, it is clear that the response of cantilever-based sensors is strongly influenced by the reproducibility of their functionalisation layer. A poor repeatability of the film will result in a poor repeatability of the cantilever output. In comparison, MSS are less sensitive to this problem. This fundamental difference comes from the design of the MSS itself. The piezoresistor on cantilevers detects local changes of surface stress, i.e. only the polymer located on top if it will have an influence on its output. In the case of the MSS however, local surface stresses on the membrane are transduced to the four hinges and the piezoresistors sense a global stress. Hence, the MSS output is less influenced by non-uniformities of the membrane coating.

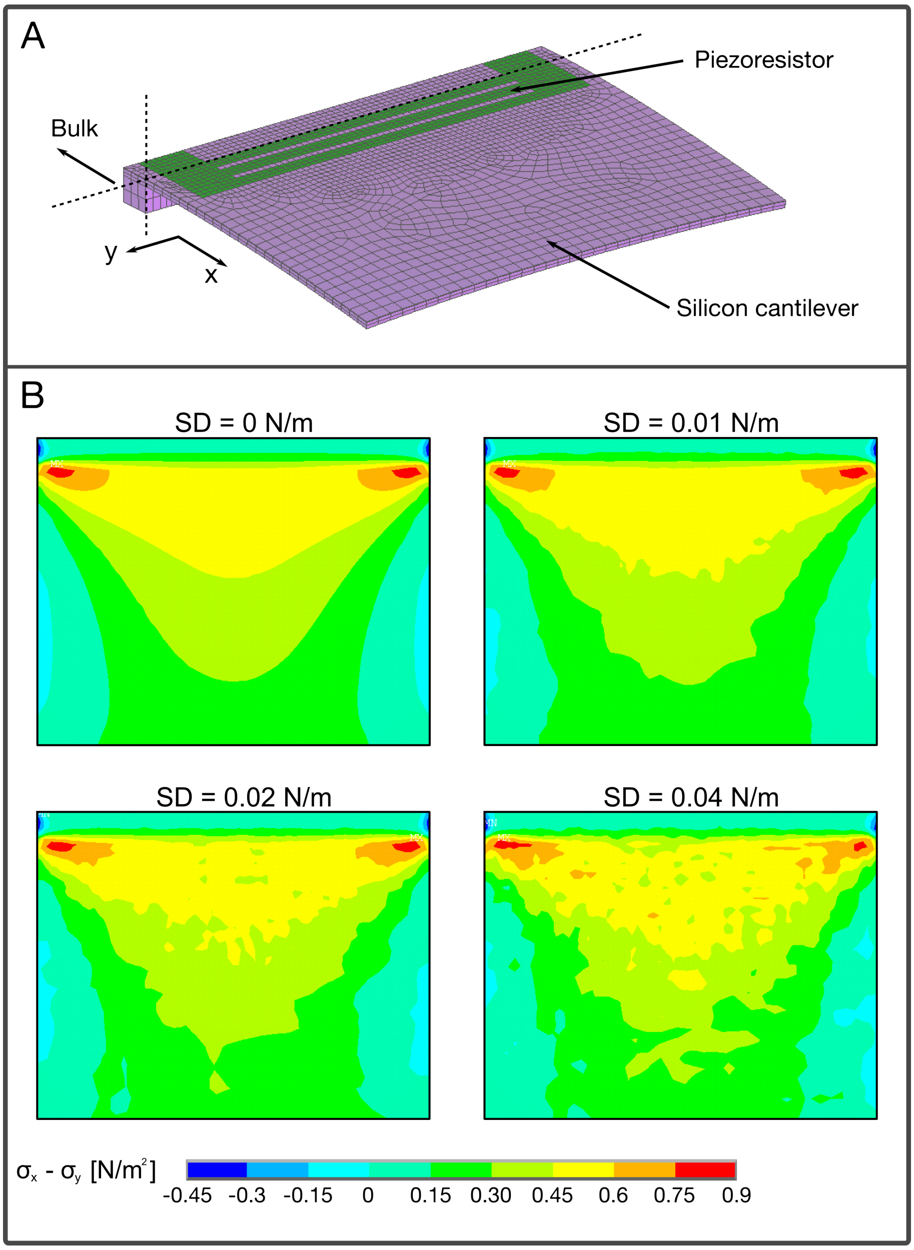

Figure 8.12: (A) Piezoresistive cantilever (100 μm x 140 μm x 2 μm) modelled with Ansys. The resistor is composed of three lines (100 μm x 5 μm x 0.2 μm) connected in parallel. (B) Top views of the simulated cantilever loaded with a surface stress of 0.2 N/m and various standard deviations SD. The colour map represents the simulated stress difference $\sigma_x - \sigma_y$.

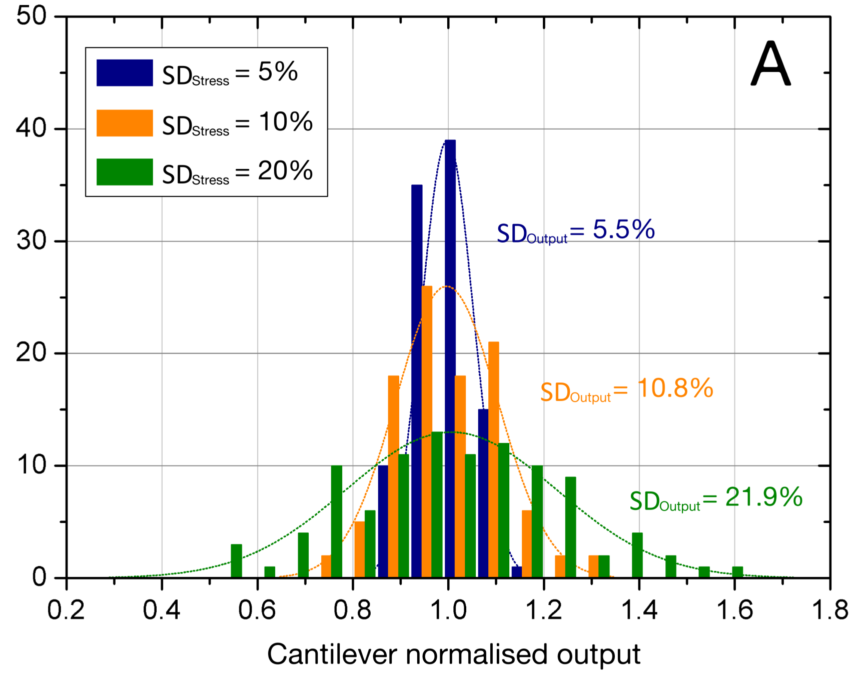

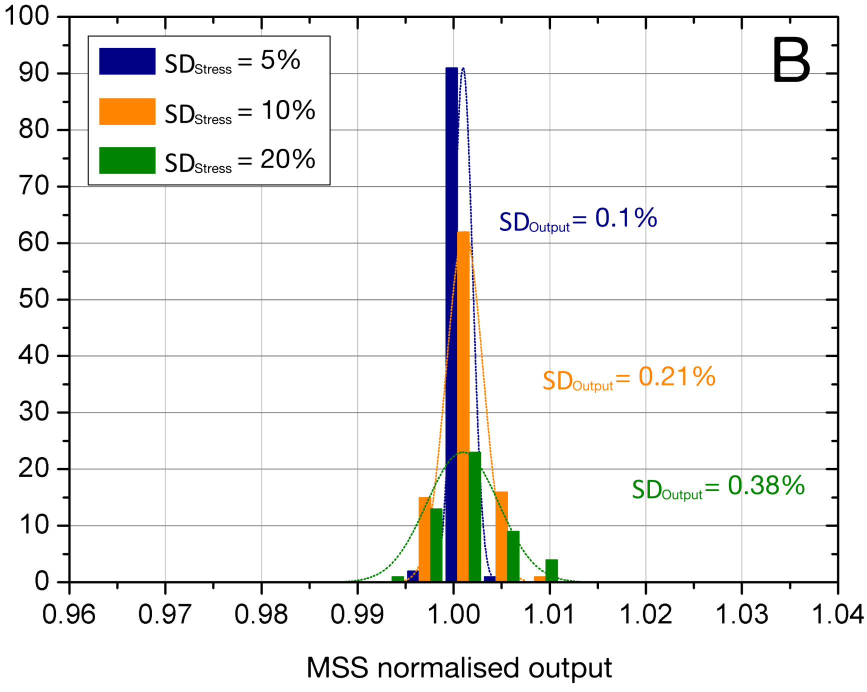

Figure 8.13: Sensor output distributions of 100 simulated cantilevers (A) and MSS (B) while a random surface stress is applied on their surface.

8.4 | Summary and design guidelines

Cantilever-based sensors and MSS were optimised with a piezoresistive simulation tool that allows the simulation of actual resistor shapes and the introduction of electrical noises. SNR, instead of sensitivity alone, is therefore defined as the performance target. Sensor and resistor geometries, doping level, and frequency bandwidth are the parameters of the developed simulation tool. However, it does not take into account process parameters, such as non-uniform doping profiles, annealing temperatures, or passivation layer thickness. Hence, this tool is much more useful for the relative comparison between sensor designs than for the prediction of the absolute performances of their microfabricated versions. The thermal effects due to the piezoresistor self-heating were not taken into account. Unlike their AFM versions, cantilevers for surface stress sensing have a large clamping area that limits the temperature increase. Similarly, the large membrane of the MSS serves as an efficient heat-sink. Hence, the noises added by thermal variations were neglected. However, if this simulation tool would be used to simulate other MEMS designs, the thermal effects may need to be incorporated as well.

I have first optimised and compared the cantilever-based and MSS designs. I have found, in agreement with previous studies, that wide cantilevers are best for piezoresistive surface stress sensing. Increasing the width above 200 μm does not significantly improve the SNR any more. In addition, resistors designed as lines oriented perpendicularly to the cantilever length are well suited for frequency bandwidths up to 1 kHz. In order to keep the current flow as parallel to the resistor as possible, I suggest a design composed of several narrow lines connected in parallel instead of a single, wide resistor. The final geometry should also be designed with the amplifier noise in mind. Optimised MSS design still showed more than 10 x better performances, both in sensitivity and SNR, compared to the best simulated cantilever design. Since several parameters were not varied, the proposed designs are not fully optimised but still show better performances compared to more classical shapes.

Finally, I have been able to assess the reproducibility of both sensors in a way that could not been possible with mechanical-only simulations. Hundred cantilevers and MSS were simulated with randomly distributed surface stress, which is closer to realistic functionalisation layers compared to uniform surface stress. While the cantilever response tend to be as variable as its coating, the MSS shows a strong robustness against it. Hence, I expect MSS to be much more sensor-to-sensor reproducible compared to cantilever-based sensors.

9 || Fabrication and characterisation

In this chapter, I present the fabrication of the first generation of MSS. Cantilever-based sensors optimised towards low level of detection were also fabricated as a comparison. The platforms were finally characterised as humidity sensors. Sensitivity, response time, but also sensor-to-sensor repeatability will be discussed.

As their fabrication began before the completion of the design guidelines described in the conclusion of the previous chapter, their designs were based on mechanical-only simulations and slightly differ from the optimum design found with the piezoresistive simulations. Figure 9.1 shows the layouts of both MSS and cantilever-type sensor of first generation.

Piezoresistive simulations showed that the 1st generation MSS design is 15.41x more sensitive and has a 13.90x lower limit of detection compared to the 1st generation cantilever design. As the latter is narrower than its optimised case, its sensitivity is slightly decreased.

9.1 | Process flow

Figure 9.2 shows the major steps in the fabrication process of MSS. The cross section shows one of the four constricted beams with a partial view of the suspended membrane. The process starts with an SOI wafer with a device layer of 3.5 μm that is thinned down to 2.5 μm by thermal oxidation and a subsequent removal of the silicon dioxide (Figure 9.2 a). The p-type piezoresistors are then created with two distinct doping processes: deep and highly conductive zones are initially created with the deposition of boron silicate glass (BSG) and diffusion of the boron atoms into the silicon at 1000°C during 30 minutes. Shallow layers, which are very sensitive to surface stress, are then created by ion implantation (Figure 9.2 b-c). The boron ions are implanted with a dose of 2.5E+14 $/\mathrm{cm}^2$ at 45 keV followed by a rapid thermal annealing (RTA) at 1000°C during 10s. After a deposition of an 80 nm thick layer of Si_3N_4 as a passivation layer by low-pressure chemical vapour deposition (LPCVD) (Figure 9.2 d), aluminium wires are structured and encapsulated with a thick SiO_2 layer of 1 μm by plasma enhanced chemical vapour deposition (PECVD). The membrane and its sensing beams are then structured into the device layer with DRIE (Figure 9.2 e). A 5 μm thick layer of Parylene is deposited on the front side to protect the membrane prior to its final backside release by DRIE (Figure 9.2 f-g). The Parylene serves as both mechanical stiffening of the membrane during

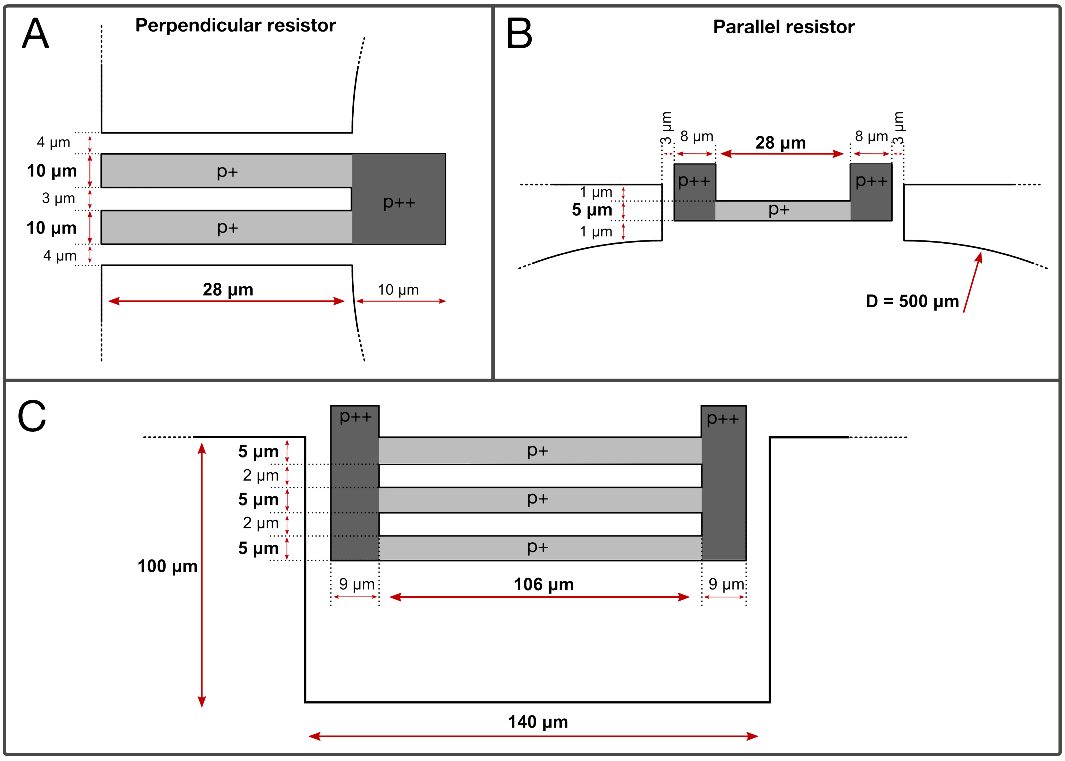

Figure 9.1: Layouts of the first generation of MSS (A and B) and piezoresistive cantilevers (C).

the DRIE and protection layer during the wet etching of the buried oxide in buffered HF. At the last step of the fabrication process, the Parylene is removed by oxygen plasma. Optimised cantilever-based sensors were designed on the same wafers and fabricated at the same time. Figure 9.3 shows SEM pictures of MSS with close-up views on its hinges. The size of the chip is 13 mm × 10 mm, on which two arrays of 8 sensors are designed. Cantilever-based sensors optimised as shown in section 8.4 were similarly fabricated on the same wafers (Figure 9.4). More details on the process parameters can be found in Appendix D.

9.2 | Characterisation methods

The MSS has been designed for bio/chemical detection based on molecular absorption into polymers. VOCs in gaseous media are therefore the primary analytes. I have, however, characterised the MSS as a humidity sensor. Since the absorption of water molecules is very similar to that of VOCs, the preliminary results obtained as a humidity sensor would also be true for other volatile molecules.

9.2.1 | Functionalisation by inkjet printing

Two different inkjet spotters with different drop algorithms were used. The first one is a Dimatix DMP2831 inkjet dispenser. It can form a grid of closely spaced droplets on the membrane

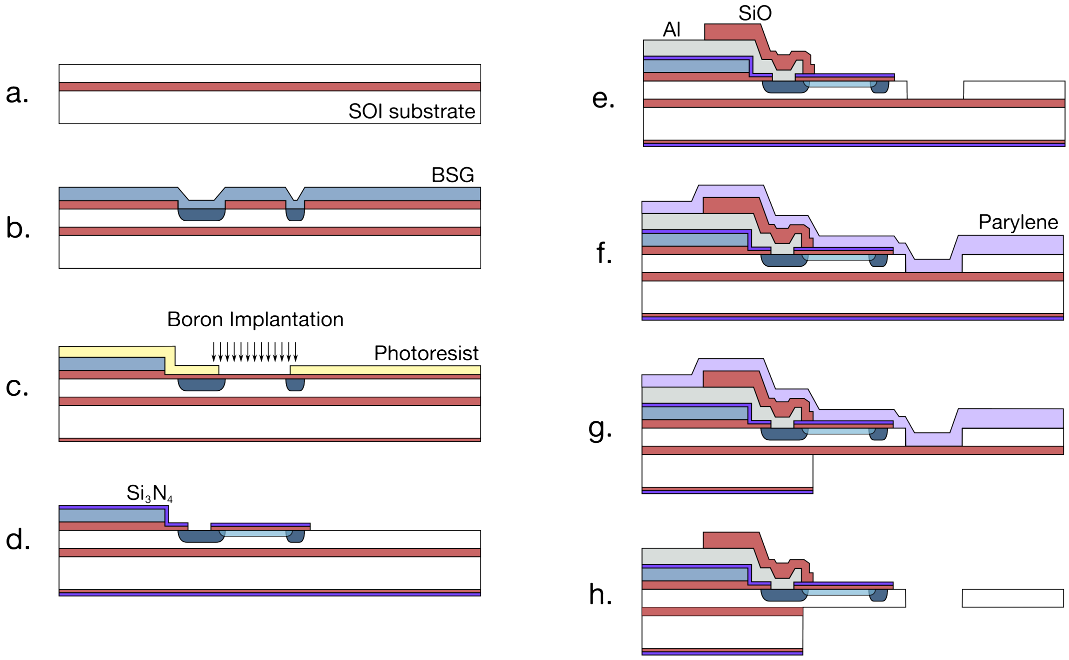

Figure 9.2: Process flow of the membrane-type sensor fabrication. The cross section represents one of the four constricted beams with an integrated piezoresistor, according to Figure 7.9. The membrane is separated from the beam for clarity (e to g).

(Figure 9.5 A). This allows the formation of rather uniform layers that can be superposed onto each others. A drawback of this technique is that the number of deposited droplets cannot be precisely controlled and it varies depending on the alignment of the grid relative to the membrane. Figure 9.5 B shows an MSS functionalised with four successively coated layers of polymers.

The second inkjet spotter is the Autodrop MD-P-802 inkjet printer from Microdrop Technologies. Unlike the previous printing method where each droplet within the same grid layer has to dry out before the next one hits the surface, the printed droplets form a big drop on the entire surface of the membrane (Figure 9.5 C). The solvent eventually evaporates, creating the well-known coffee-ring shape of polymer on the membrane (Figure 9.5 D). Since all the droplets reach the surface of the sensor, the amount of printed polymer is well controlled.

9.2.2 | Measurement setup

The sensor arrays were tested in a custom-made gas flow chamber (Figure 9.6). Dry and wet nitrogen fluxes were mixed and introduced into the chamber with two mass flow controllers (Bronkhorst EL-FLOW). A total flow rate of 500 ml/min was always maintained. A commercial humidity sensor (Sensirion HT21) was also mounted inside the chamber to measure the relative humidity.

The output voltage of each sensor was amplified (200x) and filtered (< 3 Hz) by an amplification

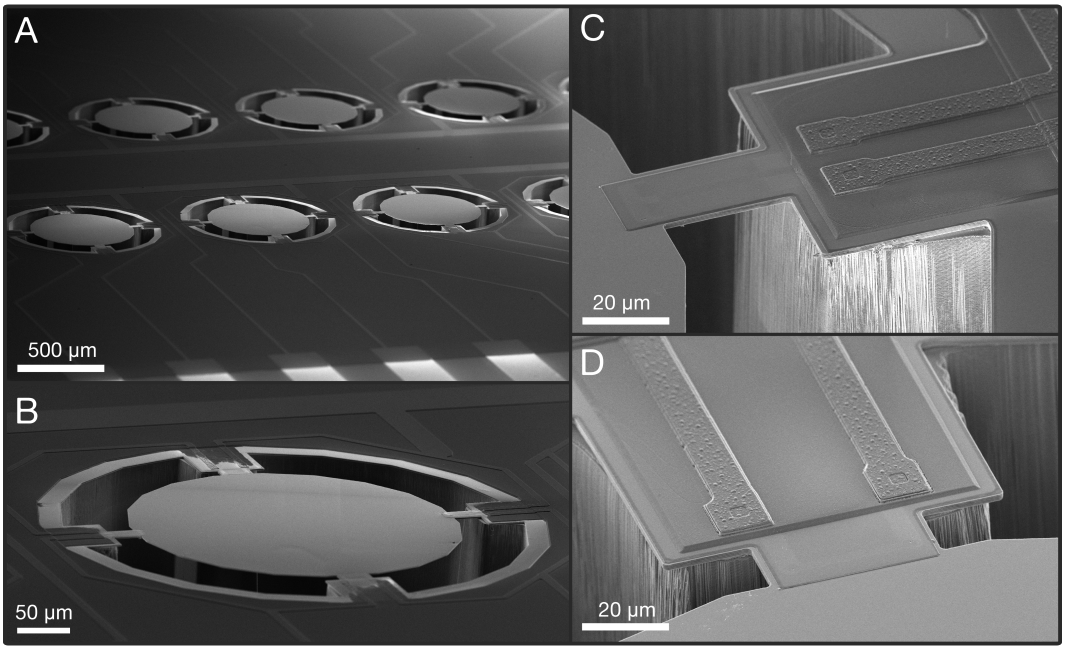

Figure 9.3: SEM observations showing (A) two MSS arrays with their electrical connections, (B) an MSS with its four suspended beams, and close views on the latter (C and D).

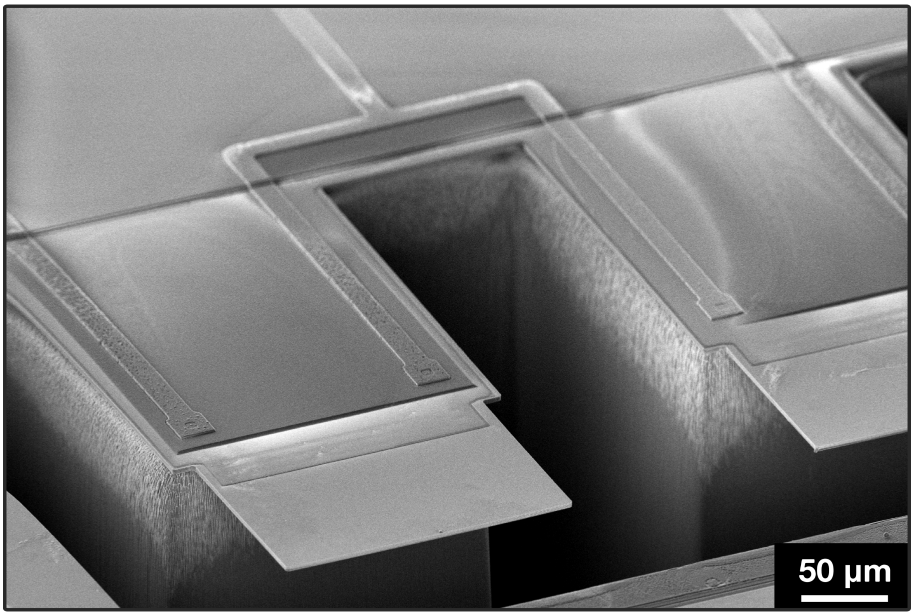

Figure 9.4: SEM observation of a cantilever-based sensor (L = 100 μm, w = 130 μm). Its piezoresistor is composed of three lines (l = 5 μm, w = 100 μm) connected in parallel.

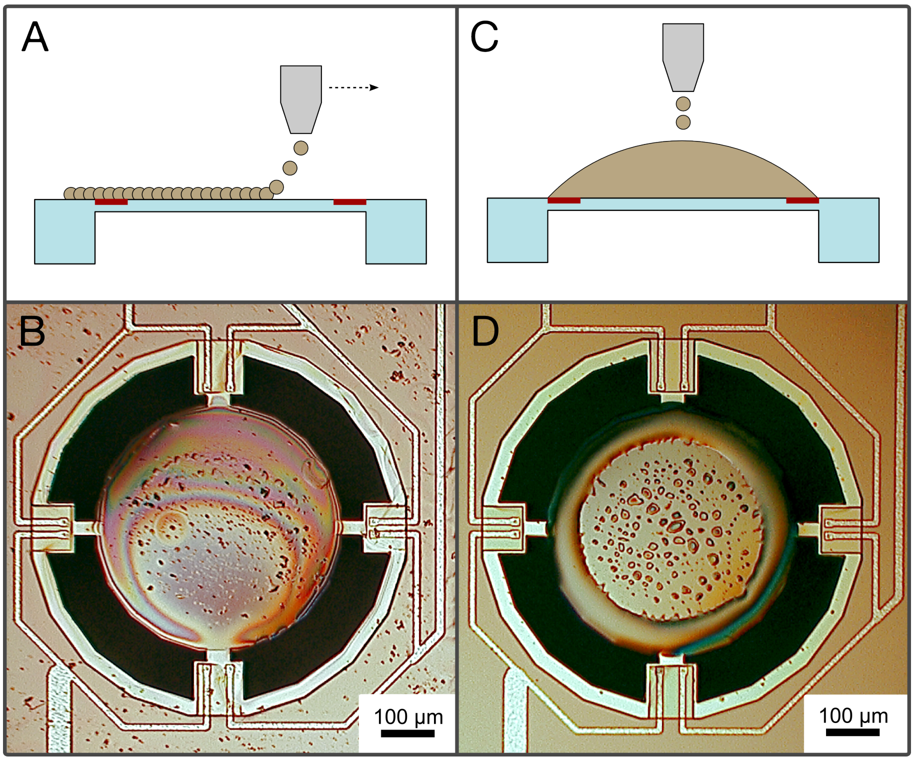

Figure 9.5: (A) Functionalisation of MSS has been performed first by inkjet printing in a grid pattern, resulting in roughly regular polymer layers. (B) An MSS functionalized with 4 layers of cellulose acetate butyrate (CAB) using the Dimatix printer. (C) In a second method, the droplets are rapidly printed at the same location and form a bigger drop on the membrane. The evaporation of the solvent creates a coffee-ring pattern, where most of the polymer is concentrated on the membrane periphery. (D) An MSS functionalised with 500 droplets (10 pl) of Dextran dissolved in water (1 mg/ml).

stage using low power instrument amplifiers (AD627). The cantilever-based sensors were measured in pairs (a coated cantilever in series with a reference one) (Figure 9.7 A). In the case of the MSS, the output voltage corresponds to that of the full Wheatstone bridge (Figure 9.7 A). The PCBs were designed and fabricated by Andreas Tonin from the University of Basel. The bridge voltage of all sensors was set at -0.5 V. An acquisition card from National Instruments (USB-6215) was used to record all the signals with a programmed Labview interface.

9.3 | Reproducibility

The reproducibility of both cantilever- and membrane-based sensors is assessed in this section. In section 8.3, I have already simulated the influence of an inhomogeneous coating on the electrical responses of both sensors. While MSS were clearly more robust to variations of their coating, I wanted first to quantify the variability of inkjet deposited films in a preliminary study. The experimental comparison between MSS and cantilever-based sensors is then presented.

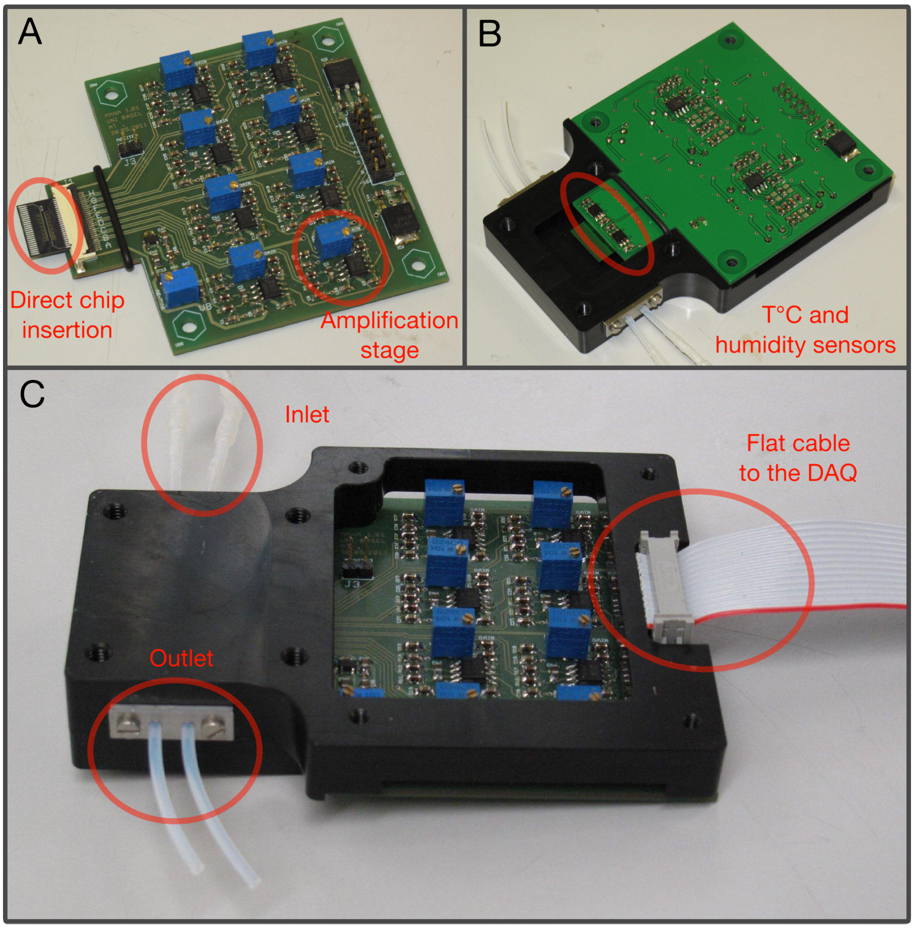

Figure 9.6: Custom made amplifier stage PCB and gas chamber by Andreas Tonin of University of Basel. The silicon chip is directly inserted into the PCB with a zero insertion force (ZIF) connector (A). At the rear of the PCB are a temperature and a humidity sensors that are introduced in the gas chamber (B). Once closed, the chamber has a volume of $\approx 3\ \text{cm}^3$ (C). A flat cable connects the PCB to the acquisition card.

9.3.1 | Preliminary study

The work presented in this section has been mainly achieved by Vivien Lacour during a Semester project that took place between September 2011 and January 2012. Vivien assisted me during the microfabrication steps. He then wrote the Matlab code for the analysis of the profiles acquired by white light interferometry. He finally created the Labview interface that was used for the humidity characterisation.

The coating of a surface by inkjet spotting is challenging due to the coffee stain effect, which appears during the evaporation of the solvent. In order to quantify the repeatability of this phenomena, we designed and fabricated circular patterns on silicon wafers by means of hydrophobic/hydrophilic surface modification (Figure 9.8 A). As the hydrophilic surface is surrounded by hydrophobic "walls", a water-based solution deposited by inkjet printing would be precisely delimited into the pattern shape. After evaporation of the water, we were able to

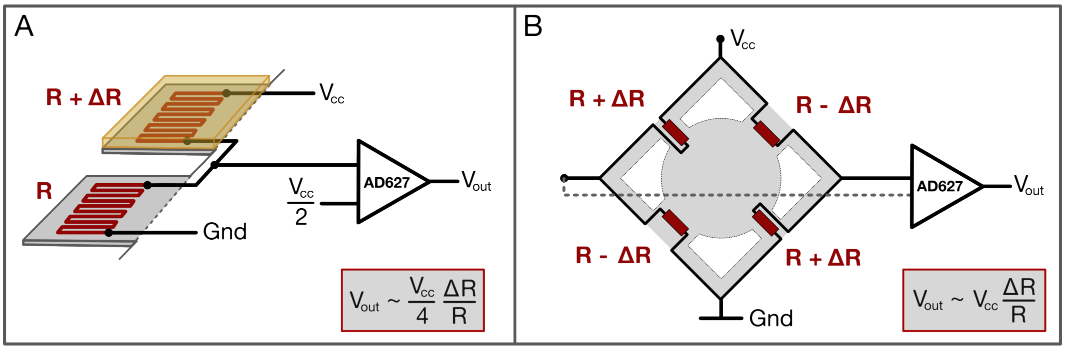

Figure 9.7: Electronic circuit configurations for (A) cantilever and (B) MSS readout.

observe the topology remaining polymer by white light interferometry.

Creation of the patterns

Figure 9.8 shows the process followed to create the hydrophobic patterns. First, they are transferred by lithography onto silicon wafers presenting a native oxide (Figure 9.8 1-2). A superhydrophobic Teflon-based polymer (≈ 2nm thick) is then deposited by molecular vapor deposition (MVD) and structured with a lift-off process (Figure 9.8 3-4). The patterns are ready to be coated with a chosen solution of polymer by inkjet printing (Figure 9.8 5). After the evaporation of the solvent, a thin layer of aluminium is sputtered on the surface to allow the observation of the polymer patterns by white light interferometry (Figure 9.8 6-8).

Two different hydrophilic patterns were created (Figure 9.9 A). While the disc shape models the geometry of a membrane-type sensor, we also designed a disc with four hydrophobic stripes oriented towards the centre. The purpose of this design is to confine the polymer into chambers which could either suppress the coffee stain effect or decrease its irregularities.

Inkjet printing and results

In order to observe the coffee ring effect, we used the Autodrop inkjet system. We printed 500 droplets of a water-based solution of Dextran (1 mg/ml) on each structure. The accumulation of these droplets forms a big drop covering the whole surface. With a droplet volume of 10 pl, the total amount of remaining polymer after evaporation on the structure is 5 ng. 24 plain discs and 24 crossed discs were coated and their topology was measured by white light interferometry. A custom Matlab code was then used to merge the obtained profiles into statistical results.

The average thickness and its standard deviation for both structures are shown in Figure 9.9 B and C, respectively. We used a custom-made Matlab script to align and compile all the 3D profiles measured with the interferometer into a single, averaged, profile. Figure 9.9 B shows the obtained profile for both the plain and crossed patterns. In order to highlight the

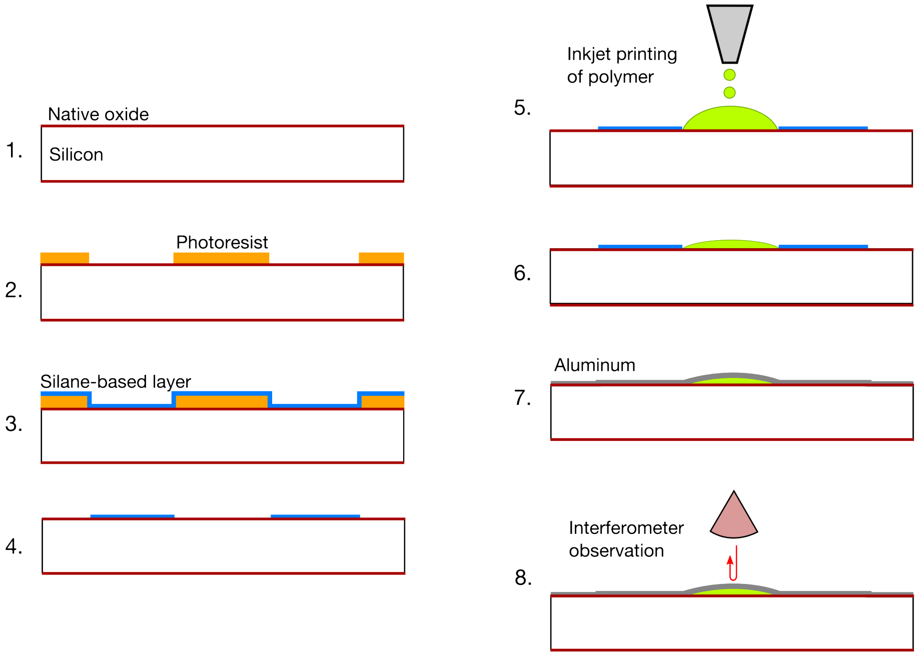

Figure 9.8: Fabrication of defined hydrophobic zones for localised inkjet printing. A Teflon-based polymer is deposited by MVD to create the super-hydrophobic patterns. After the dispensing of the polymer, a thin aluminium layer is deposited on top of it to allow its observation by interferometry.

reproducibility of these coatings, their standard deviations is shown in Figure 9.9 C.

As expected, the evaporation process created a strong migration of the polymer to the edge of the plain disc with an average thickness of about 2 μm compared to a centre thickness of 185 nm. While the overall pattern of the coffee stain is similar in the 24 observed cases, its repeatability is not very good with a standard deviation of about 20% where the polymer is the thickest, which represents variations of ± 400 nm.

In the case of the crossed disc, the coffee stain effect has not been suppressed but the repeatability of the coating has slightly improved with only localised areas of poor reproducibility. The use of hydrophobic zones placed on the sensor to guide the polymer during solvent evaporation could therefore be an interesting solution to increase its reproducibility. The impact of these structures on the sensor sensitivity would need however to be assessed.

This preliminary study clearly shows a poor reproducibility of the coatings. While the ring shape is well defined in all the printed structures, local thickness variations exist even if the deposited amount of polymer was similar.

9.3.2 | Membranes vs. cantilevers

In the previous section, controlled zones were coated with Dextran by inkjet printing and a standard deviation of about 20-25% was obtained. With such a poor reproducibility in the

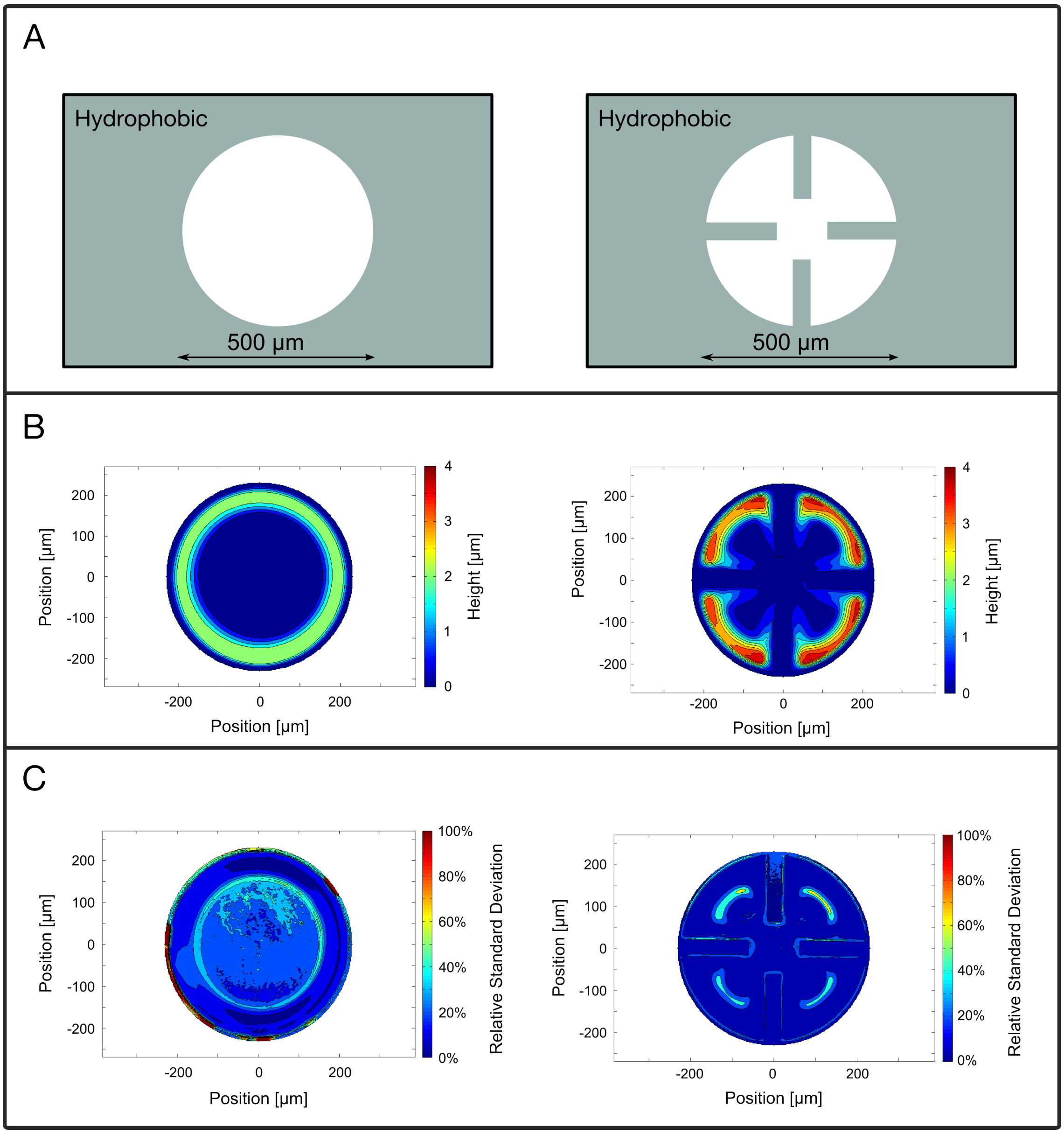

Figure 9.9: (A) Two hydrophobic/philic patterns were created to assess the reproducibility of inkjet dispensing. (B and C) Average and standard deviation values of 24 structures similarly coated with 500 droplets of a Dextran-based solution.

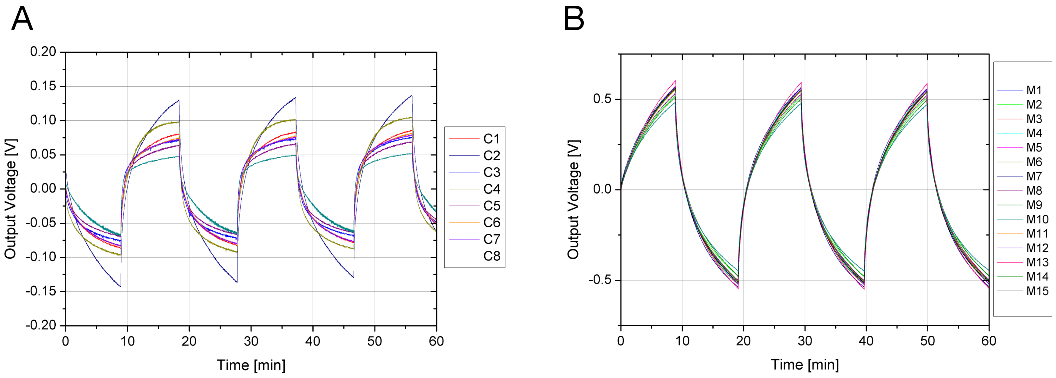

Figure 9.10: Dynamic responses of (A) eight cantilevers and (B) fifteen MSS to humidity pulses of 5%. All sensors were similarly coated with Dextran by an Autodrop inkjet printer. The output voltages are amplified 200 times.

coating of flat surfaces, the functionalisation of suspended membranes and cantilevers will likely behave similarly. As highlighted during the FE simulations in Section 8.3, MSS should however not be impacted too much by the variability of their coating, unlike cantilevers.

In order to obtain a coating quality comparable with that of the preliminary study, Dextran was again selected to be printed with the Autodrop system. 500 droplets were dropped on each MSS. On the cantilever-based sensors, 280 droplets of the same solution were dispensed to obtain approximately the same amount of polymer per unit surface area. 8 cantilevers and 15 MSS were functionalised to quantitatively compare their sensitivity and reproducibility. The respective dynamic responses to humidity cycles of 0% and 5% are shown in Figure 9.10 A and B.

In order to quantify the reproducibility of each sensor, the peak-to-peak voltage of three cycles for each sensor was measured and their mean value and standard deviation were calculated. In average, the measured output of the cantilever was 0.167 V while the MSS had an average value of 1.010 V, which represents a 6.05 times higher signal. The cantilever-based sensors showed a standard deviation of 27.7%, which roughly corresponds to that of the coating measured in the preliminary study. On the other hand, MSS showed a standard deviation that is five times smaller with a value of 5.4%.

9.4 | Humidity measurements

For the humidity characterisation, cellulose acetate butyrate (CAB) was selected as a functionalisation polymer owing to its good affinity with water molecules [264]. The CAB is dissolved in hexyl acetate (1 mg/ml) in order to be printed with the Dimatix DMP2831 inkjet dispenser, as described in section 9.2.1. The volume of one droplet was approximately 10 pl and the grid pitch was 20 μm. With these conditions, a CAB layer with a thickness of about 500 nm can be printed on a flat surface.

Three individual MSS in the same array were coated with different thicknesses: one, two and four layers of CAB. The fourth MSS was uncoated. Its signal served as a reference and used as the baseline of the signals from the other sensors. Figure 9.5 B shows the MSS functionalised with four successively coated CAB layers.

The MSS were exposed to different relative humidity levels up to 70%, which was the upper limit of the gas mixing system. I present in the following paragraphs its dynamic and static responses. Due to the large response distribution of cantilever-based sensors, five of them were similarly functionalised and their responses were averaged.

9.4.1 | Dynamic response

Figure 9.11 shows the dynamic responses of three MSS coated with one, two and four CAB layers, respectively. The membranes were coated by the Dimatix inkjet spotter with the technique explained in Figure 9.5 A. All sensors reacted to humidity with response times (63.2%) of 0.8 ± 0.1 s for all steps. Normally, if the thickness of the CAB coating is different, the time constant should differ due to different diffusion time of the molecule into the polymer layer. This was not the case. Possibly, the measured time constant was that of the gas flux filling the chamber. The response time of the three sensors could therefore be even shorter. At this time scale however, the measurement setup is not precise enough to distinguish such time differences.

Overshoots in the sensor responses, as explained in Section 7.1.2 were observed (Figure 9.12). This fact indicates that the swelling rate of the CAB coating was faster than its relaxation rate and the sensors could not exactly follow the change in relative humidity due to the slower relaxation rate. They are much pronounced in case of higher humidity levels but slightly decrease with the polymer thickness. To obtain monotonic responses, a suitable polymer having either slower absorption rate or faster relaxation rate should be employed.

9.4.2 | Static response

Static response of each sensor was also measured (Figure 9.13). Their responses as a function of relative humidity are linear through the entire range of measurements. The linearity coefficients were 0.997, 0.999, and 0.998, for sensors with one, two and four layers of CAB, respectively. From these linear fits, I obtain 0.9 mV/%RH, 3.2 mV/%RH, and 5.7 mV/%RH. The sensitivity of the two-layer sensor is almost half of that of the four-layer sensor. However, if I compare the values from the one-layer and two-layer sensors, the thickness dependence is hardly observed. This is most likely due to the poor surface coverage of the one-layer sensor with the polymer. A discontinuous layer of polymer is formed, due to some uncoated areas of the membrane, and the surface stress was not generated as much as expected. It corresponds to the situation with a standard deviation of more than 100%. In such extreme condition (yet, it is actually happening in this experiment), the sensor reproducibility may be diminished

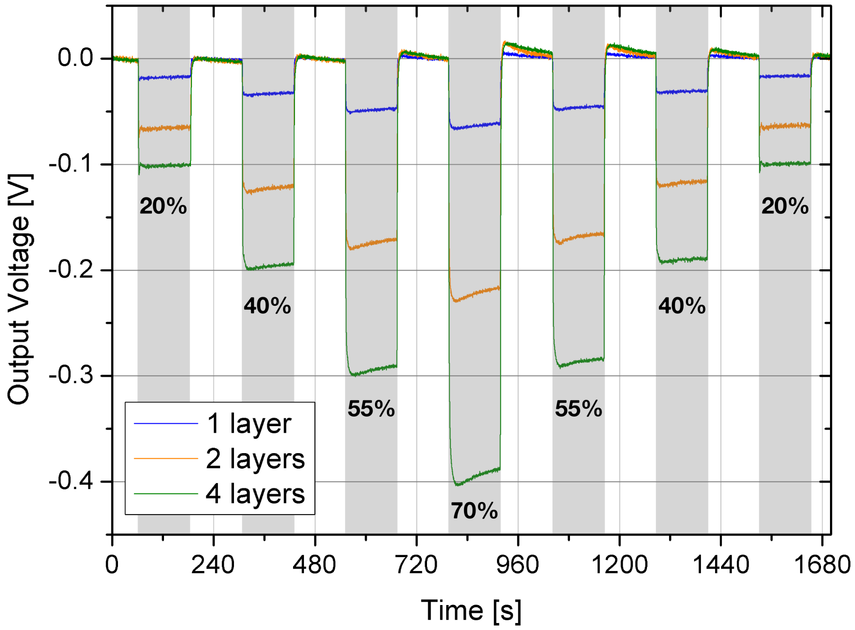

Figure 9.11: Dynamic responses of three MSS coated with one, two, and four layers of CAB. They were exposed to mixtures of dry and wet nitrogen at room temperature (25°C). Cycles of 120 s were performed.

despite its robustness against coatings variations.

Five optimised cantilevers were also coated with four layers of CAB to compare their responses with that of MSS. Because of their sensor-to-sensor variations, the five signals were averaged. Figure 9.14 shows the average static response of the cantilevers compared to that of the MSS. With a sensitivity of 0.76±0.08 mV/%RH, the cantilevers are in average 7.49 times less sensitive. Regarding their reproducibility, standard deviations between 10% and 15%, depending on the humidity level, were obtained. The signal distribution is less spread compared to that obtained during the reproducibility tests. This observation signifies that the deposition of the polymer, based on a grid pattern method (Figure 9.5 A and B), is more reproducible than the second method, where the droplets forms a bigger drop at the centre.

9.5 | Discussions and summary

The characterisation of the MSS and the cantilever platforms was conducted in two phases. First, the sensor-to-sensor repeatability was assessed. I used the Autodrop printing system to dispense a known quantity of Dextran on the MSS and cantilevers. As expected, the cantilevers were not very reproducible. In fact, the distribution of their responses matches that of the polymer patterns presented in section 9.3.1. On the other hand, MSS were much more reproducible despite a similar coating quality. While the latter showed a variability of ≈ 25%,

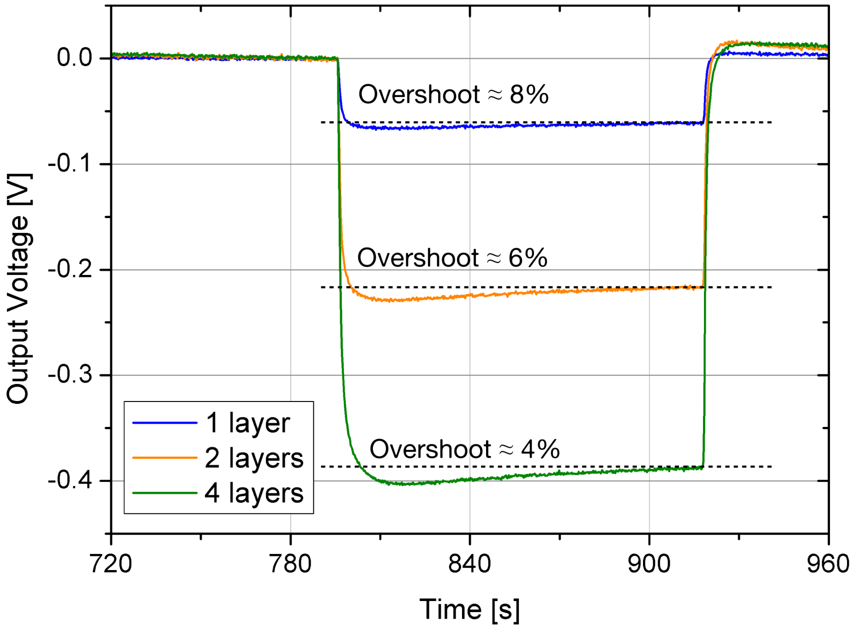

Figure 9.12: Measured overshoots of the three MSS responses for 70% of humidity.

the MSS responses were very similar with a standard deviation of 5.4% only.

These results confirm the findings obtained by FE simulations on sensors reproducibility (section 8.3). In the case of cantilevers, their repeatability is closely related to that of the polymer coating. MSS, however, is a very robust platform against such variabilities. The distinction between the sensing and the transducing parts is instrumental in this robustness. While the piezoresistor in a cantilever measures local stress differences, the MSS hinges detect a global variation and are less impacted by local coating imperfections.

In a second phase, I have presented static and dynamic behaviours of MSS as humidity sensors. CAB was used as the functionalisation layer and showed sub-second absorption rates with slight overshoots. As expected, the responses were linear through the entire humidity range and the sensitivity increases with the polymer layer thickness. Sub-second response times were obtained. As a comparison, the typical response time of commercially available humidity sensors is 8-10 s. Cantilevers were similarly coated and showed a 7.5 times lower sensitivity in average. The simulations predicted however a factor of 15.41 times. The discrepancy is significant but can be counterbalanced with several factors:

1. **Sensor thickness:** While all sensors came from the same SOI wafer, the latter is subject to thickness variations of ± 500 nm according to the manufacturer. Individual measurements showed that the MSS had a thickness of 2.4 μm while the cantilevers measured 2.2 μm. This difference accounts however for only about 10% of the sensitivity.
2. **Heavily doped zones:** The latter are supposed to considerably decrease the negative

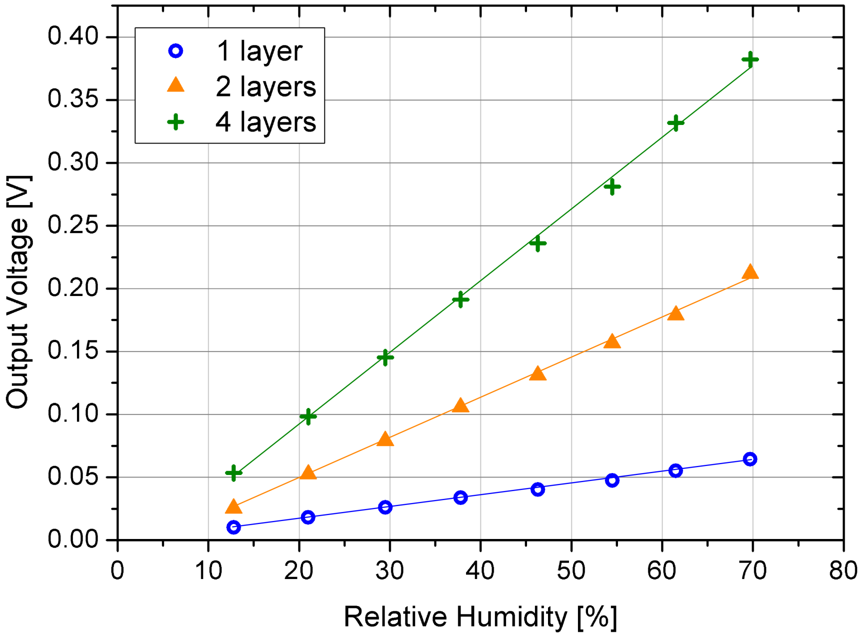

Figure 9.13: Static responses of three MSS coated with one, two, and four layers of CAB. They are linear through the measurements range between 12% and 70% of humidity.

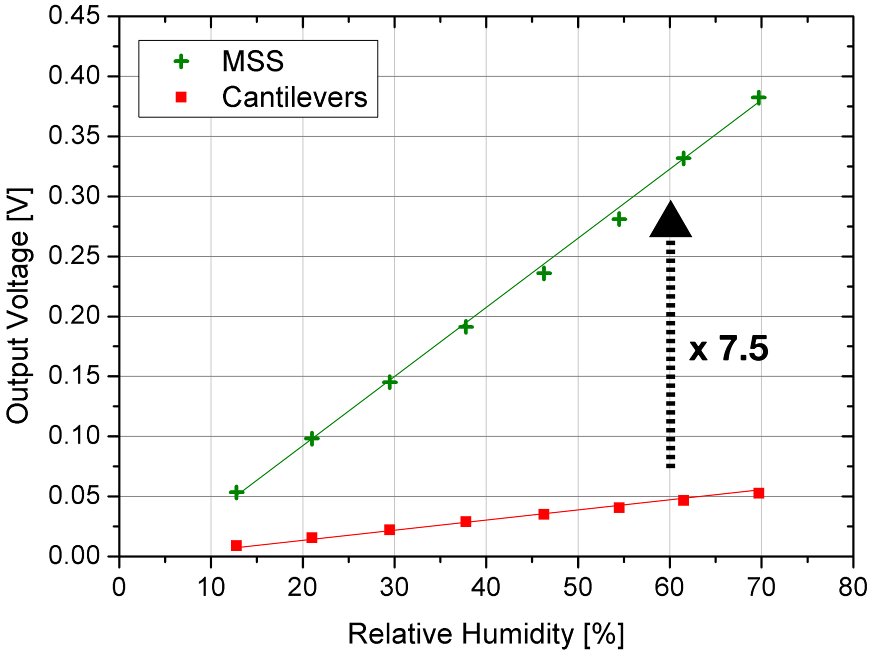

Figure 9.14: Average static response of five cantilevers compared to that of the MSS. All sensors were similarly coated with four layers of CAB.

contributions of the resistor elements, e.g. U-turns. In the simulations, such zones were not implemented. Based on stress mapping results, it can be observed that the negative contributions are more significant in the cantilever design compared to the MSS. Hence, the sensitivity of the cantilever design was underestimated by the simulation.

3. **Coating thickness:** Due to the coffee ring effect, the polymer layer is not homogeneous and tends to be thicker at the periphery. Since the piezoresistor is situated near the clamping edge of the cantilever, the polymer layer situated above is certainly thicker and induces a larger surface stress. Based on the large thickness dispersion previously observed, this factor is probably the major source of difference between the simulations and the experimental results.

In a nutshell, the fabricated MSS showed fast and linear responses. Their sensitivity outperformed that of optimised cantilever-based sensors. Moreover, they are much more robust against coating variabilities. Hence, their sensor-to-sensor reproducibility is very good. Finally, these experimental results confirmed half of those obtained by the FE simulations. While the reproducibility results were in good agreement, the sensitivity comparison was significantly overestimated by the simulations. Several factors were identified as probable causes.

9.6 | Characterisation outlook

During this characterisation, I have focused on the repeatability and the sensitivity comparison between MSS and cantilever-based sensors. The limit of detection was however not investigated, despite its importance. The main reason for this omission is that it was not possible to extrapolate the surface stress created by the polymer swelling. Experimentally first, a gas chamber with an transparent window was built to measure the membrane deflection by white light interferometry. The polymer coating prevented however a good reflection and the measurements were not conclusive. In theory, a surface stress value could also be extrapolated from the polymer characteristics. The lack of information on the hygroscopic strain of CAB and Dextran, as well as the non-uniformity of their deposition, prevents me from providing a surface stress value sufficiently precise to draw any conclusion. The simulations provided a limit of detection of 1.62 mN/m but this absolute value depends eventually on the fabrication process parameters.

The MSS limit of detection could however be easily determined by other experiments with known surface stress. Chemical reactions, such as DNA hybridisation or antigen-antibody bindings have, for instance, defined surface stress values that depend entirely on the chemistry [265, 266]. As the next generation of MSS has been designed towards liquid experiments, it will be possible to assess the minimum detectable surface stress of this platform.

10 || Cancer diagnosis via breath analysis

So far, the MSS platform has been characterised as a humidity sensor. Coated with CAB, it showed linear responses with sub-second time constants. In term of sensitivity, it outperformed optimised cantilevers similarly fabricated. Its most distinguishable feature remains however its high sensor-to-sensor reproducibility, which makes it very competitive against other molecular detection schemes.

In this chapter is presented a possible application of the MSS as a PoC device. It has been integrated in an electronic nose system as a cancer diagnostic tool via the analysis of breath samples only. All the results and the setup picture presented in this chapter were kindly provided by Dr. Hans Peter Lang from the University of Basel (UniBas).

10.1 | Introduction

As discussed in Section 6.3, it is established that many tumours produce VOCs in types and concentrations that differ from their corresponding healthy tissue. A portable electronic nose, with a built-in library of scents, could therefore serve as a convenient and rapid screening tool for these cancers. However, the inherent limitations of electronic noses prevent them from specifically recognising a particular VOC in a complex mixture of gases. False positives or false negatives, e.g. influence of humidity, could also arise as the functionalisation layers used in electronic noses are only partially specific. A special care should therefore be taken during the breath sampling and analysis to prevent external influences and cross-talks.

Previous studies on cancer screening focused on the differentiation between two groups, healthy and unhealthy. The effect of external parameters, such as drug treatments, food, or smoking habits, were then ruled out with correlation statistics [207]. Another method that was, as far as I know, never pursued, is to add a third group composed of breath samples from the same unhealthy donors once their tumour has been removed. Hence, the initial difference between the healthy and the unhealthy groups should normally disappear together with the cancer removal. If not, the differentiation is due to other factors. This strategy has been chosen for the following study.

In collaboration with the University Hospital of Lausanne (CHUV), a double-blind clinical trial was conducted with patients suffering from head-and-neck cancer (head and neck squamous cell carcinoma, HNSCC). As this tumour is located in the respiratory system, a simple breath sample should suffice to collect its VOCs. The choice of this particular cancer lies also in its removal procedure. Indeed, surgical ablation is usually the standard procedure and neither radiotherapy nor chemotherapy, which could have an influence on the exhaled breath composition, is required.

10.2 | Methods

10.2.1 | Breath sampling

Breath samples were taken from patients suffering from head-and-neck cancer (head and neck squamous cell carcinoma, HNSCC) before and after the surgical removal of the tumour. The patient inclusion criteria was based on histologically confirmed tumour at a comparable stage. All patients were of the same age group. Breath samples were also taken from healthy donors of the same age group and having a similar way of living, e.g. all were smokers. Patients and donors were asked to breathe into a 1l Tedlar bag (purchased from Celscientific) on an empty stomach. The bags were then stored at 4°C until analysis.

10.2.2 | Setup

The setup is composed of a gas chamber that contains the MSS array and its amplification stage, two gas inputs independently controlled by mp6 micropumps from Bartels, and data acquisition card. All these components fit in a portable metallic box and are USB-powered from a laptop (Figure 10.1). The Tedlar bag containing the breath sample to be analysed is connected to one inlet while a second one filled with nitrogen is connected to the other. Knobs situated on the metallic box control the micropumps for the injection and purge cycles.

The eight MSSs within the array were coated with polymers empirically selected by Dr. Lang for their affinity towards VOCs influenced by head-and-neck tumours. The polymer list is: Carboxymethyl cellulose (CMC), polyethylene glycol (PEO), polyethylene glycol methyl ether methacrylate macromer (PEGMEMA), hydroxypropyl cellulose (HPC), poly(acrylic acid) (PAA-AA), poly(vinylpyridine) (PVPy), butyl rubber (PIB), and polyethylenimine (PEI).

Each breath sample was then pumped into the chamber at a constant flow rate of ≈ 15 ml/min for 30 seconds and then purged with nitrogen for another 30 seconds. Six injections were performed and recorded for each breath sample (Figure 10.2).

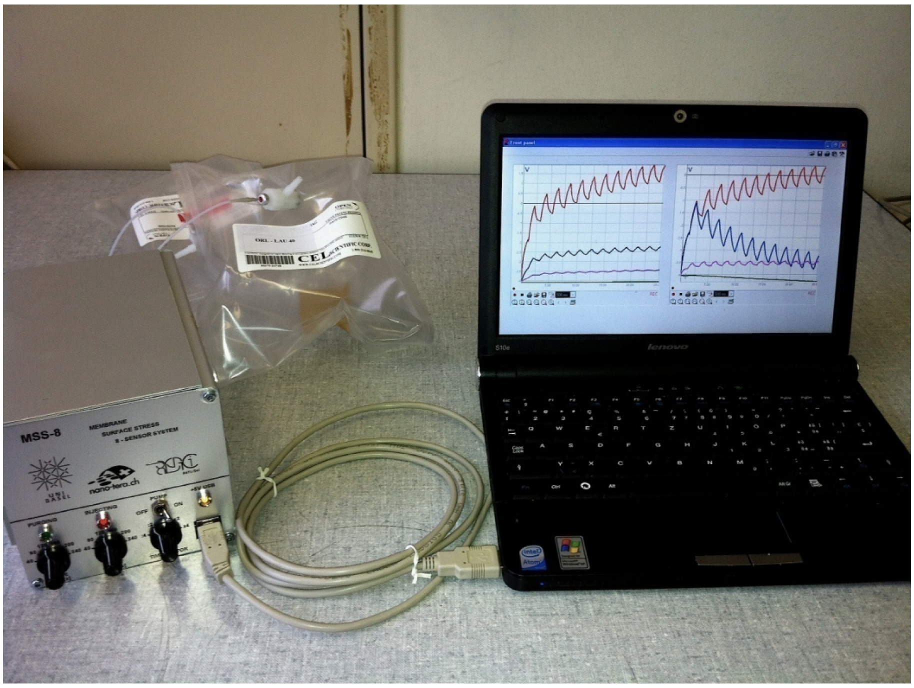

Figure 10.1: Portable USB-powered setup for mobile characterization of patients' breath samples using polymer-coated membrane surface stress sensors. Two Tedlar bags are connected at the rear of the metallic box.

10.2.3 | Data analysis

Once recorded, the fingerprints have to be converted to interpretable data. As discussed in section 7.1.2, both the absorption rate and absolute swelling are required to distinguish the gas mixtures. For each polymer curve of every breath sample, points are retrieved at various intervals (Figure 10.3 A). A matrix M of dimensions ixj, or dataset, comprises the different values as follows:

$$[M] = \begin{pmatrix} m_1 \\ m_2 \\ \dots \\ m_i \end{pmatrix} = \begin{pmatrix} A_{11}-A_{10} & A_{12}-A_{10} & \dots & A_{1j}-A_{10} & B_{11}-B_{10} & \dots & H_{1j}-H_{10} \\ A_{21}-A_{20} & A_{22}-A_{20} & \dots & A_{2j}-A_{20} & B_{21}-B_{20} & \dots & H_{2j}-H_{20} \\ \dots & \dots & \dots & \dots & \dots & \dots & \dots \\ A_{i1}-A_{i0} & A_{i2}-A_{i0} & \dots & A_{ij}-A_{i0} & B_{i1}-B_{i0} & \dots & H_{ij}-H_{i0} \end{pmatrix} \tag{10.1}$$

where $A-H$, are the eight polymer curves, $j+1$ is the number of points taken per curve, and $i=6n$ where n is the number of breath samples (6 injections per sample). Figure 10.3 B displays the data of such a dataset for an array of two polymers and two injections when four points are taken from each curve.

The differential measurements between the points compensate possible drifts between injections. Ideally, injections of a particular breath sample should produce similar vectors m. In reality, small variations may appear due to pressure differences during the emptying of the

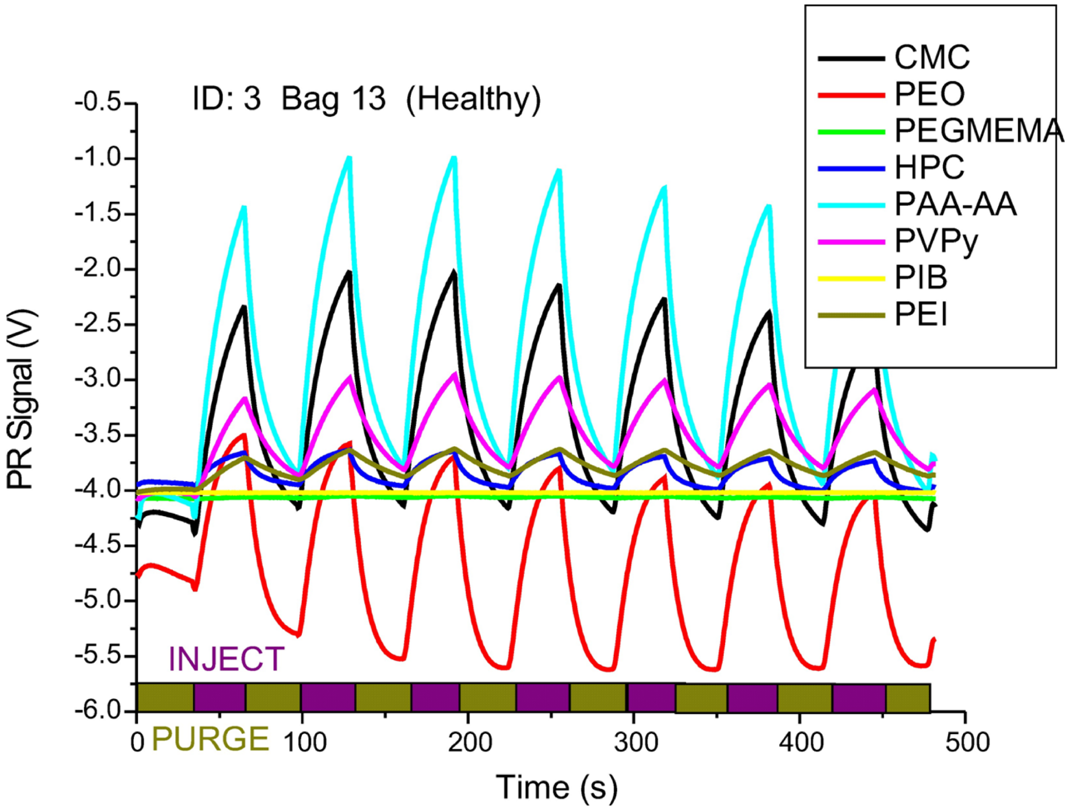

Figure 10.2: Typical "fingerprint" of a breath sample obtained by recording the absorption and desorption responses of the MSS array. 6 injections are recorded for each sample.

bags.

Once the dataset has been built, it contains the fingerprints of all breath samples. One has to find ways of (i) highlighting their differences and (ii) grouping the samples into viewable clusters, i.e. healthy vs. sick. This is done with clustering analysis. From the existing statistical clustering algorithms, principal component analysis (PCA) and hierarchical tree analysis were chosen for this study.

Principal component analysis

PCA is defined as a change of the current dataset space to a new one, which maximises its variance (σ^2). To illustrate this method, one can compare it to a photographic challenge: during a visit of the city of Sydney, I would like to take a picture of its opera house. If I consider that I can move freely around this monument, which angle will show the most details about it? Figure 10.4 shows several views of the Sydney opera house and, clearly, Figure 10.4 D is the best angle option. This shot provides the most information about a three-dimensional object in a two-dimensional projection. Similarly, PCA orients a dataset of dimension N and project it into a new space of dimension 2 or 3, which yields the greatest information, i.e. variance.

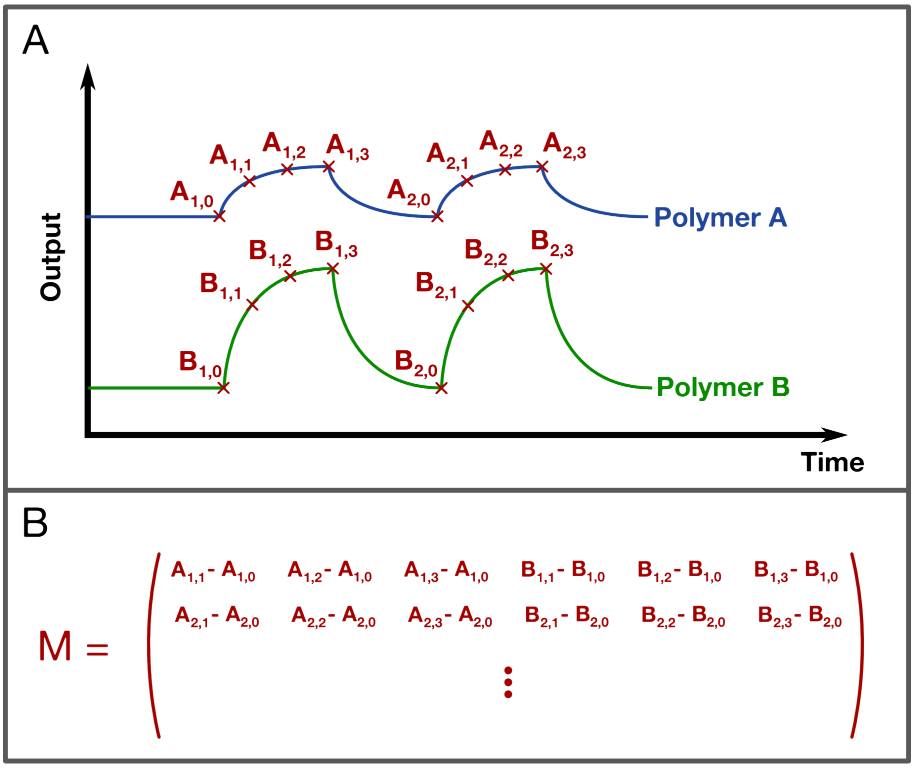

Figure 10.3: (A) Dynamic responses of two sensors coated with polymers A and B. (B) Four points are retrieved from each injection to populate the data matrix M. One line corresponds to a single injection.

Mathematically, this requires first to calculate the covariance matrix of the matrix M and retrieve its eigenvectors. The latter are called the PCA axes and serve as the new coordinate system to project the data.

Hierarchical tree analysis

In a hierarchical tree analysis, the data are separated by pairing each vector of the dataset M together with its closest neighbour. Then, the second closest vector is linked to this initial cluster, and so on, until all the vectors are incorporated. A tree representation is then plotted, from the initial ramifications to the last bifurcations. Clusters are then identified depending on the latter.

The distance between two vectors can be defined with the Euclidean distance:

$$d = \|a - b\| = \sqrt{\sum_{k=1}^{i} (a_k - b_k)^2} \tag{10.2}$$

where a_k and b_k are the k-th elements of vectors a and b, respectively, and i is their length. This distance quantifies the difference between two vectors.

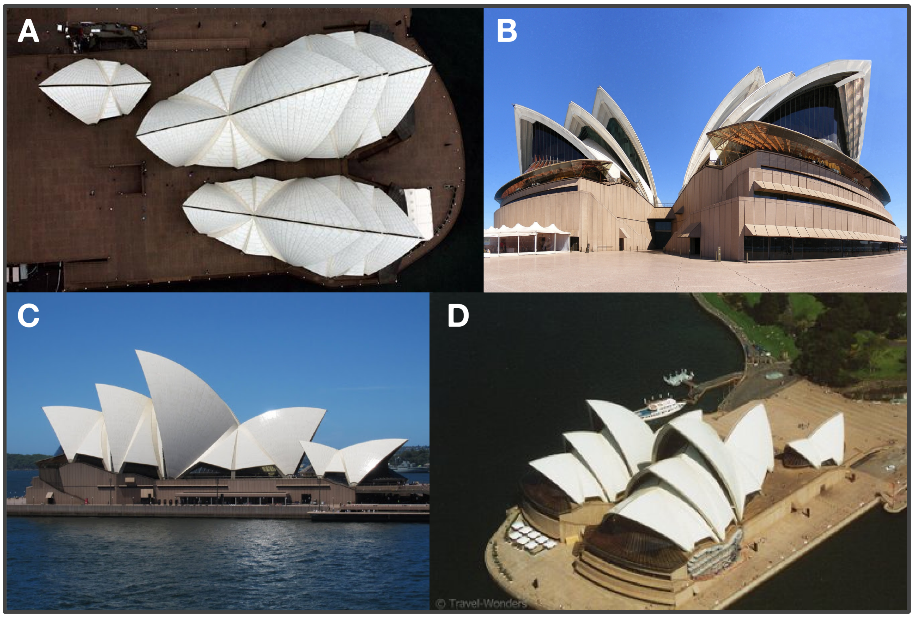

Figure 10.4: Sydney opera house from different angles. View D shows the most information about the 3D shape of the monument. PCA works in a similar way for data clustering analysis.

10.3 | Results and discussions

Figure 10.5 shows the PCA results for a dataset composed of three samples of patients before surgery, the same three after surgery, and four samples from healthy patients. Each point represents one vector of the dataset. There are six points per sample, one for each injection. Ideally, the six points should be at the same position in the PCA graph. First of all, there is a clear distinction between pre-surgery and healthy samples. This electronic nose has been able to differentiate breath from cancer patients from those of healthy persons. Second, the points corresponding to breath from post-surgery patients are at a similar location as those from the healthy persons. This result indicates (i) that the initial difference measured with the electronic nose was due to the presence of the tumour and (ii) that the removal of the tumour has been successful.

The same set of breath samples was analysed with a hierarchical tree method (Figure 10.6). The tree diagram (dendrogram) shows bifurcations for distinct distances between pairs of measurements. First, the bifurcation distance between cancerous and healthy samples is clear. Second, the samples taken after surgery are mixed with the healthy ones. Hence, it is not possible to distinguish the two clusters from a hierarchical tree analysis.

From this initial study, the performance of the MSS sensor has been demonstrated. Compared to previously published studies on cancer detection by breath analyses [267, 147], the duration of this trial (three months) allows measuring and comparing breath samples at radically different stages, i.e. before and after surgery. No drift was experienced during that time and the three sets of breath samples were successfully identified. The fact that the post-operation samples are mixed with the healthy ones clearly suggests that the initial difference was due to the tumour itself and not to any parasitic effect.

The small number of samples limits however this study to promising but preliminary conclusions. As additional samples may increase the dispersion and, hence, the size of the clusters, the distinction may not be as clear in case of cluster overlaps. The next phase of this trial is to collect 30 breath samples from each group to increase the confidence of the results.

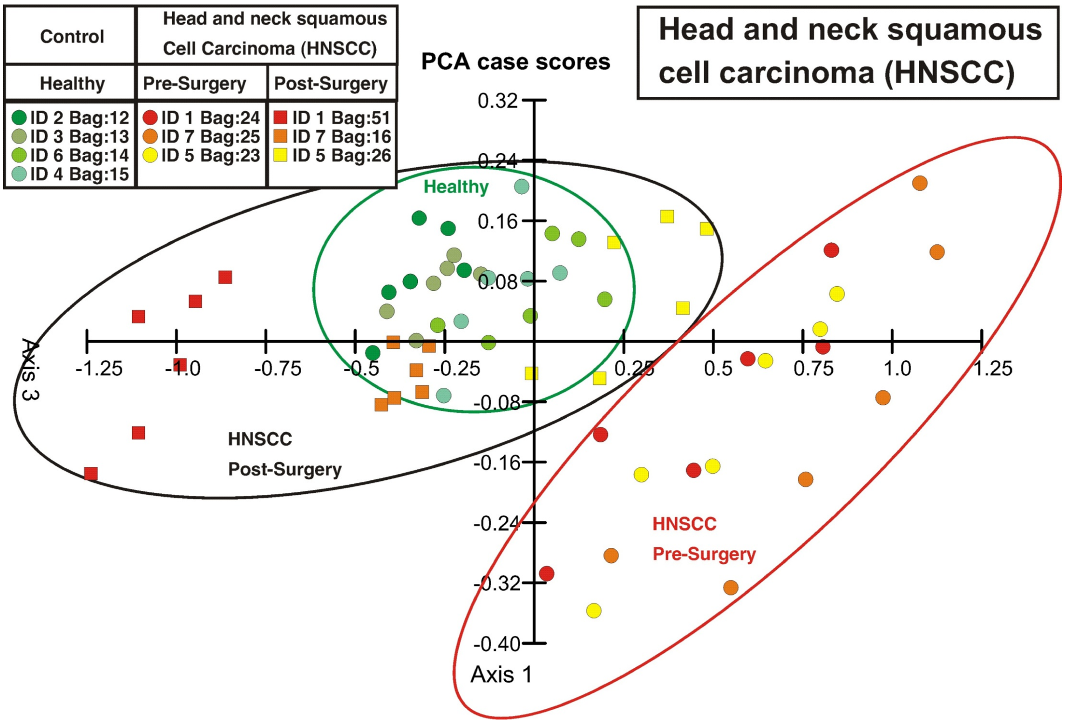

Figure 10.5: Principal Component Analysis plot showing three distinct clusters (indicated with ellipses) that represent healthy control persons, HNSCC patients before surgery and HNSCC patients after surgery, i.e. after removal of the tumour by operation.

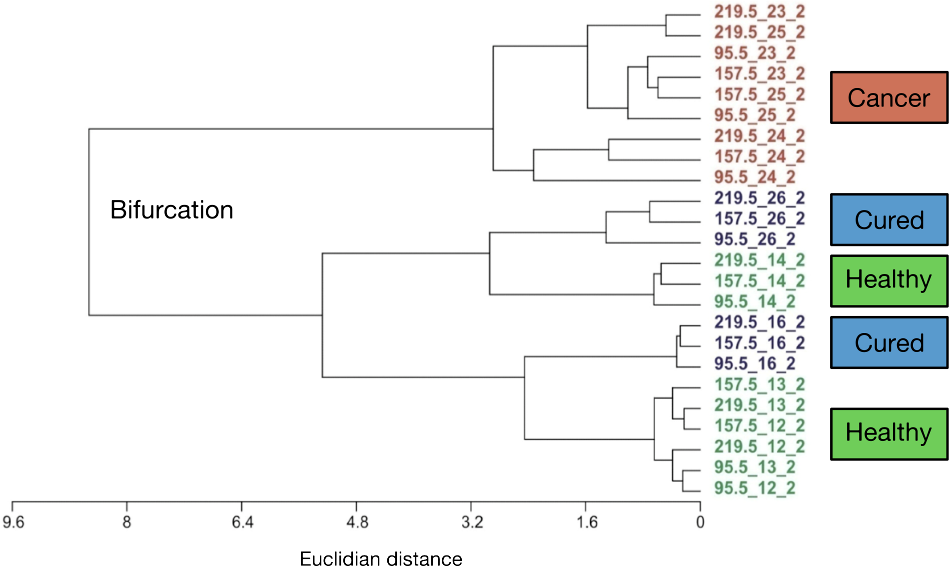

Figure 10.6: Hierarchical cluster analysis using the Euclidean distance as a classification.

11 || Conclusion and outlook

11.1 | Conclusion

In the next five to ten years, point-of-care (PoC) systems are expected to create an exciting new paradigm in health care services. In cancer therapy, these devices could serve as early and convenient screening tools for a wide range of cancers. Eventually, they will also allow following the evolution of the tumour state with a cartridge and a simple drop of blood. The treatments could be rapidly and smoothly adapted in consequence. Hence, cancer patients would probably see their life expectancy extended and their quality of life would definitely increase.

The central part of PoC devices lies in the sensor technology. Ideally, it has to be highly sensitive, real-time, and reliable. Unlike the current gold standards of molecular detection, PoC systems are required to fit in the pocket and be affordable. Many current research programs in academics but also in industry are converging towards these goals. Cantilever-based surface stress sensors have been, for more than a decade, a promising technology for molecular detection. Despite their competitive performances in term of portability and sensitivity, these sensors are still in the shadow of other platforms due to their mediocre reproducibility.

In this second part of my thesis, I have presented the development of a membrane-type surface stress sensor (MSS) with piezoresistive readout, as initially proposed by Yoshikawa et al. [260]. Unlike the cantilever platform, the sensing and transducing elements are distinct. The MSS benefits also from a full Wheatstone bridge configuration. Compared to a standard cantilever-based sensor, these two key aspects help to increase the sensitivity while reducing the thermal drift. More importantly, I have demonstrated that the decoupling of the sensing parts (the hinges) from the transducing element (the membrane) significantly increases the MSS robustness to the variability of the functionalisation layer. While the reproducibility of cantilevers is closely correlated with that of their coating, the MSS were five times less sensitive to the same coating variability. These experimental results were confirmed by finite element simulations. The high sensor-to-sensor reproducibility, combined with a sub-second response time and linear behaviour, makes the MSS a powerful platform for molecular detection.

The potential of this sensor was revealed with its integration into an electronic nose device specially developed for cancer diagnostics. An array of eight MSSs, each of them being functionalised with a different polymer, was used to collect the "fingerprints" of breath samples from both sick and healthy donors. In this double-blind clinical study, it was possible to differentiate the two groups. The setup, developed by the University of Basel, was portable and USB-powered. Moreover, its stability allowed conducting the trial for more than three months without any drift.

11.2 | Future developments

11.2.1 | Finite element simulations

The proposed simulation tool in Chapter 8 has been useful to simulate an actual piezoresistor in a silicon-based sensor. Unlike mechanical-only simulations, the simulated sensitivity and signal-to-noise ratio are not calculated from approximated equations any more. Moreover, I could directly compare the output signals of the modelled sensors. It allowed, for instance, simulating the influence of the coating variability on surface stress sensors.

However, several assumptions were made to simplify the modelling. Process parameters, such as diffusion time or doping profile, were not taken into account and the additional noises from the piezoresistor self-sensing were not considered. Implementing these effects in the existing modelling script would improve its accuracy and probably yield additional design guidelines.

Finally, even a model as simple as a cantilever has many parameters to take into account during its optimisation. In the case study presented in Section 8.2, some of them were constrained. Hence, the sensors were optimised under a few defined conditions. Optimisation strategies, such as genetic algorithms or design of experiments, could be implemented to efficiently approach the optimum sensor.

11.2.2 | Applications in gaseous phase

The electronic nose concept can be adapted for numerous applications. Beside the diagnosis of cancer, we recently started a collaboration with the Laboratory of Fundamental and Applied Research in Chemical Ecology from the University of Neuchâtel with the goal of detecting VOCs emitted by plants. It has been shown that some plants, such as maize, produce VOCs while they are being attacked by an insect or a fungus [268]. The released chemicals attracted then other organisms, which have an aggressive behaviour towards the initial attacker and protect the plant.

The real-time monitoring of VOCs in a maize field could therefore help farmers managing their cultures and deciding of an appropriate action. Increased yield and reduced used of insecticide can be expected from such a strategy.

11.2.3 | Applications in liquid phase

The MSS has even more potential in liquid applications. As a molecular sensor, DNA or antigens could be specifically detected on its surface. While the electronic nose suffers from heavy limitations, e.g. molecular cross-talk or comparative results only, these reactions are highly selective. Cross-talk and false positives are significantly reduced while the data analysis is simplified.

In addition, the piezoresistive readout allows analysing opaque samples, such as whole blood. This is usually impossible for sensing platforms with an optical readout for which blood serum has to be prepared prior to the analysis. Piezoresistors allow as well miniaturising the whole setup, which is hardly feasible with current optical-based solutions.

Within the PATLiSci framework, the University of Basel has recently detected cancerous mutations of total RNA from melanoma cells using cantilever arrays [269]. The deflection of the cantilevers were measured optically. We plan to use the MSS platform for a similar experiment to compare its performances in liquid media with state-of-the-art optical cantilevers. In addition, as the hybridisation of this particular RNA has been quantified, we will be able to define the MSS limit of detection, which could not be assessed experimentally during this thesis.

Thesis conclusion

More than 200 years ago, aristocrats from all over Europe discovered Pierre Jaquet-Droz's automata with excitement and probably also some fear in their eyes. Although these dolls were only composed of metals, glasses, and fabrics, they were seen as magical and mysterious. When my friends learnt that I was helping to develop breathalysers for cancer detection, I could see similar expressions of surprise and suspicion on their faces. Yet, silicon and polymers replaced metal and fabrics, and no magic lies under the metallic box. While the results presented in this thesis are promising, there are still many challenges to overcome until everyone could breathe on their smartphone to check their health. Reliability, cost, but also the psychological impact of such devices on our daily life still need to be assessed and understood.

Nevertheless, I have presented and discussed how microfabricated sensors could advantageously drive cancer research, but also life sciences in general, forward. According to the numerous laboratories and research centres in the world that combine MEMS and biology, the potential applications, from electronic skin to molecular transistors, are almost unlimited and will probably only dry out together with the imagination of researchers.

At a more personal level, I have taken tremendous pleasure in working on this project. With two sub-tasks running in parallel, I never had time to get bored and plenty of it was spent in the cleanroom. Initially, four complete process flows were planned along the duration of the project. While I often had to deal with time constraints, three batches were delivered on time to our partners who could use them as highlighted in this thesis. Since the first MSS generation worked already very well, we could delay the second generation, which is currently being finalised and planned to be used for liquid applications.

A || Spring constant calculations

A.1 | Slitted cantilever

Figure A.1 shows the model of a slitted cantilever (top and side views) with its dimensions. In order to calculate its spring constant, one can divide it in three sections with distinct moments of inertia. It suffices then to calculate its deflection z upon a force F to retrieve its spring constant. The cantilever is modelled as an Euler-Bernoulli beam, i.e. small deflections only and shear deformations are negligible.

The bending moment of any beam is given by:

$$M(x) = -EIz''(x) \tag{A.1}$$

where z(x) is its z-deflection, E is its Young's modulus , and I is its cross-sectional moment of inertia. One can write this equation, as well as its first and second integrals, for each section of our beam.

For $0 < x < a$:

$$EI_1 z_1''(x) = -F(L_c - x) \tag{A.2}$$

$$EI_1 z_1'(x) = -FL_c x + \frac{Fx^2}{2} + A_1 \tag{A.3}$$

$$EI_1 z_1(x) = -\frac{FL_c x^2}{2} + \frac{Fx^3}{6} + A_1 x + A_2 \tag{A.4}$$

For $a < x < b$:

$$EI_2 z_2''(x) = -F(L_c - x) \tag{A.5}$$

$$EI_2 z_2'(x) = -FL_c x + \frac{Fx^2}{2} + B_1 \tag{A.6}$$

$$EI_2 z_2(x) = -\frac{FL_c x^2}{2} + \frac{Fx^3}{6} + B_1 x + B_2 \tag{A.7}$$

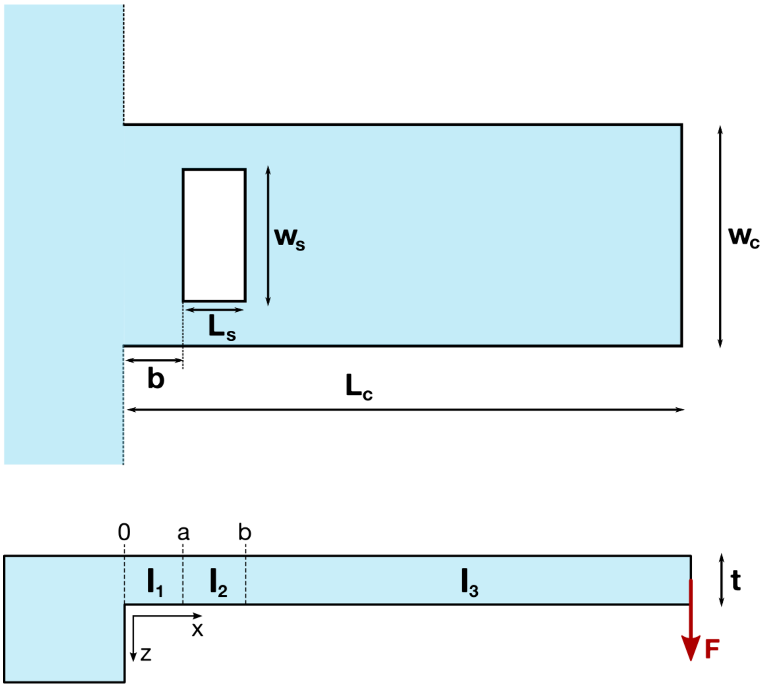

Figure A.1: Top and side views of a slitted cantilever.

For $b < x < L_c$:

$$EI_3 z_3''(x) = -F(L_c - x) \tag{A.8}$$

$$EI_3 z_3'(x) = -FL_c x + \frac{Fx^2}{2} + C_1 \tag{A.9}$$

$$EI_3 z_3(x) = -\frac{FL_c x^2}{2} + \frac{Fx^3}{6} + C_1 x + C_2 \tag{A.10}$$

As these equations describe the same beam, six boundary conditions apply, from which the terms A_1, A_2, B_1, B_2, C_1, and C_2 can be calculated:

$$z_1'(0) = 0 \qquad z_1(0) = 0$$

$$z_1'(a) = z_2'(a) \qquad z_1(a) = z_2(a)$$

$$z_2'(b) = z_3'(b) \qquad z_2(b) = z_3(b)$$

With all terms known, the z-deflection at the end of the beam is:

$$z_2(L_c) = \frac{FL_c^3}{3EI_3} + \frac{Fa}{E}\left(\frac{1}{I_1} - \frac{1}{I_2}\right)\left(\frac{a^2}{3} - aL_c + L_c^2\right) + \frac{Fb}{E}\left(\frac{1}{I_2} - \frac{1}{I_3}\right)\left(\frac{b^2}{3} - bL_c + L_c^2\right) \tag{A.11}$$

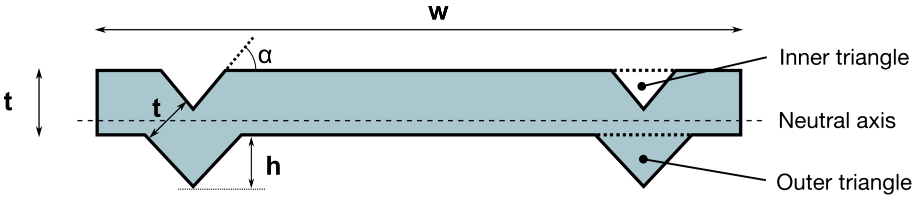

Figure A.2: Cross-section of a cantilever with two V-grooves.

In the case of a slitted cantilever, I_1 and I_3 correspond to the moment of inertia of the plain cantilever while I_2 corresponds to that of the slit:

$$I_1 = I_3 = \frac{w_c t^3}{12} \tag{A.12}$$

$$I_2 = \frac{(w_c - w_s)\, t^3}{12} \tag{A.13}$$

The cantilever spring constant can finally be calculated by dividing the force F by its z-deflection $z_2(L_c)$:

$$k = \frac{1}{\frac{L_c^3}{3EI_3} + \frac{a}{E}\left(\frac{1}{I_1} - \frac{1}{I_2}\right)\left(\frac{a^2}{3} - aL_c + L_c^2\right) + \frac{b}{E}\left(\frac{1}{I_2} - \frac{1}{I_3}\right)\left(\frac{b^2}{3} - bL_c + L_c^2\right)} \tag{A.14}$$

Figure 2.2 shows the spring constant calculations of silicon nitride cantilevers with various slit dimensions based on the above equation.

A.2 | Cantilever with V-grooves

The cantilever with integrated V-grooves is treated slightly differently. Again, the Euler-Bernoulli beam theory is chosen to calculate its spring constant. Unlike the slitted cantilever, the moment of inertia I is constant along the cantilever. Hence, its deflection at the end can be calculated from the following equation:

$$z(L_c) = \frac{FL_c^3}{3EI} \tag{A.15}$$

The moment of inertia I is however unknown due to the introduced V-grooves. Figure A.2 shows a cross-sectional view of a cantilever with two V-grooves as modelled in this analytical calculation. The thickness of the cantilever is kept between the flat portions and the V-grooves.

The cantilever cross section can be separated in simpler shapes: a rectangle of area $w_c t$, two inner triangles $(w_i h_i/2)$, and two outer triangles $(w_o h_o/2)$. The cantilever moment of inertia can be calculated from these shapes:

$$I = I_r + N(I_o - I_i) \tag{A.16}$$

where I_r is the moment of inertia of the rectangle, I_o and I_i is that of the outer and inner triangles, and N is the number of V-grooves. Since the different sections are not centred with the neutral axis of the beam, their moments of inertia have to be calculated with the Steiner theorem, also known as parallel axis theorem:

$$I_x = I'_x + d^2 A \tag{A.17}$$

where I_x is the moment of inertia of any section in relation with the neutral axis, I'_x is its moment of inertia calculated as if the neutral axis were centred with the section, d is the distance between the section centre and the neutral axis, and A is the area of this section.

The neutral axis should be placed in t/2 but the V-grooves introduce a shift. Its new position is given by the centre of mass of the system:

$$\begin{aligned} \delta &= \frac{1}{A_r}\iint z dx dz + N\frac{1}{A_i}\iint z dx dz - N\frac{1}{A_o}\iint z dx dz && \text{(A.18)} \\ &= \frac{w_c t^2 + t w_i \tan\alpha + \frac{1}{6}\tan^2\alpha (w_o - w_i)^3}{2 t w_c + N(w_o - w_i)^2} && \text{(A.19)} \end{aligned}$$

where δ is the neutral axis position from the origin, A_r is the rectangle area, A_i is the inner triangle area, and A_o is the outer triangle area. The three moments of inertia become:

$$I_r = \frac{w_c t^3}{12} + t w \left(\delta - \frac{t}{2}\right)^2 \tag{A.20}$$

$$I_o = \frac{w_o t^4 \tan^3\alpha}{288} + \frac{w_o t^2 \tan\alpha}{4}\left(\delta - \frac{w_o \tan\alpha}{6}\right)^2 \tag{A.21}$$

$$I_i = \frac{w_i t^4 \tan^3\alpha}{288} + \frac{w_i t^2 \tan\alpha}{4}\left(t - \delta + \frac{w_i \tan\alpha}{6}\right)^2 \tag{A.22}$$

I have supposed that the layer deposition is conformal. Its thickness is constant both in the flat areas and in the V-grooves. Consequently, the inner triangles are slightly smaller than the inner ones. Their width w_i is fully defined by that of the outer triangles and by α:

$$w_i = w_o - 2t\left(\frac{1}{\cos\alpha} - 1\right)\frac{1}{\tan\alpha} \tag{A.23}$$

Finally, the cantilever spring constant is calculated from equation A.15:

$$k = \frac{3EI}{L_c^3} \tag{A.24}$$

Figure 2.3 shows the spring constant calculations of silicon nitride cantilevers with various V-grooves numbers and dimensions. α has been set to 54.74° for the KOH etching.

B || 2D cantilever array fabrication

The fabrication of the 2D cantilever arrays is presented in detailed in the following table. It shows the steps that were designed and followed for the second generation of cantilevers, those with the spherical tips. This process uses two <100> wafers of thickness 300 μm and 390 μm for the mould and frame, respectively. Each step is designed either for the mould wafer (M), for the frame (F), or for both (B).

Step	Description	Program / Parameters	Target	Remarks
0-B	WAFER PREPARATION			
0.1	Stock out			300 μm wafers for the mould and 390 μm wafers for the frame
0.2	Wafer inspection			
0.3	Standard cleaning	Standard cleaning		
1-M	THERMAL OXIDATION - mask for KOH etching			
1.1	Thermal oxidation	wet oxidation @ 1050°C	200 nm	
2-M	PHOTOLITHOGRAPHY 1 - grooves and alignment tips			
2.1	HMDS	30 minutes at 150°C		Wafer dehydration and surface functionalization
2.2	PR spinning	Standard 1518 / 40s @ 4000 rpm	1.8 μm	
2.3	PR soft bake	60s @ 100°C		
2.4	Mask illumination	Hard Contact	40 mJ	
2.5	PR development	AZ351 + DI water (1:4) during 60s		
2.6	PR postbake	60 min @ 85°C		
3-M	GROOVES AND ALIGNMENT TIPS STRUCTURATION			
3.1	RIE of silicon oxide		200 nm	
3.2	PR stripping	30 minutes in oxygen plasma		Acetone and IsoP before plasma
3.3	KOH etching	KOH 40% @ 60°C, 15 μm/h	40 μm	
3.4	Silicon oxide removal	70 nm per min.	200 nm	
4-M	WAFER OXIDATION - mask for mould etching			

4.1	Standard cleaning	Standard cleaning		
4.2	Thermal oxidation	wet oxidation at 1050°C	200 nm	
5-M	PHOTOLITHOGRAPHY 2 - indentation tips			
5.1	HMDS	30 minutes at 150°C		Wafer dehydration and surface functionalization
5.2	PR spinning	1813 / 40s @ 2500 rpm	1.8 μm	
5.3	PR soft bake	60s @ 100°C		
5.4	Mask illumination	Hard Contact	40 mJ	
5.5	PR development	AZ351 + DI water (1:4) during 60s		
5.6	PR postbake	60 min @ 85°C		
6-M	INDENTATION TIPS ETCHING			
6.1	RIE of silicon oxide		200 nm	
6.2	DRIE of silicon		20 μm	
6.3	PR stripping	30 minutes in oxygen plasma		Acetone and IsoP before plasma
6.4	Silicon oxide removal	70 nm per min.	200 nm	
6.5	Standard cleaning	Standard cleaning		
7-M	MOULD ROUNDING			
7.1	Thermal oxidation	wet oxidation at 1050°C	2’000 nm	first oxidation
7.2	Silicon oxide removal	70 nm per min.	2’000 nm	
7.3	Standard cleaning	Standard cleaning		
7.4	Thermal oxidation	wet oxidation at 1050°C	2’000 nm	second oxidation
7.5	Silicon oxide removal	70 nm per min.	2’000 nm	
7.6	Standard cleaning	Standard cleaning		
7.7	Thermal oxidation	wet oxidation at 1050°C	2’000 nm	third oxidation, expected radius of curvature: 4 μm
7.8	Silicon oxide removal	70 nm per min.	2’000 nm	
7.9	Standard cleaning	Standard cleaning		
7.10	Thermal oxidation	wet oxidation at 1050°C	200 nm	oxide protective layer for the cantilevers
8-M	SILICON NITRIDE DEPOSITION			
8.1	SiNx deposition	Low stress, by LPCVD	350 μm	
9-M	PHOTOLITHOGRAPHY 3 - cantilevers			
9.1	HMDS	30 minutes at 150°C		Wafer dehydration and surface functionalization
9.2	PR spinning	1813 / 40s @ 2500 rpm	1.8 μm	
9.3	PR soft bake	60s @ 100°C		
9.4	Mask illumination	Hard Contact	40 mJ	
9.5	PR development	AZ351 + DI water (1:4) during 60s		
9.6	PR postbake	60 min @ 85°C		
10-M	CANTILEVERS STRUCTURATION			

10.1	RIE dry etching		350 nm	
10.2	PR stripping	30 minutes in oxygen plasma		Acetone and IsoP before plasma
11-F	THERMAL OXIDATION - mask for alignment marks			
11.1	Thermal oxidation	wet oxidation @ 1050°C	200 nm	
12-F	PHOTOLITHOGRAPHY 4 - alignment marks			
12.1	HMDS	30 minutes at 150°C		Wafer dehydration and surface functionalization
12.2	PR spinning	Standard 1518 / 40s @ 3000 rpm	2.2 μm	
12.3	PR soft bake	60s @ 100°C		
12.4	Mask illumination	Hard Contact	40 mJ	
12.5	PR development	AZ351 + DI water (1:4) during 60s		
12.6	PR postbake	60 min @ 85°C		
13-F	MARKS STRUCTURATIONS			
13.1	RIE dry etching		1000 nm	
13.2	PR stripping	30 minutes in oxygen plasma		Acetone and IsoP before plasma
14-F	PHOTOLITHOGRAPHY 5 - backside frame			
14.1	HMDS	30 minutes at 150°C		Wafer dehydration and surface functionalization
14.2	PR spinning	Standard 1518 / 40s @ 4000 rpm	1.8 μm	
14.3	PR soft bake	60s @ 100°C		
14.4	Mask illumination	Hard Contact	40 mJ	
14.5	PR development	AZ351 + DI water (1:4) during 60s		
14.6	PR postbake	60 min @ 85°C		
15-F	FRAME STRUCTURATION			
15.1	RIE dry etching		200 nm	silicon oxide opening
15.2	DRIE dry etching		50 μm	
15.3	PR stripping	30 minutes in oxygen plasma		Acetone and IsoP before plasma
15.4	Standard cleaning	Standard cleaning		
16-F	PROTECTION DURING KOH ETCHING			
16.1	Thermal oxidation	wet oxidation @ 1050°C	500 nm	
16.2	SiNx deposition	PECVD on wafer frontside	300 nm	
17-B	GOLD LAYER FOR THERMO BONDING			
17.1	Piranha cleaning	$H_2SO_4 + H_2O_2$	5 min.	
17.2	Gold deposition	preceded by Cr deposition of 20 nm	500 nm	

18-M	PHOTOLITHOGRAPHY 6 - gold structuration			
18.1	HMDS	30 minutes at 150°C		Wafer dehydration and surface functionalization
18.2	PR spinning	1813 / 40s @ 2500 rpm	1.8 μm	
18.3	PR soft bake	60s @ 100°C		
18.4	Mask illumination	Hard Contact	40 mJ	The vertical alignment will define the final cantilever length
18.5	PR development	AZ351 + DI water (1:4) during 60s		
18.6	PR postbake	60 min @ 85°C		
19-M	GOLD STRUCTURATION			
19.1	Gold etching	Au etch + H_2O (1:2)	5 min.	
19.2	Chromium etching	Cr etch	30 s	
19.3	Pirahna cleaning	H_2SO_4 + H_2O_2	10 min.	
20-B	THERMOCOMPRESSIVE BONDING			
20.1	Pirahna cleaning	H_2SO_4 + H_2O_2	5 min.	to be done right before the bonding
20.2	Bonding	8000 Pa @ 300°C during 2h		
21-B	PHOTOLITHOGRAPHY 7 - KOH release			
21.1	HMDS	30 minutes at 150°C		Wafer dehydration and surface functionalization
21.2	PR spinning	1518 / 40s @ 3000 rpm	2.2 μm	
21.3	PR soft bake	25 min. @ 85°C		Done in the hoven
21.4	Mask illumination	Hard Contact	40 mJ	
21.5	PR development	AZ351 + DI water (1:4) during 60s		Spray development
21.6	PR postbake	60 min @ 85°C		
22-B	KOH RELEASE			
22.1	RIE dry etching	Backside etching	500 nm	silicon oxide and nitride opening
22.2	PR stripping	30 minutes in oxygen plasma		Acetone and IsoP before plasma
22.3	RIE dry etching	Frontside etching	600 nm	silicon oxide and nitride etching
22.4	KOH etching	KOH 40% @ 60°C, 15 μm/h	300 μm	The mould wafer will be completely etched
23-B	FINAL RELEASE AND REFLECTIVE COATING			
23.1	Silicon oxide removal	70 nm per min.	200 nm	
23.2	Gold etching	Au etch + H_2O (1:4)	1 min.	
23.3	Gold coating	4 nm Ti + 40 nm Au		

C || Ansys simulation scripts

```
!____________________________________________________________
!
! Macro to calculate static piezoresistive response of
! a cantilever loaded with a surface stress. The piezoresistor
! is based on a meanders configuration.
! 9 required arguments :
!
!ARG1 : Cantilever Length [um]
!ARG2 : Cantilever Width [um]
!ARG3 : Piezo Length [um]
!ARG4 : Piezo Width [um]
!ARG5 : Meanders number (1,2,3,etc) [um]
!ARG6 : Resistivity [TOhm.um]
!ARG7 : Piezo Coefficient p44 [MPa-1]
!ARG8 : Carriers Density [um-3]
!ARG9 : Thin Film Stress [N/m]
!
!example call from ANSYS apdl command line or /INP,batchfile,inp
!
!Canti_Meanders,120,240,60,5,1,1.96639E-9,144.0005094E-5,1.00E+5,0.1
!
!The macro should be placed in the ANSYS workspace
!
! The results are written in the output file "Cantilever_Results.dat".
!____________________________________________________________
!

finish
/clear,nostart
/FILENAME, PiezoCantilever
/TITLE, Simple 3D-Cantilever with 1 piezoresistance - uMKSV system of units
!______________________________________________
!
! LOAD PARAMETERS
!______________________________________________
!
Vp = 1                  ! applied voltage [V]
!SurfaceStress = 0.1
SurfaceStress = ARG9

!______________________________________________
!
! GEOMETRIC PARAMETERS
!______________________________________________
!
Lc = ARG1   ! Cantilever length
Wc = ARG2   ! Cantilever width
Tc = 3      ! Cantilever thickness

Tp = 0.2    ! Piezoresistance thickness
Wp = ARG4       ! Piezoresistance width
Lp = ARG3       ! Piezoresistance Length
Np = ARG5       ! Number of Meanders

Pitch = 2   ! Pitch between 2 legs
LpEnd = 15  ! Length of the end of the resistance

OffsetP = (Wc-(2*Np*Wp+(2*Np-1)*Pitch))/2

LegsVolume = Lp*Np*Wp*Tp

Tb = 10     ! Bulk thickness
Lb = LpEnd+5

LpStart = 10    ! Start of the resistance

Orientation = -45   ! Cantilever orientation [°]

MeshSide = 1    ! dimension of the resistor meshings [um]
MeshVolume = MeshSide*MeshSide*Tp   ! volume of the resistor elements
```

```
!______________________________________________
!
! NOISES PARAMETERS
!______________________________________________
!
CarriersD = ARG8    ! Carriers density [um-3]   cm-3 => um-3  =  /10e12
HoogeK = 1e-6       ! Hooge's constant      depends on annealing temperature
BoltzK = 1.38e-23   ! Boltzmann's constant
T = 293             ! Temperature [°K]

!______________________________________________
!
! MATERIAL PROPERTIES
!______________________________________________

!  Stiffness,  MPa :  Silicon
!    [c11 c12 c12  0   0  0 ]
!    [c12 c11 c12  0   0  0 ]
!    [c12 c12 c11  0   0  0 ]
!    [ 0   0   0  c44  0  0 ]
!    [ 0   0   0   0  c44 0 ]
!    [ 0   0   0   0   0 c44]

c11= 16.57e4
c12= 6.39e4
c44= 7.96e4

!  Resistivity (p-type Si), TOhm*um => should be varied with impurity concentration
rho = ARG6  ! for a carriers density of 1e18 (Byu clean room website)

!  Piezoresistive coefficients (p-type Si), (MPa)^(-1)
!    [p11 p12 p12  0   0  0 ]
!    [p12 p11 p12  0   0  0 ]
!    [p12 p12 p11  0   0  0 ]
!    [ 0   0   0  p44  0  0 ]
!    [ 0   0   0   0  p44 0 ]
!    [ 0   0   0   0   0 p44]

p11=6.5e-5
p12=-1.1e-5
p44=ARG7        ! for doping concentration 1e18 (paper from Richter 2008)
!______________________________________________
!
! COORDINATE SYSTEMS
!______________________________________________
! ! Specify material orientation
LOCAL,11,,,,,Orientation
WPROTA,Orientation,0,0 ! X-axis along [110] direction. MATERIAL CS
!______________________________________________
!
! ELEMENT TYPES
!______________________________________________
!
/prep7
/UNITS, UMKS        ! units in uMKS
ET,1,solid226,101   ! piezoresistive element type
ET,2,solid186       ! structural element type
ET,3,mesh200,7      !"dummy" mesh of surface of lever
ET,4,surf154,,0     ! element for surface stress coating
!______________________________________________
!
! ANISOTROPIC MATERIAL PROPERTIES
! GENERATE MATERIAL IN CSYS,13
!______________________________________________
!
! Specify material properties:

! Material 1 Properties (p-doped Silicon)
! anisotropic elasticity matrix
```

```
TB,ANEL,1
TBDATA,1,c11,c12,c12
TBDATA,7,c11,c12
TBDATA,12,c11
TBDATA,16,c44
TBDATA,19,c44
TBDATA,21,c44

! piezoresistive stress matrix
TB,PZRS,1,,,,0
TBDATA,1,p11,p12,p12
TBDATA,7,p12,p11,p12
TBDATA,13,p12,p12,p11
TBDATA,22,p44
TBDATA,29,p44
TBDATA,36,p44

! resistivity
MP,RSVX,1,rho
MP,RSVY,1,rho
MP,RSVZ,1,rho

! Material 2 Properties (undoped Silicon)
! anisotropic elasticity matrix
TB,ANEL,2
TBDATA,1,c11,c12,c12
TBDATA,7,c11,c12
TBDATA,12,c11
TBDATA,16,c44
TBDATA,19,c44
TBDATA,21,c44

!______________________________________________
!
! CREATE GEOMETRIES
!______________________________________________
!
CSYS,11
!start from a surface mesh and extrude it
BLC4,0,0,Lc,Wc

BLC4,0,OffsetP+Wp,-Lb,Wc-2*(OffsetP+Wp)
BLC4,0,0,-LpStart,OffsetP+Wp
BLC4,0,Wc,-LpStart,-OffsetP-Wp
BLC4,0,OffsetP,-LpStart,Wp
BLC4,0,Wc-Offsetp,-LpStart,-Wp
*IF,Np,GT,1,THEN
    BLC4,-LpEnd,OffsetP+Wp,-(Lb-LpEnd),(2*Np-1)*Pitch+(2*Np-2)*Wp
*ENDIF
BLC4,0,0,Lp,OffsetP
BLC4,0,Wc,Lp,-OffsetP
BLC4,Lp+LpEnd,0,Lc-Lp-LpEnd,Wc


OffsetLeg = OffsetP
*DO,i,0,2*Np-1,1          ! create the Meanders areas
    BLC4,0,OffsetLeg,Lp,Wp
    OffsetLeg = OffsetLeg+Wp+Pitch
*ENDDO

OffsetLeg = OffsetP
*DO,i,0,Np-1,1        ! create the turn areas
    BLC4,Lp,OffsetLeg,LpEnd,2*Wp+Pitch
    OffsetLeg = OffsetLeg+2*Wp+2*Pitch
*ENDDO

*IF,2*Np,GT,2,THEN
    OffsetLeg = OffsetP+Wp+Pitch
    *DO,i,0,Np-2,1        ! create the turn areas
        BLC4,0,OffsetLeg,-LpEnd,2*Wp+Pitch
```

```
        OffsetLeg = OffsetLeg+2*Wp+2*Pitch
    *ENDDO
*ENDIF

AOVLAP,all
ALLSEL
APLOT   !plot the selected areas

ASEL,s,loc,x,-Lb,Lp+LpEnd
ASEL,r,loc,y,OffsetP,Wc-OffsetP
TYPE,3      ! use dummy mesh to mesh the areas
ESIZE,MeshSide      !relatively fine setting.
AMESH,all   ! mesh the resistor area
ALLSEL
ESIZE,4     !relatively coarse setting.
AMESH,all   ! mesh the rest
EPLOT

! extrude volumes -with mesh- to lever thickness (2 steps)
! using strutural element type 2 and material mat 2
! resulting mesh is hex-dominant and automatically conformal
! at interfaces between volumes. No need to merge nodes.

TYPE,2
MAT,2               ! undoped silicon
EXTOPT,esize,1      !1 divisions along extrusion direction (refine as needed)
EXTOPT,aclear,1     !clear dummy mesh - no longer needed
VEXT,all,,,,,Tp     !extrude to thickness of piezo region

ASEL,s,loc,z,Tp     !select new top areas for cantilever extrusion
EXTOPT,esize,2      !2 divisions along extrusion direction (refine as needed)
VEXT,all,,,,,Tc-Tp  !extrude remaining thickness

ASEL,s,loc,x,-Lb,0
ASEL,r,loc,z,Tc,Tc
EXTOPT,esize,2      !2 divisions along extrusion direction (refine as needed)
VEXT,all,,,,,Tb-Tc  !extrude remaining thickness

ALLSEL
EPLOT

! re-assign elements in volume corresponding to piezo
! to piezo element type 1 and mat 1

VSEL,s,loc,x,-LpStart,0
VSEL,r,loc,y,OffsetP,OffsetP+Wp
VSEL,r,loc,z,0,Tp
ESLV
EMODIF,all,mat,1
EMODIF,all,type,1

VSEL,s,loc,x,-LpStart,0
VSEL,r,loc,y,OffsetP+(2*Np-1)*Wp+(2*Np-1)*Pitch,OffsetP+2*Np*Wp+(2*Np-1)*Pitch
VSEL,r,loc,z,0,Tp
ESLV
EMODIF,all,mat,1
EMODIF,all,type,1

OffsetLeg = OffsetP
*DO,i,0,2*Np-1,1        ! modify the Legs areas
    VSEL,s,loc,x,0,Lp
    VSEL,r,loc,y,OffsetLeg,OffsetLeg+Wp
    VSEL,r,loc,z,0,Tp
    ESLV
    EMODIF,all,mat,1
    EMODIF,all,type,1
    OffsetLeg = OffsetLeg+Wp+Pitch
*ENDDO

OffsetLeg = OffsetP
```

```
*DO,i,0,Np-1,1      ! modify the turn areas
    VSEL,s,loc,x,Lp,Lp+LpEnd
    VSEL,r,loc,y,OffsetLeg,OffsetLeg+2*Wp+Pitch
    VSEL,r,loc,z,0,Tp
    ESLV
    EMODIF,all,type,1
    EMODIF,all,mat,1
    OffsetLeg = OffsetLeg+2*Wp+2*Pitch
*ENDDO

OffsetLeg = OffsetP+Wp+Pitch
*DO,i,0,Np-2,1      ! modify the turn areas
    VSEL,s,loc,x,-LpEnd,0
    VSEL,r,loc,y,OffsetLeg,OffsetLeg+2*Wp+Pitch
    VSEL,r,loc,z,0,Tp
    ESLV
    EMODIF,all,type,1
    EMODIF,all,mat,1
    OffsetLeg = OffsetLeg+2*Wp+2*Pitch
*ENDDO

! coat the cantilever surface with
! SURF154 elements and add a transversal stress
R,999, , , , ,-SurfaceStress,,0 ! define the element real constant (surface tension)

TYPE,4
REAL,999
ESEL,all
NSEL,s,loc,z,0      ! select the surface of the cantilever
ESURF

ALLSEL
EPLOT
!______________________________________________
!
! CHANGE THE VIEWING POINT
!______________________________________________
!
/USER,1
/VIEW,1,0.91,-0.14,-0.38
/ANG,1,87.17
/FOCUS,1,70,6,-5.5
/DIST,1,90
!/ZOOM,1,SCRN,-0.398905,0.311499,-0.264599,0.293985
/REPLO
!______________________________________________
!
! CREATE ELECTRICAL BC's
!______________________________________________
!
! select the right electrode
NSEL,s,loc,x,-LpStart
NSEL,r,loc,y,OffsetP,OffsetP+Wp
NSEL,r,loc,z,0,Tp
CM,ElectrodeR,node      !create named set of nodes "ElectrodeR"
CP,1,VOLT,all           ! Select voltage DoF
D,all,volt,Vp           ! apply source voltage Vp

! select the left electrode
NSEL,s,loc,x,-LpStart
NSEL,r,loc,y,Wc-OffsetP-Wp,Wc-OffsetP
NSEL,r,loc,z,0,Tp
CM,ElectrodeL,node      !create named set of nodes "ElectrodeL"
D,all,volt,0    ! Apply ground voltage
!______________________________________________
!
! CREATE STRUCTURAL BC's
!______________________________________________
!
ALLSEL
```

```
! Stuck
NSEL,s,loc,x,-Lb
D,all,ux,0
D,all,uy,0
D,all,uz,0

NSEL,s,loc,x,-LpStart
NSEL,r,loc,y,0,OffsetP
D,all,ux,0
D,all,uy,0
D,all,uz,0

NSEL,s,loc,x,-LpStart
NSEL,r,loc,y,Wc-OffsetP,Wc
D,all,ux,0
D,all,uy,0
D,all,uz,0

NSEL,s,loc,z,Tb
D,all,ux,0
D,all,uy,0
D,all,uz,0

ALLSEL
/pbc,u,,1       ! plot boundary conditions
/pbc,volt,,1
/pbc,cp,,1
/pnum,mat,1 ! show colors
/number,1
eplot
FINISH
!_______________________________________________
!
! SOLUTION
!_______________________________________________
!
/solu ! Solution
antype,static
CNVTOL,amps,1000,0.1
solve
/post1
!_______________________________________________
!
! CALCULATE CURRENT
!_______________________________________________
!
CMSEL,s,ElectrodeL                      !select ground electrode
fsum                                    !sums "forces" on nodes selected(current in this
    case)
*GET,PiezoCurrent,fsum,0,item,amps      !retrieve result for current (item: amps)
PiezoResistor=Vp/(PiezoCurrent*1e-12)   ! Resistor in Ohms
ALLSEL

!_______________________________________________
!
! CALCULATE NUMBER OF CARRIERS
!_______________________________________________
!
ALLSEL

ETABLE,CurrentD,JC,SUM

LocalCurrentD = 0
elem_num = 0
Temp1 = 0
VB2ByN = 0  ! Vb^2/N

elem_Total = elmiqr(0,13)   ! Number of elements
*DO,elements,1,elem_Total
    elem_num=ndnext(elem_num)
```

```
    *GET,LocalCurrentD,ETAB,1,ELEM,elem_num
    Temp1 = (LocalCurrentD**2)**2*Rho**2/CarriersD/PiezoCurrent**2
    VB2ByN = VB2ByN + Temp1*MeshVolume
*ENDDO

!_______________________________________________
!
! RETRIEVE MAXIMUM DEFLECTION
!_______________________________________________
!
NSEL,s,loc,y,Wc/2-tol,Wc/2+tol
NSORT,u,z,0,1,1                  ! Sort the nodes by deflection value in z
*GET,MaxDeflection,SORT,0,MAX    ! Get the first max value

!_______________________________________________
!
! PLOT (SigmaX-SigmaY)
!_______________________________________________
!
ALLSEL
/CONTOUR,1,9,AUTO
RSYS,11
ESEL,s,type,,1,2             ! Don't select the surface stress
SABS,1
ETABLE,SigmaX,s,x        ! Select longitudinal stress
ETABLE,SigmaY,s,y        ! Select transversal stress
SADD,SigmaReal,SigmaX,SigmaY,1,-1,0 !SigmaReal = Sx-Sy
PLETAB,SigmaReal,AVG     ! plot SigmaReal
/TRIAD,OFF      ! don't show the global CS
CSYS,11
!_______________________________________________
!
! APPEND MACRO CALL PARAMETERS AND RESULTS TO DATA FILE
!_______________________________________________
!
/OUTPUT,'Cantilever_Results','dat','.',append
*VWRITE,SurfaceStress,Vp,Lc,Wc,Tc,Lp,Wp,Tp,Np,CarriersD,PiezoResistor,VB2ByN,
    MaxDeflection
%14.2G %14.2G %14.2G %14.2G %14.2G %14.2G %14.2G %14.2G %14.2G %14.7G %14.7G %14.7G %14.7
    G
/OUTPUT,TERM
```

D || MSS fabrication

Step	Description	Program / Parameters	Target	Remarks
0	WAFER PREPARATION			
0.1	Stock out			SOI wafers
0.2	Wafer inspection			
0.3	Standard cleaning	Standard cleaning		
1	DEVICE LAYER THINNERING			
1.1	Thermal oxidation	wet oxidation @ 1050°C	2'000 nm	The device layer is thinned down from 3 μm to 2 μm.
1.2	BHF etching		2'000 nm	
1.3	Standard cleaning	Standard cleaning		
1.4	Thermal oxidation	wet oxidation @ 1050°C	600 nm	Mask for the diffusion doping step
2	PHOTOLITHOGRAPHY 1 - diffusion doping			
2.1	HMDS	30 minutes at 150°C		Wafer dehydration and surface functionalization
2.2	PR spinning	Standard 1518 / 40s @ 4000 rpm	1.8 μm	
2.3	PR soft bake	60s @ 100°C		
2.4	PR BS spinning	Standard 1518 / 40s @ 4000 rpm	1.8 μm	Backside (BS) protection to keep the BS oxide
2.5	PR soft bake	30 min @ 85°C		In hoven
2.6	Mask illumination	Hard Contact	40 mJ	
2.7	PR development	AZ351 + DI water (1:4) during 60s		
2.8	PR postbake	60 min @ 85°C		
2.9	Descum	2 minutes in oxygen plasma		surface hydrophilicity
3	SILICON DIOXIDE STRUCTURATION			
3.1	Silicon oxide removal	70 nm per min.	600 nm	
3.2	PR stripping	30 minutes in oxygen plasma		Acetone and IsoP before plasma
3.3	Standard cleaning	Standard cleaning		BHF for 10s
4	DIFFUSION DOPING			

4.1	BSG deposition	gas flux: 1’500 sccm	150 nm	
4.2	undoped SiO2		500 nm	
4.3	Thermal diffusion	30 minutes @ 950°C without O2		
5	PHOTOLITHOGRAPHY 2 - oxide removal			
5.1	HMDS	30 minutes at 150°C		Wafer dehydration and surface functionalization
5.2	PR spinning	Standard 1518 / 40s @ 4000 rpm	1.8 μm	
5.3	PR soft bake	60s @ 100°C		
5.4	PR BS spinning	Standard 1518 / 40s @ 4000 rpm	1.8 μm	Backside (BS) protection to keep the BS oxide
5.5	PR soft bake	30 min @ 85°C		In hoven
5.6	Mask illumination	Hard Contact	40 mJ	
5.7	PR development	AZ351 + DI water (1:4) during 60s		
5.8	PR postbake	60 min @ 85°C		
5.9	Descum	2 minutes in oxygen plasma		surface hydrophilicity
6	SILICON DIOXIDE STRUCTURATION			
6.1	Silicon oxide removal	70 nm per min.	600 nm	
6.2	PR stripping	30 minutes in oxygen plasma		Acetone and IsoP before plasma
6.3	Standard cleaning	Standard cleaning		BHF for 10s
6.4	Thermal oxidation	dry oxidation @ 1050°C	8 0 nm	first passivation layer
7	PHOTOLITHOGRAPHY 3 - implantation doping			
7.1	HMDS	30 minutes at 150°C		Wafer dehydration and surface functionalization
7.2	PR spinning	Standard 1518 / 40s @ 3500 rpm	2.2 μm	
7.3	PR soft bake	70s @ 100°C		
7.4	Mask illumination	Hard Contact	40 mJ	
7.5	PR development	AZ351 + DI water (1:4) during 60s		
7.6	PR postbake	120 min @ 85°C		
8	IMPLANTATION DOPING			
8.1	Ions implantation	B+, 40 keV, 2.5E14/cm2, 7°		
8.2	PR stripping	60 minutes in oxygen plasma		No Acetone and IsoP before plasma!!
8.3	Rapid thermal annealing	ramping 10s, 10s @ 1000°C, cooling 60s		
9	PASSIVATION			
9.1	Standard cleaning	Standard cleaning		no BHF!!!
9.2	LPCVD low stress SiNx		100 nm	
10	PHOTOLITHOGRAPHY 4 - resistors contacts			

10.1	HMDS	30 minutes at 150°C		Wafer dehydration and surface functionalization
10.2	PR spinning	Standard 1518 / 40s @ 4000 rpm	1.8 μm	
10.3	PR soft bake	60s @ 100°C		
10.4	Mask illumination	Hard Contact	40 mJ	
10.5	PR development	AZ351 + DI water (1:4) during 60s		
10.6	PR postbake	60 min @ 85°C		
11	CREATE CONTACTS			
11.1	RIE etching of SiNx		100 nm	
11.2	Descum	Oxygen plasma for 2 min		
11.3	BHF etching of SiO2	70 nm per min.	80 nm	
11.4	PR stripping	30 minutes in oxygen plasma		Acetone and IsoP before plasma
11.5	BHF dipping		1 s	
11.6	Al deposition	With planetary	1 μm	
12	PHOTOLITHOGRAPHY 5 - aluminium connections			
12.1	HMDS	30 minutes at 150°C		Wafer dehydration and surface functionalization
12.2	PR spinning	Standard 1518 / 40s @ 4000 rpm	1.8 μm	
12.3	PR soft bake	60s @ 100°C		
12.4	Mask illumination	Hard Contact	40 mJ	
12.5	PR development	AZ351 + DI water (1:4) during 60s		
12.6	PR postbake	60 min @ 85°C		
12.7	Descum	2 minutes in oxygen plasma		surface hydrophilicity
13	CREATE CONNECTIONS AND PASSIVATION			
13.1	Aluminium etching	wet bath for about 4.5 minutes	1 μm	
13.2	PR stripping	Acetone and IsoP		No plasma!!!
13.3	SiO2 deposition	PECVD SiO2	1.5 μm	
14	PHOTOLITHOGRAPHY 6 - open pads			
14.1	HMDS	30 minutes at 150°C		Wafer dehydration and surface functionalization
14.2	PR spinning	Standard 1518 / 40s @ 4000 rpm	1.8 μm	
14.3	PR soft bake	60s @ 100°C		
14.4	Mask illumination	Hard Contact	40 mJ	
14.5	PR development	AZ351 + DI water (1:4) during 60s		
14.6	PR postbake	60 min @ 85°C		
14.7	Descum	2 minutes in oxygen plasma		surface hydrophilicity
15	OPEN ALUMINIUM PADS			

15.1	SiO2 etching	BHF bath	1.5 μm	
15.2	PR stripping	30 minutes in oxygen plasma		Acetone and IsoP before plasma
16	PHOTOLITHOGRAPHY 7 - sensors structuration			
16.1	HMDS	30 minutes at 150°C		Wafer dehydration and surface functionalization
16.2	PR spinning	9260 / 40s @ 4000 rpm	6.2 μm	
16.3	PR soft bake	150s @ 115°C		
16.4	Mask illumination	Hard Contact	250 mJ	
16.5	PR development	AZ400 + DI water (1:4) during 3m45s		
16.6	PR postbake	120 min @ 85°C		
17	FRONTSIDE DRIE			
17.1	Frontside DRIE		2-3 μm	
17.2	PR stripping	30 minutes in oxygen plasma		Acetone and IsoP before plasma
18	FRONTSIDE PROTECTION			
18.1	Parylene coating		5 μm	
18.2	Removal on backside	dry etching of parylene		Acetone and IsoP before plasma
19	PHOTOLITHOGRAPHY 8 - backside DRIE			
19.1	HMDS	30 minutes at 150°C		Wafer dehydration and surface functionalization
19.2	PR spinning	9260 / 40s @ 3000 rpm	10 μm	
19.3	PR soft bake	40 min @ 85°C in hoven		
19.4	Mask illumination	Hard Contact	250 mJ	
19.5	PR development	AZ400 + DI water (1:4) during 3m45s		
19.6	PR postbake	120 min @ 85°C		
20	BACKSIDE DRIE			
20.1	SiNx and SiO2 removal	Backside RIE	80 + 700 nm	
20.2	Backside DRIE		350 μm	
21	CHIPS RELEASE			
21.1	Resist stripping	Acetone and IP only!!		
21.2	Remove box oxide	Vapour HF	10-13 min	
21.3	Parylene Stripping	Dry etching	5 μm	

Bibliography

[1] P. Nowell, "The clonal evolution of tumor cell populations," *Science*, vol. 194, no. 4260, pp. 23–28, 1976.

[2] D. Hanahan and R. Weinberg, "The hallmarks of cancer," *Cell*, vol. 100, pp. 57–70, 2000.

[3] D. Hanahan and R. Weinberg, "Hallmarks of cancer: the next generation," *Cell*, vol. 144, pp. 646–74, Mar. 2011.

[4] U. Cavallaro and G. Christofori, "Cell adhesion and signalling by cadherins and Ig-CAMs in cancer," *Nature reviews. Cancer*, vol. 4, pp. 118–32, Feb. 2004.

[5] B.-Z. Qian and J. W. Pollard, "Macrophage diversity enhances tumor progression and metastasis," *Cell*, vol. 141, pp. 39–51, Apr. 2010.

[6] G. P. Gupta and J. Massagué, "Cancer metastasis: building a framework," *Cell*, vol. 127, pp. 679–95, Nov. 2006.

[7] R. O'Hagan, M. Chalfie, and M. B. Goodman, "The MEC-4 DEG/ENaC channel of Caenorhabditis elegans touch receptor neurons transduces mechanical signals," *Nature neuroscience*, vol. 8, pp. 43–50, Jan. 2005.

[8] B. C. Petzold, S.-J. Park, E. A. Mazzochette, M. B. Goodman, and B. L. Pruitt, "MEMS-based force-clamp analysis of the role of body stiffness in C. elegans touch sensation," *Integrative biology : quantitative biosciences from nano to macro*, vol. 5, pp. 853–64, May 2013.

[9] A. J. Engler, S. Sen, H. L. Sweeney, and D. E. Discher, "Matrix elasticity directs stem cell lineage specification," *Cell*, vol. 126, pp. 677–89, Aug. 2006.

[10] S. Obi, K. Yamamoto, N. Shimizu, S. Kumagaya, T. Masumura, T. Sokabe, T. Asahara, and J. Ando, "Fluid shear stress induces arterial differentiation of endothelial progenitor cells," *Journal of applied physiology*, vol. 106, pp. 203–11, Jan. 2009.

[11] B. Alberts, J. Alexander, L. Julian, M. Raff, K. Roberts, and P. Walter, *Molecular Biology of the Cell*. Garland Science, 5th editio ed., 2007.

[12] M. Ruiz, "Wikipedia website," 2006.

[13] P. Yeagle, “Cholesterol and the cell membrane,” *Biochimica et Biophysica Acta*, vol. 822, pp. 267–287, 1985.

[14] K. N. Dahl, A. J. S. Ribeiro, and J. Lammerding, “Nuclear shape, mechanics, and mechanotransduction,” *Circulation research*, vol. 102, pp. 1307–18, June 2008.

[15] F. Guilak, J. R. Tedrow, and R. Burgkart, “Viscoelastic properties of the cell nucleus,” *Biochemical and biophysical research communications*, vol. 269, pp. 781–6, Mar. 2000.

[16] S. Suresh, “Biomechanics and biophysics of cancer cells,” *Acta biomaterialia*, vol. 3, pp. 413–38, July 2007.

[17] T. Svitkina and G. Borisy, “Arp2/3 complex and actin depolymerizing factor/cofilin in dendritic organization and treadmilling of actin filament array in lamellipodia,” *The Journal of cell biology*, vol. 145, no. 5, pp. 1009–1026, 1999.

[18] F. Gittes, B. Mickey, J. Nettleton, and J. Howard, “Flexural rigidity of microtubules and actin filaments measured from thermal fluctuations in shape,” *The Journal of cell biology*, vol. 120, pp. 923–34, Feb. 1993.

[19] C. Guzmán, S. Jeney, L. Kreplak, S. Kasas, A. J. Kulik, U. Aebi, and L. Forró, “Exploring the mechanical properties of single vimentin intermediate filaments by atomic force microscopy.,” *Journal of molecular biology*, vol. 360, pp. 623–30, July 2006.

[20] R. D. Goldman, S. Khuon, Y. H. Chou, P. Opal, and P. M. Steinert, “The function of intermediate filaments in cell shape and cytoskeletal integrity.,” *The Journal of cell biology*, vol. 134, pp. 971–83, Aug. 1996.

[21] H. Maiato, P. Sampaio, and C. E. Sunkel, “Microtubule-associated proteins and their essential roles during mitosis,” *International Review of Cytology*, vol. 241, pp. 55–153, 2004.

[22] I. H. L. Hamelers, C. Olivo, A. E. E. Mertens, D. M. Pegtel, R. A. van der Kammen, A. Sonnenberg, and J. G. Collard, “The Rac activator Tiam1 is required for (alpha)3(beta)1-mediated laminin-5 deposition, cell spreading, and cell migration,” *The Journal of cell biology*, vol. 171, pp. 871–81, Dec. 2005.

[23] D. T. Butcher, T. Alliston, and V. M. Weaver, “A tense situation: forcing tumour progression,” *Nature reviews. Cancer*, vol. 9, pp. 108–22, Feb. 2009.

[24] G. Y. H. Lee and C. T. Lim, “Biomechanics approaches to studying human diseases,” *Trends in biotechnology*, vol. 25, pp. 111–8, Mar. 2007.

[25] M. J. Paszek, N. Zahir, K. R. Johnson, J. N. Lakins, G. I. Rozenberg, A. Gefen, C. A. Reinhart-King, S. S. Margulies, M. Dembo, D. Boettiger, D. A. Hammer, and V. M. Weaver, “Tensional homeostasis and the malignant phenotype,” *Cancer cell*, vol. 8, pp. 241–54, Sept. 2005.

[26] M. Plodinec and M. Loparic, “The nanomechanical signature of breast cancer,” *Nature Nanotechnology*, vol. 7, pp. 757–765, 2012.

[27] S. E. Cross, Y.-S. Jin, J. Rao, and J. K. Gimzewski, “Nanomechanical analysis of cells from cancer patients,” *Nature Nanotechnology*, vol. 2, pp. 780–3, Dec. 2007.

[28] J. Guck, S. Schinkinger, B. Lincoln, F. Wottawah, S. Ebert, M. Romeyke, D. Lenz, H. M. Erickson, R. Ananthakrishnan, D. Mitchell, J. Kas, S. Ulvick, and C. Bilby, “Optical deformability as an inherent cell marker for testing malignant transformation and metastatic competence,” *Biophysical journal*, vol. 88, pp. 3689–98, May 2005.

[29] G. Weder, M. C. Hendriks-Balk, R. Smajda, D. Rimoldi, M. Liley, H. Heinzelmann, A. Meister, and A. Mariotti, “Increased plasticity of the stiffness of melanoma cells correlates with their acquisition of metastatic properties,” *Nanomedicine : nanotechnology, biology, and medicine*, vol. in press, pp. 1–8, July 2013.

[30] W. A. Lam, M. J. Rosenbluth, and D. A. Fletcher, “Chemotherapy exposure increases leukemia cell stiffness,” *Blood*, vol. 109, pp. 3505–8, Apr. 2007.

[31] G. Kotzar, M. Freas, P. Abel, A. Fleischman, S. Roy, C. Zorman, J. M. Moran, and J. Melzak, “Evaluation of MEMS materials of construction for implantable medical devices,” *Biomaterials*, vol. 23, pp. 2737–50, July 2002.

[32] G. Voskerician, M. S. Shive, R. S. Shawgo, H. V. Recum, J. M. Anderson, M. J. Cima, and R. Langer, “Biocompatibility and biofouling of MEMS drug delivery devices,” *Biomaterials*, vol. 24, pp. 1959–1967, May 2003.

[33] S. I. Ertel, B. D. Ratner, A. Kaul, M. B. Schway, and T. A. Horbett, “In vitro study of the intrinsic toxicity of synthetic surfaces to cells,” *Journal of Biomedical Materials Research*, vol. 28, no. 6, pp. 667–675, 2004.

[34] M. Ni, W. H. Tong, D. Choudhury, N. A. A. Rahim, C. Iliescu, and H. Yu, “Cell culture on MEMS platforms: a review,” *International journal of molecular sciences*, vol. 10, pp. 5411–41, Dec. 2009.

[35] J. Deutsch, D. Motlagh, B. Russell, and T. A. Desai, “Fabrication of microtextured membranes for cardiac myocyte attachment and orientation,” *Journal of biomedical materials research*, vol. 53, pp. 267–75, Jan. 2000.

[36] O. Zinger, G. Zhao, Z. Schwartz, J. Simpson, M. Wieland, D. Landolt, and B. Boyan, “Differential regulation of osteoblasts by substrate microstructural features,” *Biomaterials*, vol. 26, pp. 1837–47, May 2005.

[37] S. P. Low, K. A. Williams, L. T. Canham, and N. H. Voelcker, “Evaluation of mammalian cell adhesion on surface-modified porous silicon,” *Biomaterials*, vol. 27, pp. 4538–46, Sept. 2006.

[38] N. Faucheux, R. Schweiss, K. Lutzow, C. Werner, and T. Groth, "Self-assembled monolayers with different terminating groups as model substrates for cell adhesion studies," *Biomaterials*, vol. 25, pp. 2721–30, June 2004.

[39] M. A. Lan, C. A. Gersbach, K. E. Michael, B. G. Keselowsky, and A. J. Garcia, "Myoblast proliferation and differentiation on fibronectin-coated self assembled monolayers presenting different surface chemistries," *Biomaterials*, vol. 26, pp. 4523–31, Aug. 2005.

[40] K. B. McClary, T. Ugarova, and D. W. Grainger, "Modulating fibroblast adhesion, spreading, and proliferation using self-assembled monolayer films of alkylthiolates on gold," *Journal of biomedical materials research*, vol. 50, pp. 428–39, June 2000.

[41] J. N. Lee, C. Park, and G. M. Whitesides, "Solvent compatibility of poly(dimethylsiloxane)-based microfluidic devices," *Analytical chemistry*, vol. 75, pp. 6544–54, Dec. 2003.

[42] K. Wouters and R. Puers, "Diffusing and swelling in SU-8: insight in material properties and processing," *Journal of Micromechanics and Microengineering*, vol. 20, p. 095013, Sept. 2010.

[43] C. Martin, A. Llobera, G. Villanueva, A. Voigt, G. Gruetzner, J. Brugger, and F. Perez-Murano, "Stress and aging minimization in photoplastic AFM probes," *Microelectronic Engineering*, vol. 86, pp. 1226–1229, Apr. 2009.

[44] G. Binnig, C. Quate, and C. Gerber, "Atomic force microscope," *Physical Review Letters*, vol. 56, no. 9, pp. 930–933, 1986.

[45] M. Radmacher, "Studying the mechanics of cellular processes by atomic force microscopy," *Methods in cell biology*, vol. 83, pp. 347–72, Jan. 2007.

[46] H. Hertz, "Über die Berührung fester elastischer Körper," *Journal für die Reine und Angewandte Mathematik*, vol. -, pp. 156–171, 1881.

[47] I. Sneddon, "The relation between load and penetration in the axisymmetric Boussinesq problem for a punch of arbitrary profile," *International Journal of Engineering Science*, vol. 3, no. 638, pp. 47–57, 1965.

[48] Q. S. Li, G. Y. H. Lee, C. N. Ong, and C. T. Lim, "AFM indentation study of breast cancer cells," *Biochemical and biophysical research communications*, vol. 374, pp. 609–13, Oct. 2008.

[49] K. Johnson, "Surface energy and the contact of elastic solids," *Proceedings of the Royal Society of London Series A*, vol. 324, no. 1558, pp. 301–313, 1971.

[50] L. Scheffer, A. Bitler, E. Ben-Jacob, and R. Korenstein, "Atomic force pulling: probing the local elasticity of the cell membrane," *European Biophysics Journal*, vol. 30, pp. 83–90, May 2001.

[51] E. A-Hassan, W. F. Heinz, M. D. Antonik, N. P. D'Costa, S. Nageswaran, C. A. Schoenenberger, and J. H. Hoh, "Relative microelastic mapping of living cells by atomic force microscopy.," *Biophysical journal*, vol. 74, pp. 1564–78, Mar. 1998.

[52] A. Raman, S. Trigueros, A. Cartagena, A. P. Z. Stevenson, M. Susilo, E. Nauman, and S. A. Contera, "Mapping nanomechanical properties of live cells using multi-harmonic atomic force microscopy," *Nature nanotechnology*, pp. 1–6, Nov. 2011.

[53] A. Beaussart, S. El-Kirat-Chatel, P. Herman, D. Alsteens, J. Mahillon, P. Hols, and Y. F. Dufrêne, "Single-cell force spectroscopy of probiotic bacteria.," *Biophysical journal*, vol. 104, pp. 1886–92, May 2013.

[54] D. J. Beebe, G. Mensing, and G. Walker, "Physics and applications of microfluidics in biology," *Annual review of biomedical engineering*, vol. 4, pp. 261–86, Jan. 2002.

[55] J. El-Ali, P. K. Sorger, and K. F. Jensen, "Cells on chips," *Nature*, vol. 442, pp. 403–11, July 2006.

[56] G. Tomaiuolo, M. Barra, V. Preziosi, A. Cassinese, B. Rotoli, and S. Guido, "Microfluidics analysis of red blood cell membrane viscoelasticity," *Lab on a chip*, vol. 11, pp. 449–54, Feb. 2011.

[57] A. D. van der Meer, A. A. Poot, J. Feijen, and I. Vermes, "Analyzing shear stress-induced alignment of actin filaments in endothelial cells with a microfluidic assay," *Biomicrofluidics*, vol. 4, p. 11103, Jan. 2010.

[58] D. Irimia and M. Toner, "Spontaneous migration of cancer cells under conditions of mechanical confinement," *Integrative biology : quantitative biosciences from nano to macro*, vol. 1, pp. 506–12, Sept. 2009.

[59] S. S. Shevkoplyas, T. Yoshida, S. C. Gifford, and M. W. Bitensky, "Direct measurement of the impact of impaired erythrocyte deformability on microvascular network perfusion in a microfluidic device," *Lab on a chip*, vol. 6, pp. 914–20, July 2006.

[60] D. Huh, B. D. Matthews, A. Mammoto, M. Montoya-Zavala, H. Y. Hsin, and D. E. Ingber, "Reconstituting organ-level lung functions on a chip," *Science*, vol. 328, pp. 1662–8, June 2010.

[61] O. du Roure, A. Saez, A. Buguin, R. Austin, P. Chavrier, P. Silberzan, P. Siberzan, and B. Ladoux, "Force mapping in epithelial cell migration," *Proceedings of the National Academy of Sciences of the United States of America*, vol. 102, pp. 2390–5, Feb. 2005.

[62] M. Yang, N. Sniadecki, and C. Chen, "Geometric Considerations of Micro- to Nanoscale Elastomeric Post Arrays to Study Cellular Traction Forces," *Advanced Materials*, vol. 19, pp. 3119–3123, Oct. 2007.

[63] K. Kim, R. Taylor, J. Sim, S.-J. Park, J. Norman, G. Fajardo, D. Bernstein, and B. Pruitt, "Calibrated micropost arrays for biomechanical characterisation of cardiomyocytes," *Micro and Nano Letters*, vol. 6, no. 5, p. 317, 2011.

[64] N. J. Sniadecki, A. Anguelouch, M. T. Yang, C. M. Lamb, Z. Liu, S. B. Kirschner, Y. Liu, D. H. Reich, and C. S. Chen, "Magnetic microposts as an approach to apply forces to living cells," *Proceedings of the National Academy of Sciences of the United States of America*, vol. 104, pp. 14553–8, Sept. 2007.

[65] A. Ashkin, "Acceleration and trapping of particles by radiation pressure," *Physical review letters*, vol. 24, no. 4, pp. 24–27, 1970.

[66] A. Ashkin and J. Dziedzic, "Optical trapping and manipulation of viruses and bacteria," *Science*, vol. 235, no. 4795, pp. 1517–1520, 1987.

[67] H. Zhang and K.-K. Liu, "Optical tweezers for single cells," *Journal of the Royal Society, Interface / the Royal Society*, vol. 5, pp. 671–90, July 2008.

[68] M. M. Wang, E. Tu, D. E. Raymond, J. M. Yang, H. Zhang, N. Hagen, B. Dees, E. M. Mercer, A. H. Forster, I. Kariv, P. J. Marchand, and W. F. Butler, "Microfluidic sorting of mammalian cells by optical force switching," *Nature biotechnology*, vol. 23, pp. 83–7, Jan. 2005.

[69] J. Guck, R. Ananthakrishnan, H. Mahmood, T. J. Moon, C. C. Cunningham, and J. Käs, "The optical stretcher: a novel laser tool to micromanipulate cells," *Biophysical journal*, vol. 81, pp. 767–84, Aug. 2001.

[70] C. Lim, E. Zhou, A. Li, S. Vedula, and H. Fu, "Experimental techniques for single cell and single molecule biomechanics," *Materials Science and Engineering: C*, vol. 26, pp. 1278–1288, Sept. 2006.

[71] K. Neuman and A. Nagy, "Single-molecule force spectroscopy: optical tweezers, magnetic tweezers and atomic force microscopy," *Nature methods*, vol. 5, no. 6, pp. 491–505, 2008.

[72] C. Haber and D. Wirtz, "Magnetic tweezers for DNA micromanipulation," *Review of Scientific Instruments*, vol. 71, no. 12, p. 4561, 2000.

[73] C. Gosse and V. Croquette, "Magnetic tweezers: micromanipulation and force measurement at the molecular level," *Biophysical journal*, vol. 82, pp. 3314–29, June 2002.

[74] R. Bausch, F. Ziemann, A. Boulbitch, K. Jacobson, and E. Sackmann, "Local measurements of viscoelastic parameters of adherent cell surfaces by magnetic bead microrheometry," *Biophysical journal*, vol. 75, pp. 2038–49, Oct. 1998.

[75] A. H. B. de Vries, B. E. Krenn, R. van Driel, and J. S. Kanger, "Micro magnetic tweezers for nanomanipulation inside live cells," *Biophysical journal*, vol. 88, pp. 2137–44, Mar. 2005.

[76] P. P. Lehenkari, G. T. Charras, A. Nykänen, and M. A. Horton, “Adapting atomic force microscopy for cell biology,” *Ultramicroscopy*, vol. 82, pp. 289–95, Feb. 2000.

[77] J. M. Mann, R. H. W. Lam, S. Weng, Y. Sun, and J. Fu, “A silicone-based stretchable micropost array membrane for monitoring live-cell subcellular cytoskeletal response,” *Lab on a chip*, vol. 12, pp. 731–40, Feb. 2012.

[78] R. A. Flynn, A. L. Birkbeck, M. Gross, M. Ozkan, B. Shao, M. M. Wang, and S. C. Esener, “Parallel transport of biological cells using individually addressable VCSEL arrays as optical tweezers,” *Sensors and Actuators B: Chemical*, vol. 87, pp. 239–243, Dec. 2002.

[79] F. Amblard, B. Yurke, A. Pargellis, and S. Leibler, “A magnetic manipulator for studying local rheology and micromechanical properties of biological systems,” *Review of Scientific Instruments*, vol. 67, no. 3, p. 818, 1996.

[80] G. Meyer and N. M. Amer, “Novel optical approach to atomic force microscopy,” *Applied Physics Letters*, vol. 53, no. 12, p. 1045, 1988.

[81] M. J. Madou, *Fundamentals of Microfabrication and Nanotechnology*. 3rd revision ed., 2009.

[82] M. Morita, T. Ohmi, E. Hasegawa, M. Kawakami, and M. Ohwada, “Growth of native oxide on a silicon surface,” *Journal of Applied Physics*, vol. 68, no. 3, p. 1272, 1990.

[83] B. E. Deal and A. S. Grove, “General Relationship for the Thermal Oxidation of Silicon,” *Journal of Applied Physics*, vol. 36, no. 12, p. 3770, 1965.

[84] C. Gonzalez and J. McVittie, “A study of trenched capacitor structures,” *Electron Device Letters, IEEE*, vol. 6, no. 5, pp. 215–218, 1985.

[85] D.-B. Kao, J. P. McVittie, W. D. Nix, and K. C. Saraswat, “Two-dimensional thermal oxidation of silicon-I . Experiments,” *Transactions on Electron Devices*, vol. 34, no. 5, pp. 1008–1017, 1987.

[86] R. Marcus and T. Sheng, “The oxidation of shaped silicon surfaces,” *Journal of the Electrochemical Society*, vol. I, no. 6, pp. 1278–1282, 1982.

[87] H. Seidel and L. Csepregi, “Anisotropic etching of crystalline silicon in alkaline solutions I. Orientation dependence and behavior of passivation layers,” *Journal of The Electrochemical Society*, vol. 137, no. 11, pp. 249–260, 1990.

[88] K. Reck, C. O stergaard, E. V. Thomsen, and O. Hansen, “Fusion bonding of silicon nitride surfaces,” *Journal of Micromechanics and Microengineering*, vol. 21, p. 125015, Dec. 2011.

[89] A. Hanneborg and M. Nese, “Silicon-to-thin film anodic bonding,” *Journal of Micromechanics and Microengineering*, vol. 117, pp. 117–121, 1992.

[90] N. Panousis and P. Hall, “Applications of grain boundary diffusion studies to soldering and thermocompression bonding,” *Thin Solid Films*, vol. 53, pp. 183–191, 1978.

[91] F. Niklaus, P. Enoksson, E. Kälvesten, and G. Stemme, “Low-temperature full wafer adhesive bonding,” *Journal of Micromechanics and Microengineering*, vol. 11, pp. 100–107, Mar. 2001.

[92] O. Wolter, “Micromachined silicon sensors for scanning force microscopy,” *Journal of Vacuum Science and Technology B: Microelectronics and Nanometer Structures*, vol. 9, p. 1353, Mar. 1991.

[93] A. Boisen, O. Hansen, and S. Bouwstra, “AFM probes with directly fabricated tips,” *Journal of Micromechanics and Microengineering*, vol. 6, pp. 58–62, Mar. 1996.

[94] R. B. Marcus, T. S. Ravi, T. Gmitter, K. Chin, D. Liu, W. J. Orvis, D. R. Ciarlo, C. E. Hunt, and J. Trujillo, “Formation of silicon tips with <1 nm radius,” *Applied Physics Letters*, vol. 56, no. 3, p. 236, 1990.

[95] J. A. Harley and T. W. Kenny, “High-sensitivity piezoresistive cantilevers under 1000 A thick,” *Applied Physics Letters*, vol. 75, no. 2, p. 289, 1999.

[96] T. R. Albrecht, “Microfabrication of cantilever styli for the atomic force microscope,” *Journal of Vacuum Science and Technology A: Vacuum, Surfaces, and Films*, vol. 8, p. 3386, July 1990.

[97] G. Genolet and J. Brugger, “Soft, entirely photoplastic probes for scanning force microscopy,” *Review of Scientific Instruments*, vol. 70, no. 5, pp. 2398–2401, 1999.

[98] E. J. Luber, B. C. Olsen, C. Ophus, V. Radmilovic, and D. Mitlin, “All-metal AFM probes fabricated from microstructurally tailored Cu-Hf thin films,” *Nanotechnology*, vol. 20, p. 345703, Aug. 2009.

[99] S. Akamine, “Low temperature thermal oxidation sharpening of microcast tips,” *Journal of Vacuum Science and Technology B: Microelectronics and Nanometer Structures*, vol. 10, p. 2307, Sept. 1992.

[100] W. Ducker, T. Senden, and R. Pashley, “Direct measurement of colloidal forces using an atomic force microscope,” *Nature*, vol. 353, pp. 239–241, 1991.

[101] M. Thie, R. Röspel, W. Dettmann, M. Benoit, M. Ludwig, H. E. Gaub, and H. W. Denker, “Interactions between trophoblast and uterine epithelium: monitoring of adhesive forces,” *Human Reproduction*, vol. 13, pp. 3211–9, Nov. 1998.

[102] G. Pucci, M. D. Santo, G. Carbone, and R. Barberi, “A novel method to prepare probes for atomic force spectroscopy,” *Digest Journal of Nanomaterials and Biostructure*, vol. 1, no. 3, pp. 99–103, 2006.

[103] G. Huttl, V. Klemm, R. Popp, F. Simon, and E. Muller, "Tailored colloidal AFM probes and their TEM investigation," *Surface and Interface Analysis*, vol. 33, pp. 50–53, Feb. 2002.

[104] G. Kim, A. Kovalgin, J. Holleman, and J. Brugger, "Replication molds having nanometer-scale shape control fabricated by means of oxidation and etching," *Journal of Nanoscience*, vol. 2, pp. 55–59, 2002.

[105] M. K. Yapici and J. Zou, "Microfabrication of colloidal scanning probes with controllable tip radii of curvature," *Journal of Micromechanics and Microengineering*, vol. 19, p. 105021, Oct. 2009.

[106] G. E. Fantner, G. Schitter, J. H. Kindt, T. Ivanov, K. Ivanova, R. Patel, N. Holten-Andersen, J. Adams, P. J. Thurner, I. W. Rangelow, and P. K. Hansma, "Components for high speed atomic force microscopy," *Ultramicroscopy*, vol. 106, no. 8-9, pp. 881–7, 2006.

[107] T. Ando, "High-speed atomic force microscopy coming of age," *Nanotechnology*, vol. 23, p. 062001, Mar. 2012.

[108] S. C. Minne, S. R. Manalis, and C. F. Quate, "Parallel atomic force microscopy using cantilevers with integrated piezoresistive sensors and integrated piezoelectric actuators," *Applied Physics Letters*, vol. 67, no. 26, p. 3918, 1995.

[109] P. Vettiger, J. Brugger, M. Despont, U. Drechsler, U. Durig, W. Haberle, M. Lutwyche, H. Rothuizen, R. Stutz, and R. Widmer, "Ultrahigh density, high-data-rate NEMS-based AFM data storage system," *Microelectronic Engineering*, vol. 46, pp. 11–17, May 1999.

[110] G. Binnig, M. Despont, U. Drechsler, W. Haeberle, M. Lutwyche, P. Vettiger, H. J. Mamin, B. W. Chui, and T. W. Kenny, "Ultrahigh-density atomic force microscopy data storage with erase capability," *Applied Physics Letters*, vol. 74, no. 9, p. 1329, 1999.

[111] D. Pires, J. L. Hedrick, A. De Silva, J. Frommer, B. Gotsmann, H. Wolf, M. Despont, U. Duerig, and A. W. Knoll, "Nanoscale three-dimensional patterning of molecular resists by scanning probes," *Science*, vol. 328, pp. 732–5, May 2010.

[112] M. Favre, J. Polesel-Maris, T. Overstolz, P. Niedermann, S. Dasen, G. Gruener, R. Ischer, P. Vettiger, M. Liley, H. Heinzelmann, and A. Meister, "Parallel AFM imaging and force spectroscopy using two-dimensional probe arrays for applications in cell biology," *Journal of Molecular Recognition*, vol. 24, no. 3, pp. 446–52, 2011.

[113] B. J. Lutzenberger and D. L. Dickensheets, "Fabrication and modeling of rib-stiffened thin films," *Journal of Micromechanics and Microengineering*, vol. 19, p. 095003, Sept. 2009.

[114] C. Keller and R. Howe, "Hexsil Bimorphs For Vertical Actuation," *Proceedings of the International Solid-State Sensors and Actuators Conference*, vol. 1, pp. 99–102, 1995.

[115] H.-Y. Lin, "Rib-reinforced micromachined beam and its applications," *Journal of Micromechanics and Microengineering*, vol. 10, pp. 93–99, Feb. 2000.

[116] J. Brugger, G. Beljakovic, and M. Despont, “Silicon micro/nanomechanical device fabrication based on focused ion beam surface modification and KOH etching,” *Microelectronic*, vol. 35, no. 1997, pp. 401–404, 1997.

[117] SILVACO International Inc., “ATHENA User’s Manual 2D PROCESS SIMULATION SOFTWARE,” Tech. Rep. August, 2004.

[118] M. Tortonese, “Characterization of application-specific probes for SPMs,” *Proceedings of SPIE*, vol. 3009, no. 1, pp. 53–60, 1997.

[119] R. S. Gates and J. R. Pratt, “Prototype cantilevers for SI-traceable nanonewton force calibration,” *Measurement Science and Technology*, vol. 17, pp. 2852–2860, Oct. 2006.

[120] J. L. Hutter and J. Bechhoefer, “Calibration of atomic-force microscope tips,” *Review of Scientific Instruments*, vol. 64, no. 7, p. 1868, 1993.

[121] G. H. Ballantyne, “Robotic surgery, telerobotic surgery, telepresence, and telementoring. Review of early clinical results.,” *Surgical endoscopy*, vol. 16, pp. 1389–402, Oct. 2002.

[122] M. J. Elliott, P. De Coppi, S. Speggiorin, D. Roebuck, C. R. Butler, E. Samuel, C. Crowley, C. McLaren, A. Fierens, D. Vondrys, L. Cochrane, C. Jephson, S. Janes, N. J. Beaumont, T. Cogan, A. Bader, A. M. Seifalian, J. J. Hsuan, M. W. Lowdell, and M. a. Birchall, “Stem-cell-based, tissue engineered tracheal replacement in a child: a 2-year follow-up study.,” *Lancet*, vol. 380, pp. 994–1000, Sept. 2012.

[123] M. L. Metzker, “Sequencing technologies - the next generation.,” *Nature reviews. Genetics*, vol. 11, pp. 31–46, Jan. 2010.

[124] . OECD, *Health at a Glance: Europe 2012.* 2012.

[125] V. Gubala, L. F. Harris, A. J. Ricco, M. X. Tan, and D. E. Williams, “Point of care diagnostics: status and future,” *Analytical chemistry*, vol. 84, pp. 487–515, Jan. 2012.

[126] E. Lee-Lewandrowski and K. Lewandrowski, “Perspectives on cost and outcomes for point-of-care testing,” *Clinics in laboratory medicine*, vol. 29, pp. 479–89, Sept. 2009.

[127] J. Ehrenkranz, “Home and Point-of-Care Pregnancy Tests: A Review of the Technology,” *Epidemiology*, vol. 13, no. 3, pp. 15–18, 2002.

[128] J. Hönes, P. Müller, and N. Surridge, “The Technology Behind Glucose Meters: Test Strips,” *Diabetes Technology and Therapeutics*, vol. 10, pp. S–10–S–26, June 2008.

[129] Biomarker, “http://www.cancer.gov/dictionary?CdrID=45618.”

[130] S. I. Hajdu, “A note from history: landmarks in history of cancer, part 1,” *Cancer*, vol. 117, pp. 1097–102, Mar. 2011.

[131] S. I. Hajdu, “A note from history: landmarks in history of cancer, part 3,” *Cancer*, vol. 118, pp. 1155–68, Feb. 2012.

[132] S. I. Hajdu, "A note from history: landmarks in history of cancer, part 4," *Cancer*, vol. 118, pp. 4914–28, Oct. 2012.

[133] R. Etzioni, N. Urban, S. Ramsey, M. McIntosh, S. Schwartz, B. Reid, J. Radich, G. Anderson, and L. Hartwell, "The case for early detection," *Nature reviews. Cancer*, vol. 3, pp. 243–52, Apr. 2003.

[134] P. Gotzsche and M. Nielsen, "Screening for breast cancer with mammography," *Cochrane Database Syst Rev*, vol. 1, 2011.

[135] R. Nishihara, K. Wu, P. Lochhead, T. Morikawa, X. Liao, Z. R. Qian, K. Inamura, S. a. Kim, A. Kuchiba, M. Yamauchi, Y. Imamura, W. C. Willett, B. a. Rosner, C. S. Fuchs, E. Giovannucci, S. Ogino, and A. T. Chan, "Long-term colorectal-cancer incidence and mortality after lower endoscopy," *The New England journal of medicine*, vol. 369, pp. 1095–105, Sept. 2013.

[136] W. Jiang, "Overcoming the Deficiency of Singular Detection by Antibody Arrays in Cancer Biomarker Discovery," *Journal of Molecular Biomarkers and Diagnosis*, vol. 03, no. 04, 2012.

[137] J. a. Ludwig and J. N. Weinstein, "Biomarkers in cancer staging, prognosis and treatment selection," *Nature reviews. Cancer*, vol. 5, pp. 845–56, Nov. 2005.

[138] D. Sidransky, "Emerging molecular markers of cancer," *Nature reviews. Cancer*, vol. 2, pp. 210–9, Mar. 2002.

[139] T. M. Gorges and K. Pantel, "Circulating tumor cells as therapy-related biomarkers in cancer patients," *Cancer immunology, immunotherapy : CII*, vol. 62, pp. 931–9, May 2013.

[140] D. C. Danila, M. Fleisher, and H. I. Scher, "Circulating tumor cells as biomarkers in prostate cancer," *Clinical cancer research : an official journal of the American Association for Cancer Research*, vol. 17, pp. 3903–12, June 2011.

[141] Y. M. Lo, "Circulating nucleic acids in plasma and serum: an overview," *Annals of the New York Academy of Sciences*, vol. 945, pp. 1–7, Sept. 2001.

[142] F. Oshita, I. Nomura, and K. Yamada, "Detection of K-ras mutations of bronchoalveolar lavage fluid cells aids the diagnosis of lung cancer in small pulmonary lesions," *Clinical cancer research*, vol. 5, pp. 617–620, 1999.

[143] D. V. Makarov and H. B. Carter, "The discovery of prostate specific antigen as a biomarker for the early detection of adenocarcinoma of the prostate," *The Journal of urology*, vol. 176, pp. 2383–5, Dec. 2006.

[144] B. Buszewski, M. Kesy, T. Ligor, and A. Amann, "Human exhaled air analytics: biomarkers of diseases," *Biomedical chromatography*, vol. 566, pp. 553–566, 2007.

[145] A. Amann, G. Poupart, S. Telser, M. Ledochowski, A. Schmid, and S. Mechtcheriakov, “Applications of breath gas analysis in medicine,” *International Journal of Mass Spectrometry*, vol. 239, pp. 227–233, Dec. 2004.

[146] P. Fuchs, C. Loeseken, J. K. Schubert, and W. Miekisch, “Breath gas aldehydes as biomarkers of lung cancer,” *International journal of cancer*, vol. 126, pp. 2663–70, June 2010.

[147] M. Hakim, S. Billan, U. Tisch, G. Peng, I. Dvrokind, O. Marom, R. Abdah-Bortnyak, A. Kuten, and H. Haick, “Diagnosis of head-and-neck cancer from exhaled breath,” *British journal of cancer*, vol. 104, pp. 1649–55, May 2011.

[148] R. M. Lequin, “Enzyme immunoassay (EIA)/enzyme-linked immunosorbent assay (ELISA),” *Clinical chemistry*, vol. 51, pp. 2415–8, Dec. 2005.

[149] E. P. Diamandis, “Mass spectrometry as a diagnostic and a cancer biomarker discovery tool: opportunities and potential limitations,” *Molecular and cellular proteomics*, vol. 3, pp. 367–78, Apr. 2004.

[150] P. Dykstra, V. Roy, and C. Byrd, “Microfluidic electrochemical sensor array for characterizing protein interactions with various functionalized surfaces,” *Analytical Chemistry*, vol. 83, pp. 5920–5927, 2011.

[151] J. Liu, R. Bombera, L. Leroy, Y. Roupioz, D. R. Baganizi, P. N. Marche, V. Haguet, P. Mailley, and T. Livache, “Selective individual primary cell capture using locally biofunctionalized micropores,” *PloS one*, vol. 8, p. e57717, Jan. 2013.

[152] A. a. Yanik, M. Huang, O. Kamohara, A. Artar, T. W. Geisbert, J. H. Connor, and H. Altug, “An Optofluidic Nanoplasmonic Biosensor for Direct Detection of Live Viruses from Biological Media,” *Nano letters*, vol. in press, Nov. 2010.

[153] J. W. Grate and H. Abraham, “Solubility interactions coatings for chemical and the design of chemically sensors and arrays selective sorbent,” *Sensors and Actuators B: Chemical*, vol. 3, pp. 85–111, 1991.

[154] W.-D. Zhang and W.-H. Zhang, “Carbon Nanotubes as Active Components for Gas Sensors,” *Journal of Sensors*, vol. 2009, pp. 1–16, 2009.

[155] T. Ahuja and D. Kumar, “Recent progress in the development of nano-structured conducting polymers/nanocomposites for sensor applications,” *Sensors and Actuators B: Chemical*, vol. 136, pp. 275–286, Feb. 2009.

[156] B. Tse Sum Bui and K. Haupt, “Molecularly imprinted polymers: synthetic receptors in bioanalysis,” *Analytical and bioanalytical chemistry*, vol. 398, pp. 2481–92, Nov. 2010.

[157] M. Tudorache and C. Bala, “Biosensors based on screen-printing technology, and their applications in environmental and food analysis,” *Analytical and bioanalytical chemistry*, vol. 388, pp. 565–78, June 2007.

[158] T. Kaufmann and B. J. Ravoo, "Stamps, inks and substrates: polymers in microcontact printing," *Polymer Chemistry*, vol. 1, no. 4, p. 371, 2010.

[159] E. Tekin, P. J. Smith, and U. S. Schubert, "Inkjet printing as a deposition and patterning tool for polymers and inorganic particles," *Soft Matter*, vol. 4, no. 4, p. 703, 2008.

[160] O. D. Renedo, M. a. Alonso-Lomillo, and M. J. A. Martínez, "Recent developments in the field of screen-printed electrodes and their related applications," *Talanta*, vol. 73, pp. 202–19, Sept. 2007.

[161] H. Li, B. Muir, G. Fichet, and W. Huck, "Nanocontact printing: A route to sub-50-nm-scale chemical and biological patterning," *Langmuir*, vol. 19, no. 14, pp. 1963–1965, 2003.

[162] S. Alom Ruiz and C. S. Chen, "Microcontact printing: A tool to pattern," *Soft Matter*, vol. 3, no. 2, p. 168, 2007.

[163] A. Bietsch, J. Zhang, M. Hegner, H. P. Lang, and C. Gerber, "Rapid functionalization of cantilever array sensors by inkjet printing," *Nanotechnology*, vol. 15, pp. 873–880, Aug. 2004.

[164] H. Hu and R. G. Larson, "Evaporation of a Sessile Droplet on a Substrate," *The Journal of Physical Chemistry B*, vol. 106, pp. 1334–1344, Feb. 2002.

[165] J. Perelaer, P. J. Smith, E. van den Bosch, S. S. C. van Grootel, P. H. J. M. Ketelaars, and U. S. Schubert, "The Spreading of Inkjet-Printed Droplets with Varying Polymer Molar Mass on a Dry Solid Substrate," *Macromolecular Chemistry and Physics*, vol. 210, pp. 495–502, Mar. 2009.

[166] A. Yarin, "Drop Impact Dynamics: Splashing, Spreading, Receding, Bouncing," *Annual Review of Fluid Mechanics*, vol. 38, pp. 159–192, Jan. 2006.

[167] E. Tekin and B. D. Gans, "Ink-jet printing of polymers – from single dots to thin film libraries," *Journal of Materials Chemistry*, vol. 14, pp. 2627–2632, 2004.

[168] J. D. Newman and A. P. F. Turner, "Home blood glucose biosensors: a commercial perspective," *Biosensors and bioelectronics*, vol. 20, pp. 2435–53, June 2005.

[169] A. P. F. Turner, "Biosensors: sense and sensibility," *Chemical Society reviews*, vol. 42, pp. 3184–96, Apr. 2013.

[170] Q. Fang, D. Chetwynd, J. Covington, C.-S. Toh, and J. Gardner, "Micro-gas-sensor with conducting polymers," *Sensors and Actuators B: Chemical*, vol. 84, pp. 66–71, Apr. 2002.

[171] H. Bai and G. Shi, "Gas Sensors Based on Conducting Polymers," *Sensors*, vol. 7, pp. 267–307, Mar. 2007.

[172] A. Bielanski, J. Deren, and J. Haber, “Electric conductivity and catalytic activity of semiconducting oxide catalysts,” *Nature*, vol. 179, pp. 668–669, 1957.

[173] S. Morrison, “Selectivity in semiconductor gas sensors,” *Sensors and Actuators*, vol. 12, pp. 425–440, 1987.

[174] B. de Lacy Costello, R. Ewen, N. Ratcliffe, and P. Sivanand, “Thick film organic vapour sensors based on binary mixtures of metal oxides,” *Sensors and Actuators B: Chemical*, vol. 92, pp. 159–166, July 2003.

[175] R. M. Penner, “Chemical sensing with nanowires,” *Annual review of analytical chemistry*, vol. 5, pp. 461–85, Jan. 2012.

[176] P. Bergveld, “The development and application of FET-based biosensors,” *Biosensors*, vol. 2, pp. 15–33, Jan. 1986.

[177] J. Fritz, E. B. Cooper, S. Gaudet, P. K. Sorger, and S. R. Manalis, “Electronic detection of DNA by its intrinsic molecular charge,” *Proceedings of the National Academy of Sciences of the United States of America*, vol. 99, pp. 14142–6, Oct. 2002.

[178] D. Branton, D. W. Deamer, A. Marziali, H. Bayley, S. a. Benner, T. Butler, M. Di Ventra, S. Garaj, A. Hibbs, X. Huang, S. B. Jovanovich, P. S. Krstic, S. Lindsay, X. S. Ling, C. H. Mastrangelo, A. Meller, J. S. Oliver, Y. V. Pershin, J. M. Ramsey, R. Riehn, G. V. Soni, V. Tabard-Cossa, M. Wanunu, M. Wiggin, and J. a. Schloss, “The potential and challenges of nanopore sequencing,” *Nature biotechnology*, vol. 26, pp. 1146–53, Oct. 2008.

[179] M. Wanunu, W. Morrison, and Y. Rabin, “Electrostatic focusing of unlabelled DNA into nanoscale pores using a salt gradient,” *Nature Nanotechnology*, vol. 5, no. 2, pp. 160–165, 2009.

[180] M. a. Cooper, “Optical biosensors in drug discovery,” *Nature reviews. Drug discovery*, vol. 1, pp. 515–28, July 2002.

[181] P. Preechaburana, M. C. Gonzalez, A. Suska, and D. Filippini, “Surface plasmon resonance chemical sensing on cell phones,” *Angewandte Chemie*, vol. 51, pp. 11585–8, Nov. 2012.

[182] L. He and M. Musick, “Colloidal Au-enhanced surface plasmon resonance for ultrasensitive detection of DNA hybridization,” *Journal of the American Chemical Society*, vol. 122, no. 25, pp. 9071–9077, 2000.

[183] F. Vollmer, D. Braun, A. Libchaber, M. Khoshsima, I. Teraoka, and S. Arnold, “Protein detection by optical shift of a resonant microcavity,” *Applied Physics Letters*, vol. 80, no. 21, p. 4057, 2002.

[184] H. Zhu, I. M. White, J. D. Suter, P. S. Dale, and X. Fan, “Analysis of biomolecule detection with optofluidic ring resonator sensors.,” *Optics express*, vol. 15, pp. 9139–46, July 2007.

[185] C. Mah and K. B. Thurbide, “Acoustic methods of detection in gas chromatography,” *Journal of Separation Science*, vol. 29, pp. 1922–1930, Aug. 2006.

[186] K. A. Marx, “Quartz crystal microbalance: a useful tool for studying thin polymer films and complex biomolecular systems at the solution-surface interface,” *Biomacromolecules*, vol. 4, no. 5, pp. 1099–120, 2003.

[187] K. Länge, B. E. Rapp, and M. Rapp, “Surface acoustic wave biosensors: a review,” *Analytical and bioanalytical chemistry*, vol. 391, pp. 1509–19, July 2008.

[188] P. Si, J. Mortensen, A. Komolov, J. Denborg, and P. J. Mø ller, “Polymer coated quartz crystal microbalance sensors for detection of volatile organic compounds in gas mixtures.,” *Analytica chimica acta*, vol. 597, pp. 223–30, Aug. 2007.

[189] A. Boisen and T. Thundat, “Design and fabrication of cantilever array biosensors,” *Materials Today*, vol. 12, pp. 32–38, Sept. 2009.

[190] B. Ilic, D. Czaplewski, M. Zalalutdinov, H. G. Craighead, P. Neuzil, C. Campagnolo, and C. Batt, “Single cell detection with micromechanical oscillators,” *Journal of Vacuum Science and Technology B: Microelectronics and Nanometer Structures*, vol. 19, no. 6, p. 2825, 2001.

[191] M. Li, H. X. Tang, and M. L. Roukes, “Ultra-sensitive NEMS-based cantilevers for sensing, scanned probe and very high-frequency applications,” *Nature Nanotechnology*, vol. 2, pp. 114–20, Feb. 2007.

[192] G. Abadal, Z. Davis, B. Helbo, and X. Borrise, “Electromechanical model of a resonating nano-cantilever-based sensor for high-resolution and high-sensitivity mass detection,” *Nanotechnology*, vol. 12, pp. 100–104, 2001.

[193] S. Shin, J. P. Kim, S. J. Sim, and J. Lee, “A multisized piezoelectric microcantilever biosensor array for the quantitative analysis of mass and surface stress,” *Applied Physics Letters*, vol. 93, no. 10, p. 102902, 2008.

[194] A. Loui, T. V. Ratto, T. S. Wilson, S. K. McCall, E. V. Mukerjee, A. H. Love, and B. R. Hart, “Chemical vapor discrimination using a compact and low-power array of piezoresistive microcantilevers,” *The Analyst*, vol. 133, pp. 608–15, May 2008.

[195] L. Pinnaduwage, T. Thundat, J. Hawk, D. Hedden, P. Britt, E. Houser, S. Stepnowski, R. McGill, and D. Bubb, “Detection of 2,4-dinitrotoluene using microcantilever sensors,” *Sensors and Actuators B: Chemical*, vol. 99, pp. 223–229, May 2004.

[196] Y. Arntz, J. Seelig, H. Lang, and J. Zhang, “Label-free protein assay based on a nanomechanical cantilever array,” *Nanotechnology*, vol. 86, no. 14, 2003.

[197] M. Calleja, J. Tamayo, A. Johansson, P. Rasmussen, L. M. Lechuga, and A. Boisen, “Polymeric Cantilever Arrays for Biosensing Applications,” *Sensor Letters*, vol. 1, pp. 20–24, Dec. 2003.

[198] J. L. Arlett, E. B. Myers, and M. L. Roukes, “Comparative advantages of mechanical biosensors,” *Nature nanotechnology*, vol. 6, pp. 203–15, Apr. 2011.

[199] M. McCulloch, T. Jezierski, M. Broffman, A. Hubbard, K. Turner, and T. Janecki, “Diagnostic accuracy of canine scent detection in early- and late-stage lung and breast cancers,” *Integrative cancer therapies*, vol. 5, pp. 30–9, Mar. 2006.

[200] J.-N. Cornu, G. Cancel-Tassin, V. Ondet, C. Girardet, and O. Cussenot, “Olfactory detection of prostate cancer by dogs sniffing urine: a step forward in early diagnosis,” *European urology*, vol. 59, pp. 197–201, Feb. 2011.

[201] R. Moncrieff, “An instrument for measuring and classifying odors,” *Journal of applied physiology*, vol. 16, no. 4, pp. 742–749, 1961.

[202] K. Persaud and G. Dodd, “Analysis of discrimination mechanisms in the mammalian olfactory system using a model nose,” *Nature*, vol. 299, pp. 352–355, 1982.

[203] F. Rock, N. Barsan, and U. Weimar, “Electronic nose: current status and future trends,” *Chemical reviews*, vol. 108, pp. 705–25, Feb. 2008.

[204] A. K. Deisingh, D. C. Stone, and M. Thompson, “Applications of electronic noses and tongues in food analysis,” *International Journal of Food Science and Technology*, vol. 39, pp. 587–604, June 2004.

[205] A. P. Turner and N. Magan, “Electronic noses and disease diagnostics,” *Nature reviews. Microbiology*, vol. 2, pp. 161–6, Feb. 2004.

[206] G. Peng, U. Tisch, O. Adams, M. Hakim, N. Shehada, Y. Y. Broza, S. Billan, R. Abdah-Bortnyak, A. Kuten, and H. Haick, “Diagnosing lung cancer in exhaled breath using gold nanoparticles,” *Nature Nanotechnology*, vol. 4, pp. 669–73, Oct. 2009.

[207] G. Peng, M. Hakim, Y. Y. Broza, S. Billan, R. Abdah-Bortnyak, A. Kuten, U. Tisch, and H. Haick, “Detection of lung, breast, colorectal, and prostate cancers from exhaled breath using a single array of nanosensors,” *British journal of cancer*, vol. 103, pp. 542–51, Aug. 2010.

[208] C. Jin and E. T. Zellers, “Limits of recognition for binary and ternary vapor mixtures determined with multitransducer arrays,” *Analytical chemistry*, vol. 80, pp. 7283–93, Oct. 2008.

[209] C. Jin and P. Kurzawski, “Evaluation of multitransducer arrays for the determination of organic vapor mixtures,” *Analytical chemistry*, vol. 80, no. 1, pp. 227–236, 2008.

[210] J. Park, W. Groves, and E. Zellers, “Vapor recognition with small arrays of polymer-coated microsensors. A comprehensive analysis,” *Analytical chemistry*, vol. 71, no. 17, pp. 3877–3886, 1999.

[211] M. Hsieh and E. Zellers, "Limits of recognition for simple vapor mixtures determined with a microsensor array," *Analytical chemistry*, vol. 76, no. 7, pp. 1885–1895, 2004.

[212] C. Herring, "Some theorems on the free energies of crystal surfaces," *Physical Review*, vol. 82, no. 1, 1951.

[213] J. Vermaak, C. Mays, and D. Kuhlmann-Wilsdorf, "On surface stress and surface tension: I. Theoretical considerations," *Surface Science*, vol. 12, pp. 128–133, 1968.

[214] F. Spaepen, "Interfaces and stresses in thin films," *Acta Materialia*, vol. 48, pp. 31–42, Jan. 2000.

[215] P. J. Burnett and T. F. Page, "An investigation of ion implantation-induced near-surface stresses and their effects in sapphire and glass," *Journal of Materials Science*, vol. 20, no. 12, pp. 4624–4646, 1985.

[216] D. Ramos, J. Mertens, M. Calleja, and J. Tamayo, "Study of the origin of bending induced by bimetallic effect on microcantilever," *Sensors*, vol. 7, pp. 1757–1765, 2007.

[217] R. Mukhopadhyay, M. Lorentzen, J. Kjems, and F. Besenbacher, "Nanomechanical sensing of DNA sequences using piezoresistive cantilevers," *Langmuir*, vol. 21, pp. 8400–8, Aug. 2005.

[218] J. Fritz, "Translating Biomolecular Recognition into Nanomechanics," *Science*, vol. 288, pp. 316–318, Apr. 2000.

[219] V. Tabard-Cossa, M. Godin, L. Beaulieu, and P. Grütter, "A differential microcantilever-based system for measuring surface stress changes induced by electrochemical reactions," *Sensors and Actuators B: Chemical*, vol. 107, pp. 233–241, May 2005.

[220] X. Fan, "Mechanics of Moisture for Polymers : Fundamental Concepts and Model Study," in *9th. Int. Conf. on Thermal, Mechanical and Multiphysics Simulation and Experiments in Micro-Electronics and Micro-Systems*, pp. 1–14, 2008.

[221] S. M. Heinrich, M. J. Wenzel, F. Josse, and I. Dufour, "An analytical model for transient deformation of viscoelastically coated beams: Applications to static-mode microcantilever chemical sensors," *Journal of Applied Physics*, vol. 105, no. 12, p. 124903, 2009.

[222] S. Yoon, "Measurement of the Hygroscopic Swelling Coefficient of Thin Film Polymers Used in Semiconductor Packaging," *IEEE Transactions on Components and Packaging Technologies*, vol. 33, pp. 340–346, June 2010.

[223] M.-C. Ferrari, E. Piccinini, M. Giacinti Baschetti, F. Doghieri, and G. C. Sarti, "Solvent-Induced Stresses during Sorption in Glassy Polycarbonate: Experimental Analysis and Model Simulation for a Novel Bending Cantilever Apparatus," *Industrial and Engineering Chemistry Research*, vol. 47, pp. 1071–1080, Feb. 2008.

[224] Q. Liu, X. Wang, and D. De Kee, “Mass transport through swelling membranes,” *International Journal of Engineering Science*, vol. 43, pp. 1464–1470, Dec. 2005.

[225] G. Yoshikawa, “Mechanical analysis and optimization of a microcantilever sensor coated with a solid receptor film,” *Applied Physics Letters*, vol. 98, no. 17, p. 173502, 2011.

[226] G. G. Stoney, “The tension of metallic films deposited by electrolysis,” *Proceedings of the Royal Society of London Series A*, vol. 82, no. 553, pp. 172–175, 1909.

[227] J. E. Sader, “Surface stress induced deflections of cantilever plates with applications to the atomic force microscope: Rectangular plates,” *Journal of Applied Physics*, vol. 89, no. 5, p. 2911, 2001.

[228] H. Hencke, “Piezoresistive sensors: the pressure goes on,” *Sensor Review*, vol. 9, no. 3, pp. 137–139, 1989.

[229] F. T. Geyling and J. J. Forst, “Semiconductor Strain Transducers,” *The Bell System Technical Journal*, vol. 39, pp. 705–731, 1960.

[230] A. Johansson, M. Calleja, P. Rasmussen, and A. Boisen, “SU-8 cantilever sensor system with integrated readout,” *Sensors and Actuators A: Physical*, vol. 123-124, pp. 111–115, Sept. 2005.

[231] C. Smith, “Piezoresistance effect in germanium and silicon,” *Physical Review*, vol. 94, no. 1, p. 42, 1954.

[232] Y. Kanda, “A graphical representation of the piezoresistance coefficients in silicon,” *Transactions on Electron Devices*, vol. 29, pp. 64–70, Jan. 1982.

[233] J. Richter, J. Pedersen, M. Brandbyge, E. V. Thomsen, and O. Hansen, “Piezoresistance in p-type silicon revisited,” *Journal of Applied Physics*, vol. 104, no. 2, p. 023715, 2008.

[234] S. M. Sze and M. K. Lee, *Semiconductor devices.*

[235] J. Williams, “Ion implantation of semiconductors,” *Materials Science and Engineering: A*, vol. 253, pp. 8–15, Sept. 1998.

[236] J. Gibbons, “Ion implantation in semiconductors—Part II: Damage production and annealing,” *Proceedings of the IEEE*, vol. 6, no. 9, 1972.

[237] J. D. Souza, “The doping of silicon with boron by rapid thermal processing,” *Semiconductor Science and Technology*, vol. 277, 1988.

[238] W. Yoo and T. Fukada, “Rapid thermal annealing of arsenic implanted silicon wafers,” *Extended Abstracts of International Workshop on Junction Technology*, vol. -, pp. 71–74, 2001.

[239] G. Yang and H. Xie, "Mechanical Derivation of the Longitudinal and Transverse Piezoresistive Coefficient on Piezoresistive Pressure Sensor," *Procedia Engineering*, vol. 29, pp. 1612–1617, Jan. 2012.

[240] A. Barlian, W.-T. Park, J. Mallon, A. Rastegar, and B. Pruitt, "Review: semiconductor piezoresistance for microsystems," *Proceedings of the IEEE. Institute of Electrical and Electronics Engineers*, vol. 97, pp. 513–552, Jan. 2009.

[241] G. Yoshikawa, H.-P. Lang, T. Akiyama, L. Aeschimann, U. Staufer, P. Vettiger, M. Aono, T. Sakurai, and C. Gerber, "Sub-ppm detection of vapors using piezoresistive microcantilever array sensors," *Nanotechnology*, vol. 20, p. 015501, Jan. 2009.

[242] J. C. Doll, S.-J. Park, and B. L. Pruitt, "Design optimization of piezoresistive cantilevers for force sensing in air and water," *Journal of applied physics*, vol. 106, p. 64310, Sept. 2009.

[243] S.-J. Park, J. C. Doll, and B. L. Pruitt, "Piezoresistive cantilever performance-part I: analytical model for sensitivity," *Journal of Microelectromechanical Systems*, vol. 19, pp. 137–148, Feb. 2010.

[244] S.-J. Park, J. C. Doll, A. J. Rastegar, and B. L. Pruitt, "Piezoresistive cantilever performance-part II: optimization," *Journal of Microelectromechanical Systems*, vol. 19, pp. 149–161, Jan. 2010.

[245] P. A. Rasmussen, O. Hansen, and A. Boisen, "Cantilever surface stress sensors with single-crystalline silicon piezoresistors," *Applied Physics Letters*, vol. 86, no. 20, p. 203502, 2005.

[246] N. L. Privorotskaya and W. P. King, "The mechanics of polymer swelling on microcantilever sensors," *Microsystem Technologies*, vol. 15, pp. 333–340, July 2008.

[247] M. Yang, X. Zhang, K. Vafai, and C. S. Ozkan, "High sensitivity piezoresistive cantilever design and optimization for analyte-receptor binding," *Journal of Micromechanics and Microengineering*, vol. 13, pp. 864–872, Nov. 2003.

[248] J. Mallon and A. Rastegar, "Low 1/f noise, full bridge, microcantilever with longitudinal and transverse piezoresistors," *Applied physics letters*, vol. 92, no. 3, p. 033508, 2008.

[249] J. Harley and T. Kenny, "1/f noise considerations for the design and process optimization of piezoresistive cantilevers," *Journal of Microelectromechanical Systems*, vol. 9, no. 2, pp. 226–235, 2000.

[250] F. Hooge, "1 / f Noise Sources," *IEEE Transactions on Electron Devices*, vol. 41, no. 11, pp. 1926–1935, 1994.

[251] L. K. J. Vandamme and W. M. G. Bokhoven, "Conductance noise investigations with four arbitrarily shaped and placed electrodes," *Applied Physics*, vol. 14, pp. 205–215, Oct. 1977.

[252] F. Morin, T. Geballe, and C. Herring, “Temperature dependence of the piezoresistance of high-purity silicon and germanium,” *Physical Review*, vol. 1104, no. 1955, 1957.

[253] A. Loui, S. Elhadj, D. J. Sirbuly, S. K. McCall, B. R. Hart, and T. V. Ratto, “An analytic model of thermal drift in piezoresistive microcantilever sensors,” *Journal of Applied Physics*, vol. 107, no. 5, p. 054508, 2010.

[254] J. Thaysen, a. Boisen, O. Hansen, and S. Bouwstra, “Atomic force microscopy probe with piezoresistive read-out and a highly symmetrical Wheatstone bridge arrangement,” *Sensors and Actuators A: Physical*, vol. 83, pp. 47–53, May 2000.

[255] M. Z. Ansari and C. Cho, “On self-heating in piezoresistive microcantilevers with short piezoresistor,” *Journal of Physics D: Applied Physics*, vol. 44, p. 285402, July 2011.

[256] J. C. Doll, E. a. Corbin, W. P. King, and B. L. Pruitt, “Self-heating in piezoresistive cantilevers,” *Applied physics letters*, vol. 98, p. 223103, May 2011.

[257] M. Z. Ansari and C. Cho, “A conduction–convection model for self-heating in piezoresistive microcantilever biosensors,” *Sensors and Actuators A: Physical*, vol. 175, pp. 19–27, Mar. 2012.

[258] J. Mertens, M. Calleja, D. Ramos, A. Taryn, and J. Tamayo, “Role of the gold film nanostructure on the nanomechanical response of microcantilever sensors,” *Journal of Applied Physics*, vol. 101, no. 3, p. 034904, 2007.

[259] F. Bosco, M. Bache, E.-T. Hwu, C. Chen, S. Andersen, K. Nielsen, S. Keller, J. Jeppesen, I.-S. Hwang, and A. Boisen, “Statistical analysis of DNT detection using chemically functionalized microcantilever arrays,” *Sensors and Actuators B: Chemical*, vol. 171-172, pp. 1054–1059, Aug. 2012.

[260] G. Yoshikawa, T. Akiyama, S. Gautsch, P. Vettiger, and H. Rohrer, “Nanomechanical membrane-type surface stress sensor,” *Nano Letters*, vol. 11, pp. 1044–8, Mar. 2011.

[261] L. Aeschimann, A. Meister, T. Akiyama, B. W. Chui, P. Niedermann, H. Heinzelmann, N. F. De Rooij, U. Staufer, and P. Vettiger, “Scanning probe arrays for life sciences and nanobiology applications,” *Microelectronic Engineering*, vol. 83, pp. 1698–1701, Apr. 2006.

[262] S. SHAPIRO, “Carrier mobilities m silicon empirically related to doping and field,” *Proceedings of the IEEE*, vol. December, pp. 2192–2193, 1967.

[263] O. Hansen and A. Boisen, “Noise in piezoresistive atomic force microscopy,” *Nanotechnology*, vol. 10, pp. 51–60, Mar. 1999.

[264] M. Matsuguchi, S. Umeda, Y. Sadaoka, and Y. Sakai, “Characterization of polymers for a capacitive-type humidity sensor based on water sorption behavior,” *Sensors and Actuators B: Chemical*, vol. 49, pp. 179–185, July 1998.

[265] R. McKendry, J. Zhang, Y. Arntz, T. Strunz, M. Hegner, H. P. Lang, M. K. Baller, U. Certa, E. Meyer, H.-J. Güntherodt, and C. Gerber, “Multiple label-free biodetection and quantitative DNA-binding assays on a nanomechanical cantilever array,” *Proceedings of the National Academy of Sciences of the United States of America*, vol. 99, pp. 9783–8, July 2002.

[266] S. Wu, T. Nan, C. Xue, T. Cheng, H. Liu, B. Wang, Q. Zhang, and X. Wu, “Mechanism and enhancement of the surface stress caused by a small-molecule antigen and antibody binding,” *Biosensors and bioelectronics*, vol. 48, pp. 67–74, Oct. 2013.

[267] A. Bajtarevic, C. Ager, M. Pienz, M. Klieber, K. Schwarz, M. Ligor, T. Ligor, W. Filipiak, H. Denz, M. Fiegl, W. Hilbe, W. Weiss, P. Lukas, H. Jamnig, M. Hackl, A. Haidenberger, B. Buszewski, W. Miekisch, J. Schubert, and A. Amann, “Noninvasive detection of lung cancer by analysis of exhaled breath,” *BMC cancer*, vol. 9, p. 348, Jan. 2009.

[268] M. Erb, D. Balmer, E. S. De Lange, G. Von Merey, C. Planchamp, C. a. M. Robert, G. Röder, I. Sobhy, C. Zwahlen, B. Mauch-Mani, and T. C. J. Turlings, “Synergies and trade-offs between insect and pathogen resistance in maize leaves and roots,” *Plant, cell and environment*, vol. 34, pp. 1088–103, July 2011.

[269] F. Huber, H. P. Lang, N. Backmann, D. Rimoldi, and C. Gerber, “Direct detection of a BRAF mutation in total RNA from melanoma cells using cantilever arrays,” *Nature Nanotechnology*, vol. 8, pp. 125–9, Feb. 2013.

Acknowledgements

A thesis is never the result of a single person's work and this one is no exception. During the four years of my PhD, I received the help of many people. I would first like to thank my thesis director, Professor Nico de Rooij, for letting me be part of his laboratory. The SAMLAB was not only a great environment to work in, it was also a fantastic place to live in and Nico de Rooij helped in many ways to create a friendly atmosphere. I would like to acknowledge my thesis co-director and supervisor Dr. Sebastian Gautsch, who has been a great supervisor and a fantastic person. He managed to guide me with pertinent advice and suggestions while leaving me the freedom to experiment new things, sometimes with failure, sometimes with success. He made me feel responsible for my project, which helped me take initiatives and plan my work. I would also like to warmly thank Dr. Peter Vettiger who followed my work regularly, always with great interest and positivity. For his numerous advice, scientific and personal, and for his strong ethics and values as a scientist, I consider him like a mentor.

There were several times when I felt stuck in front of a technical problem and I could always find someone to help me resolve it. During my first semester project, back in 2007, I had already the task to develop the analytical model of a cantilever deflection and I was helped by Professor Thomas Gmür of the Mechanical Department at EPFL. I thank him again today for having given me additional help for the analytical modelling of my cantilevers. I would also like to thank Dr. Hugo Rothuizen from IBM Research-Zürich for his help and advice with Ansys. Finally, I want to acknowledge all the people who helped me during the microfabrication of my devices. The staff of CSEM Microtechnology Division was instrumental in the success of my thesis and I thank them all, especially Pierre-André Clerc for his excellent work on dry etching, Stéphane Ischer for his numerous oxidations and depositions, as well as Dr. Sébastien Lani for his help and advice throughout all my processes. I would also like to warmly thank Dr. Laure Aeschimann from Nanoworld AG for her technical support, her availability, but most importantly for all the laughs that we shared inside and outside the cleanroom.

It was a great pleasure to work and share everyday moments with my colleagues at SAMLAB. Their positive emulation has been a powerful mean to develop new ideas or to solve problems. I do not forget either our numerous after-work events that heavily contributed to create and reinforce our bonds. For all these reasons, I thank all of them. I would like to thank particularly my office mates Yexian Wu and Rokhaya Gueye for their laughs and cheerfulness. I also thank Dr. Terunobu Akiyama for his precious help and advice during the microfabrication of my

devices as he took a significant part in establishing the processes, as well as Dr. Peter Van der Wal for his chemistry expertise that helped avoid many catastrophes. I express my gratitude to Dr. Giorgio Mattana for his advice on chemical sensors characterisation. I am grateful to him for his kindness and unconditional help despite him being very busy. As I am at the end of my thesis, I have a special thought for Dr. Alexandra Homsy who literally pushed me into this crazy experience. She played an important role in my PhD commencement at SAMLAB and I thank her for her support and encouragement.

There have also been many people directly involved in my project. I would like to express my gratitude to Dr. Cristina Martin-Olmos, Dr. Mélanie Favre, and Dr. André Meister from CSEM for the fruitful discussions on cell force spectroscopy and all the material kindly given for my thesis. Similarly, I would like to thank Dr. Hans Peter Lang and Andreas Tonin from the University of Basel for their help in the functionalisation and characterisation of my devices and for their permission to integrate their results on the breath analyses in my thesis. While Dr. Genki Yoshikawa from the International Center for Materials Nanoarchitectonics in Tsukuba (Japan) was not part of the PATLiSci project, our collaboration on the MSS has been instrumental in its success. I am grateful to him for his continuous help and the fruitful discussions we had together about cantilever-based sensors as well as all the theory behind these devices. I would also like to acknowledge Bartjan den Hartogh from FemtoTools AG and Emmanuel Paris from Bruker AXS S.A.S. for their assistance in measuring the spring constants of my cantilevers.

In order for our professional life to be really rewarding, I think that it also needs to be balanced with a good social and personal life. Thanks to all my friends, I could evacuate my frustration or share my victories against Murphy around a nice bottle of wine. Thanks as well to my sister Olivia for being so close and for all the small things that make her a great little sister. I would also like to thank my wife Danielle for her love and the strong complicity that we share. I highly value her unconditional support throughout all these years, especially during the last couple of months. Finally, I would like to tell my parents, Evelyne and Denis, how much I owe them. If I stand where I am today, it is because of their inspiration and guidance, as well as their patience and love.

Neuchâtel, 10 February 2014 F. L.

Frédéric Loizeau

Ingénieur EPFL en Microtechnique

Av. de France 5
1004 Lausanne, Switzerland
+41 76 440 12 13
frederic.loizeau@gmail.com

29 years old
Married
French and Swiss
Born in La Chaux-de-Fonds, Switzerland

Education

• 2010 – Present	École Polytechnique Fédérale de Lausanne, Lausanne, Switzerland. **PhD thesis on "Microfabricated Sensor Arrays for Life Science Applications"**
• 2008	University of British Columbia, Vancouver, Canada. Masters thesis on "Inkjet Printing of Living Cells into 3D Scaffolds"
• 2002 – 2008	EPFL, Lausanne, Switzerland. Bachelor and Masters in Micro-engineering

Professional experience

• 2010 – Present	EPFL, Neuchâtel, Switzerland. PhD student and teaching assistant. Development and fabrication of advanced microsystems in a class 100 clean room. **Presentations at several international conferences (MEMS2013, Transducers2013, Eurosensors, etc.). Peer-reviewed publications.**
• 2008 – 2010	FiveCo Innovative Engineering, Renens, Switzerland. R&D project leader. Design of mechatronics devices for various customers in Switzerland.

Extracurricular activities

• 2004	Vice-president and logistics manager, Sysmic, student festival (EPFL)
• 2003	Catering, Balélec festival (EPFL)

Skills

- Technology: Microengineering, cleanroom processing, piezoresistive sensors, inkjet printing, electronics, bio-chemical sensing, mechanics
- Simulation: Ansys APDL (mechanical, electrical, and piezoresistive simulations)
- Computer: Latex, MS Office, Assembler, C, C++, Matlab, Labview
- CAD: Solidworks, Clewin, Expert
- Soft skills: Independent, **creative**, flexible; accept and learn from feedback

Languages

French: Mother tongue
English: Fluent both oral and written
German: Conversational

Personal interests

- Contemporary design
- Chocolate cakes
- Winter sports
- Going to festivals (music, animated movies, street theatre)